

AD A044509

**TABULATION OF IMPURITY ABSORPTION
SPECTRA - ULTRAVIOLET AND VISIBLE**
VOLUME I

M. SPARKS, PRINCIPAL INVESTIGATOR, 213/451-9916

H. VORA

M. FLANNERY

XONICS, INCORPORATED

SANTA MONICA, CALIFORNIA 90401

NINTH TECHNICAL REPORT
30 JUNE 1977

DISTRIBUTION STATEMENT A

Approved for public release;
Distribution Unlimited

**CONTRACT TITLE: THEORETICAL STUDIES OF HIGH-POWER
ULTRAVIOLET AND INFRARED MATERIALS**

CONTRACT NO. DAHC 15-73-C-0127

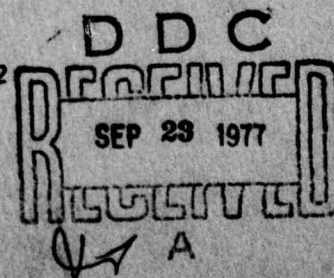
EFFECTIVE DATE OF CONTRACT: 7 DECEMBER 1972

CONTRACT EXPIRATION DATE: 31 MARCH 1978

PREPARED FOR
DEFENSE SUPPLY SERVICE - WASHINGTON, D.C.

SPONSORED BY DEFENSE ADVANCED RESEARCH PROJECTS AGENCY
DARPA ORDER NO. 1989, AMENDMENT NO. 10, PROGRAM CODE NO. 6D10

AD No. _____
DDC FILE COPY



Unclassified

SECURITY CLASSIFICATION OF THIS PAGE (When Data Entered)

REPORT DOCUMENTATION PAGE		READ INSTRUCTIONS BEFORE COMPLETING FORM
1. REPORT NUMBER	2. GOVT ACCESSION NO.	3. RECIPIENT'S CATALOG NUMBER
4. TITLE (and Subtitle) TABULATION OF IMPURITY ABSORPTION SPECTRA - ULTRAVIOLET AND VISIBLE, VOLUME I.		5. TYPE OF REPORT Ninth Technical Report, 1 Jan - 1977 through 30 June 1977, 6. PERFORMING ORG. REPORT NUMBER
7. AUTHOR(s) H. Vora, M. Flannery, and M. Sparks		8. CONTRACT OR GRANT NUMBER(s) DAHC 15-73-C-0127, W.DARPA Order 1969
9. PERFORMING ORGANIZATION NAME AND ADDRESS Xonics, Incorporated 1333 Ocean Avenue Santa Monica, California 90401		10. PROGRAM ELEMENT, PROJECT, TASK AREA & WORK UNIT NUMBERS
11. CONTROLLING OFFICE NAME AND ADDRESS Defense Supply Service Room 1D245 - The Pentagon Washington, D.C. 20310		12. REPORT DATE 30 June 1977
14. MONITORING AGENCY NAME & ADDRESS (if different from Controlling Office) Defense Advanced Research Projects Agency 1400 Wilson Boulevard Arlington, Virginia 22209		13. NUMBER OF PAGES 258 (12) 259A
15. SECURITY CLASS. (of this report) Unclassified		15a. DECLASSIFICATION DOWNGRADING SCHEDULE
16. DISTRIBUTION STATEMENT (of this Report) This document may be further distributed only with specific prior approval of the Defense Supply Service, Washington, D.C.		
<div style="border: 1px solid black; padding: 5px; text-align: center;"> DISTRIBUTION STATEMENT A Approved for public release; Distribution Unlimited </div>		
17. DISTRIBUTION STATEMENT (of the abstract entered in Block 20, if different from Report)		
18. SUPPLEMENTARY NOTES		
19. KEY WORDS (Continue on reverse side if necessary and identify by block number) impurity absorption, ultraviolet absorption, visible absorption, LiF, NaF, KCl, MgF ₂ , CaF ₂ , MgO, Al ₂ O ₃ , SiO ₂ , silicate glasses, spectra tabulation, laser windows, laser materials		
20. ABSTRACT (Continue on reverse side if necessary and identify by block number) The optical-absorption spectra of commonly occurring impurities in several ultraviolet-transparent solids are tabulated and discussed, and the assignments of the absorption bands are reviewed. The wavelength region included extends from the very near infrared, at 1 μ m (0.124 eV), through the vacuum-ultraviolet region. The host materials covered are LiF, NaF, KCl, MgF ₂ , CaF ₂ , MgO, Al ₂ O ₃ , SiO ₂ , and silicate glasses. The results are presented in a way useful in locating impurities that absorb at specified wavelengths, in determining the		

DD FORM 1 JAN 73 1473

EDITION OF 1 NOV 65 IS OBSOLETE

Unclassified

SECURITY CLASSIFICATION OF THIS PAGE (When Data Entered)

409988

DDC
RECEIVED
SEP 23 1977
A

Unclassified

SECURITY CLASSIFICATION OF THIS PAGE(When Data Entered)

wavelength region in which a specific impurity absorbs, and for general use in several current and envisioned programs, including: reducing the residual optical absorption of materials in order to increase the power of ultraviolet and visible lasers and to increase the resistance of materials to damage by high-intensity radiation in laboratory and space environments; understanding the origin of the residual absorption in order to provide guidance for further improvement of materials and to estimate the expected materials limits set by residual imperfections; and reducing the absorptance of dielectric reflectors and antireflection coatings. The coatings problem is especially important since it is believed that impurities in deposited films is a major factor limiting the absorptance of both types of coatings, and high-power reflectors require the use of dielectric coatings in order to obtain low absorptance. The features of the spectra are summarized in tables and figures. Peak positions, approximate line widths, and when available, the oscillator strengths of all bands are summarized in correlation-type graphs for each material. The intrinsic and extrinsic absorption spectra are categorized according to the type of host material, e.g., alkali halides, alkaline-earth halides, and oxides, and according to the type of impurity, e.g., halogens, H and D centers, OH and OD centers, O, S, Se centers, color centers, radiation-induced defect centers, transition-metal ions, and rare-earth ions. Comparisons of results for various host materials, and also for various impurities, are given in the form of tables and figures whenever possible.

ACCESSION FOR

MTAB White Section ☒
DUC Buff Section ☐
UNCLASSIFIED ☐
JUSTIFICATION

Letter on file

BY

DISTRIBUTION/AVAILABILITY CODES

Dist. AVAIL. AND OF SPECIAL

A

Unclassified

SECURITY CLASSIFICATION OF THIS PAGE(When Data Entered)

PREFACE

This Ninth Technical Report describes the work performed on Contract Number DAHC15-73-C-0127 on Theoretical Studies of High-Power Ultraviolet and Infrared Materials during the period from 1 January 1977 through 30 June 1977. The work on the current contract is a continuation of that of the previous Contract Number DAHC15-72-C-0129.

In view of the increasing importance of impurity absorption in high-power laser materials for use as windows, this report and the following report are dedicated to a tabulation of impurity spectra of important materials in the ultraviolet and visible regions. The previous infrared impurity-absorption study, which emphasized the CO_2 -laser wavelengths near $10.6\text{ }\mu\text{m}$, is being updated to include a greater number of impurities, particularly those of importance at other infrared wavelengths. The results, along with the results of our other ongoing programs will be presented in subsequent reports. Previously reported results are not repeated in the present report.

The following investigators contributed to this report:

Dr. H. Vora, consultant, University of Washington, Seattle, Wash.

Dr. T. G. Stoebe, consultant, University of Washington, Seattle, Wash.

Mr. M. R. Flannery, research assistant

Mr. Eugene Loh, Jr., research assistant

Dr. M. Sparks, principal investigator

Lona Case and Frances Rossiter typed the manuscript and prepared the art work with their usual skill and care.

TABLE OF CONTENTS

Section	Page
PREFACE	iii
LIST OF ILLUSTRATIONS	x
LIST OF TABLES	xxvii
I INTRODUCTION.	1
II ALKALI HALIDES.	60
A. Intrinsic Properties of Alkali Halides	60
B. Comparisons of Alkali-Halide Impurity Spectra.	68
C. Lithium Fluoride	82
1. Lowest energy exciton peak	82
2. Purity and storage of LiF.	82
3. U center in LiF.	93
4. The OH^- absorption peak in LiF	96
5. Oxygen-doped LiF	96
6. Transition-metal ions in LiF	96
a. Ti^{3+} and Ti^{2+} in LiF	100
b. V^{2+} in LiF	109
c. Cr in LiF.	109
d. Mn^{2+} in LiF.	109
e. Fe^{2+} in LiF.	112
f. Co^{2+} in LiF.	113
g. Ni^{2+} in LiF.	113
7. Trapped electron and hole centers in LiF	113
a. F center in LiF.	113
b. F-related centers.	117

TABLE OF CONTENTS - VOLUME I (Cont.)

<u>Section</u>	<u>Page</u>
II	
c. V_K center, or self-trapped hole, in LiF	117
d. V_3 center, or F_3^- molecular ion, in LiF. . . .	117
e. Color centers in magnesium-doped LiF.	121
8. Colloid bands in LiF.	125
D. Sodium Fluoride	134
1. Negative-ion impurities in NaF.	137
a. OH^- , O_2^- and H^- ions and F and M centers in NaF.	138
b. Cl^- and Br^- ions in NaF	145
2. Transition-metal ions in NaF.	151
a. Titanium.	155
b. Vanadium.	158
c. Manganese	158
d. Cobalt.	158
e. Nickel.	159
3. VUV spectra of some commercial-purity and high-purity NaF	159
4. Additive and electrolytic coloration of NaF	164
E. Potassium Chloride.	166
1. Intrinsic exciton	166
2. U, U_1 , U_2 , α , OH^- and O^- bands in KCl	166
3. H and H^- in KCl	166
4. OH in KCl	174
5. OD^- and OH^- in KCl.	176

TABLE OF CONTENTS - VOLUME I (Cont.)

<u>Section</u>		<u>Page</u>
II	6. O_2^- , O^- and O^{2-} in KCl.	179
	7. Correlation of O^{2-} bands with the F and L bands in KCl.	181
	8. Photochemical production of O^- centers from O^{2-} centers.	186
	9. Annealing KCl crystals containing O^{2-}	189
	10. SH^- , S^- and S^{2-} in KCl.	191
	11. Photochemical conversion of SH^- to S^-	191
	12. Reduction of SH^- with F centers to produce S^{2-}	196
	13. Photochemical bleaching of S^{2-} in KCl	198
	14. Annealing of S^{2-} centers in KCl	200
	15. Comparison of SH^- and OH^- centers	203
	16. Photochemical conversion of SH^- to S^- in KCl.	203
	17. SeH^- in KCl	204
	18. Photochemical conversion of SeH^- to Se^-	204
	19. Reduction of SeH^- by F centers, and thermal annealing	208
	20. Spin-orbit splitting of the selenium bands.	210
	21. Br^- and I^- in KCl	212
	CONTENTS OF PRESENT AND PREVIOUS REPORTS	219
	LIST OF PUBLICATIONS	223

TABLE OF CONTENTS - VOLUME II*

<u>Section</u>	<u>Page</u>
III ALKALINE EARTH FLUORIDES	
A. Intrinsic Properties of Calcium Fluoride	
B. Calcium Fluoride	
1. O^{2-} and S^{2-} in CaF_2	
2. Transition-metal ions in CaF_2	
a. Mn^{2+} in CaF_2	
b. Co^{2+} in CaF_2	
c. Ni^{2+} in CaF_2	
3. Rare-earth ions in CaF_2	
a. Trivalent rare-earth ions in CaF_2	
b. Divalent rare-earth ions in CaF_2	
c. Photochromic centers in CaF_2	
4. Actinide ions in CaF_2	
a. U^{4+} and U^{6+} in CaF_2	
b. Np^{3+} in CaF_2	
c. Pu^{3+} and Pu^{4+} in CaF_2	
d. Am^{2+} and Am^{3+} in CaF_2	
e. Cm^{3+} and Cm^{4+} in CaF_2	
f. Es^{3+} and Es^{2+} in CaF_2	
g. Color centers in actinide-doped CaF_2	
5. Color centers in CaF_2	
a. Subtractively colored CaF_2	
b. H and F bands in CaF_2	
c. M and M^+ centers in CaF_2	

*To be published in December 1977.

TABLE OF CONTENTS - VOLUME II (Cont.)

<u>Section</u>	<u>Page</u>
III	d. F_{AE} centers in Sr-doped and Ba-doped CaF_2 . . e. Self-trapped hole in CaF_2 f. Color centers in $CaF_2:Mn^{2+}$
IV	OXIDES AND GLASSES A. Silicon Dioxide and Some Silicate Glasses 1. Some common impurities in SiO_2 2. Fundamental and common impurity-related UV absorption in SiO_2 3. Impurity absorption in silicate glasses 4. Optical absorption in irradiated SiO_2 5. Aluminum-alkali system 6. Gallium-lithium system 7. Transient radiation effects in SiO_2 and silicate glasses 8. Ion-implantation effects in fused silica B. Aluminum Oxide 1. Transition-metal ions in Al_2O_3 2. Radiative coloration of Al_2O_3 C. Magnesium Oxide 1. Transition-metal ions in MgO a. V^{3+} in MgO b. Cr^{3+} in MgO c. Fe^{2+} and Fe^{3+} in MgO d. Co^{2+} in MgO e. Ni^{2+} in MgO

TABLE OF CONTENTS - VOLUME II (Cont.)

<u>Section</u>		<u>Page</u>
IV	2. Radiation-induced absorptions in MgO	
	a. V-type centers in MgO	
	b. Na in MgO	
	c. F and F ⁺ centers in MgO	
	d. F-aggregate centers in MgO	
	e. Ne ⁺ irradiation of MgO	

LIST OF ILLUSTRATIONS - VOLUME I

Figure		Page
1.1	Summary of the peak positions (λ), widths ($\Delta\lambda$), and oscillator strengths (numbers) of the impurity spectra for LiF.	4
1.2	Summary of the peak positions (λ), widths ($\Delta\lambda$), and oscillator strengths (numbers) of the impurity spectra for NaF.	9
1.3	Summary of the peak positions (λ), widths ($\Delta\lambda$), and oscillator strengths (numbers) of the impurity spectra for KCl.	13
1.4	Summary of the peak positions (λ), widths ($\Delta\lambda$), and oscillator strengths (numbers) of the impurity spectra for MgF ₂	16
1.5	Summary of the peak positions (λ), widths ($\Delta\lambda$), and oscillator strengths (numbers) of the impurity spectra for CaF ₂	18
1.6	Summary of the peak positions (λ), widths ($\Delta\lambda$), and oscillator strengths (numbers) of the impurity spectra for MgO.	29
1.7	Summary of the peak positions (λ), widths ($\Delta\lambda$), and oscillator strengths (numbers) of the impurity spectra for Al ₂ O ₃	32
1.8	Summary of the peak positions (λ), widths ($\Delta\lambda$), and oscillator strengths (numbers) of the impurity spectra for SiO ₂	37
1.9	Summary of the peak positions (λ), widths ($\Delta\lambda$), and oscillator strengths (numbers) of the impurity spectra for silicate glasses	41
1.10	Summary of the positions of important impurity-absorption lines in LiF shown with respect to the ultraviolet and infrared cutoff frequencies.	43
1.11	Summary of the positions of important impurity-absorption lines in MgF ₂ shown with respect to the ultraviolet and infrared cutoff frequencies.	44
1.12	Summary of the positions of important impurity-absorption lines in CaF ₂ shown with respect to the ultraviolet and infrared cutoff frequencies.	45

LIST OF ILLUSTRATIONS - VOLUME I (Cont.)

Figure	Page
1.13 Summary of the positions of important impurity-absorption lines in SiO_2 shown with respect to the ultraviolet and infrared cutoff frequencies.	46
1.14 Summary of the positions of important impurity-absorption lines in Al_2O_3 shown with respect to the ultraviolet and infrared cutoff frequencies.	47
2.1 Absorption spectra of several fluorides showing the Urbach edges.	61
2.2 Absorption spectrum above the absorption edge for thin LiF films.	62
2.3 Optical absorption near and above the absorption edges of alkali-halide thin films deposited on LiF.	63
2.4 Room-temperature values of refractive indices of alkali halides in the visible and ultraviolet regions	69
2.5 Sketches of F-band absorptions in several alkali halides	70
2.6a Ivey relations (power-law dependence) of the positions of the absorption maxima of OH^- , U, F, and V_3 bands as functions of the lattice constants, for alkali halides	71
2.6b Ivey relations (power-law dependence) of the positions of the absorption maxima of OH^- , U, F, and V_3 bands as functions of the lattice constants, for alkali halides	72
2.7 Effects of starting-material purity and growth conditions on the ultraviolet transmittance of LiF.	89
2.8 Effects of oxygen in LiF on the ultraviolet transmittance.	90
2.9 Effects of storage and cleaning on the ultraviolet transmittance of LiF.	91
2.10 Typical degradation of the transmittance of LiF at 121.6 nm resulting from storage in air of two different samples	92
2.11 Ultraviolet absorption by OH^- in LiF	94
2.12 Absorption by Mg^{2+} and OH^- in LiF.	97
2.13 Absorption by oxygen-doped LiF	98

LIST OF ILLUSTRATIONS - VOLUME I (Cont.)

Figure		Page
2.14	Optical Absorption spectrum of LiF:Ti ³⁺	101
2.15	Absorption spectra of divalent transition-metal ions in LiF	102
2.16	Absorption spectra of pure and Ti-doped LiF crystals	103
2.16A	Titanium-concentration dependence of the 200 nm absorption band in LiF	108
2.17	Optical absorption of LiF:10 ³ ppm Mn ²⁺	110
2.18	Optical absorption of LiF:20 ppm Mn ²⁺	111
2.19	Optical absorption spectra of LiF:Ni ²⁺	114
2.20	Typical absorption spectra of X-irradiated LiF at 78 K . . .	116
2.21	Absorption spectra of spatially oriented V _K centers in LiF	118
2.22	Anisotropic absorption of V _K center in LiF	119
2.23	Optical absorption of X-irradiated, magnesium-doped LiF. . .	120
2.24	Absorption spectrum of a γ-irradiated, OH ⁻ -free LiF.	122
2.25	Optical absorption of LiF:Mg quenched from 600 C and X-irradiated at room temperature	123
2.26	Optical absorption of unquenched LiF:Mg, X-irradiated at room temperature.	124
2.27	Optical absorption spectra of LiF irradiated at room temperature.	126
2.28	Absorption spectrum evolution of a LiF sample.	127
2.29	Absorption spectrum evolution of a LiF sample.	128
2.30	Absorption spectrum evolution of a LiF sample.	129
2.31	Absorption spectra of LiF crystal irradiated with 10 ¹⁷ neutron/cm ² and annealed at 350 C.	130
2.32	Absorption spectra of NaF single crystals in the VUV region	135

LIST OF ILLUSTRATIONS - VOLUME I (Cont.)

Figure		Page
2.33	Experimental and theoretical Urbach tails of NaF single crystals.	135
2.34	Analyzed spectra of absorption constant in cm^{-1}	136
2.35	Lattice-constant dependence of absorption maximum of OH^- -, U- and F-bands in various alkali halides.	139
2.36	Absorption spectrum of an unirradiated NaF crystal doped with OH^- , measured at 190 K	139
2.37	(a) Absorption spectrum of NaF: OH^- crystal after being irradiated for 2.5 hours at 190 K. (b) The VUV spectrum of absorption difference, after and before the X irradiation	140
2.38	(a) Absorption spectra of an OH^- -doped NaF before and after the irradiation in the OH^- band. (b) Change in vacuum ultraviolet absorption spectrum after irradiation in the OH^- band	142
2.39	Optical absorption of NaF: OH^- in vacuum UV region at room temperature.	143
2.40	Difference spectra (increase in absorption coefficient) of NaF: OH^- at room temperature.	144
2.41	The absorption spectra of NaF(Br) single crystals at (a) RT and (b) 110 K.	146
2.42	Concentration dependence of the integrated absorption by Br^- before and after thermal treatment	146
2.43	Far UV absorption spectra of NaF(Cl) single crystals with different amounts of Cl ions	150
2.44	Dependence of the absorption coefficient of the Cl band in NaF single crystals.	150
2.45	Absorption spectra of the Cl band in NaF single crystals at different temperatures	152
2.46	Absorption spectra for NaF and for divalent transition metal ions in NaF	156
2.47	Absorption spectrum of Co^{2+} -doped NaF	160

LIST OF ILLUSTRATIONS - VOLUME I (Cont.)

Figure		Page
2.48	Absorption spectra of NaF single crystals with Fe ion impurity.	162
2.49	Absorption spectra of NaF single crystals	163
2.50	Absorption spectra of several additively colored NaF crystals.	165
2.51	Summary of the peak positions (λ), widths ($\Delta\lambda$), and oscillator strengths (numbers) of the impurity spectra for KCl	168
2.52	Optical absorption of hydride-doped KCl, KBr, and NaCl, showing the effects of UV irradiation and thermal annealing	172
2.53	Optical absorption of hydroxide-doped KCl, KBr, and NaCl, showing the effect of UV irradiation and thermal annealing	173
2.54	U ₂ -band absorption in NaCl, KCl, and RbCl	177
2.55	Temperature dependence of the bandwidth at half maximum of OH ⁻ and OD ⁻ bands in KCl	178
2.56	Temperature dependence of the maximum of OH ⁻ and OD ⁻ bands in KCl.	178
2.57	Absorption spectrum of KCl grown in oxygen.	180
2.58	Absorption spectra of KCl containing $3.1 \times 10^{18} \text{ cm}^{-3}$ O ₂ ⁻ centers	182
2.59	Absorption spectra of KCl containing $7.5 \times 10^{17} \text{ cm}^{-3}$ O ²⁻ centers	182
2.60	Composition of various O ²⁻ bands and the color-center bands in KCl.	185
2.61	Absorption spectrum of zone-refined KCl, showing color-center bands L ₂ , L ₃ , and L ₄	187
2.62	Absorption spectra of KCl containing O ₂ ⁻ and O ²⁻ centers	188
2.63	Absorption spectra of KCl containing O ²⁻ centers.	190

LIST OF ILLUSTRATIONS - VOLUME I (Cont.)

Figure		Page
2.64	Ultraviolet absorption of $\text{KCl}:\text{SH}^-$ grown under 3 torr of H_2S partial pressure.	192
2.65	Ultraviolet absorption of $\text{KCl}:\text{SH}^-$	192
2.66	Photochemical decomposition of SH^-	193
2.67	Absorption of S^- centers in KCl at 78 K and 20 C	195
2.68	Absorption spectrum of $\text{KCl}:\text{S}^-$ showing the weak absorption band between the strong S^- bands at 4.87 eV and 6.42 eV.	195
2.69	Absorption spectrum of a SH^- -doped KCl crystal after reduction with F centers	197
2.70	Optical-absorption spectra showing the effect of photochemical conversion of S^{2-} to S^-	199
2.71	Spectra showing the effect of annealing on S^{2-} centers in KCl crystals.	202
2.72	Absorption spectra of $\text{KCl}:\text{KSH}$	205
2.73	Absorption spectra of SeH^- in a KCl crystal.	207
2.74	Photochemical decomposition of SeH^- in KCl	207
2.75	The formation of the precipitated K_2Se double band after annealing of quenched KCl	209
2.76	The absorption spectrum of Br^- in KCl	213
2.77	Absorption bands of I^- in KCl for various iodine concentrations N	214

LIST OF ILLUSTRATIONS - VOLUME II*

Figure

- 3.1 Oxygen and hydroxyl contamination of CaF_2 : (a) before thermal treatment, (b) after 3 hours at 765 C in air.
- 3.2 Absorption spectra of typical doped CaF_2 crystals before (primed) and after (unprimed) X irradiation of 4×10^3 R.
- 3.3 Absorption spectra after X irradiation; I and II, 7×10^3 R; and III, 4×10^4 R.
- 3.4 X-ray dose dependence of coloration of $\text{CaF}_2:\text{O}^{2-}$ crystals at low oxygen concentrations: (a) 0.0 R, (b) 4×10^3 R, and (c) 2.5×10^5 R.
- 3.5 Absorption spectrum of $\text{CaF}_2:\text{Mn}^{2+}$.
- 3.6 Absorption spectra of Mn^{2+} in different host crystals.
- 3.7 Absorption spectra of $\text{CaF}_2:\text{Co}^{2+}$ in the region of the ${}^4\text{A}_{2g} \rightarrow {}^4\text{T}_{1g}$ (P) transition.
- 3.8 Absorption spectra of $\text{CaF}_2:\text{Co}^{2+}$ in the region of the ${}^4\text{A}_{2g} \rightarrow {}^4\text{T}_{1g}$ (F) transition (0.66 - 1.05 eV) and the ${}^4\text{A}_{2g} \rightarrow {}^4\text{T}_{2g}$ (F) transition (0.37 - 0.66 eV).
- 3.9 Optical absorption spectra of Co^{2+} in fluoride-type lattices.
- 3.10 Absorption spectra of Co^{2+} in fluoride-type lattices.
- 3.11 Absorption spectra of Co^{2+} in fluoride-type lattices.
- 3.12 Absorption spectra of Ni^{2+} in CaF_2 and CdF_2 .
- 3.13 The lowest $4f \rightarrow 5d$ absorption band of trivalent rare-earth ions in CaF_2 host crystals at room temperature.
- 3.14 Absorption spectra of the divalent rare-earth ions in CaF_2 at room temperature.
- 3.15 Excitation spectra and fluorescence spectra of Tm^{2+} , Er^{2+} , Ho^{2+} , and Dy^{2+} at 77 K.
- 3.16 Optical absorption spectrum of additively colored rare-earth-doped CaF_2 .

*To be published in December 1977.

LIST OF ILLUSTRATIONS - VOLUME II (Cont.)

Figure

- 3.17 Absorption-band energy as a function of the trivalent ion radius of the impurity.
- 3.18 Ultraviolet absorption spectra of photochromic centers in CaF_2 :0.1% La.
- 3.19 Ultraviolet absorption spectra of photochromic centers in CaF_2 :0.1% Ce.
- 3.20 Ultraviolet absorption spectra of photochromic centers in CaF_2 :Gd.
- 3.21 Ultraviolet absorption spectra of photochromic centers in CaF_2 :0.1% Tb.
- 3.22 Ultraviolet absorption spectra of photochromic centers in CaF_2 :0.3% Y.
- 3.23 Ultraviolet absorption spectra of photochromic centers in CaF_2 :0.1% Lu.
- 3.24 Green crystals of uranium-doped CaF_2 .
- 3.25 Absorption spectrum of a brown crystal of CaF_2 :1% UO_2 .
- 3.26 Yellow crystals of uranium-doped CaF_2 .
- 3.27 Comparison of the absorption spectra of Np ions in various media.
- 3.28 Absorption spectra of CaF_2 : Np^{3+} .
- 3.29 Absorption spectra of CaF_2 : Np^{3+} .
- 3.30 Absorption spectra of CaF_2 :Pu.
- 3.31 Sharp line spectra of Pu^{4+} ions at 77 K in various media.
- 3.32 Optical spectra of CaF_2 :Am crystals.
- 3.33 Absorption bands of Cm^{3+} and Cm^{4+} in various matrices.
- 3.34 Broad absorption spectra of color centers in actinide-doped CaF_2 after 3 hours of γ irradiation.

LIST OF ILLUSTRATIONS - VOLUME II (Cont.)

Figure

- 3.35 Absorption spectra of additively colored and quenched CaF_2 measured at various temperatures.
- 3.36 Temperature dependence of the peak position of the α band of CaF_2 and the F band in KCl and NaCl .
- 3.37 Absorption spectra of additively colored and slowly quenched CaF_2 measured at various temperatures.
- 3.38 Absorption spectrum of CaF_2 colored by X irradiation.
- 3.39 Absorption spectra of CaF_2 after X irradiation.
- 3.40 Absorption spectrum of CaF_2 irradiated with neutrons.
- 3.41 Additively colored pure and Y-doped CaF_2 .
- 3.42 Fluorite-type lattice showing the two variants of tetrahedral F_4 centers.
- 3.43 The effect of Na^+ ion impurity on the X-ray coloration sensitivity of CaF_2 .
- 3.44 X-ray coloration of low concentrations of Na^+ ions in CaF_2 .
- 3.45 Optical absorption spectrum of F centers in CaF_2 produced by X irradiation and by additive coloration.
- 3.46 Thermal bleaching of the 377 nm F band and the 314 nm H band produced by X irradiation of CaF_2 at 4 K.
- 3.47 Model of the CaF_2 lattice showing two fluorine vacancies along the $[001]$ axis forming an M center.
- 3.48 Comparison of the energy level diagrams for the M and M^+ centers aligned with the $[001]$ axis in CaF_2 .
- 3.49 Absorption spectrum of additively colored CaF_2 showing the two strong M-center absorption bands at 519 and 366 nm.
- 3.50 Dichroism in the M-band region.
- 3.51 Dichroism in the M_F -band region.
- 3.52 Absorption spectra of $\text{CaF}_2\text{:Sr}$.

LIST OF ILLUSTRATIONS - VOLUME II (Cont.)

Figure

- 3.53 Absorption spectra of $\text{CaF}_2\text{:Ba}$.
- 3.54 Comparison of the absorption spectra of CaF_2 and SrF_2 crystals after additive coloration, subtractive coloration by X irradiation, and X-irradiated Li^+ , Na^+ and K-doped crystals.
- 3.55 Absorption spectrum of pure and manganese-doped CaF_2 crystals prior to X irradiation.
- 3.56 Absorption spectrum of X-irradiated pure and manganese-doped CaF_2 .
- 4.1 Two-dimensional representation of (a) crystalline, and (b) glassy SiO_2 .
- 4.2 Schematic representation of modified silicate network.
- 4.3 Ultraviolet absorption edges of high-purity (1) crystalline quartz, (2) fused silica, and (3) $\text{NRL } 2 \text{ SiO}_2 - 1 \text{ Na}_2\text{O}$ glass.
- 4.4 Reflectance spectra of high-purity (1) crystalline quartz, and (2) of fused silica showing the lowest energy peaks at 10.2 eV and 11.5 eV above the absorption edge.
- 4.5 Intrinsic scattering loss of fused silica, soda-lime-silicate, and for comparison, the liquid CCl_4 .
- 4.6 Intrinsic absorption loss for fused silica and soda-lime-silicate.
- 4.7 Total intrinsic loss, which is the sum of the absorption and scattering losses, in fused silica and soda-lime-silicate.
- 4.8 Effect of aluminum addition on the ultraviolet transmittance of alkali-doped SiO_2 .
- 4.9 Reflectance spectra of two binary silicate glasses.
- 4.10 Transmittance spectra, showing the onset of optical absorption, of several Corning and Amersil glasses.
- 4.11 Optical absorption edges of several typical high-purity silicate glasses.

LIST OF ILLUSTRATIONS - VOLUME II (Cont.)

Figure

- 4.12 Optical absorption spectra of undoped and iron-doped 3 SiO₂ - 1 Na₂O glass melted in an oxidizing atmosphere.
- 4.13 Absorption spectra of copper-doped glasses melted in a reducing atmosphere.
- 4.14 Absorption spectra of copper-doped glasses melted in air.
- 4.15 Absorption spectrum of irradiated fused silica resolved into individual bands.
- 4.16 Model of the E₂' center.
- 4.17 Absorption spectra of undoped fused silica unexposed and exposed to various doses, and exposed to 5 × 10⁵ rad after heat treatment.
- 4.18 Optical absorption of α-quartz crystal as a function of irradiation and thermal treatment.
- 4.19 Transmittance of fused SiO₂ before and after irradiation by 10¹¹ electrons/cm² at 1.0 MeV and at 2.0 MeV.
- 4.20 Transmittance of Corning 7940 fused SiO₂ before and after irradiation resulting from 10¹⁴ electrons/cm² at 2.0 MeV incident on a sapphire shield.
- 4.21 Transmittance of Dynasil 1850A fused SiO₂ before and after irradiation resulting from 10¹⁴ electrons/cm² at 2.0 MeV incident on a sapphire shield.
- 4.22 Transmittance of Corning 9-54 (Vycor) before and after irradiation resulting from 10¹⁴ electrons/cm² at 2.0 MeV incident on a sapphire shield.
- 4.23 Transmittance of Corning 7-54 before and after irradiation resulting from 10¹⁴ electrons/cm² at 2.0 MeV incident on a sapphire shield.
- 4.24 Optical absorption spectra of X-irradiated (exposure ≈ 10⁶ R), alkali-doped fused silica showing the E₂' and E₁' bands at 5.4 and 5.8 eV and the hole band at 7.6 eV.
- 4.25 Absorption spectra of alkali-doped fused silica γ-irradiated to 10⁷ rad.
- 4.26 Absorption spectra of fused silica doped with 0.2% Al and 0.2% of the various alkalis and γ-irradiated to 10⁷ rad.

LIST OF ILLUSTRATIONS - VOLUME II (Cont.)

Figure

- 4.27 Optical absorption of X-irradiated ($\approx 10^6$ R) fused silica co-doped with aluminum and alkali.
- 4.28 Absorption spectra of fused silica doped with 2.0% Al and γ -irradiated to various doses.
- 4.29 Comparison of irradiated fused silica and irradiated quartz.
- 4.30 Optical absorption spectra of two X-irradiated, air-melted, high-purity silicate glasses.
- 4.31 Absorption spectra of fused silica doped with 0.2% Li and 0.2% Al and γ -irradiated to various doses.
- 4.32 Absorption spectra of fused silica doped with 0.2% Cs and 0.2% Al and γ -irradiated to various doses.
- 4.33 Resolution of an absorption spectrum into individual Gaussian bands.
- 4.34 Absorption spectra of fused silica doped with various amounts of Ga and Li and exposed to various doses.
- 4.35 A comparison of the permanent damage observed in Corning 7943 silica (after Arnold and Compton) with the transient coloration measured immediately after the electron pulse irradiation.
- 4.36 The decay rate of the transient absorption and emission at 4.2 K.
- 4.37 Schematic diagram of postulated steps involved in the formation and annihilation of transient E' center.
- 4.38 Proposed band gap model of the transient radiation effects of SiO_2 , permitting both radiative and non-radiative recombination of holes with E' centers.
- 4.39 Optical absorption in fused silica (Corning 7940) implanted with H^+ , He^+ , A^+ , Kr^+ , and Xe^+ ions.
- 4.40 Optical absorption in fused silica (Corning 7940) which was first implanted with 5×10^{15} 400 keV Xe^+ ions/cm² and then with 1×10^{14} 400 keV H^+ ions/cm².

LIST OF ILLUSTRATIONS - VOLUME II (Cont.)

Figure

- 4.41 Proposed models for the 215 nm absorption band, the 245 nm impurity band, and the 245 nm (B_2) damage band.
- 4.42a Absorption coefficient of pure Al_2O_3 , showing the sharp rise in the absorption coefficient at the absorption edge near 8.64 eV and the rather long and strong secondary absorption tail extending to approximately 7.2 eV.
- 4.42b Our replot of the average β from 4.42a analog scale showing that β is not exponential.
- 4.43 Transmittance spectra of Al_2O_3 , showing the effects of electron irradiation.
- 4.44 Absorption spectrum of Ti^{3+} in Al_2O_3 .
- 4.45 Absorption spectrum of V^{3+} in Al_2O_3 .
- 4.46 Absorption spectrum of Cr^{3+} in Al_2O_3 .
- 4.47 Absorption spectrum of Mn^{3+} in Al_2O_3 .
- 4.48 Absorption spectrum of Co^{3+} in Al_2O_3 .
- 4.49 Absorption spectrum of Ni^{3+} in corundum.
- 4.50 Vibrational structure of the first strong band of Co^{3+} in Al_2O_3 .
- 4.51 Vibrational structure of the first strong band of V^{3+} in Al_2O_3 .
- 4.52 Vibrational structure of the first strong band of Cr^{3+} in Al_2O_3 .
- 4.53 Absorption spectra of Cr^{3+} in Al_2O_3 at various temperatures.
- 4.54 Absorption spectra of Co^{3+} in Al_2O_3 at various temperatures.
- 4.55 Absorption spectrum of Al_2O_3 doped with V^{3+} showing the charge-transfer threshold at 5.75 eV and the low-energy bands due to intra-d-shell transitions.
- 4.56 Absorption spectrum of Al_2O_3 doped with Ti^{3+}

LIST OF ILLUSTRATIONS - VOLUME II (Cont.)

Figure

- 4.57 Absorption spectrum of Al_2O_3 doped with Cr^{3+} (ruby) showing an intense charge-transfer peak at 6.94 eV.
- 4.58 Absorption spectra of Al_2O_3 doped with Mn^{4+} .
- 4.59 Absorption spectrum of Al_2O_3 doped with Fe^{3+} .
- 4.60 Absorption spectrum of Al_2O_3 doped with Ni^{3+} .
- 4.61 Energy-level diagram for d^5 and the absorption spectrum of a natural yellow Al_2O_3 containing 0.99% Fe^{3+} .
- 4.62 Absorption spectrum (E perpendicular to C) of a synthetic Al_2O_3 doped with 0.7% Fe at various temperatures.
- 4.63 Absorption spectrum of a natural blue-green Al_2O_3 containing titanium and 0.62 percent iron.
- 4.64 Absorption spectra of two Al_2O_3 crystals X-irradiated to saturation.
- 4.65 Absorption spectrum of a γ -irradiated Al_2O_3 following bleaching.
- 4.66 Absorption spectra of neutron-irradiated and electron-irradiated Al_2O_3 .
- 4.67 Absorption spectra at 20 and -185 C of Al_2O_3 neutron-irradiated at pile temperature.
- 4.68 Anisotropy of absorption induced by neutron irradiation of Al_2O_3 .
- 4.69 Anisotropy of absorption induced by electron irradiation of Al_2O_3 .
- 4.70 Absorption spectra of neutron-irradiated UV-grade Al_2O_3 .
- 4.71 Effect of optical bleaching with 410 nm (3.02 eV) light on the absorption spectrum of Al_2O_3 after neutron irradiation and γ irradiation.
- 4.72 Absorption spectra of Al_2O_3 after irradiation by 14 MeV neutrons and fission neutrons.
- 4.73 Absorption spectra of Al_2O_3 crystals implanted with H^+ , D^+ , $^4\text{He}^+$ and O^+ ions.

LIST OF ILLUSTRATIONS - VOLUME II (Cont.)

Figure

- 4.74 Absorption spectra of unirradiated and 3 MeV Ne⁺-bombarded MgO crystals.
- 4.75 Reflectance spectrum of MgO for a 15-degree angle of incidence.
- 4.76 Optical absorption in the absorption edge region of a thin film of magnesium oxide on a lithium fluoride substrate.
- 4.77 Absorption spectrum of V³⁺ in MgO.
- 4.78 Effects of consecutive heat treatments on the optical absorption in V-doped MgO.
- 4.79 Representations of the (001) plane of MgO showing the environments of Cr³⁺ ions in non-cubic sites.
- 4.80 Absorption spectrum of Cr³⁺-doped MgO.
- 4.81 Absorption spectrum of Cr³⁺-doped MgO in the region of the $^4A_2 \rightarrow ^2T_1$ transition.
- 4.82 Temperature dependence of the 4T_2 and 4T_1 bands in MgO:Cr³⁺.
- 4.83 Absorption and fluorescence in the same sample of Cr³⁺-doped MgO at liquid-nitrogen temperature.
- 4.84 Absorption and fluorescence in the same sample of Cr³⁺-doped MgO at liquid-nitrogen temperature.
- 4.85 Optical absorption spectra after three heat treatments of an MgO crystal containing 5000 ppm Fe.
- 4.86 Optical density enhancement of an MgO crystal following an annealing at 1250 C in an oxidizing atmosphere.
- 4.87 Increase in optical absorption of an MgO crystal resulting from X irradiation at room temperature.
- 4.88 Variation of the saturation absorption at 285 nm (4.35 eV) with Fe content in MgO upon γ -irradiation and upon heating in air at 1400 C.
- 4.89 Infrared spectrum of Co²⁺ in MgO.

LIST OF ILLUSTRATIONS - VOLUME II (Cont.)

Figure

- 4.90 Visible spectrum of Co^{2+} in MgO .
- 4.91 Visible spectrum of Co^{2+} in MgO .
- 4.92 Energy level diagram of Co^{2+} in MgO .
- 4.93 Near-infrared spectrum of Ni^{2+} in MgO .
- 4.94 Visible spectrum of Ni^{2+} in MgO .
- 4.95 Energy level diagram showing the assignments of the observed optical transitions of Ni^{2+} in MgO .
- 4.96 Absorption spectrum of $^3\text{T}_2$ band of MgO:Ni at 79 and 208 K.
- 4.97 Absorption spectrum of $^3\text{T}_1^{\text{a}}$ band of MgO:Ni at 8, 130, and 222 K.
- 4.98 Absorption spectrum of $^1\text{T}_2$ band of MgO:Ni at 8, 121, and 208 K.
- 4.99 Absorption spectrum of $^3\text{T}_1^{\text{b}}$ band of MgO:Ni at 8, 121, and 208 K.
- 4.100 The 2.3 eV (539 nm) band in MgO resulting from gamma or electron irradiation at 5, 78, and 295 K.
- 4.101 Room-temperature decay rates of the 2.3 eV (539 nm) band in different MgO crystals irradiated to saturation in a gamma source.
- 4.102 Absorption coefficient of the 2.3 eV (539 nm) band resulting from γ -irradiation to saturation in MgO crystals quenched from various temperatures.
- 4.103 Schematic representations of the structures of V_{OH} , V^- , V^0 , and V_{F} centers in alkaline-earth oxides.
- 4.104 Induced optical absorption spectra of X-irradiated MgO crystal.
- 4.105 Comparison of the optical absorption bands assigned to the V^- , the V_{OH} , and V^0 centers in MgO .
- 4.106 Optical absorption spectrum of MgO:Na after electron irradiation at 77 K.

LIST OF ILLUSTRATIONS - VOLUME II (Cont.)

Figure

- 4.107 The growth of the 250 nm (5.0 eV) band as a function of fast neutron dose in MgO.
- 4.108 Optical absorption spectra of a neutron-irradiated MgO crystal measured at three different temperatures.
- 4.109 Absorption spectra of an additively colored MgO crystal.
- 4.110 Absorption spectra illustrating the reproducibility of the $F \rightarrow F^+$ photoconversion process.
- 4.111 Absorption spectra of MgO crystal irradiated with 2.2×10^{18} neutrons/cm² and annealed for 10 min at the temperatures indicated.
- 4.112 Some models for orthorhombic F-aggregate centers and their possible assignments to zero-phonon lines in MgO.
- 4.113 Models and molecular orbital schemes for trigonal F-aggregate centers and their possible assignments to zero-phonon lines in MgO.
- 4.114 Comparison of the absorption spectra of MgO crystals irradiated with 2 MeV electrons or neutrons.
- 4.115 Spectra of MgO crystal irradiated with 29 MeV electrons.
- 4.116 Normalized absorption coefficient at the peak of the F band (5.0 eV) versus annealing temperature for electron-irradiated, neutron-irradiated, and additively colored MgO crystals.
- 4.117 Room-temperature spectra of MgO bombarded with 3 MeV Ne⁺ at 77 K and at 300 K to a fluence of 10^{14} cm⁻².
- 4.118 Temperature and dose dependence of the absorption spectrum of MgO before irradiation with Ne⁺ ions.
- 4.119 Room-temperature spectra of absorption remaining after isochronal annealing of samples receiving a dose of 10^{15} cm⁻².
- 4.120 Absorption spectra comparing the 5.8 eV band in MgO from Ne⁺ bombardment, deformation, and γ -irradiation.
- 4.121 Room-temperature absorption induced by 3 MeV ²⁰Ne⁺, by 3 MeV H⁺, and by fast neutrons.

LIST OF TABLES - VOLUME I

<u>Table</u>		<u>Page</u>
1.1	Defect center nomenclature and description.	49
1.2	Intrinsic crystalline structural data, ultraviolet-, infrared-cutoffs, and major color-center absorption bands	54
2.1	Positions [eV] of features in the absorption spectra of the alkali halides	67
2.2	Optical properties of F centers in alkali halides	73
2.3	Optical properties of M_1 bands in alkali halides.	74
2.4	Optical properties of R centers in alkali halides	75
2.5	Wavelength of absorption of electron trap centers (nm).	76
2.6	Wavelength of absorption of hole trap centers (nm).	77
2.7	Absorption properties of F and F_A centers	78
2.8	Position of absorption maxima (nm) for U, OH^- , Z_1 , and Z_2 centers in alkali halides.	79
2.9	Optical absorption peaks of Tl^+ (eV) in alkali halides. . . .	80
2.10	Optical absorption peaks of α and β bands (nm) in alkali halides.	81
2.11	Summary of the peak positions (λ), widths ($\Delta\lambda$), and oscillator strengths (numbers) of the impurity spectra for LiF	84
2.12	Peak positions and widths (full width at half maximum) of U-band absorption lines in LiF	95
2.13	Summary of spectral data for LiF and NaF doped with transition-metal ions	104
2.14	Peak positions, half-widths, and oscillator strengths of various color centers in LiF:Ti.	105
2.15	Absorption bands in nickel-doped LiF.	115
2.16	Colloidal bands of Li, Na, and K (nm) in LiF.	132

LIST OF TABLES - VOLUME I (Cont.)

Table		Page
2.17	Parameters of the Br^- bands in $\text{NaF}(\text{Br})$ single crystals. . . .	148
2.18	Summary of Br^- -band results of several investigators.	149
2.19	Summary of the spectral data and the energy separation values of Cl^- band in NaF at various temperatures	153
2.20	Summary of the characteristics of observed localized exciton absorptions in various alkali halides	154
2.21	Ultraviolet bands observed in transition-metal ions in NaF	157
2.22	The experimental data at 80 K and the analysis of the absorption spectrum of Co^{2+} in NaF	161
2.23	Spectral positions and bandwidths [eV] of absorption bands in hydride- and hydroxide-doped NaCl , KCl , and KBr crystals.	171
2.24	Spectral positions and bandwidth [eV] of oxygen bands in KCl at 78 K.	183
2.25	Spectral positions and bandwidths of SH^- -related centers in KCl at 78 K.	201
2.26	Absorption bands of SH^- , I^- , and S^- in KCl and KBr crystals.	206
2.27	Absorption bands of SeH^- -related centers in KCl and KBr crystals at 20 K.	211

LIST OF TABLES - VOLUME II*

Table

- 3.1 Band maxima of the absorption and emission transitions of disturbed F_2 centres in CaF_2 .
- 3.2 Spectral position [eV] of the $3d \rightarrow 3d$ peaks of Mn^{2+} in $NaCl$, LiF , and CaF_2 crystals.
- 3.3 Absorption bands of nickel in $CaF_2:Ni^{2+}$ and $CdF_2:Ni^{2+}$.
- 3.4 The ground state configurations, transition energies and absorption cross-sections of the lowest $4f \rightarrow 5d$ band of the trivalent rare-earth ions in CaF_2 at room temperature.
- 3.5 Lines which grow into $CaF_2:Pu^{3+}$ crystals due to radiation damage.
- 3.6 Comparison of centers of groups of sharp lines of Pu^{3+} .
- 3.7 Wavelengths (nm) of broad absorptions of tripositive ions in CaF_2 .
- 3.8 Position of absorption peaks in colored natural and synthetic CaF_2 crystals.
- 4.1 Energies of reflection peaks in silicate glasses.
- 4.2 Flame-photometric determination of alkali in doped silica.
- 4.3 Absorption maxima and widths of individual absorption bands in irradiated doped fused silica.
- 4.4 Partition of 250 keV accelerating energy into electronic (ϵ) and nuclear (ν) interaction processes for various ions.
- 4.5 Summary of ground- and excited-state assignments, Dq values, centroids of strong bands (ν in eV) and f -numbers ($f \times 10^4$) of observed intra-d-shell transitions of trivalent ions in Al_2O_3 at 77°K.
- 4.6 Vibrations of aluminum oxide. Symmetry classification D_{3d} .
- 4.7 Summary of data obtained from spectra of Figs. 4.55 to 4.60 and comparison with the threshold values predicted from Eq. (4.1) of the text for the charge-transfer process.

*To be published in December 1977.

LIST OF TABLES - VOLUME II (Cont.)

Table

- 4.8 Impurity analyses of Oak Ridge National Laboratory and Spicer MgO crystals.
- 4.9 Designations, impurity concentrations, and the colorability of the 2.3 eV (539 nm) V band in MgO crystals from various sources.
- 4.10 Optical parameters for V^0 , V^- and V_{OH} centers in MgO.
- 4.11 Zero-phonon lines and phonon-assisted transitions in MgO.

I. INTRODUCTION

Over the years the quality of transparent materials for the ultraviolet and visible regions has been steadily improved by the advance of various material-refinement and crystal-growth techniques^{1.1} such as the use of reactive-atmosphere processing (RAP).^{1.2, 1.3} With high-power lasers now becoming available at an increasing number of frequencies and at increasing power levels, obtaining ultra-low absorptance materials for high-power use throughout the optical frequency range is emerging as an important problem. There is in fact considerable current interest in reducing the residual optical absorption of materials in order to increase the power of ultraviolet and visible lasers and to increase the resistance of materials to damage by high-intensity radiation in laboratory and space environments. It has been shown^{1.4, 1.5} that impurity absorption is an important effect that limits the ultraviolet intensity that materials can transmit. Thus, it is important to understand the origin of the residual absorption in order to provide guidance for programs to further improve the materials and to estimate the expected materials limits set by residual imperfections. Reducing the absorptance of dielectric reflectors and of antireflection coatings are problems of growing importance. It is believed^{1.6} that impurities in deposited films is a major factor limiting the absorptance of both types of coatings. Thus, the present tabulation should be useful in identifying the impurities responsible for observed absorptance in bulk materials and coatings, in identifying potentially troublesome impurities in a given material at a given operating wavelength, and in selecting a wavelength that is likely to be less troubled by impurity absorption.

Sec. I

A study of impurity absorption in the 2 – 15 μm infrared region was completed earlier.^{1,7} A tabulation of absorption-line positions (with no spectra) for alkali halides has been given by S. C. Jain, A. V. R. Warriar, and S. K. Agarwal.^{1,7a}

In the present report, the optical-absorption spectra of commonly occurring impurities in several ultraviolet-transparent solids are tabulated and discussed, and the assignments of the absorption bands are reviewed. The wavelength region included extends from the very near infrared, at 1 μm (1000 nm, or 0.124 eV), through the vacuum-ultraviolet region. The host materials covered are LiF, NaF, KCl, MgF_2 , CaF_2 , MgO, Al_2O_3 , SiO_2 , and silicate glasses.

The features of the spectra are summarized in tables and figures. The peak positions, approximate line widths, and, when available, the oscillator strengths of all bands are summarized in correlation-type graphs for each material in Figs. 1.1 – 1.9. An abbreviated graphical summary showing the positions of several important impurity-absorption bands in several materials is given in Figs. 1.10 through 1.14, which also shows the intrinsic electron and ionic absorption edges.

The intrinsic and extrinsic absorption spectra are categorized according to the type of host material, e.g., alkali halides, alkaline-earth halides, and oxides, and according to the type of impurity, e.g., halogens, H and D centers, OH and OD centers, O, S, Se centers, color centers, radiation-induced defect centers, transition-metal ions, and rare-earth ions. Comparisons of results for various host materials, and also for various impurities, are given in the form of tables and figures whenever possible. A number of commonly occurring types of absorption centers are defined in

Sec. I

EXPLANATORY NOTES FOR FIG. 1.1

Column 1: Lists properties of pure, doped, and irradiated materials. For doped or irradiated materials the properties appear in the following order:

1. impurity or dopant (O_2^- or LiO_2)
2. radiation (electrons, neutrons, etc.)
3. color centers or color bands (V_K , F, or α , β , etc.)
4. additional information (sample color, photochromic, etc.)

Some of the Al_2O_3 spectra indicate the polarization of the electric field with respect to the c axis. The composition of silicate glasses is given before listing the impurity. The absorption edge is defined as the photon energy at which $\beta = 5 \text{ cm}^{-1}$.

Column 2: Sample temperature.

Column 3: Peak positions ($|$), widths (H), and oscillator strengths (numbers) of impurity spectra. Ellipses indicate absorption structure above the absorption edge. Some lines are labeled by their color center or impurity.

Column 4: References: T2.1 stands for Table 2.1, F2.23 stands for Fig. 2.23, and II-C ¶ 6f indicates a paragraph in the text.

LiF	Temp.	Photon Energy (eV)							Ref.
		2	4	6	8	10	12	14	
Absorption shoulder	80K								T2.1
Lowest exciton peak	RT								T2.1
Band gap	RT								T2.1
Absorption edge	RT								T2.1
Mg F, F ₃ ⁻ , V ₃	RT								F2.23
OH ⁻	RT								F2.11
LiO ₂	RT								F2.13
O ⁻	77K								T2.12

Fig. 1.1. Summary of the peak positions (|), widths (—), and oscillator strengths (numbers) of the impurity spectra for LiF. (See preceding page for key.)

LiF	Temp.	Photon Energy (eV)	Ref.
H ⁻	77K	10	T2.12
H ⁻	RT	10	T2.12
Ni	10K	0.69	T2.13
Ni ²⁺	RT	0.48	F2.19 T2.13 T2.15
Co	10K	2.2 × 10 ⁻²	T2.13
Co ²⁺	4.2K	1.7 × 10 ⁻³ 1.9 × 10 ⁻²	II-C6f
Co ²⁺	RT	1.7 × 10 ⁻³ 1.9 × 10 ⁻²	T2.13
Mg ²⁺	—	10 ⁻² 10 ⁻²	F2.25 F2.26 II-C4

Fig. 1.1 (Continued)

LiF	Temp.	Photon Energy (eV)					Ref.
Ti	10K	0.475	0.99				T2.13
Ti	RT	0.47	0.99				T2.13
Mn	10K		1.95×10^{-3}	3.55×10^{-3}			T2.13
Mn ²⁺	RT		1.3×10^{-3}				F2.17 F2.18 T2.13
V	10K		4.7×10^{-4}	5.7×10^{-3}			T2.13
V	RT	$<10^{-5}$	$<10^{-5}$	6.4×10^{-4}	4.1×10^{-3}		T2.13
Fe ²⁺	RT			5.2×10^{-3}			T2.13
Fe	10K			5.2×10^{-3}			T2.13

Fig. 1.1 (Continued)

LiF	Temp.	Photon Energy (eV)	Ref.
Ti ³⁺	RT		T2.14 F2.14
F	RT		F2.5
C _A (Na ⁺)	RT		F2.28
Neutrons W ₁	RT		F2.31
R	RT		T2.4
R ₁	78K		F2.20
V _K or X ₂ ⁻	78K		T2.6 F2.22
Neutrons W ₂ , F, C _A	RT		F2.31

Fig. 1.1 (Continued)

LiF	Temp.	Photon Energy (eV)					Ref.
R ₂	78K						F2.20
Li ⁺	77K						F2.27
Li ⁺	RT						F2.27
C _A (K ⁺)	RT						F2.29
M	78K						F2.20
C _A (Na ⁺)	RT						F2.28
N	78K						F2.20
R'	78K						F2.20
M'	78K						F2.20

Fig. 1.1 (Continued)

NaF	Temp.	1	2	4	6	8	10	12	14	Ref.
Absorption shoulder	80K									T2.1
Fe	RT						Band edge	Fe		F2.48
Band gap	RT								T2.1
Lowest exciton peak	RT									T2.1
Absorption edge	—							190K RT	100K	F2.33
Exciton edge	—							190K RT	100K	F2.33
OH ⁻	RT					u			β	F2.39
OH ⁻	190K								β	F2.36

Fig. 1.2. Summary of the peak positions (|), widths (—), and oscillator strengths (numbers) of the impurity spectra for NaF. (See Fig. 1.1 for key.)

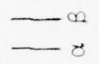
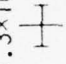
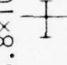
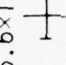

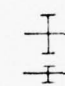

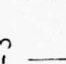
NaF	Temp.	Photon Energy (eV)	Ref.
α, β	RT	 $\alpha \quad \beta$	T2.10
Cl^-	110K	7.3×10^{-2} 	T2.20
Cl^-	RT	6.8×10^{-2} 	F2.41 F2.43 T2.20
Cl^-	350K	6.6×10^{-2} 	T2.20
Br^-	110K		T2.18 F2.41
Br^-	RT		T2.18 F2.41
O_2^-	RT		F2.39
Ni	RT	1.8×10^{-3} 	T2.22

Fig. 1.2 (Continued)

NaF	Temp.	Photon Energy (eV)			Ref.
Ni	10K				T2.22
Co	RT	5×10^{-5}	1.3×10^{-3}		F2.46 T2.22 II-D2d
Co	10K		1.3×10^{-3}		F2.46 T2.22
Co	80K	1.08×10^{-5}			T2.23
H ⁻	—				F2.35
Mn	10K				T2.22
Mn	RT				T2.22
Ti	RT 10K		3.5×10^{-2}		T2.22

Fig. 1.2 (Continued)

NaF	Temp.	Photon Energy (eV)	Ref.
V	10K	 1.7×10^{-3}	T2.22
V	RT		T2.22
F	190K		F2.35 F2.37
R	77K		T2.4
M	-		F2.37

Fig. 1.2 (Continued)

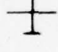
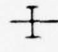
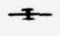
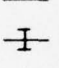
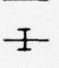
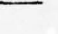

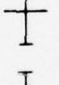


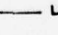
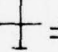
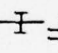
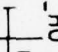
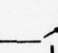
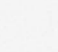
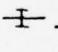
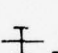
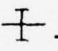

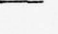
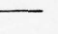
KCl	Temp.	Photon Energy (eV)							Ref.
		2	4	6	8	10	12	14	
Exciton peaks	RT								F2.3
Br ⁻	77K								F2.76
I ⁻	RT								F2.77 T2.27
α band	78K								T2.25
O ₂ ⁻	78K								T2.24
H ⁻ + OH ⁻	20K		 U ₁	 U ₂	 U OH ⁻	 O ⁻	 O ⁻ α		F2.52 F2.54 T2.23
F	78K		 L ₂	 L ₃	 L ₄				F2.61
OH ⁻ UV irradiation	RT								F2.53

Fig. 1.3. Summary of the peak positions (|), widths (—), and oscillator strengths (numbers) of the impurity spectra for KCl. (See Fig. 1.1 for key.)

KCl	Temp.	Photon Energy (eV)	Ref.
OH^-	20K		F2.53
SH^-	20K		T2.26 F2.64 F2.65
O^{2-}	78K		T2.24 F2.59
SeH^-	20K		F2.73 T2.28
S^-	RT		F2.66 F2.68 T2.26
Se^-	20K		F2.74 T2.28
OD^-	20K		II-E 5
$\text{H}^- + \text{OH}^-$	RT		T2.23

Fig. 1.3 (Continued)




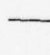
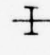
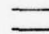
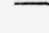
KCl	Temp.	Photon Energy (eV)	Ref.
S ²⁻	78K		F2.71
S ²⁻	78K		T2.26 F2.69
K ₂ Se	20K		F2.75 T2.28
O ²⁻ □	78K		T2.24
V ₁	78K		F2.72
Se ²⁻	20K		F2.75 T2.28
F aggregates	78K		F2.70

Fig. 1.3 (Continued)

MgF ₂	Temp.	1	2	4	6	8	10	12	14	Ref.
Neutrons	RT									F3.69
Absorption edge	RT									F3.57
Electrons	-									III-C3 F3.57
Fe ²⁺	RT									III-C2 F3.62
Fe ²⁺	4.2K									III-C2 F3.62
Co ²⁺	4.2K									T3.9
Co ²⁺	RT									T3.11 T3.9
Mn ²⁺	4.2K									T3.9

Fig. 1.4. Summary of the peak positions (|), widths (—), and oscillator strengths (numbers) of the impurity spectra for MgF₂. (See Fig. 1.1 for key.)

MgF ₂	Temp.	Photon Energy (eV)	Ref.
Mn ²⁺	RT		T3.10 T3.9
Ni	RT		T3.10
Mg vapor	RT		F3.78
γ irradiation	RT		F3.75 F3.71
M	-		III-C3
M(C _{2h})	7K		T3.13 F3.77

Fig. 1.4 (Continued)

CaF ₂	Temp.	Photon Energy (eV)					Ref.
UV absorption edge	RT						F2.1 III-A
Band gap absorption edge	RT						III-B 1
Tb ⁴⁺	RT					10 ⁻³ +	T3.4
Ce Photochromic	78K	3×10 ⁻³ +	10 ⁻² +	3×10 ⁻³ +	2×10 ⁻³ +	+	F3.19 F3.16
Y Photochromic	78K	1.4×10 ⁻³ +	3.7×10 ⁻³ +	+	+	+	F3.22 F3.16
Gd Photochromic	78K	5×10 ⁻³ +	2.1×10 ⁻² +	1.4×10 ⁻³ +	+	+	F3.20 F3.16
Yb ³⁺	RT					10 ⁻⁴ +	T3.4
Mn ²⁺	RT						F3.5 F3.6 T3.2

Fig. 1.5. Summary of the peak positions (|), widths (—), and oscillator strengths (numbers) of the impurity spectra for CaF₂. (See Fig. 1.1 for key.)

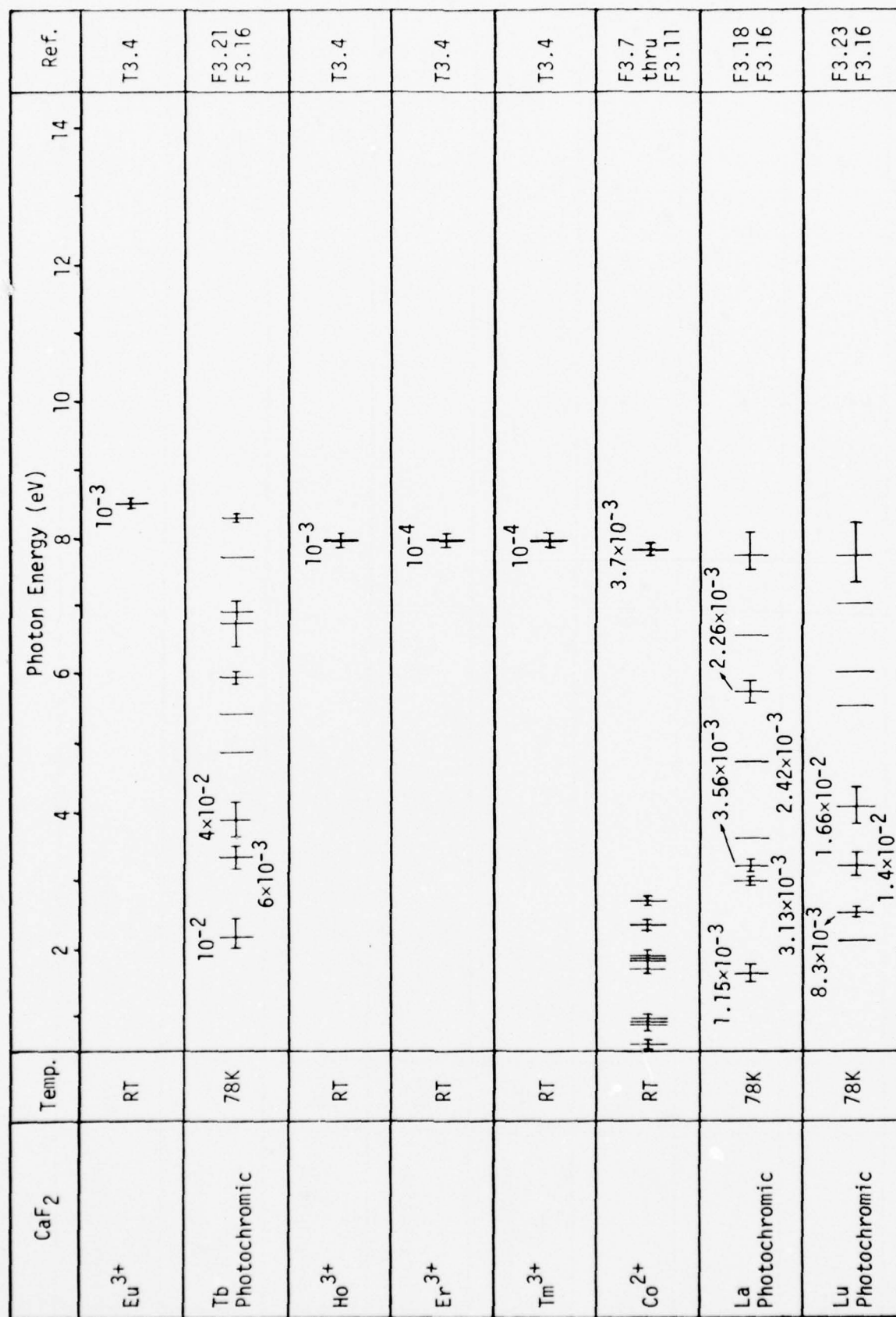


Fig. 1.5 (Continued)

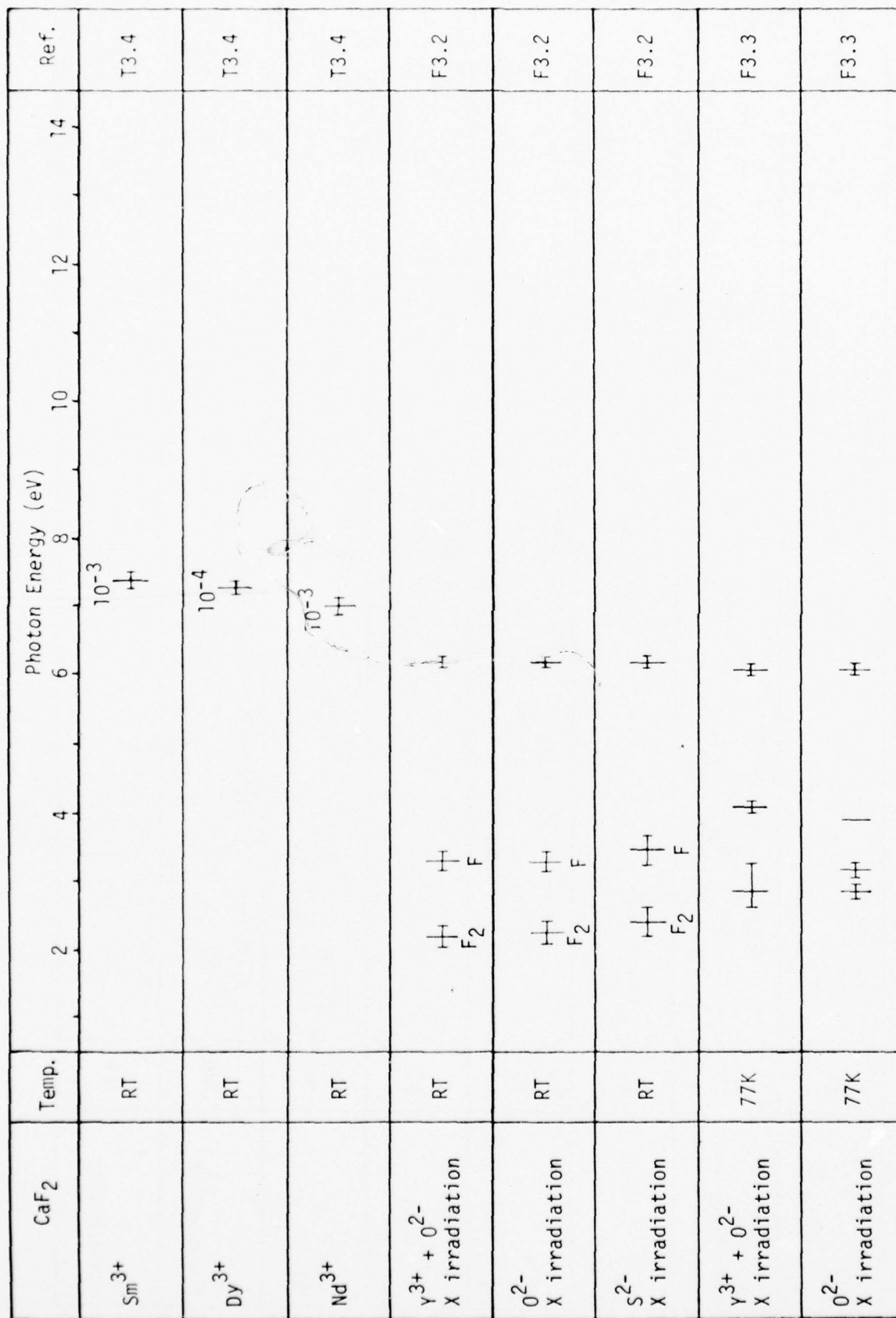


Fig. 1.5 (Continued)

CaF ₂	Temp.	Photon Energy (eV)					Ref.
S ²⁻ X irradiation	77K	2	4	6	10	14	F3.3
OH ⁻	RT						F3.1
Tb ³⁺	RT			10 ⁻⁴			T3.4
Pr ³⁺	RT			10 ⁻³			T3.4
X irradiation	RT	2	4				F3.38 T3.8
Neutrons	RT	2	4				T3.8 F3.40
Electrolytic coloration	RT	2	4				T3.8
Ca vapor	RT	2	4				T3.8

Fig. 1.5 (Continued)

CaF ₂	Temp.	Photon Energy (eV)							Ref.
		2	4	6	8	10	12	14	
Electrons	RT								T3.8
Na X irradiation	RT	+	+						T3.8 F3.43 F3.44
Ca vapor	RT								T3.8
Electrons	RT								T3.8
Tb ²⁺	RT	+	+ +						F3.14
Ni ²⁺	RT	+	+						F3.12
Ca vapor	RT								T3.8
Sr X irradiation	RT		+						F3.52

Fig. 1.5 (Continued)

CaF2	Temp.	Photon Energy (eV)	Ref.
Mn X irradiation	RT		F3.56
Ba X irradiation	RT		F3.53
Ce ³⁺	RT		T3.4
X irradiation H	4K		F3.45
Ca vapor	RT		T3.8
Tm ²⁺	RT		F3.14
He X irradiation	RT		F3.39 T3.8
Eu ²⁺	RT		F3.14

Fig. 1.5 (Continued)

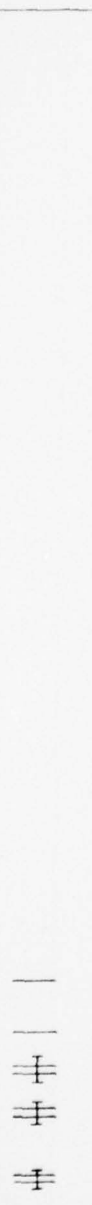
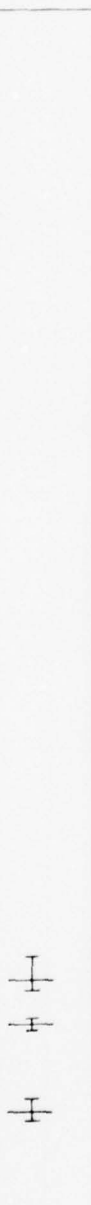

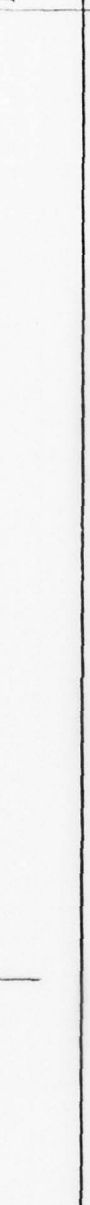




CaF ₂	Temp.	Photon Energy (eV)	Ref.
Er ²⁺	RT		F3.14
Gd ²⁺	RT		F3.14
Yb ²⁺	RT		F3.14
Tm V _K	80K		III-B ¶ 5e
X irradiation M	77K		F3.49
Cm ³⁺	RT		F3.33
Sm ²⁺	RT		F3.14
Mn X irradiation	RT		F3.56

Fig. 1.5 (Continued)

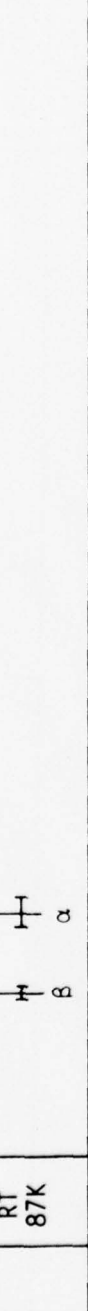
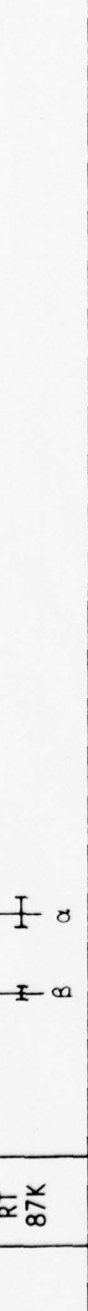
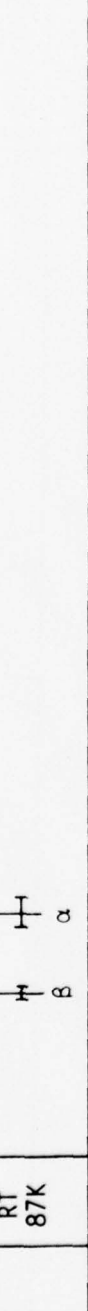
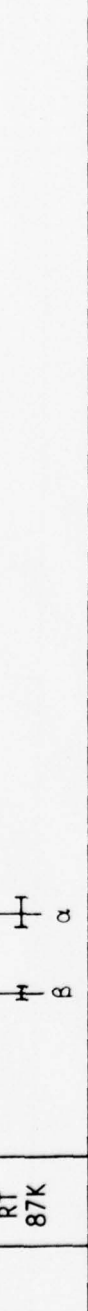
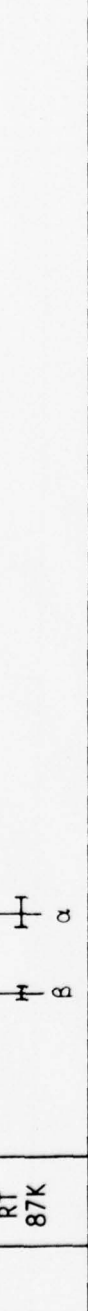
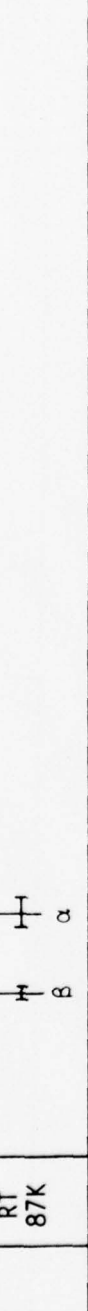
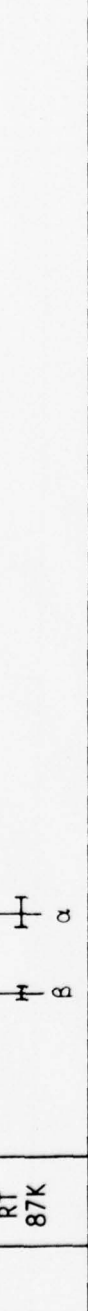
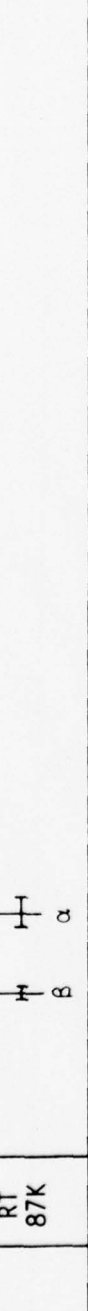
CaF ₂	Temp.	Photon Energy (eV)	Ref.
γ^{3+} F, F ₂	RT 87K		T3.8
F ₄	27K		F3.41
Electrolytic coloration	RT		T3.8
Pr ²⁺	RT		F3.14
Np ³⁺	RT		F3.34
Pu	77K		F3.31
Am	RT		F3.32
UF ₄ Green	RT		F3.24

Fig. 1.5 (Continued)

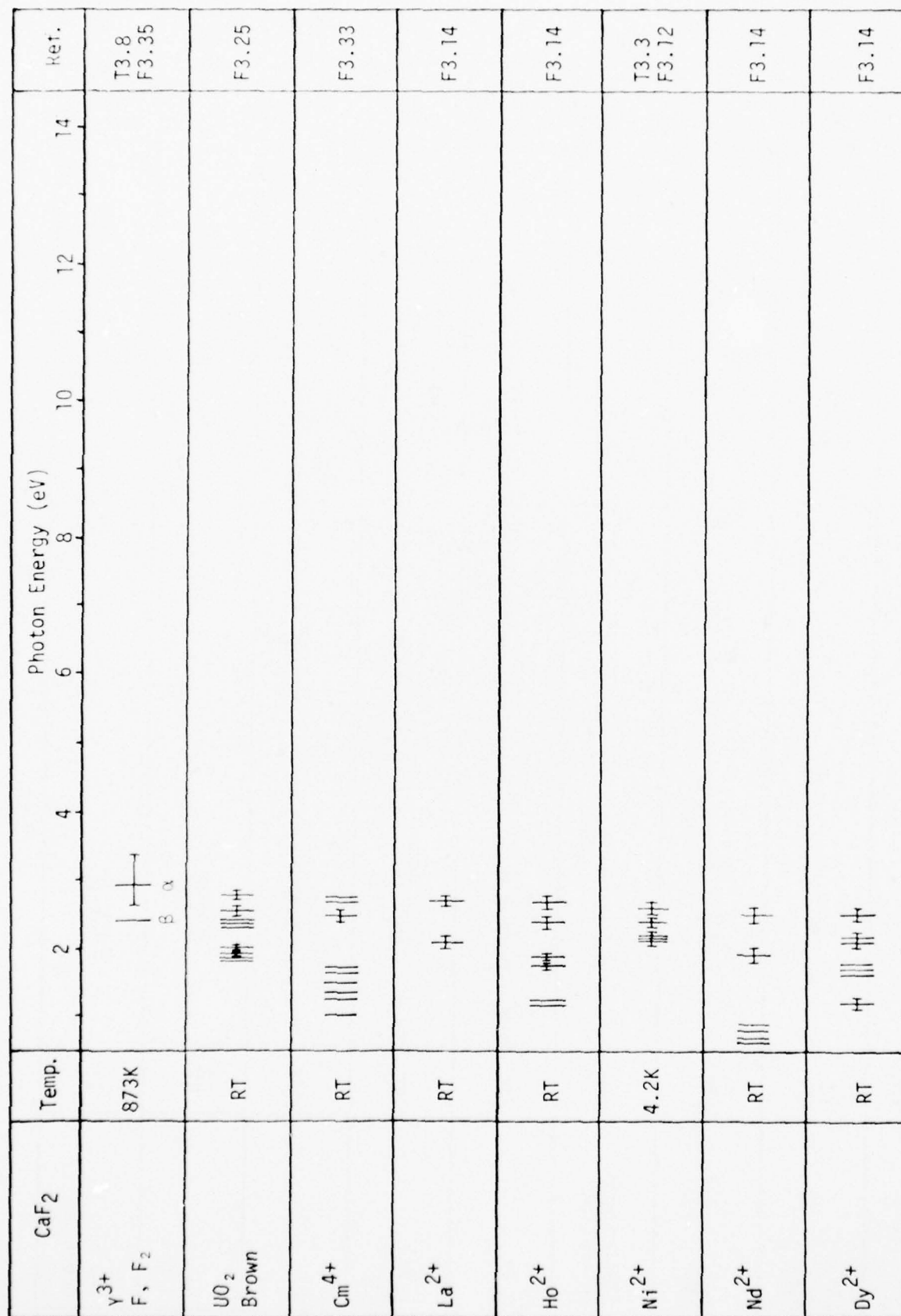


Fig. 1.5 (Continued)


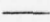

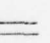
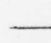
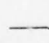
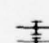
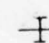
CaF ₂	Temp.	Photon Energy (eV)	Ref.
UO ₂ (NO ₃) ₂ Yellow	RT		F3.26
S ²⁻ F ₂	RT		T3.1
F ₂	RT		T3.1
O ²⁻ F ₂	RT		T3.1
Na ⁺ F ₂	RT		T3.1
Li ⁺ F ₂	RT		T3.1
Impurity color centers	77K		F3.49
Ce ²⁺	RT		F3.14

Fig. 1.5 (Continued)

CaF ₂	Temp.	Photon Energy (eV)							Ref.
		2	4	6	8	10	12	14	
X irradiation F ₃	77K	⊥							F3.49
Co ²⁺	5K	⊥							F3.8

Fig. 1.5 (Continued)


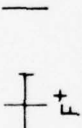

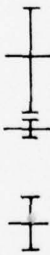
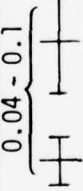

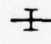

MgO	Temp.	Photon Energy (eV)	Ref.
First exciton peak	RT		F4.74
Ne ⁺ irradiated	RT		F4.74 F4.118
Fe	RT		F4.85
Fe annealed in O ₂	RT		F4.86
Fe ³⁺ X irradiation	RT		F4.87
Ne ⁺ irradiated	RT		F4.120
Fe ³⁺	RT		F4.74
V ³⁺	RT		F4.77

Fig. 1.6. Summary of the peak positions (|), widths (—|), and oscillator strengths (numbers) of the impurity spectra for MgO. (See Fig. 1.1 for key.)

MgO	Temp.	Photon Energy (eV)				Ref.
Neutrons	RT	1.5	2.0	3.0	4.0	F4.114
H ⁺	RT				5.0	F4.121
X irradiation	RT	1.5	2.0	3.0	4.0	F4.87
Ni ²⁺	RT	1.5	2.0	3.0	4.0	F4.93 F4.94
Electrons	78K	1.5	2.0	3.0	4.0	F4.115
Co ²⁺	77K	1.5	2.0	3.0	4.0	F4.91
Cr ³⁺	120K	1.5	2.0	3.0	4.0	F4.80
Cr ³⁺	RT	1.5	2.0	3.0	4.0	IV-C 1b

Fig. 1.6 (Continued)



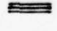

MgO	Temp.	Photon Energy (eV)	Ref.
Co ²⁺	RT		F4.90
V	5K - RT	<p>~ 0.15</p> 	F4.100
V ²⁺	RT		IV-C 1a
[Na] ⁰	77K		F4.106

Fig. 1.6 (Continued)

Al_2O_3	Temp.	Photon Energy (ev)			Ref.
Absorption edge	RT			F4.43
Fe^{3+}	RT	0.19	0.65		T4.7 F4.59
Ni^{3+}	RT	4×10^{-4}	2×10^{-3}		T4.7 F4.60
Cr^{3+}	RT				T4.7 F4.57
Ti^{3+}	RT				T4.7 F4.56
H^+ irradiation	RT				F4.73
D^+ irradiation	RT				F4.73
Neutrons γ irradiation Bleached	RT				F4.71

Fig. 1.7. Summary of the peak positions (|), widths (—), and oscillator strengths (numbers) of the impurity spectra for Al_2O_3 . (See Fig. 1.1 for key.)


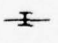

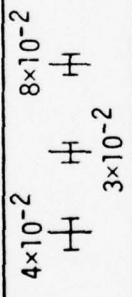



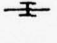
Al_2O_3	Temp.	Photon Energy (eV)	Ref.
Neutrons	77K		F4.67 F4.66
Electrons	77K		F4.66
$^4\text{He}^+$ irradiation	RT		F4.73
Mn^{4+}	RT		F4.58
V^{3+}	RT		T4.7 F4.55
γ irradiation	RT		F4.65
X irradiation	RT		F4.64
O^+ irradiation	RT		F4.73

Fig. 1.7 (Continued)

A^{2+}_3	Temp.	Photon Energy (eV)	Ref.
Cr^{3+} $E \parallel c$	77K	1.3×10^{-4} 1.3×10^{-4} 1.016×10^{-3} 1.3×10^{-4}	F4.46 T4.5
Cr^{3+} $E \perp c$	77K	4.8×10^{-4} 1.2×10^{-4} 5.88×10^{-4}	F4.46 T4.5
Mn^{3+}	RT		T4.7
Fe^{3+} $E \perp c$	194K		F4.62
Fe^{3+} $E \perp c$	10K	2.8×10^{-6} 1.6×10^{-5} 1.0×10^{-5} 2×10^{-3}	F4.62 F4.61
V^{3+} $E \parallel c$	77K	2.79×10^{-5} 5.61×10^{-4}	F4.45 T4.5
Fe^{3+} $E \parallel c$	10K	5.24×10^{-6} 9.5×10^{-6} 5.2×10^{-6}	F4.61
Fe^{3+}	77K		T4.5

Fig. 1.7 (Continued)

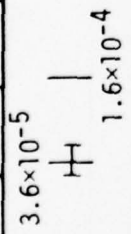
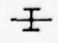
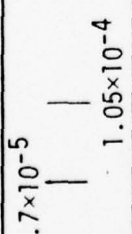
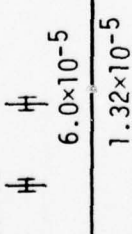
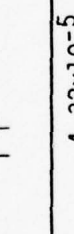
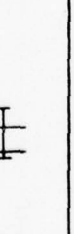
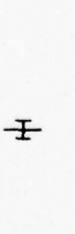
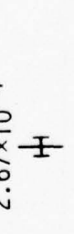
Al_2O_3	Temp.	Photon Energy (eV)	Ref.
V^{3+} $E \perp c$	77K	3.6×10^{-5}  1.6×10^{-4}	F4.45 T4.5
Ni^{3+}	35K		F4.49
Co^{3+} $E \parallel c$	77K	2.7×10^{-5}  1.05×10^{-4}	F4.48 F4.54 T4.5
Co^{3+} $E \perp c$	77K	8.7×10^{-5}  6.0×10^{-5}	F4.48 F4.54 T4.5
Ti^{3+} $E \perp c$	77K	1.32×10^{-5} 	F4.44 T4.5
Ti^{3+} $E \parallel c$	77K	4.32×10^{-5} 	F4.44 T4.5
Mn^{3+} $E \parallel c$	77K	1.77×10^{-4} 	F4.47 T4.5
Mn^{3+} $E \perp c$	77K	2.67×10^{-4} 	F4.47 T4.5

Fig. 1.7 (Continued)

Al_2O_3	Temp.	Photon Energy (eV)							Ref.
		2	4	6	8	10	12	14	
Fe, Ti E \perp c	RT								F4.63
Ni ³⁺ E \parallel c	77K								F4.49 T4.5
Ni ³⁺ E \perp c	77K								T4.5
Fe, Ti E \parallel c	10K								F4.63

Fig. 1.7 (Continued)

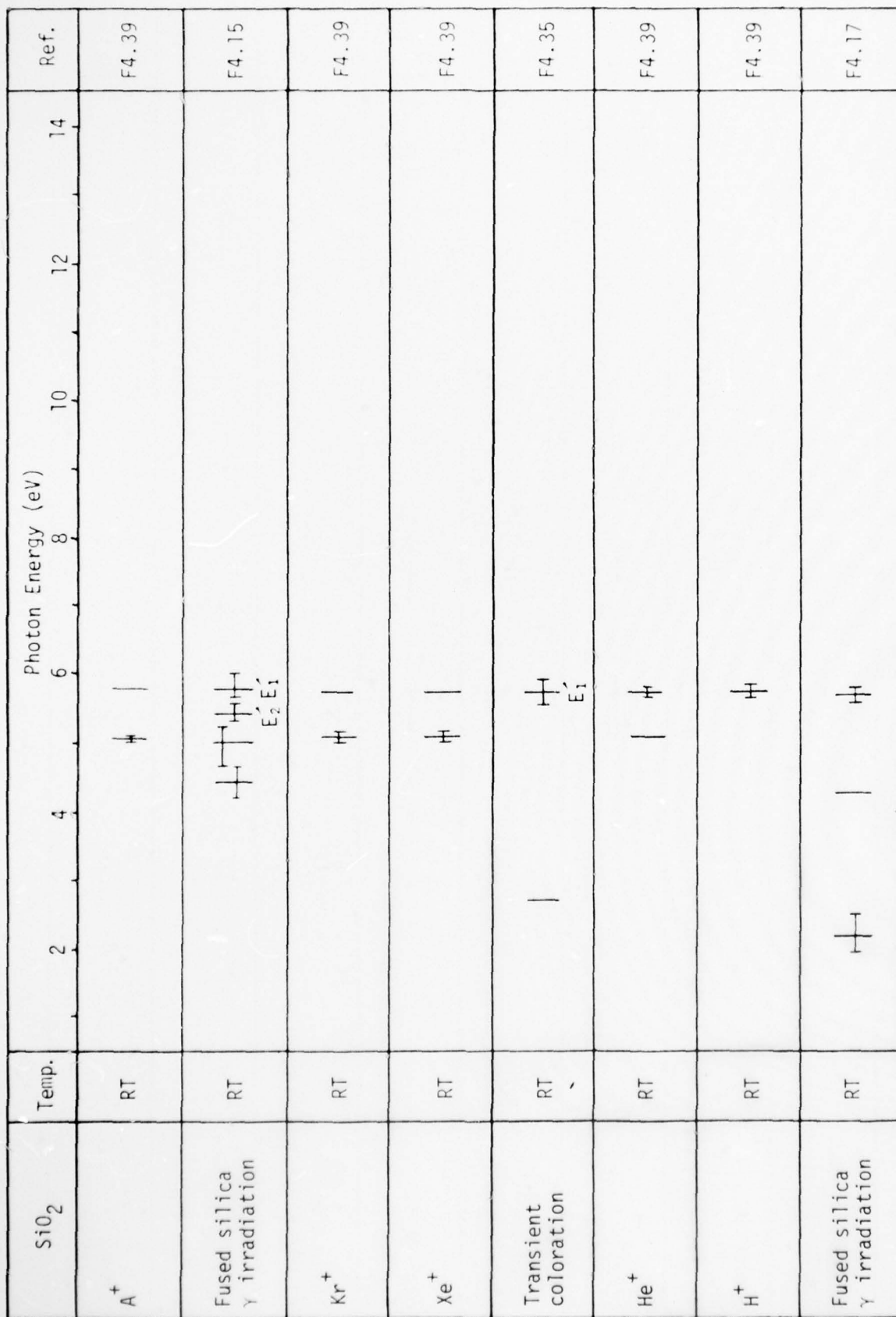


Fig. 1.8 (Continued)

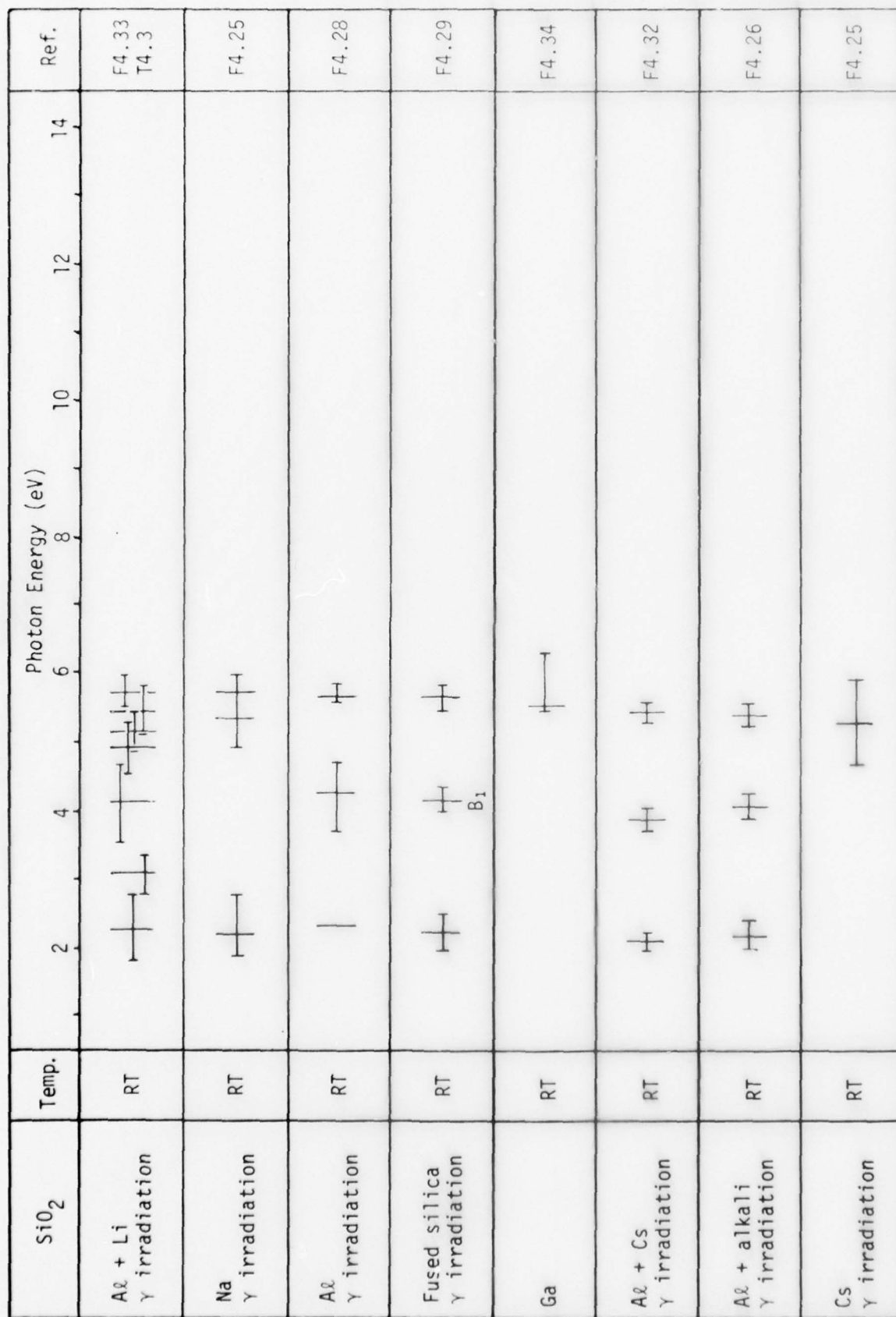


Fig. 1.8 (Continued)


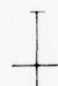
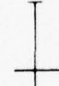
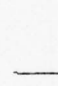
SiO ₂	Temp.	Photon Energy (eV)	Ref.
K γ irradiation	RT		F4.25
Rb γ irradiation	RT		F4.25
Ga + Li γ irradiation	RT		F4.34
Al ³⁺ □	RT		IV-A ¶ 8

Fig. 1.8 (Continued)

Silicate Glasses	Temp.	Photon Energy (eV)							Ref.
		2	4	6	8	10	12	14	
Silicate glasses Ti	—								IV-A # 3
Absorption edge 1Na ₂ O - 1Al ₂ O ₃ - 3SiO ₂	RT							F4.11
Absorption edge 1Na ₂ O - 1CaO - 3SiO ₂	RT							F4.11
3SiO ₂ - 1Na ₂ O Fe	RT								F4.12
Absorption edge 1K ₂ O - 3SiO ₂	RT							F4.11
3SiO ₂ - 1Na ₂ O X-irradiation	RT	+	+		+				F4.30
3SiO ₂ - 1K ₂ O X-irradiation	RT	+	+		+				F4.30
Absorption edge 2SiO ₂ - 1Na ₂ O	RT							F4.3

Fig. 1.9. Summary of the peak positions (|), widths (—), and oscillator strengths (numbers) of the impurity spectra for silicate glasses. (See Fig. 1.1 for key.)



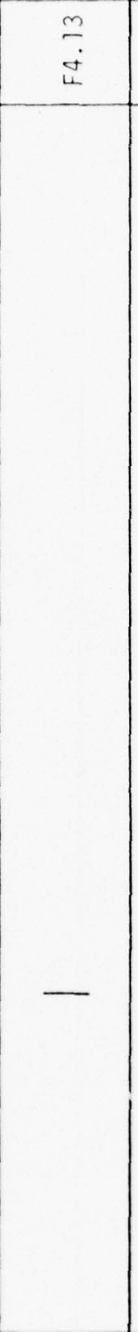
Silicate Glasses	Temp.	Photon Energy (eV)	Ref.
$3\text{SiO}_2 - 1\text{Na}_2\text{O}$ Cu	RT		F4.13 F4.14
Absorption edge Electrons	RT		F4.22
Absorption edge $3\text{SiO}_2 - 1\text{Na}_2\text{O}$ Cu	RT		F4.13

Fig. 1.9 (Continued)

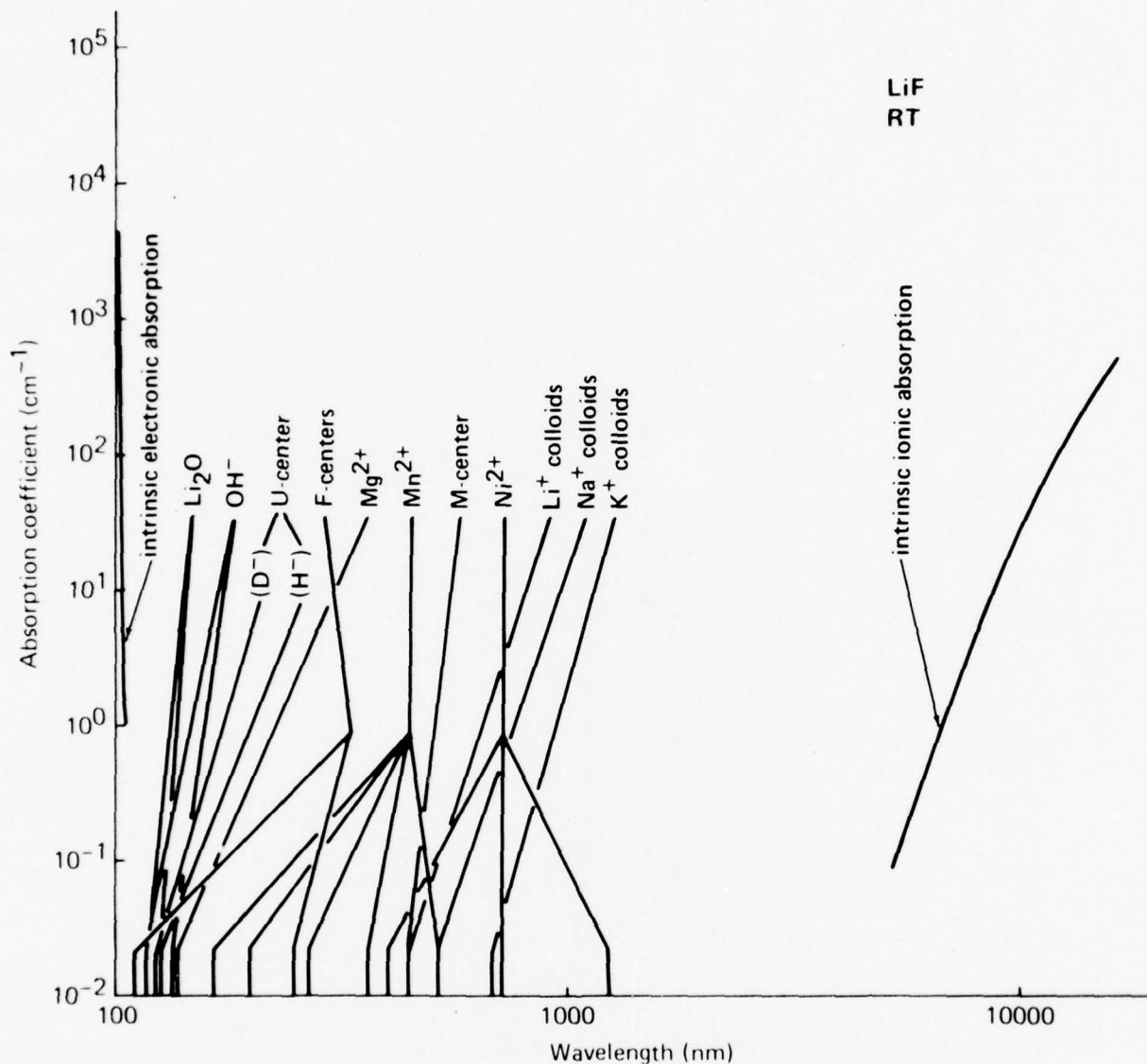


Fig. 1.10. Summary of the positions of important impurity-absorption lines in LiF shown with respect to the ultraviolet and infrared cutoff frequencies. A complete summary of absorption bands in LiF is given in Fig. 1.1.

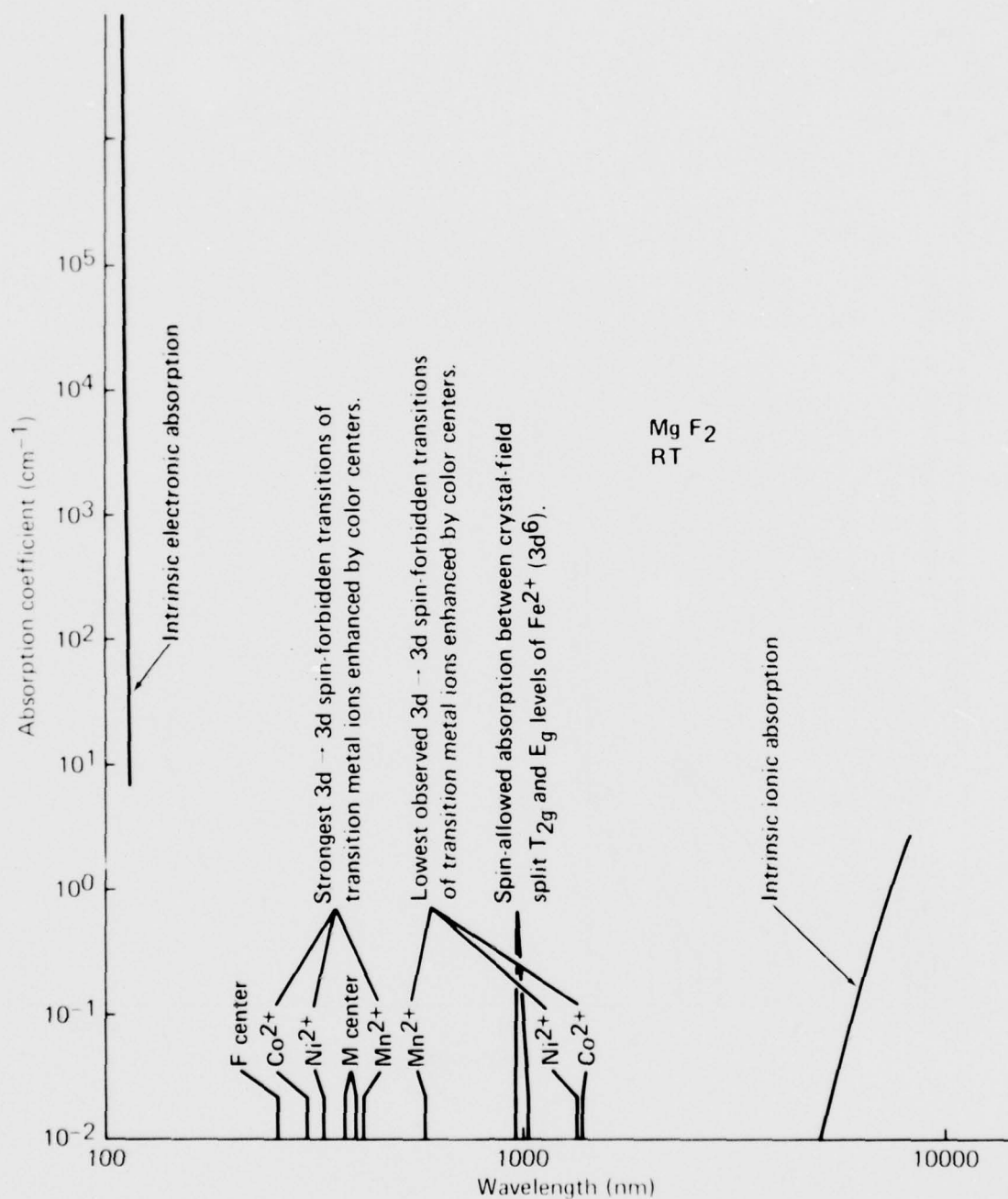


Fig. 1.11. Summary of the positions of important impurity-absorption lines in MgF₂ shown with respect to the ultraviolet and infrared cutoff frequencies. A complete summary of absorption bands in MgF₂ is given in Fig. 1.4.

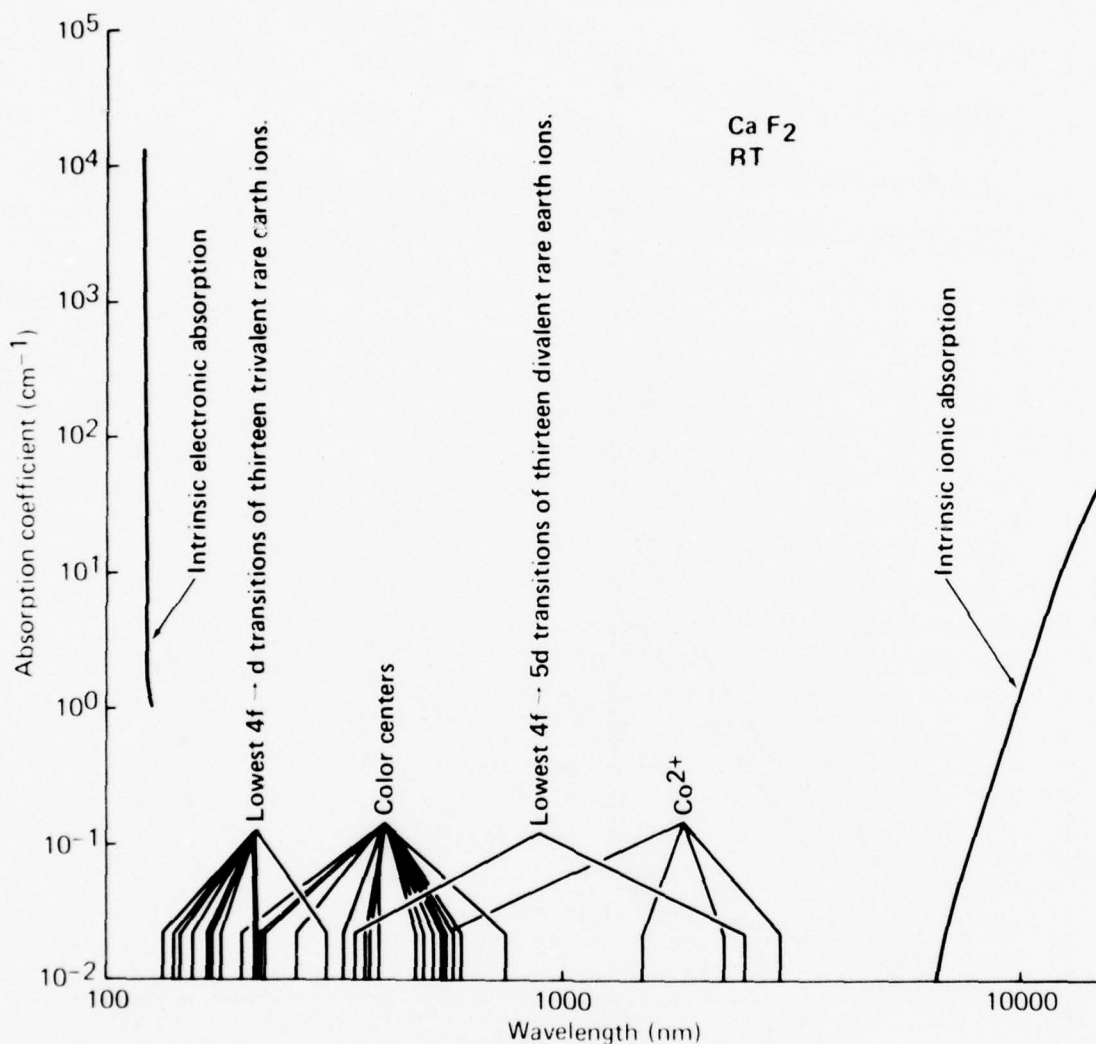


Fig. 1.12. Summary of the positions of important impurity-absorption lines in CaF₂ shown with respect to the ultraviolet and infrared cutoff frequencies. A complete summary of absorption bands in CaF₂ is given in Fig. 1.5.

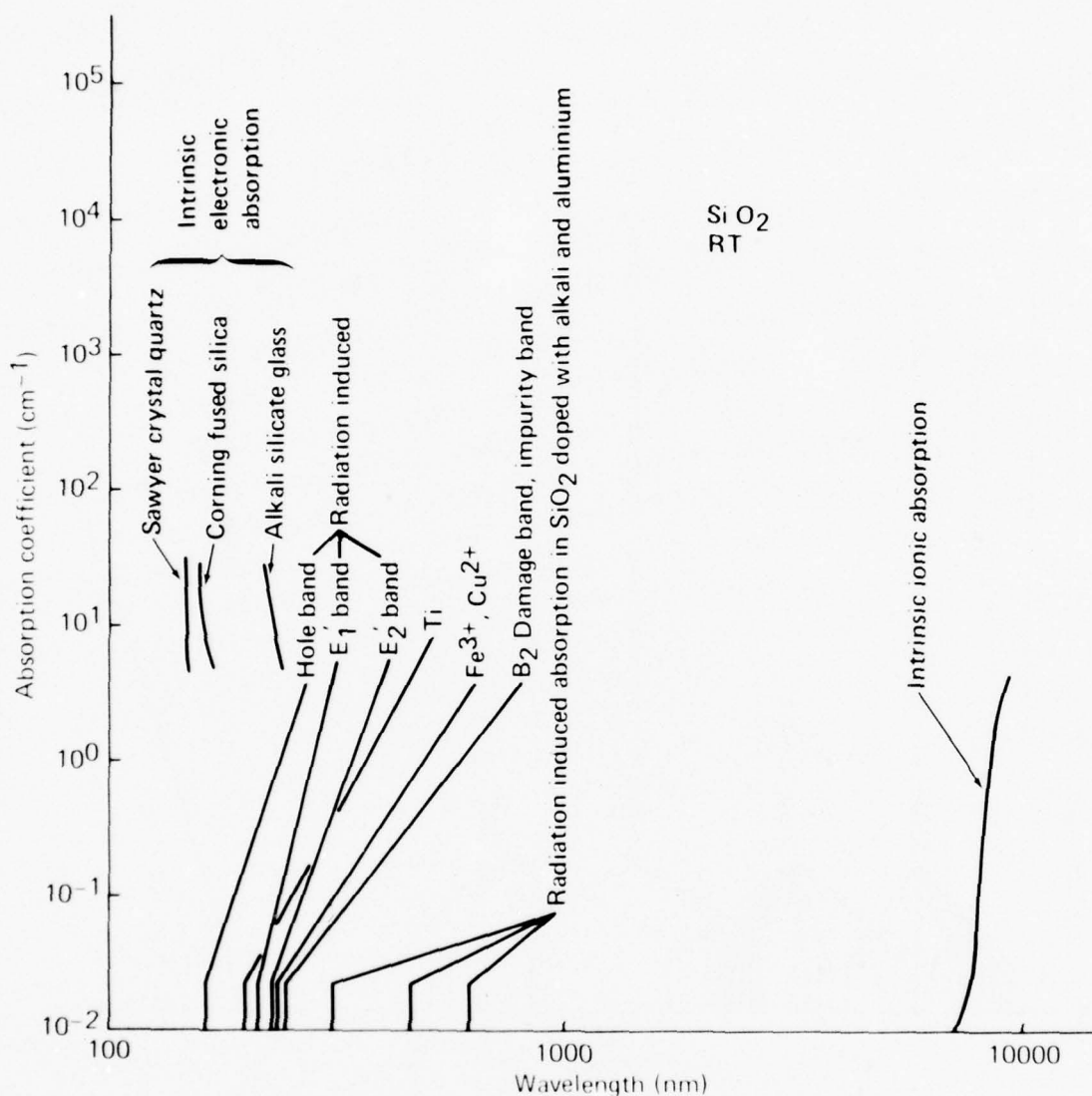


Fig. 1.13. Summary of the positions of important impurity-absorption lines in SiO₂ shown with respect to the ultraviolet and infrared cutoff frequencies. A complete summary of absorption bands in SiO₂ is given in Fig. 1.8.

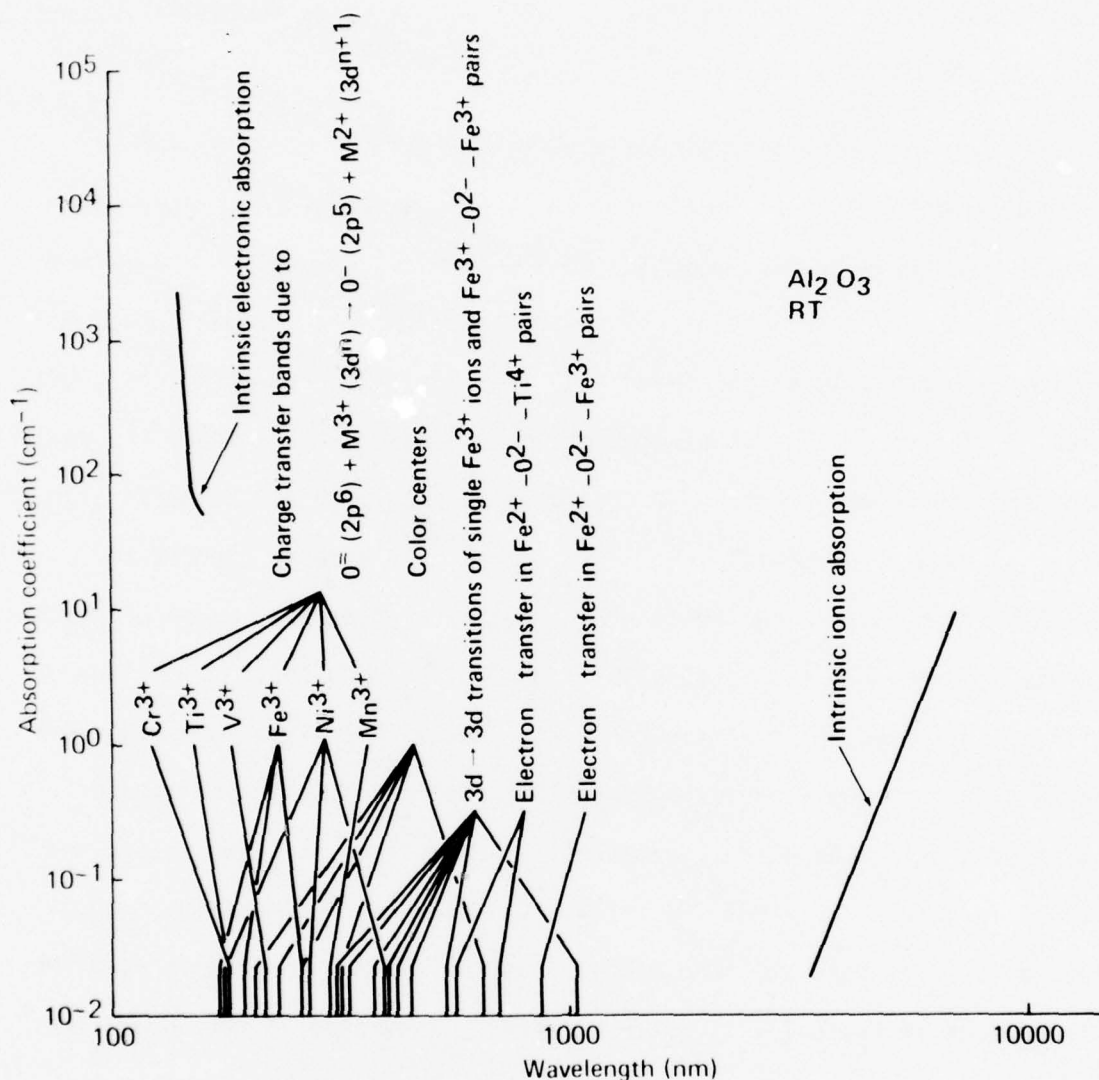


Fig. 1.14. Summary of the positions of important impurity-absorption lines in Al₂O₃ shown with respect to the ultraviolet and infrared cutoff frequencies. A complete summary of absorption bands in Al₂O₃ is given in Fig. 1.7.

Sec. I

Table 1.1. Table 1.2 summarizes the intrinsic crystalline-structure, vacuum-ultraviolet cutoff, infrared cutoff, and major color-center absorptions for the materials covered in this report.

In general, ionically bonded materials (near the edges of the periodic table) consisting of light elements are transparent to shorter wavelengths (in the UV or VUV region). The fundamental absorption across the energy gap can be described as charge transfer from the valence band, consisting of p orbitals of the anions, to the nearly-free-electron conduction band.^{1,8} The resulting Urbach absorption edges are quite steep. The deviations from the sharp Urbach-edge absorption typically occur at quite high values of absorption coefficient, from $\sim 1 \text{ cm}^{-1}$ to several hundred cm^{-1} . The absorption coefficient remains high over a considerable range of photon energies, up to $\sim 5 \text{ eV}$, as seen in Figure 2.1 below. These absorption tails are believed to be extrinsic in most cases, but Pinnow and coworkers argued that the long secondary exponential absorption (the much steeper Urbach edge being the primary exponential absorption) in fused silica and glasses is intrinsic. (Ref. 4.5, Figs. 4.4-4.6, and accompanying discussion in Sec. IV, Vol. II) The behavior of the optical absorption near the infrared cutoff typically is quite different, the value of the absorption coefficient at which the extrinsic contributions become greater than the intrinsic multiphonon absorption being as low as $\beta = 10^{-4} \text{ cm}^{-1}$ or even somewhat lower. No absorption analogous to the secondary exponential absorption has been observed in the infrared region.

This study of Pinnow and coworkers appears to be the only attempt to distinguish between absorption and scattering. This distinction is extremely important in low-power optical systems since absorption gives rise

Table 1.1. Defect center nomenclature and description. [Adapted, with additions, from E. Sonder and W. A. Sibley, in Point Defects in Solids, Vol. 1 of General and Ionic Crystals, ed. by J. W. Crawford, Jr., and L. M. Slifkin, Ch. 4.]

Notation	Description of defect	Ionic charge of normal ion at lattice site
A. Single defects		
F^+, α	Negative-ion vacancy	$\left\{ \begin{array}{l} -1^a \\ -2^a \end{array} \right\}$
F^{2+}		
F	Negative-ion vacancy with one trapped electron	$\left\{ \begin{array}{l} -1 \\ -2 \end{array} \right\}$
F^+, F_1		
F^-, F'	Negative-ion vacancy with two trapped electrons	$\left\{ \begin{array}{l} -1 \\ -2 \end{array} \right\}$
F, F'		
K, L_1, L_2, L_3	Weak bands on the short wavelength side of the F band from excited F-center states	—
V^-	Positive-ion vacancy	$\left\{ \begin{array}{l} +1 \\ +2 \end{array} \right\}$
V^{2-}		
V	Positive-ion vacancy with one hole trapped at a near neighbor	$\left\{ \begin{array}{l} +1 \\ +2 \end{array} \right\}$
V^-, V'		
I	Interstitial atom centered at an interstitial space	0^b

Table 1.1 (Continued)

Notation	Description of defect	Ionic charge of normal ion at lattice site
U_1	Interstitial H (hydrogen atom)	0
H	$\left\{ \begin{array}{l} \text{Split interstitial (atom) molecular ion at a halide site.} \\ \text{Three negative host ions and a positive host atom (3 F}^- \text{ and} \\ \text{a Li atom in LiF, for example) squeezed into the positions} \\ \text{normally occupied by three negative ions along a [110]} \\ \text{direction.} \end{array} \right\}$	-
halide	Foreign halide ion at a negative-ion site	-1
U	H^- or D^- at a negative-ion site	-1
hydroxide	OH^- at a negative-ion site	-1
I^-	Interstitial anion (singly charged) centered at an interstitial space	-
U_2	Interstitial H^-	-

Table 1.1 (Continued)

Notation	Description of defect	Ionic charge of normal ion at lattice site
B. Composite defects		
F_2, M^C	Di-F center	$\left\{ \begin{array}{l} -1 \\ -2 \end{array} \right\}$
F_2		
F_3, R^C	Tri-F center: three adjacent F centers in a [111] plane	$\left\{ \begin{array}{l} -1 \\ -2 \end{array} \right\}$
F_3		
F_4, N^C	Quadra-F center	-1
F_2^+, M^+	Ionized Di-F center	$\left\{ \begin{array}{l} -2 \\ -4 \end{array} \right\}$
F_2^+		
V_3	$\left\{ \begin{array}{l} \text{Linear molecule along a [100] direction consisting of three} \\ \text{negative host ions, one of which is in a positive-ion site,} \\ \text{with two trapped holes. Also called a } F_3 \text{ molecular ion (in} \\ \text{a fluoride)} \end{array} \right\}$	+1
C	Metallic self-colloid, such as Li in LiF, ~1-5 nm in diameter	-
C. Impurity-defect centers		
F_A^e	F center adjacent to cation impurity of same valence as host	$\left\{ \begin{array}{l} -1 \\ -2 \end{array} \right\}$
F_A^e		

Table 1.1 (Continued)

Notation	Description of defect	Ionic charge of normal ion at lattice site
F_Z^e, Z	F center adjacent to divalent cation — positive-ion vacancy pair in alkali halide	-1
Z_1	The association of an F center with a divalent positive impurity-ion/positive-ion vacancy complex	-
V_A^e	V center adjacent to an impurity	$\left. \begin{array}{l} +1 \\ +2 \end{array} \right\}$
V_F, V_{OH}		
H_A^e	H center trapped at impurity of same valence host	-
C_A	Impurity metallic colloids, such as Na in LiF	-
Me^{2+}, Me^{3+}	Transition-metal ions	0, +1, +2
	Rare-earth ions	0, +1, +2
	Heavy-metal ions: Tl, Pb	0, +1, +2
D. Simple charge defects without missing or extra ions		
$[X_2^-]^g, V_K$	Self-trapped hole	-1
$[XY^-]^g$	Hole trapped at a halide impurity	-1
$[Me^{0-g}]$	Hole trapped at a cation impurity	+1

Table 1.1 (Continued)

Notation	Description of defect	Ionic charge of normal ion at lattice site
E. Other		
color centers	Imperfections that give rise to optical absorption, not necessarily in the visible region, in transparent solids.	-
α, β	<div style="display: flex; align-items: center;"> <div style="margin-right: 10px;"> $\left\{ \begin{array}{l} \text{Transitions similar to those of the fundamental band but modified by the proximity of various imperfections (possibly negative-ion vacancies for } \alpha \text{ and F centers for } \beta). \end{array} \right.$ </div> <div>Very near fundamental absorption edge.</div> </div>	-

^aAlkali halides are singly charged; MgO is doubly charged; for such materials as MgF_2 , the cation (Mg) is doubly charged and the anion is singly charged.

^bAn interstitial site carries no charge.

^cThe M- and R-center notation for F_2 and F_3 centers is generally accepted by workers using alkali halides and is used universally in the literature. It is therefore retained.

^dIt is not known whether the interstitial atoms of a di-interstitial are at interstitial sites or have H-center-like configurations.

^eThe subscript A stands for any alkali atom impurity. The F_A center in sodium-doped KCl , for example, could be written as F_{Na} .

^fThe V_{OH} and V_{F} defects also include a hole located at a nearby divalent anion in order for charge of the composite defect to be the same as that of the perfect lattice.

^gThe letter X stands for a host halide ion; the letter Y stands for any other halide species; Me stands for any metal atom.

Table 1.2. Intrinsic crystalline structural data, ultraviolet-, infrared-cutoffs, and major color-center absorption bands in LiF, NaF, KCl, MgF₂, SiO₂, Al₂O₃, and MgO.

	LiF	NaF	KCl	MgF ₂	CaF ₂	α -SiO ₂	α -Al ₂ O ₃	MgO
1. Crystal structure	face-centered cubic (NaCl)	face-centered cubic (NaCl)	face-centered cubic (NaCl)	tetragonal (rutile)	cubic (fluorite)	trigonal	trigonal (distorted close-packed hexagonal)	face-centered cubic (NaCl)
<u>Interionic Distances [nm]</u>								
2. anion - cation	0.201	0.232	0.315	0.202	0.236	0.161 - 0.162	0.186 - 0.197	0.211
3. anion - anion	0.284	0.328	0.445	0.258, 0.281, 0.305	0.273	0.260 - 0.267	0.252 - 0.267	0.298
4. cation - cation	0.284	0.328	0.445	0.305, 0.361	0.367	0.287	0.265	0.298
5. coordination number (number of nearest anions around a cation)	6	6	6	6	8	4	6	6
6. cationic radius [nm]	0.06 (Li ⁺)	0.098 (Na ⁺)	0.133 (K ⁺)	0.065 (Mg ²⁺)	0.099 (Ca ²⁺)	0.041 (Si ⁴⁺)	0.05 (Al ³⁺)	0.065 (Mg ²⁺)
7. cationic impurity radii [nm] divalent-transition-metal ions trivalent-transition-metal ions tetraivalent-transition-metal ions trivalent-rare-earth ions 4+, 4+, 4+, 4+ Si ⁴⁺ , Ge ⁴⁺ , Sn ⁴⁺	— 0.062 - 0.076 — — —	0.076 - 0.10 0.072 - 0.10 — — —	0.093 - 1.10 — — 0.093 - 1.14 —	0.072 - 0.09 0.062 - 0.076 — — —	0.072 - 0.09 — — ~ 0.1 —	— 0.062 - 0.069 0.064 - 0.069 — 0.041 - 0.071	— 0.062 - 0.069 0.064 - 0.069 — 0.041 - 0.071	— 0.062 - 0.081 — — —
8. anionic radius [nm]	0.136 (F ⁻)	0.136 (F ⁻)	0.181 (Cl ⁻)	0.136 (F ⁻)	0.136 (F ⁻)	0.13 (O ²⁻)	0.14 (O ²⁻)	0.14 (O ²⁻)
9. effective radius [nm] of interstitial site	0.037	0.065	0.092	0.092	0.099	0.12 ^a	0.01	0.043
10. effective interstitial-site to host-cation spacing [nm]	0.173	0.201	0.273	0.294	0.273	0.267	~ 0.19	0.183
11. ultraviolet cutoff [nm] [eV]	105 11.8	128 9.7	180 6.9	115 10.8	125 9.9	160 7.75	144 8.62	172 7.2
12. infrared cutoff [nm]	8.1	14.8	26.1	7.0	11.0	4.0	6.0	10.0
13. major color centers or radiation-induced absorption bands: [nm] [eV]	248 5.00	505, 340 2.46, 3.65	539 2.30	260 4.77	552, 480, 382 2.25, 2.59, 3.31	234, 214, 163 5.30, 5.79, 7.61	400, 204 3.10, 6.08	539, 250 2.30, 5.0

^aThe large interstitial site in quartz enables it to accommodate large alkali ions, e.g., 0.095 nm (Na⁺) and 0.133 nm (K⁺).

Sec. I

to heating that can cause fracture or excessive optical distortion. With the current interest in high-power optical systems in the ultraviolet and visible regions, additional absorption measurements may be forthcoming.

The impurity absorption in transparent crystals may be grossly divided into two types:

In intra-impurity absorption, the electron transitions are between two energy levels of the absorption center. Examples^{1.8} include most of the absorption bands of H^- , OH^- , O_2^- , O^{2-} , F centers, such positive-ion impurities as Tl^+ , In^+ , Sn^{++} , and Pb^{++} having outer electronic configuration s^2 , Ag^+ , and Cu^+ with d^{10} configuration, transition-metal ions with $d^n < 10$, and rare-earth ions with $f^n < 14$. The intra-impurity transitions can be weak or strong, depending on the selection rules for the transition from the ground state to the particular excited state of the ion or defect.^{1.9} For example, both the 3d to 3d transition of transition-metal ions and the 4f to 4f transition of the rare-earth ions are weak since they are parity-forbidden. However, the 3d to 3d transitions are generally stronger and broader than the 4f to 4f transitions in solids because the 3d orbitals are more strongly coupled to vibrational modes than are the 4f orbitals because the 4f electrons of the rare-earth ions are shielded from the surroundings by the outer $5s^2$ and $5p^6$ electrons, while there are no outer electrons to shield the 3d electrons. The vibronic coupling mixes the parity so that the transitions are no longer forbidden.

Interconfigurational transitions can be weak or strong, depending on the particular selection rule. For example, the 3d to 4s absorption of transition-metal ions is weaker (oscillator strength $\sim 10^{-3}$) than the 3d to 4p absorption (oscillator strength $\sim 10^{-2}$) or the 4f to 5d absorption of

Sec. I

the rare-earth ions (oscillator strength $\sim 10^{-1}$) since the 3d to 4s absorptions are parity-forbidden while the latter are parity-allowed. The parity-allowed transitions are strong only if they are also spin-allowed.

Charge-transfer processes usually involve the transition of an electron from a p orbital of a negative ion to the nearly-free-electron conduction band or to the s or d orbitals of transition-metal ions,^{1.10-1.12} or to the s, d, or f orbitals of rare-earth ions. The impurity can be either a positive or negative ion. The charge-transfer transitions involve more than one ion and are usually allowed.

Absorption lines are often characterized by the value β_{mx} of the absorption coefficient β at the center of the line, the line width $\Delta\hbar\omega$ (full width at one-half the maximum value), and the oscillator strength f , which are related by the expression

$$Nf = (8.7 \times 10^{16} \text{ cm}^{-2} \text{ eV}^{-1}) \frac{n_r}{(n_r^2 + 2)^2} \beta_{\text{mx}} \Delta\hbar\omega \quad (1.1)$$

where N is the number of centers per cubic centimeter, n_r is the refractive index of the host material at the wavelength of the absorption band, the absorption coefficient β_{mx} at the peak is measured in cm^{-1} , and the line width $\Delta\hbar\omega$ is measured in eV. The factor 8.7, which is for Gaussian lines, is replaced by 12.9 for Lorentzian lines, thus giving the well known Smakula equation.^{1.13} For $n_r = 1.5$, $N = 2 \times 10^{22} \text{ cm}^{-3}$ (formally for a solid density), $\Delta\hbar = 0.5 \text{ eV}$, and $f = 1$ (strong absorption), (1.1) gives $\beta_{\text{mx}} = 5.5 \times 10^6 \text{ cm}^{-1}$, which is reasonable for solid densities since values of β in such strong-absorption regions as that above the fundamental absorption edge are of this order of magnitude. One part per million of a strong absorber ($f = 1$) would

Sec. I

give $\beta_{\text{mx}} = 5.5 \text{ cm}^{-1}$ for this case. The potential severity of the impurity absorption problem for high-power optics is illustrated by this same example. Values of β less than 10^{-4} cm^{-1} already are needed in high-power-laser systems. Only two parts per billion of a relatively weakly absorbing impurity ($f = 10^{-2}$) will give rise to $\beta = 10^{-4} \text{ cm}^{-1}$ at the center of the absorption band. For a strongly absorbing impurity ($f = 1$), only 0.02 parts per billion, or 4×10^{12} centers per cubic centimeter, would give $\beta = 10^{-4} \text{ cm}^{-1}$.

The absorption coefficient β is, of course, the exponential decay coefficient β in the Beer law $I = I_0 \exp(-\beta \ell)$. The optical density is defined as $\log_{10} I_{\text{inc}}/I_{\text{trans}}$, where "inc" and "trans" denote incident and transmitted. In the limit of small reflectance (negligible multiple reflections), the absorptance is given by $A = 1 - \exp(-\beta \ell)$, where ℓ is the sample thickness, the transmittance is given by $T = 1 - A - R \approx 1 - A \approx \exp(-\beta \ell) \approx I_{\text{trans}}/I_{\text{inc}}$, and the absorption coefficient can be obtained from the optical density from the expression

$$\beta \approx 2.30 \ell^{-1} \times (\text{optical density}) \quad (1.2)$$

for reflectance $R \ll 1$.

A sample with 9.0 percent reflectance for two surfaces and no absorptance has an optical density of $\log_{10} [1/(1 - 0.09)] = 4.10 \times 10^{-2}$. For samples with a well defined base line, such as in Fig. 4.1, the base-line value of the optical density is subtracted from the reported value and (1.2) is used to estimate the value of β . For example, in Fig. 4.1,

$$\beta = 2.30(0.1)^{-1} (1.0 - 0.04) = 22.1 \text{ cm}^{-1} .$$

Sec. I - References

REFERENCES

- 1.1 F. Rosenberger, "Purification of Alkali Halides," in Ultrapurity: Methods and Techniques, M. Zief and R. M. Speights, eds., Dekker Publishers, New York, 1972.
- 1.2 W. J. Fredericks, L. M. Schuerman, and L. C. Lewis, Oregon State University, Department of Chemistry, Final Report on Air Force Contract AF-AFOSR-217-66, 1966.
- 1.3 R. C. Pastor and K. Aritz, Mat. Res. Bull. 10, 493 (1975).
- 1.4 M. Sparks, "Overview of Materials for High-Power Visible and Ultraviolet Lasers," Proceedings of the Infrared Laser Window Materials Meeting, Boulder, Colorado, 12 July 1976.
- 1.5 M. Sparks and C. J. Duthler, Xonics, Inc. Third, Fourth, and Fifth Technical Reports, Contract No. DAHC15-73-C-0127, 30 June 1974, 6 December 1974, and 30 June 1975.
- 1.6 M. Sparks, Theoretical Studies of Materials for High-Power Infrared Coatings, Xonics, Inc. Sixth Technical Report, under Contract No. DAHC15-73-C-0127, 31 December 1976.
- 1.7 C. J. Duthler, J. Appl. Phys. 45, No. 6, 2668 (1974).
- 1.7a S. C. Jain, A. V. R. Warriar, and S. K. Agarwal, Electronic Absorption and Internal and External Vibrational Data of Atomic and Molecular Ions Doped in Alkali Halide Crystals, Report No. NSRDS - NBS 52, National Bureau of Standards, Washington, D.C. (1974).
- 1.8 R. S. Knox and K. J. Teegarden, in Physics of Color Centers, W. B. Fowler, ed., Academic Press, New York and London, 1968, p. 1-51.
- 1.9 W. B. Fowler, in Physics of Color Centers, W. B. Fowler, ed., Academic Press, New York and London, 1968, p. 53-179.

Sec. I - References

- 1.10 Y. Sakisaka, T. Ishii, and T. Sagawa, J. Phys. Soc. Japan 36, 1365 (1974).
- 1.11 Y. Sakisaka, J. Phys. Soc. Japan 38, 505 (1975).
- 1.12 H. H. Tippins, Phys. Rev. B1, 126 (1970).
- 1.13 A. Smakula, Z. Physik 59, 603 (1930).

II. ALKALI HALIDES

A. Intrinsic Properties of Alkali Halides

The intrinsic Urbach ultraviolet absorption edge at 105 nm (11.8 eV) and the onset of infrared absorption at $\sim 4 - 10 \mu\text{m}$ (4000 - 10000 nm, or 0.311 - 0.124 eV), which define the edges of the broad transmitting region of LiF, are shown in Fig. 1.10, along with representative absorption-peak positions. The Urbach ultraviolet absorption edges and the beginning of the extrinsic absorption spectra are shown in Fig. 2.1 for LiF, NaF, CaF_2 , SrF_2 , and BaF_2 .^{2.1} The intrinsic exciton and interband absorption spectrum of thin LiF films^{2.2} is given in Fig. 2.2. Figure 2.3 summarizes the intrinsic UV spectra of other alkali-halide films on LiF substrates at room temperature and 80 K.^{2.3} Similar spectra have been measured^{2.4} at 10 K.

The band gap is sometimes taken to be equal to the value of the absorption shoulder,^{2.5} for example at 8.5 eV (146 nm) in KCl as indicated by the vertical arrow in Fig. 2.3(g). The positions at 80 K of these absorption shoulders, which correspond to the onset of interband transitions, along with the positions of the lowest-energy exciton peak at 300 K, the American Institute of Physics Handbook values of the band gaps, and the room-temperature absorption edges (which were taken as the position in the Urbach-tail region at which the absorption coefficient $\beta = 5 \text{ cm}^{-1}$), are summarized in Table 2.1 for the alkali halides. It is seen that the room-temperature absorption edges range from 8.2 to 11.8 eV for the fluorides, from 6.6 to 7.4 eV for the chlorides, from 6.1 to 6.4 eV for the bromides, and from 5 to 5.3 eV for the iodides.

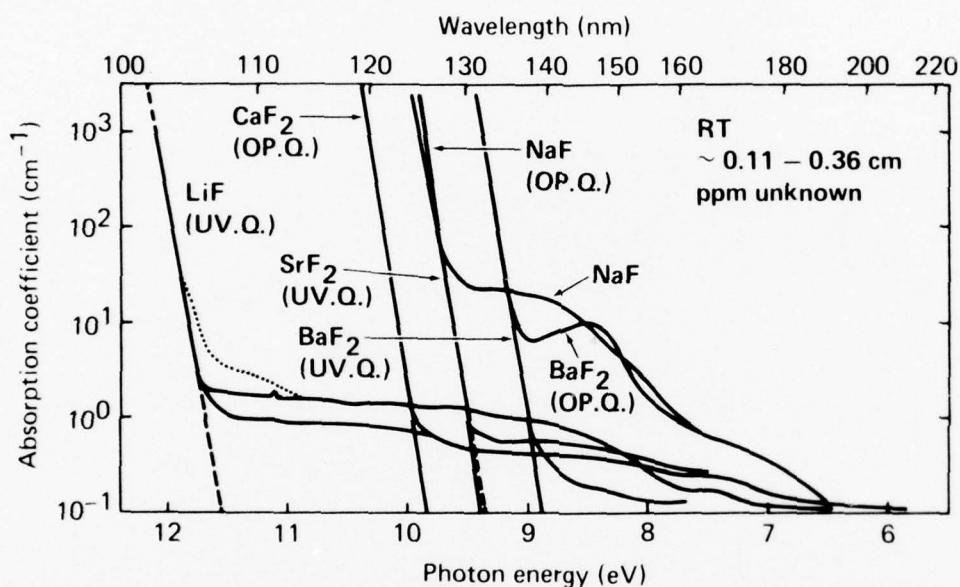


Fig. 2.1. Absorption spectra of several fluorides, showing the Urbach edges and the large values ($\sim 0.1\text{--}30\text{ cm}^{-1}$) of extrinsic absorption extending over several electron volts below the edge. [T. Tomiki and T. Miyata, J. Phys. Soc. Japan 27, 658 (1969).]

Sec. II-A Alkali Halides

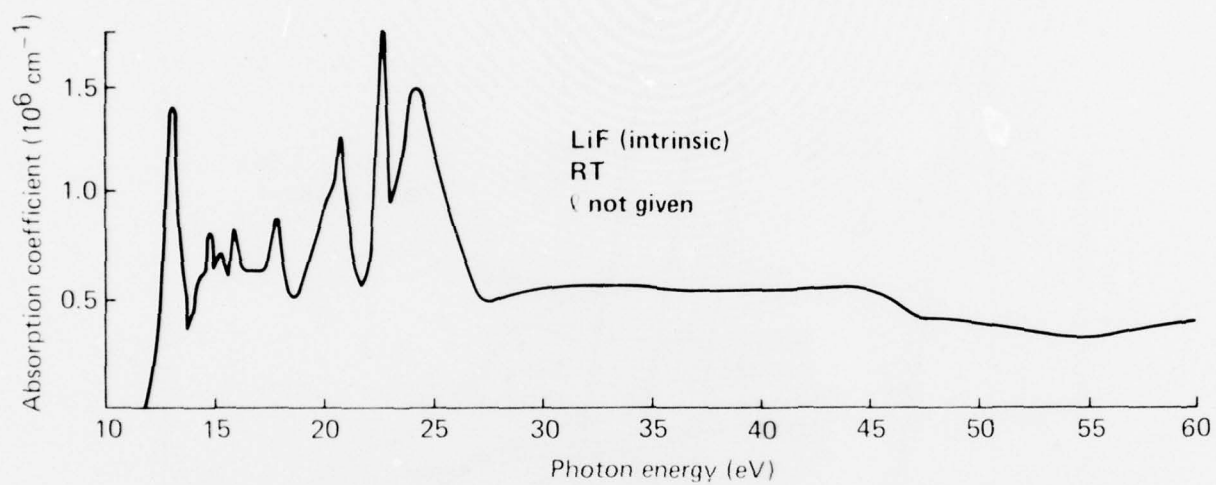


Fig. 2.2. Absorption spectrum above the absorption edge for thin LiF films (~ 10 nm thick) evaporated on 5-25 nm thick celluloid substrates. [A. Milgram and M. P. Givens, Phys. Rev. 125, 1506 (1962).]

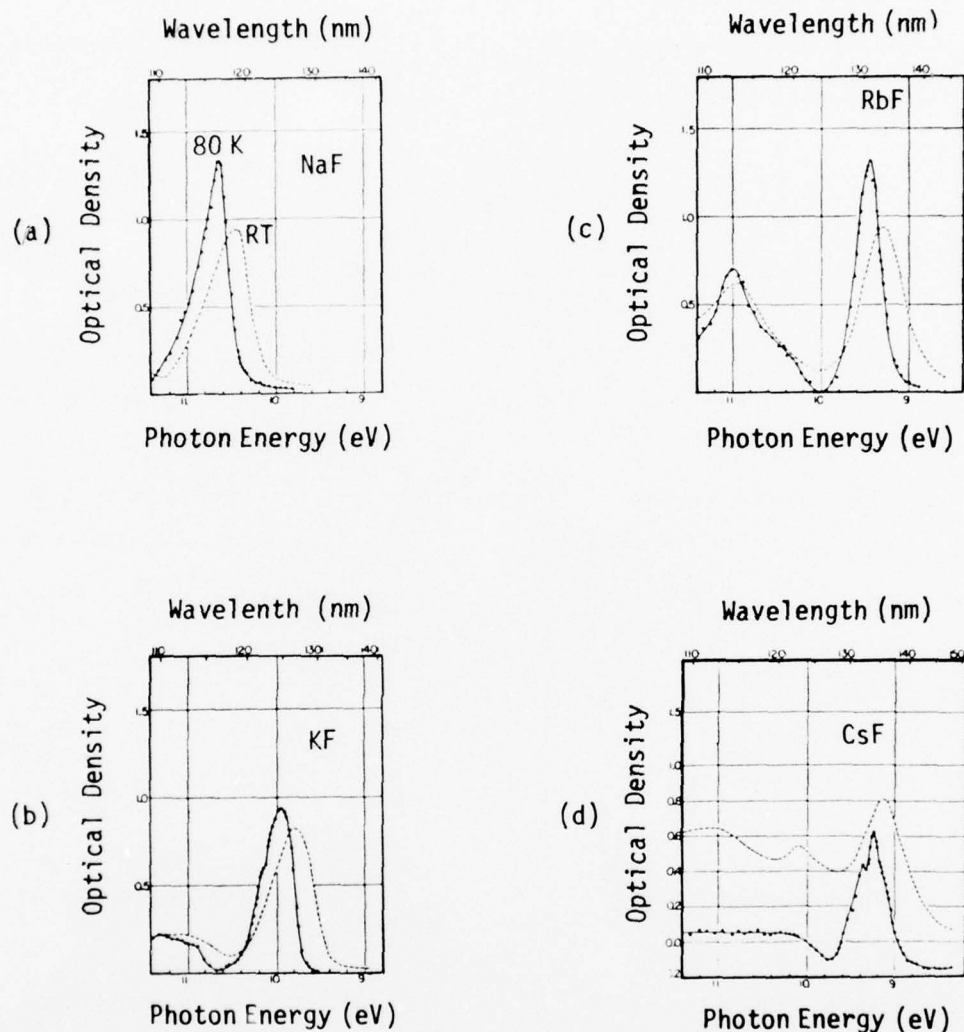


Fig. 2.3. Optical absorption near and above the absorption edges of alkali-halide thin films deposited on LiF and measured at 80 K (solid curves) and room temperature (dashed curves). For CsCl, curve I (i) represents a freshly evaporated film, believed to correspond to the NaCl-type crystal structure. Curve II (j) is for the same film after annealing at room temperature for about ten hours and is believed to correspond to the CsCl-type crystal structure. [J. E. Eby, K. J. Teegarden, and D. B. Dutton, *Phys. Rev.* **116**, 1099 (1959).]

Sec. II-A Alkali Halides

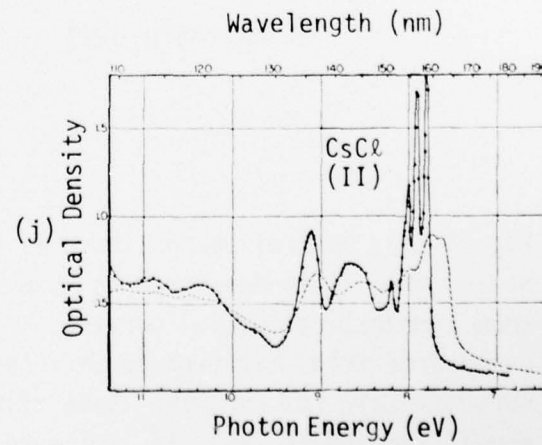
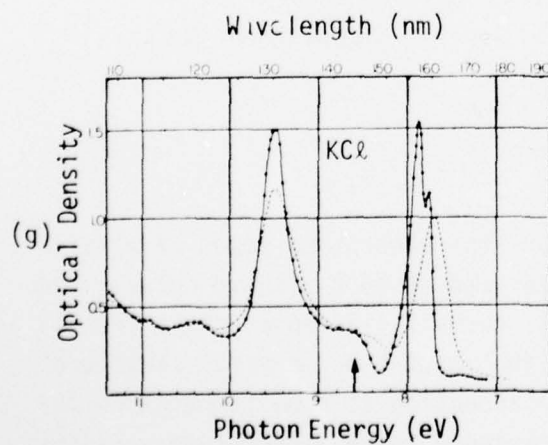
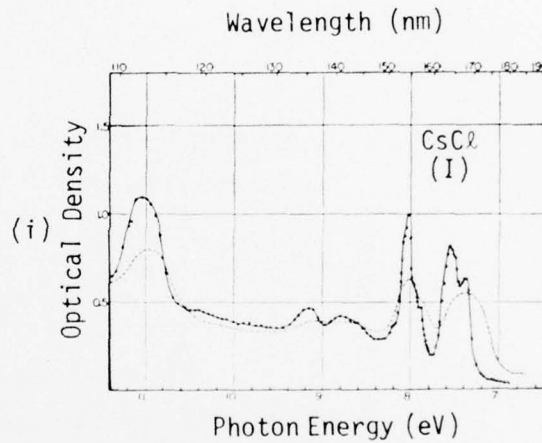
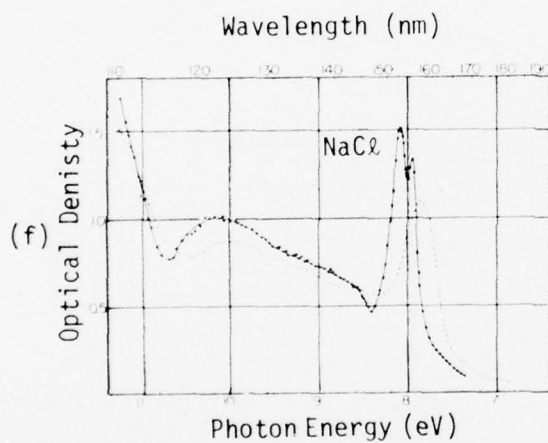
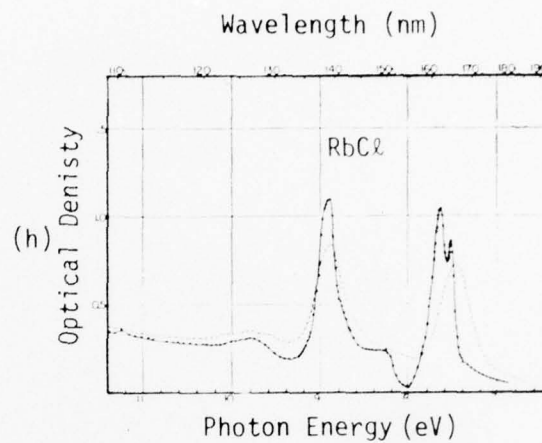
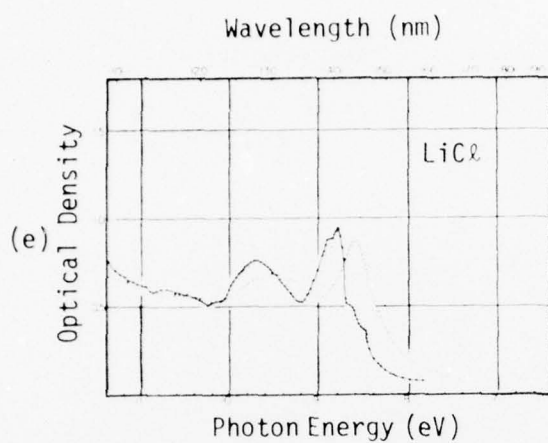


Fig. 2.3 (Continued)

Sec. II-A Alkali Halides

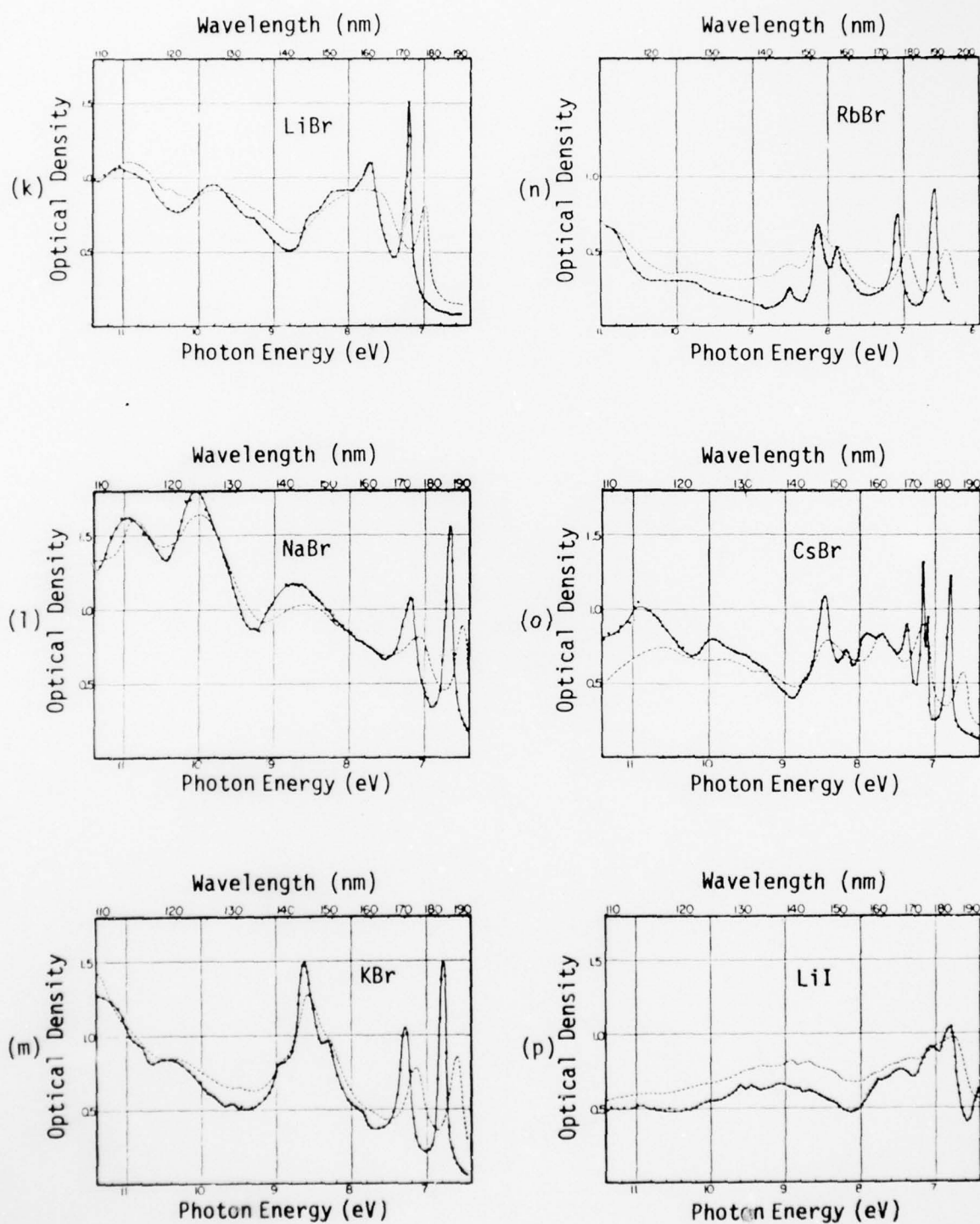


Fig. 2.3 (Continued)

Sec. II-A Alkali Halides

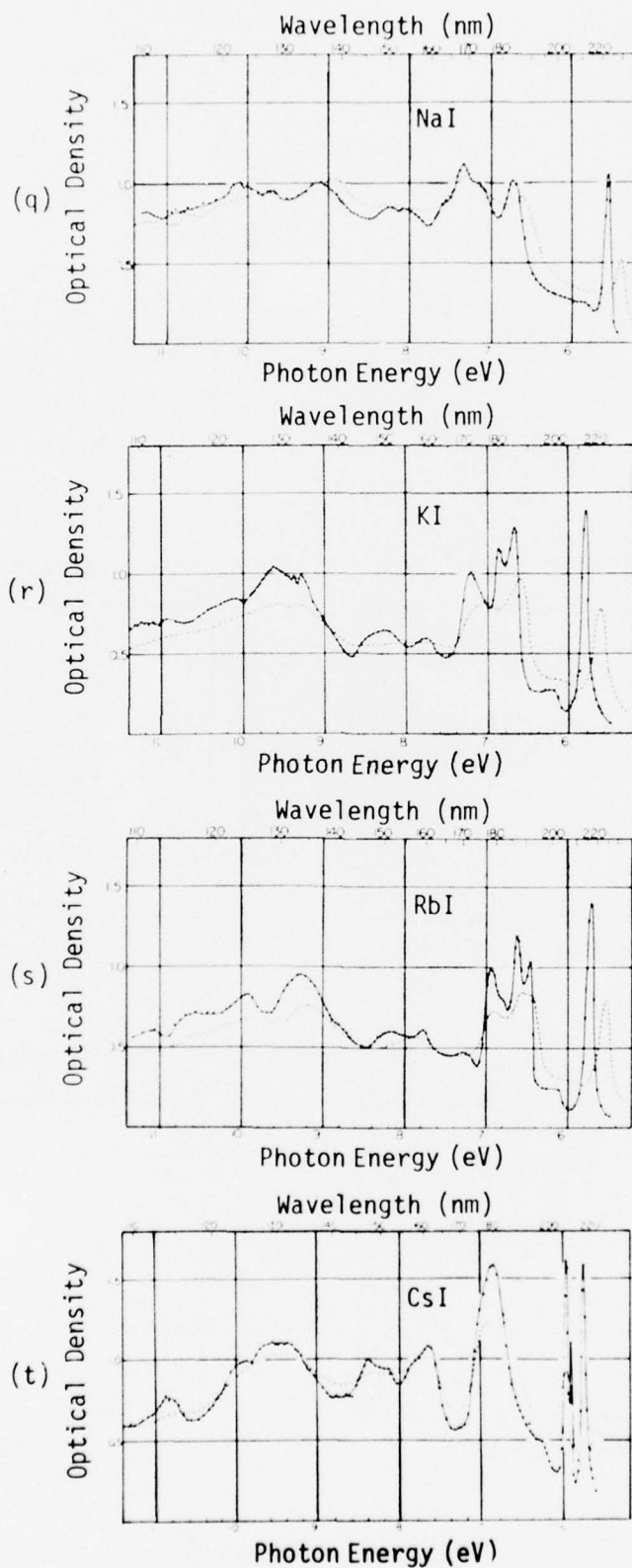


Fig. 2.3 (Continued)

Table 2.1. Positions [eV] of features in the absorption spectra of the alkali halides. The four numbers for each material correspond to the four variables listed in the key at the bottom of the figure. The data for LiF films are from Milgram and Givens^{2.2}, for LiF crystal from Tomiki and Miyata^{2.1}, and the remaining data are from Eby and coworkers^{2.3}.

	F		Cl		Br		I
Li	14 ~12	12.9 11.8	9.2 ~10	8.6 7.4	~8.6 ~8.5	7 6.4	~5.9 ≥ 5.9 5
Na	~11.5 ≥ 10.5	10.45 9.6	8.6 8.6	7.85 6.8	7.7 7.7	6.5 6.1	~5.8 ≥ 5.8 5.43 5
K	10.9 10.9	9.75 9	8.5 8.5	7.7 6.9	7.8 7.8	6.6 6.2	6.2 ≥ 6.2 5.63 5.34
Rb	10.4 10.4	9.35 8.6	8.2 8.2	7.45 6.7	7.7 7.7	6.45 6	6.1 ≥ 6.1 5.5 5.1
Cs	10 10	9.17 8.2	~7.8 ≥ 7.5	7.4 6.6	7.6 7.8	6.6 6.1	6.3 ≥ 6.3 5.6 5.16
Key	80 K absorption shoulder AIP HP band gap			lowest RT exciton peak RT absorption edge			

Sec. II-B Alkali Halides

Values of the index of refraction of alkali-halide crystals in the transparent regions are summarized in the four panels of Fig. 2.4.^{2.6} The American Institute of Physics Handbook^{2.7} contains extensive tables of values of the index of refraction.

A general survey of the literature on the optical absorption of impurities in alkali halides shows that the following host crystals have been extensively studied: LiF and NaF in fluorides, NaCl and KCl in chlorides, KBr in bromides, and KI in iodides.

B. Comparisons of Alkali-Halide Impurity Spectra

Results from the spectra to be presented below and in Volume II are summarized in Figs. 1.1 - 1.14 (all spectra), in Fig. 2.5 (F-center spectra^{2.5}), in Fig. 2.6 (Ivey relations for OH^- , U, and F-band positions as a function of lattice constant), and in Tables 2.2 - 2.10 (peak positions and other information for several important, strongly absorbing centers^{1.9,2.7,2.8}).

Sec. II-A Alkali Halides

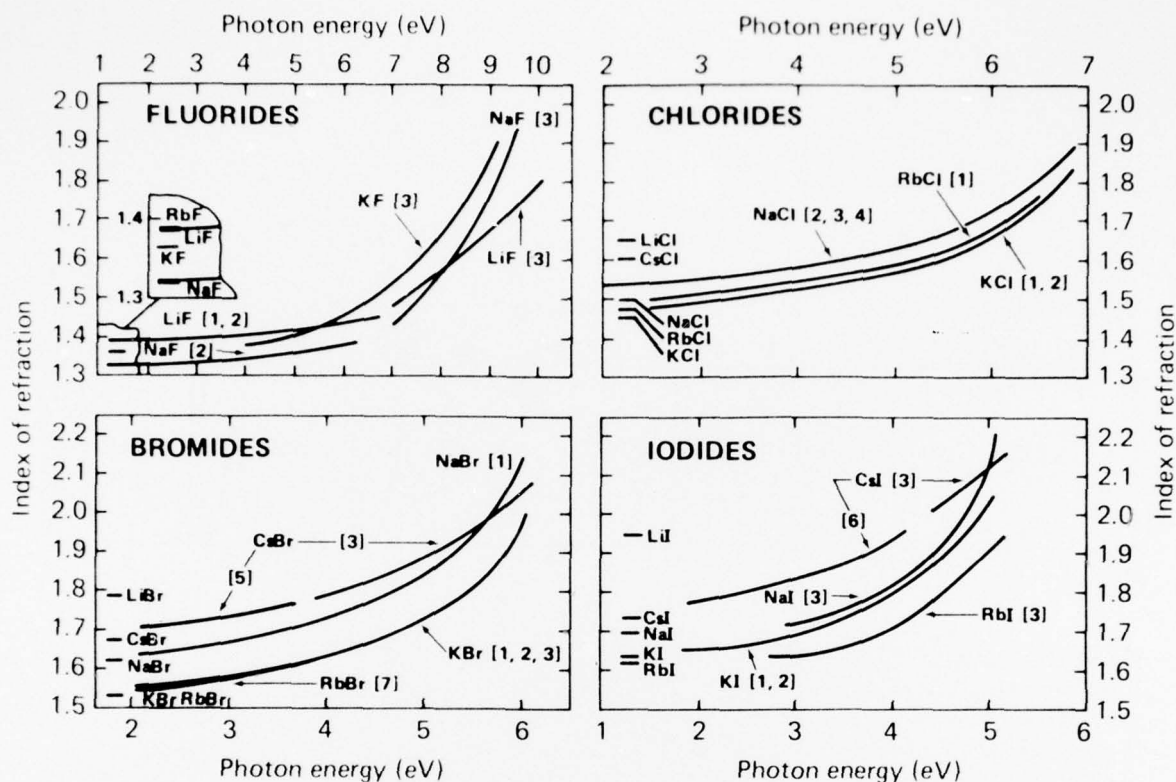


Fig. 2.4. Room-temperature values of refractive indices of alkali halides in the visible and ultraviolet regions. The short horizontal lines at the left denote the values of $\epsilon_\infty^{1/2}$, where ϵ_∞ is the "high-frequency dielectric constant" generally quoted. The numbers in brackets denote the following references: (1) Z. Gyulai, *Z. Physik* **46**, 80 (1928); (2) H. Harting, *Z. Instrumentenk.* **63**, 125 (1943); (3) D. M. Roessler, Thesis, Kings College, London, unpublished (1966); (4) F. F. Martens, *Ann. Physik* [4], **6**, 603 (1901); (5) W. S. Rodney and R. J. Spindler, *J. Res. Natl. Bur. Std.* **51**, 123 (1953); (6) W. S. Rodney, *J. Opt. Soc. Am.* **45**, 987 (1955); (7) A. Kublitzky, *Ann. Physik* **20**, 791 (1935). [R. S. Knox and K. J. Teegarden, in *Physics of Color Centers*, W. Beall Fowler, ed., Academic Press, New York, 1968.]

Sec. II-B Alkali Halides

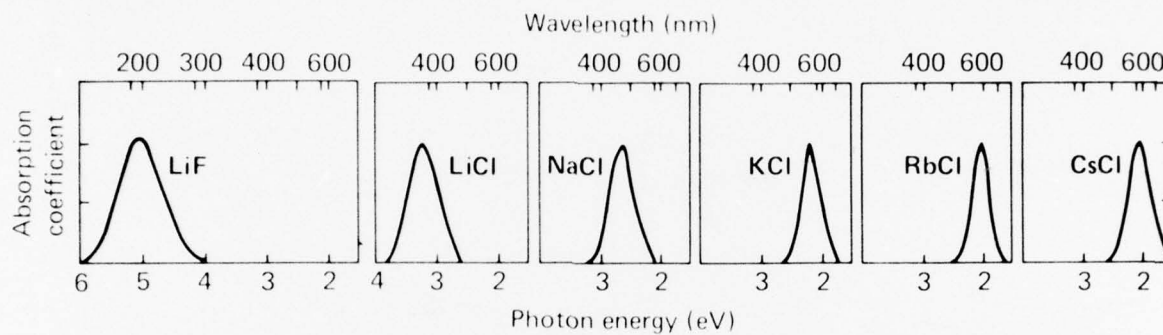


Fig. 2.5. Sketches of F-band absorptions in several alkali halides. A complete tabulation of F-band absorption data is given in Tables 2.2, 2.5, and 2.7. [C. Kittel, *Introduction to Solid State Physics*, Fourth Edition, John Wiley & Sons, New York, 1971; with LiF added by the present authors.]

Sec. II-B Alkali Halides

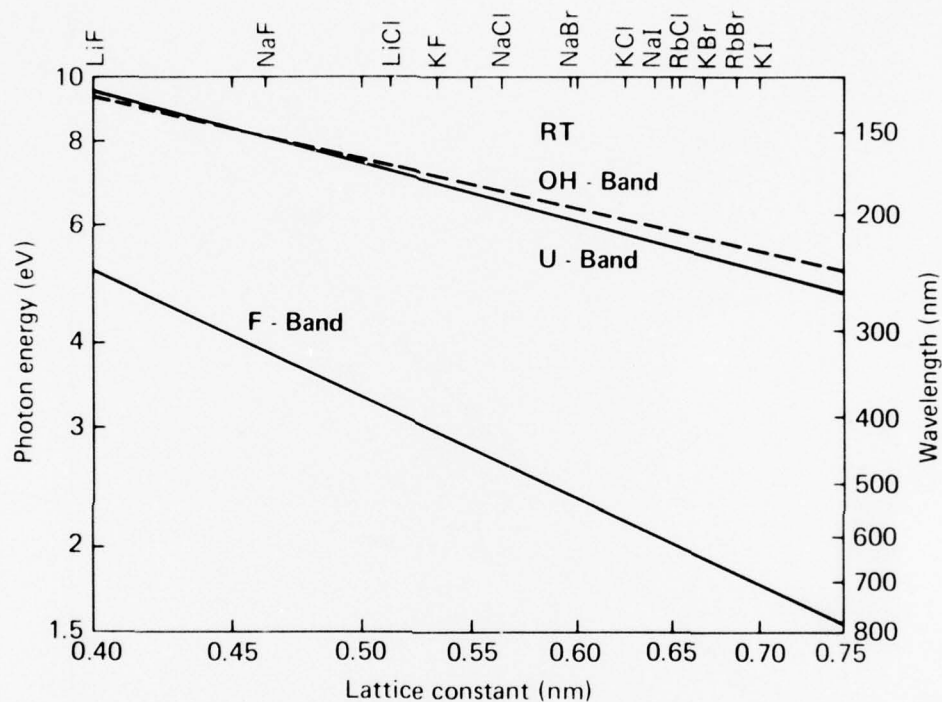


Fig. 2.6a. Ivey relations (power-law dependence) of the positions of the absorption maxima of OH^- , U, F, and V_3 bands as functions of the lattice constants, for alkali halides. [E. Freytag, Z. Physik 177, 206 (1964).]

Sec. II-B Alkali Halides

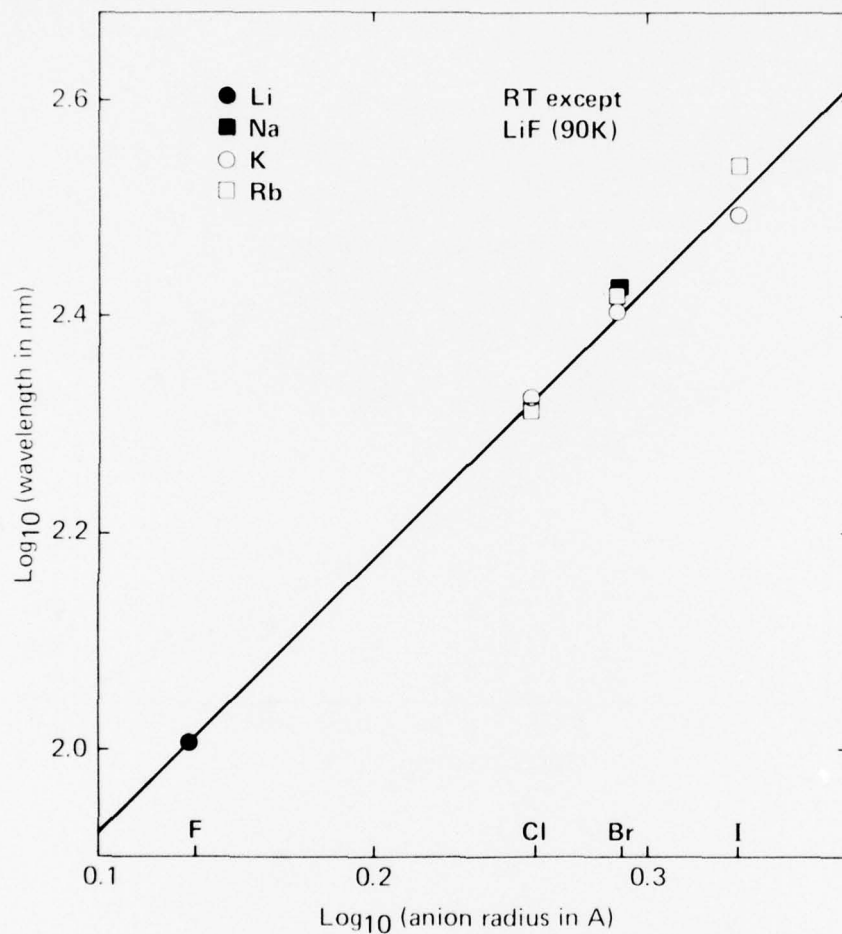


Fig. 2.6b. Ivey relations (power-law dependence) of the positions of the absorption maxima of OH^- , U, F, and V_3 bands as functions of the lattice constants, for alkali halides. [M. R. Mayhugh and R. W. Christy, Phys. Rev. B2, 3330 (1970).]

Sec. II-B Alkali Halides

Table 2.2. Optical properties of F centers in alkali halides. The subscripts A and E refer to absorption and emission, respectively; $\hbar\omega_A$ and $\hbar\omega_E$ are peak transition energies; $\Delta\hbar\omega_A$ and $\Delta\hbar\omega_E$ are zero-point half-widths, and ω_A and ω_E are the effective frequencies for line broadening, which are compared with the longitudinal optical mode frequency ω_{LO} . The oscillator strength is f and τ_E is the radiative lifetime of the excited state, whose thermal ionization energy is ΔE . [W. Beall Fowler, in Physics of Color Centers, W. Beall Fowler, ed., Academic Press, New York and London, 1968.]

Crystal	$\hbar\omega_A$ (eV)	$\hbar\omega_E$ (eV)	$\Delta\hbar\omega_A$ (eV)	$\Delta\hbar\omega_E$ (eV)	ω_A (10^{13} sec^{-1})	ω_E (10^{13} sec^{-1})	ω_{LO} (10^{13} sec^{-1})	f	τ_E (10^{-8} sec)	ΔE (eV)
LiF	5.102		0.596		5.86		12.6			0.16
LiCl	3.30		0.4				7.5			
NaF	3.723	1.665	0.366	0.39	5.10		8.1		0.1	0.055
NaCl	2.770	0.975	0.255	0.337	2.77	3.71	5.1	0.6	1.00	0.074
NaBr	2.3						3.98			
NaI	2.1						3.47			
KF	2.847	1.66	0.228	0.385	2.78	3.48	6.1		0.21	0.138
KCl	2.313	1.215	0.163	0.261	1.86	2.86	4.02	0.85	0.57	0.150
								0.6		
KBr	2.064	0.916	0.158	0.215	1.76	2.36	3.21	0.75	1.11	0.135
KI	1.875	0.827	0.155	0.185	1.60	2.05	2.70	0.83	2.22	0.11
RbF	2.428	1.328	0.199	0.335	2.47		5.4		0.42	0.08
RbCl	2.050	1.090	0.145	0.237	1.54	2.10	3.4	0.85	0.60	0.13
RbBr	1.857	0.87	0.133	0.190	1.35	1.89	2.45	0.70	0.84	0.11
RbI	1.708	0.81	0.121	0.148	1.04	1.44	2.04	0.81		0.082
CsF	1.89	1.42		0.10		1.11			0.05	
CsCl	2.17	1.255		0.245			3.1			
CsBr	1.96	0.910		0.184			1.98		1.54	0.04
CsI	1.68	0.740		0.140			1.79			0.052

Sec. II-B Alkali Halides

Table 2.3. Optical properties of M_1 bands in alkali halides.
(The symbols and references are the same as for Table 2.2.)

Crystal	$\hbar\omega_A$ (eV)	$\hbar\omega_E$ (eV)	$\Delta\hbar\omega_A$ (eV)	$\Delta\hbar\omega_E$ (eV)	f	τ_E (10^{-8} sec)
LiF	2.8	1.85				1.3
LiCl	1.9					
NaF	2.49	1.88	0.10	0.25		1.1
NaCl	1.74	1.16	0.10	0.17		
KCl	1.55	1.17	0.07	0.19	0.38	6.0
KBr	1.40		0.07		0.27	
KI	1.23					
RbBr	1.3					
CsCl	1.27		0.04			
CsBr	1.19	0.85	0.03	0.09		
CsI	1.05		0.05			

Sec. II-B Alkali Halides

Table 2.4. Optical properties of R centers in alkali halides.
[W. Beall Fowler, in Physics of Color Centers, W. Beall Fowler,
ed., Academic Press, New York and London, 1968.]

Crystal	Peak Position (eV)		T
	R_1	R_2	
LiF	4.05	3.29	RT
NaF	3.14	2.85	77K
NaCl	2.27	2.08	77K
KCl	1.88	1.70	77K
KBr	1.69	1.57	77K
KI	1.53	1.37	4K
RbBr	1.54	1.44	77K

Sec. II-B Alkali Halides

Table 2.5. Wavelength of absorption of electron trap centers (nm).
[AIP Handbook]

	L ₃	L ₂	L ₁	K	F	R ₁	R ₂	M	Width at half maxi- mum of F band (eV)
	-180 C	-180 C	-180 C	-180 C	20 C	20 C	20 C	20 C	20 C
LiF	-	-	-	-	250	313	380	444	0.82
LiCl	-	-	-	-	385	-	580	650	0.62
NaF	-	-	-	-	341	-	415	505	0.62
NaCl	-	-	-	-	458	545	596	725	0.47
NaBr	-	-	-	-	540	-	-	-	0.52
NaI	-	-	-	-	588	-	-	-	-
KF	-	-	-	-	455	-	570	-	0.41
KCl	251	288	344	457	556	658	727	825	0.35
KBr	276	316	374	525	625	735	790	892	0.345
KI	326	382	447	585	689	-	-	-	0.345
RbCl	279	335	402	523	609	-	-	-	0.31
RbBr	300	362	435	593	694	805	859	957	0.28
RbI	338	413	506	646	756	-	-	-	0.35
CsCl	-	-	-	-	605	-	-	-	-
CsBr	-	-	-	-	680	-	-	-	-

Sec. II-B Alkali Halides

Table 2.6. Wavelength of absorption of hole trap centers (nm).
[AIP Handbook]

	H	V_1	V_K or X_2^-	V_2	V_3
	4 K	77 K	77 K	300 K	300 K
LiF	-	-	348	-	-
NaCl	330	345	-	223	210
KCl	335	356	365	230	212
KBr	380	410	385	265	231
KI	-	-	404	-	-

Sec. II-B Alkali Halides

Table 2.7. Absorption properties of F and F_A centers.
[F. Lütty, in Physics of Color Centers, W. B. Fowler, ed.,
Academic Press, New York, 1968.]

System	$\hbar\omega_{\max}$ (eV)		$\Delta\hbar\omega$ (eV)		$\nu_g (10^{12} \text{ sec}^{-1})$
KCl					
F	2.31		0.16		2.96
$F_A(\text{Na})$	2.35	2.12	0.19	0.11	3.02
$F_A(\text{Li})$	2.25	1.98	0.19	0.12	3.00
KBr					
F	2.06		0.16		2.80
$F_A(\text{Na})$	2.07	1.90	—	—	—
$F_A(\text{Li})$	2.00	1.82	0.235	0.128	—
RbCl					
F	2.05		0.145		2.45
$F_A(\text{Na})$	2.09	1.85	0.17	0.10	2.24
$F_A(\text{Li})$	1.95	1.72	0.15	0.11	2.24
RbBr					
F	1.86		0.20		—
$F_A(\text{K})$	1.85	1.67	0.20	0.15	—
$F_A(\text{Li})$	1.78	1.57	0.14	0.11	—

Sec. II-B Alkali Halides

Table 2.8. Position of absorption maxima (nm) for U, OH⁻, Z₁, and Z₂ centers in alkali halides. [AIP Handbook]

	U band	OH ⁻ band	Z ₁ band	Z ₂ band
NaCl	192	185	505	512
NaBr	210	-	-	-
KCl	214	204	590	635
KBr	228	214	-	-
KI	244	-	-	-
RbCl	229	-	-	-
RbBr	242	-	-	-

Sec. II-B Alkali Halides

Table 2.9. Optical absorption peaks of Tl^+ (eV) in alkali halides. [W. Beall Fowler, in Physics of Color Centers, W. Beall Fowler, ed., Academic Press, New York and London, 1968.]

Crystal	Band				T
	A	B	C	D	
NaCl	4.87	5.77	6.19	>7.6	77K
KCl	5.03	5.94	6.36	~7.3	77K
RbCl	5.06	-	6.36	-	RT
CsCl	5.0	-	6.32	-	RT
NaBr	4.64	-	5.74	-	RT
KBr	4.79	5.58	5.93	6.50	77K
RbBr	4.80	-	5.85	-	RT
CsBr	4.71	-	5.79	-	RT
NaI	4.25	5.0	5.3	~5.4	4K
KI	4.38	5.06	5.30	5.50	77K
RbI	4.33	-	5.17	-	RT
CsI	4.15	-	5.14	-	RT

Sec. II-B Alkali Halides

Table 2.10. Optical absorption peaks of α and β bands (nm)
in alkali halides. [AIP Handbook]

	α	β
NaF	131	127
NaCl	173	168
NaBr	199	-
KCl	178	170
KBr	201	192
KI	238	226
RbBr	205	196
RbI	240	229

C. Lithium Fluoride

The positions, widths, oscillator strengths, temperatures, and references for all of the spectral bands of LiF given below are summarized in Table 2.11. Lithium fluoride is known to be susceptible to coloration by ultraviolet, X-ray, and γ -ray irradiation, by electron, neutron, or ion bombardment, by heating in Li vapor, by electrolysis, and by impurity ions. The spectra are complex, depending on thermal treatment, trace impurities, irradiation dose and temperature, and time. In spite of the great number of bands appearing in Fig. 1.1, the known susceptibility of LiF to coloration, and the unique use of LiF in the frequency region between the absorption edges of LiF and MgF_2 , there have been fewer studies of impurity spectra in LiF than in several other of the alkali halides.

1. The lowest energy exciton peak of LiF at room temperature is^{2.2} at 12.9 eV (9.62 nm), as shown in Fig. 2.2.

2. Purity and storage of LiF. The reduction in the transmittance of LiF resulting from low-purity raw materials and from contaminating crystal-growth conditions, as determined by Smushkov and coworkers,^{2.9} are shown in Figs. 2.7 and 2.8. The effects of the storage conditions and cleaning on the transmittance of LiF crystals at room temperature have been studied by Davis^{2.10} and are shown in Fig. 2.9. The lower transmittance of the polished sample (W) than that of the cleaved sample (S) presumably is a result of greater surface scattering in the polished sample. Figure 2.10 shows the reduction in the 121.6 nm (10.2 eV) transmittance of LiF with exposure time in air after being cleaned in dry argon, as reported by D. A. Patterson

EXPLANATORY NOTES FOR TABLE 2.11

Column 1: Lists properties of pure, doped, and irradiated materials. For doped or irradiated materials the properties appear in the following order:

1. impurity or dopant (O_2^- or LiO_2)
2. radiation (electrons, neutrons, etc.)
3. color centers or color bands (V_K , F, or α , β , etc.)
4. additional information (sample color, photochromic, etc.)

Column 2: Sample temperature.

Column 3: Peak positions ($|$), widths (H), and oscillator strengths (numbers) of impurity spectra. Ellipses indicate absorption structure above the absorption edge. Some lines are labeled by their color center or impurity.

Column 4: References: T2.1 stands for Table 2.1, F2.23 stands for Fig. 2.23, and II-C ¶ 6f indicates a paragraph in the text.

Table 2.11. Summary of the peak positions ($|$), widths (\pm), and oscillator strengths (numbers) of the impurity spectra for LiF. (See preceding page for key.)

LiF	Temp.	Photon Energy (eV)							Ref.
		2	4	6	8	10	12	14	
Absorption shoulder	80K								T2.1
Lowest exciton peak	RT								T2.1
Band gap	RT								T2.1
Absorption edge	RT								T2.1
Mg F, F ₃ ⁻ , V ₃	RT								F2.23
OH ⁻	RT								F2.11
LiO ₂	RT								F2.13
D ⁻	77K								T2.12

Table 2.11 (Continued)

LiF	Temp.	Photon Energy (eV)	Ref.
H ⁻	77K	10	T2.12
H ⁻	RT	10	T2.12
Ni	10K	0.69	T2.13
Ni ²⁺	RT	0.48 9×10^{-6} 4.7×10^{-5} 2.5×10^{-5}	F2.19 T2.13 T2.15
Co	10K	2×10^{-3} 2.2×10^{-2}	T2.13
Co ²⁺	4.2K	10	II-C6f
Co ²⁺	RT	1.7×10^{-3} 1.9×10^{-2}	T2.13
Mg ²⁺	—	10^{-2} 10^{-2}	F2.25 F2.26 II-C4

Table 2.11 (Continued)

LiF	Temp.	Photon Energy (eV)						Ref.
Ti	10K			0.475		0.99		T2.13
Ti	RT			0.47		0.99		T2.13
Mn	10K					1.95 $\times 10^{-3}$	3.55 $\times 10^{-3}$	T2.13
Mn ²⁺	RT					1.3 $\times 10^{-3}$		F2.17 F2.18 T2.13
V	10K					4.7 $\times 10^{-4}$	5.7 $\times 10^{-3}$	T2.13
V	RT					6.4 $\times 10^{-4}$	4.1 $\times 10^{-3}$	T2.13
Fe ²⁺	RT						5.2 $\times 10^{-3}$	T2.13
Fe	10K						5.2 $\times 10^{-3}$	T2.13

Table 2.11 (Continued)

LiF	Temp.	Photon Energy (ev)							Ref.
Ti^{3+}	RT	<p>7x10⁻² 0.23 G H E</p>							T2.14 F2.14
F	RT								F2.5
$C_A(Na^+)$	RT								F2.28
Neutrons W_1	RT								F2.31
R	RT								T2.4
R_1	78K								F2.20
V_K or X_2^-	78K								T2.6 F2.22
Neutrons W_2, F, C_A	RT								F2.31

Table 2.11 (Continued)

LiF	Temp.	Photon Energy (eV)				Ref.
R ₂	78K					F2.20
Li ⁺	77K					F2.27
Li ⁺	RT					F2.27
C _A (K ⁺)	RT	+				F2.29
M	78K	+				F2.20
C _A (Na ⁺)	RT	+				F2.28
N	78K					F2.20
R'	78K					F2.20
M'	78K					F2.20

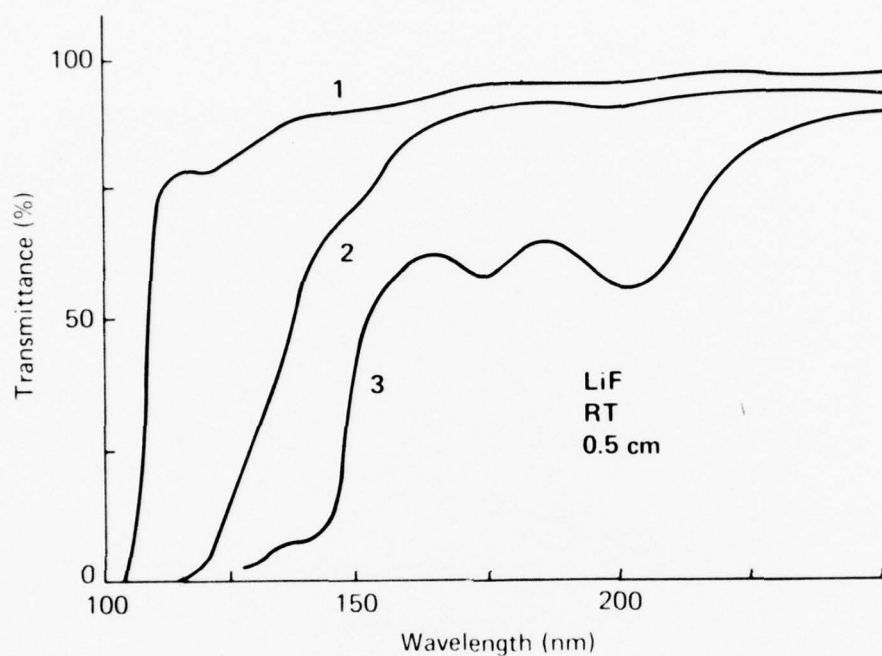


Fig. 2.7. Effects of starting-material purity and growth conditions on the ultraviolet transmittance of LiF for: (1) crystal grown in vacuum from zone-refined melt; (2) crystal grown from crystal chips which were cooled in air; and (3) crystal grown in air. [I. V. Smushkov, L. M. Soifer, and M. I. Shakhnovich, *Fiz. Vak. Últraviolet Izluch*, p. 59 (1974) (in Russian).]

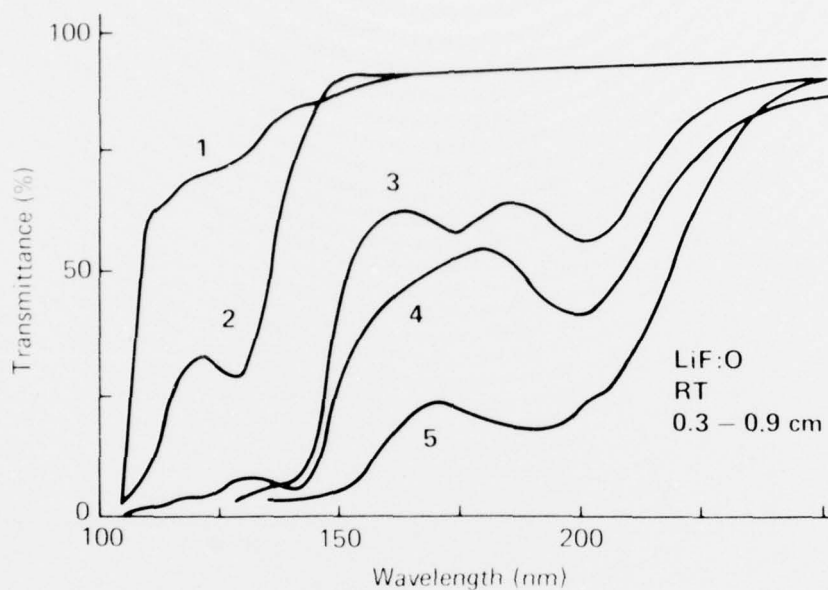


Fig. 2.8. Effects of oxygen in LiF on the ultraviolet transmittance for: (1) crystal 0.9 cm thick grown from purified salts under vacuum; (2) crystal 0.9 cm thick grown in vacuum with 3.5×10^{-3} weight percent of Li_2O added; (3) crystal 0.5 cm thick grown in air; (4) crystal 0.3 cm thick grown in dry oxygen; and (5) crystal 0.3 cm thick grown in vacuum with 3.5×10^{-2} weight percent Li_2O added. Also see Fig. 2.13. [I. V. Smushkov, L. M. Soifer, and M. I. Shakhnovich, *Fiz. Vak. Úl'tra-violet Izluch.* p. 59 (1974) (in Russian).]

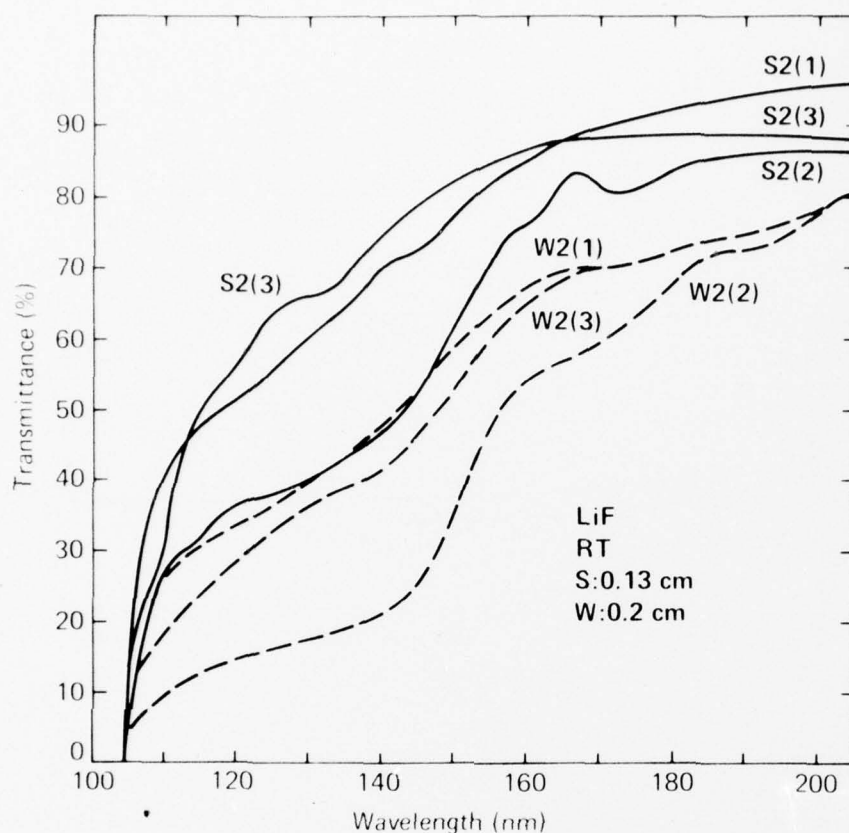


Fig. 2.9. Effects of storage and cleaning on the ultraviolet transmittance of LiF: S2(1) – freshly cleaved sample from ingot 2, measured 24 July 1963; S2(2) – same sample remeasured 31 March 1965 after 20 months storage in chemical dessiccator; S2(3) – same sample remeasured 30 April 1965 after 2-minute ultrasonic cleaning in absolute ethyl alcohol; W2(1) – polished sample from ingot 2, 0.2 cm thick, measured 28 January 1964; W2(2) – same sample remeasured 31 December 1964 after 11 months storage in uncontrolled environment (humidity never exceeding 95 percent); W2(3) – same sample remeasured 23 April 1965 after two-minute ultrasonic cleaning in absolute ethyl alcohol. [R. J. Davis, J. Opt. Soc. Am. 56, 837 (1966).]

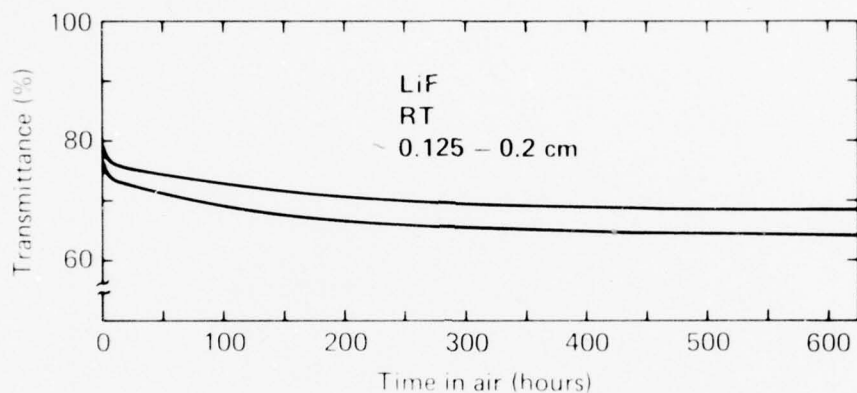


Fig. 2.10. Typical degradation of the transmittance of LiF at 121.6 nm resulting from storage in air of two different samples. Crystals were cleaved in dry argon gas. Also see Fig. 2.11. [D. A. Patterson and W. H. Vaughan, J. Opt. Soc. Am. 53, 851 (1963).]

Sec. II-C LiF

and W. H. Vaughn.^{2.11} Figure 2.11 further shows the effect of exposure to air. The reduced transmittance was attributed to a surface layer produced on the crystal by reaction with moisture, but it was not determined if this reduced transmittance resulted from scattering, absorption, or interference.

3. U center in LiF. The peak positions and widths of the absorption bands resulting from the 1S to 1P transitions in Li:H^- at 77 K and 300 K and in LiF:D^- at 77 K measured by Beaumont and coworkers^{2.12} (with no spectra presented) are given in Table 2.12. The U-band peak position for LiF falls on the extrapolation of the Ivey curve (Fig. 2.6) for the other alkali halides to within the accuracy of the experimental values.^{2.13}

The theoretical values shown in Table 2.12 were obtained by a semi-empirical molecular-orbital method developed specifically for application to defects in ionic crystals. The method is an extension of a technique known as complete neglect of differential overlap (CNDO), which was originally developed for large molecules.^{2.14} A group of 27 ions on the LiF lattice with the H^- ion situated in the center is treated as a giant molecule. In addition to the explicit consideration of the interaction within the cluster, the Madelung potential due to all other ions in the crystal is included. This leads to a difficulty in choosing the effective ionic charge q to be placed on the point-ion lattice (external to the 27-ion molecule) since the molecular-orbital calculation does not give a simple valence charge shift of ± 1 . Table 2.12 contains their results for a series of values of q . The case of $q = 0$ corresponds to completely ignoring the point-ion lattice, while the case of $q = 1$ corresponds to the idealized ionic lattice. The theoretical result for $q = 1$ agrees well with the experimental value of the cohesive energy.

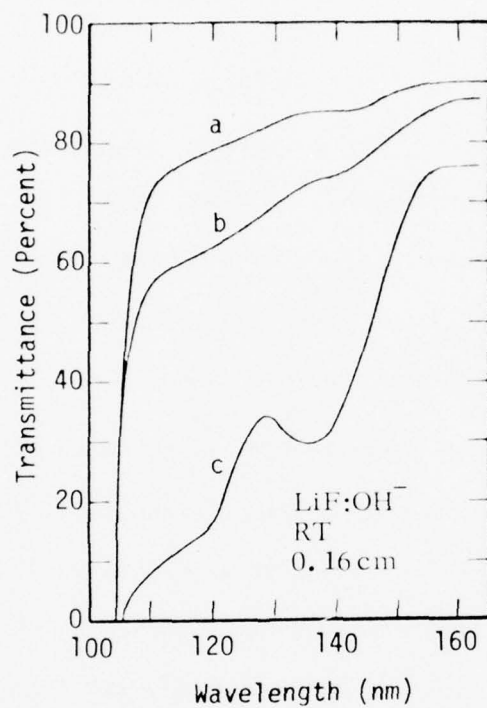


Fig. 2.11. Ultraviolet absorption by OH⁻ in LiF: (a) freshly cleaved crystal; (b) same crystal after 97 days in air; (c) another crystal, showing the OH⁻ absorption band at 136 nm (9.12 eV). [D. A. Patterson and W. H. Vaughan, J. Opt. Soc. Am. 53, 851 (1963).]

Sec. II-C LiF

Table 2.12. Peak positions and widths (full width at half maximum) of U-band absorption lines in LiF. [J. H. Beaumont, J. Bordas, A. J. Bourdilon, and M. R. Hayns, J. Phys. C: Solid State Phys. 7, L 349 (1974).]

	Experimental		Theoretical			
	FWHM (eV)	Peak Energy (eV)	Point Ion (eV)	CND0 (eV)		
				q = 0	q = 0.23	q = 1
LiF:H ⁻ (77K)	0.67	9.86	8.11	9.15	9.35	9.50
LiF:H ⁻ (RT)	0.74	9.73				
LiF:D ⁻ (77K)	0.71	9.90				

Sec. II-C LiF

4. The OH^- absorption peak in LiF is believed to occur at 136 nm (9.12 eV), as shown in Fig. 2.11. However, Kamikawa^{2.15} recently assigned the 138 nm (8.99 eV) peak in Fig. 2.12 to Mg^{2+} ions and the strong line centered at 119 nm (10.4 eV) to OH^- , since this latter absorption band is observed only in crystals showing the 2.8 μm infrared absorption by OH^- . A closer examination of Figs. 2.11 and 2.12 reveals that both the 136 nm (9.12 eV) and 119 nm bands are present in both spectra, but with opposite relative intensities. The question of the interpretation of the two lines remains unanswered. The 136 nm peak falls close to the extrapolation of the Ivey curve in Fig. 2.6, while the 119 nm peak is greater than 1 eV above the extrapolation, which suggests that the original assignment of the 136 nm band to OH^- is correct. By contrast, the great increase in the strength of the 136 nm absorption resulting from doping with magnesium suggests that this peak results from Mg^{2+} . Activation of OH^- by Mg^{2+} seems unlikely since OH^- is a strong absorber.

5. In oxygen-doped LiF, O^{2-} appears in the crystal substitutionally in an F^- site, the double charge requiring compensation. Oxygen-doped LiF shows absorption peaks at 120 nm (10.3 eV) and at 128 nm (9.72 eV), as seen in Fig. 2.13 (for $\text{LiF}:\text{Li}_2\text{O}$).^{2.16} The 120 nm band, which was assigned to centers containing anion vacancies, is stable at temperatures up to the melting point of LiF. The 128 nm band, which is not stable during thermal treatment or X-irradiation, is related to the isolated O^{2-} centers.

6. Transition-metal ions in LiF, which enter the lattice substitutionally in Li^+ sites and require compensation, give rise to several types of absorption. Such transitions as 3d to 4s or 4p that can occur in free ions are altered in position, width, and strength when the ions are

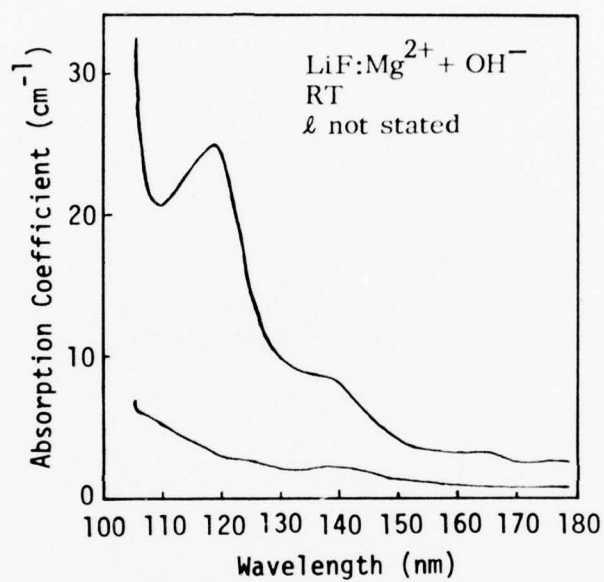


Fig. 2.12. Absorption by Mg²⁺ and OH⁻ in LiF: (a) undoped crystal; and (b) doped with Mg²⁺. The absorption peak at 119 nm (10.4 eV) was assigned to OH⁻ and the shoulder at 138 nm (8.99 eV) was assigned to Mg²⁺. [T. Kamikawa, Bull. of Yamagata Univ., Nat. Sci. 8 (4) 519 (1975).]

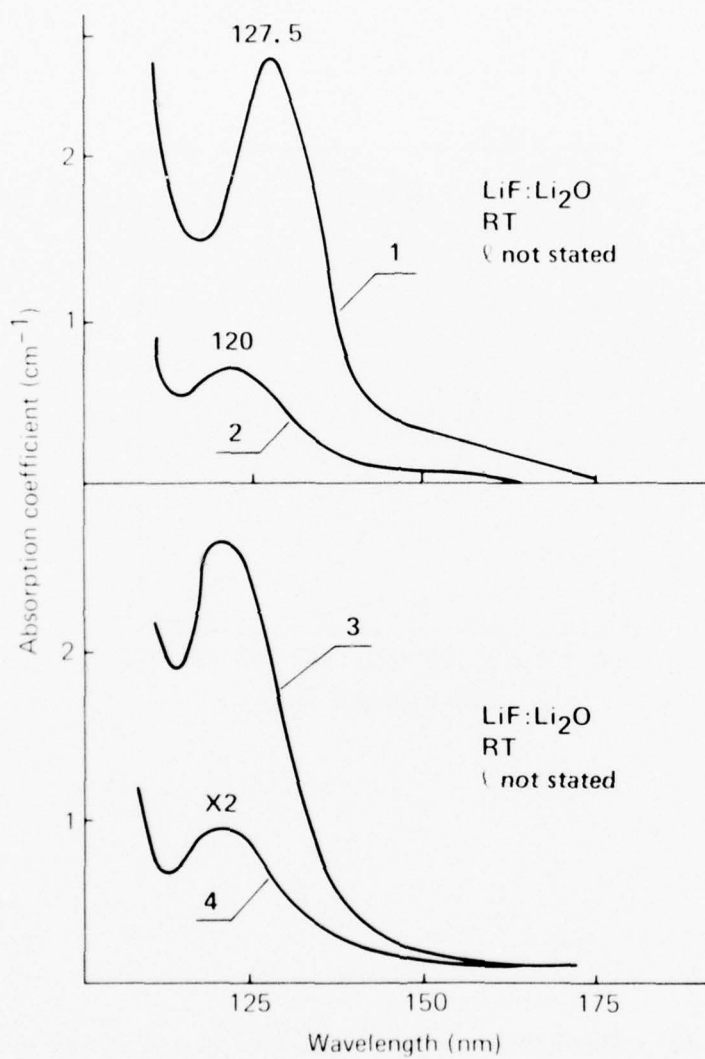


Fig. 2.13. Absorption by oxygen-doped LiF. [I. V. Smushkov and M. I. Shakhnovich, Monokrist. Tekh. no. 5, 62 (1971) (in Russian).]

incorporated into a crystal. Also, the overlap with and fields from the neighbors, or the so-called crystal-field effect, lift the degeneracy of the five d orbitals, and transitions between these orbitals are possible. In addition to these intra-ion transitions, the transition-metal ion acts as an acceptor. That is, there is a charge-transfer transition from fluorine 2p (valence-band) states to a level of the impurity ion, such as a 3d or 4s level. Apparently, selection rules prohibit donor-type transitions (from the d levels of the impurity to the bottom of the conduction band), which is reasonable since the bottom of the conduction band is s-like. Also, for fully allowed transitions across the gap and from the valence band to the impurity levels, the transitions from the impurity levels to the bottom of the conduction band are expected to be weak. Transitions to higher positions in the conduction bands would tend to be obscured by such other transitions as those across the gap.

For the fluorine 2p to impurity 3d transitions, the distance between neighboring fluorine and transition-metal ions is approximately 0.2 nm, and the overlap of the wavefunctions is approximately 10 percent; thus, the oscillator strengths are expected to be of order 10^{-2} to 10^{-3} . For the 2p to 4s transitions, the overlap is greater since the 4s orbital is larger than the 3d orbital. The oscillator strength ($\sim 10^{-2}$ to 1) is therefore greater.

In fluorides, the 4s levels of transition-metal ions are approximately 6 eV higher than the 3d levels. Consequently, the fluorine 2p to impurity 4s transitions occur at higher frequencies than those of the 2p to 3d transitions. The 3d to 3d transitions tend to occur at low frequencies because the 3d levels are degenerate in the free ions; thus the entire spacing in

Sec. II-C LiF

the crystal is a result of the crystal-field splitting. The oscillator strength of these 3d to 3d transitions can be rather large.

a. Ti^{3+} and Ti^{2+} in LiF. Absorption spectra^{2.17, 2.18} of titanium-doped lithium fluoride are shown in Figs. 2.14 - 2.16. Table 2.13 contains peak positions, half-widths, oscillator strengths, extinction coefficients, and assignments for the absorption lines in Fig. 2.15. Recall that the extinction coefficient is the sum of the absorption coefficient and the scattering coefficient, given in units of cm^{-1} per mole in the table. Figure 2.15 and the corresponding Table 2.13 also contain results for other impurities and include results for NaF to facilitate comparison. Notice that in LiF, only Ti and Ni (and not V, Mn, Fe, Co, and Cr) have strong ultraviolet absorption bands with oscillator strengths greater than ~ 0.5 , and only Ti and Ni show no blue shift (shift of peak position to higher frequency as the temperature decreases) of the strong bands (at 207 nm (5.99 eV) and 139 nm (8.39 eV) for Ti). An increase in the optical density resulting from increased scattering is seen in all six panels of Fig. 2.15. Figure 2.16 and Table 2.14 show the effect of X-irradiation on pure and on titanium-doped LiF.

In discussing these results for titanium-doped LiF, first consider the broad, low-frequency absorption band centered at 640 nm (1.94 eV) in Fig. 2.14. Chase and McClure^{2.18} reported (with no spectrum given) a similar broad absorption band at 667 nm (1.86 eV) with an oscillator strength of 1.84×10^{-3} . The Ti^{3+} ($3d^1$) ion has one 3d electron. The five-fold-degenerate d states are split by the octahedral field into two crystal-field components: $T_{2g}(d_{xy}, d_{yz}, d_{zx})$ and $E_g(d_{x^2-y^2}, d_{z^2})$. Chase and

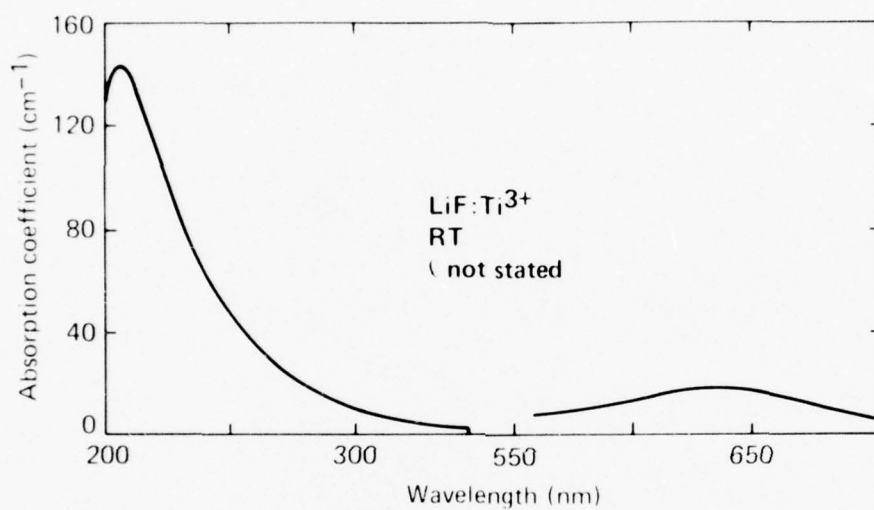


Fig. 2.14. Optical absorption spectrum of LiF:Ti³⁺.
[S. C. Jain and G. D. Sootha, Phys. Stat. Sol. 22,
505 (1967).]

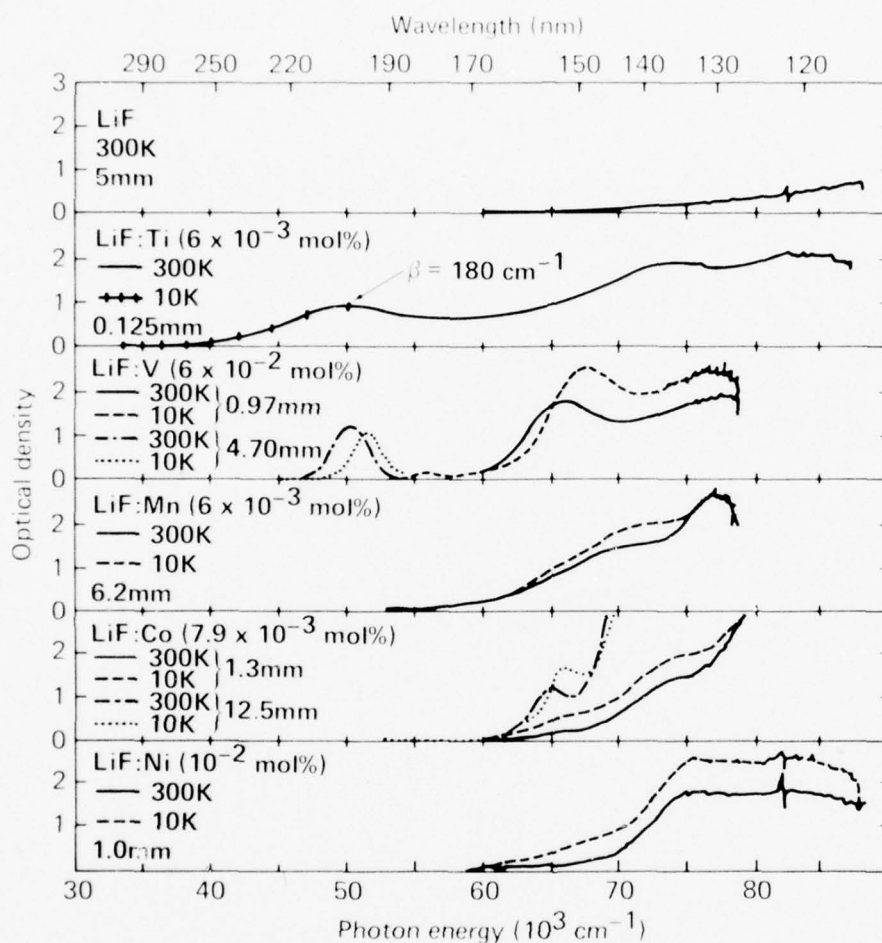


Fig. 2.15. Absorption spectra of divalent transition-metal ions in LiF. [D. B. Chase and D. S. McClure, J. Chem. Phys. 64, 74 (1976).]

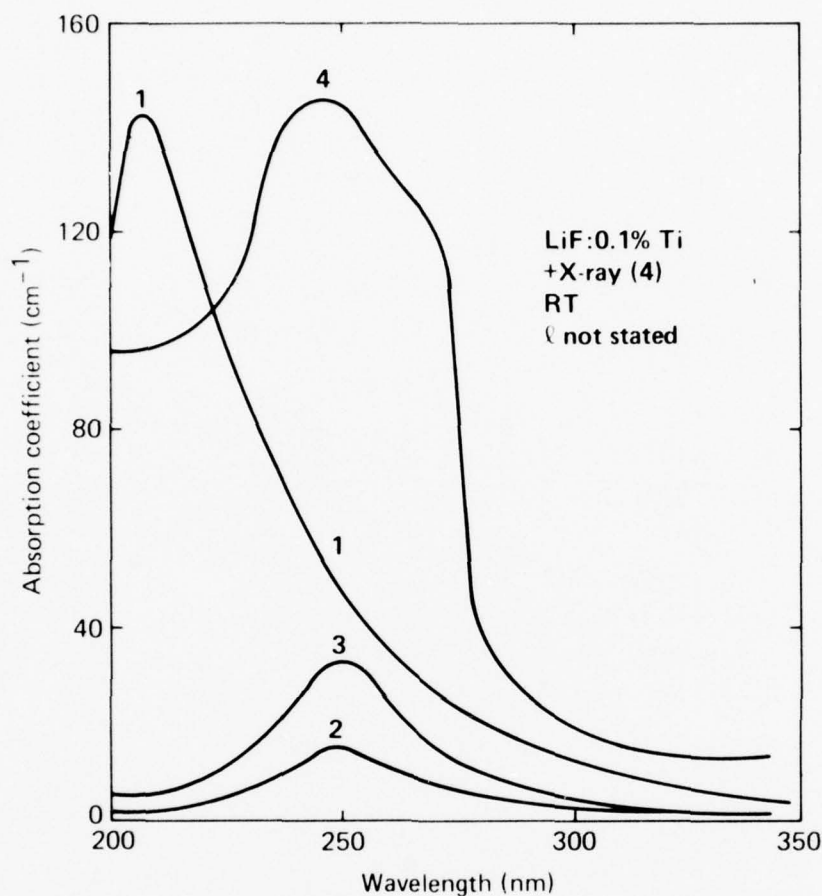


Fig. 2.16. Absorption spectra of pure and Ti-doped LiF crystals: (1) prior to irradiation, showing the broad E-band peaked at 207 nm (5.99 eV); (2) and (3) undoped LiF, and (3) LiF: 0.1% Ti, all three samples X-irradiated for seven hours (Mo target, 35 kV, 100 mA, room temperature). [S. C. Jain and G. D. Sootha, Phys. Stat. Sol. 22, 505 (1967).]

Sec. II-C LiF

Table 2.13. Summary of spectral data for LiF and NaF doped with transition-metal ions. The data for LiF were taken from Fig. 2.15. [D. B. Chase and D. S. McClure, Jour. Chem. Phys. 64, 74 (1976).]

Sample	Energy (eV)	Width (eV)	Extinction Coefficient $\text{cm}^{-1}/\text{mole}$	Oscillator Strength f
LiF:Ti	6.20 (300)	1.24	1.09×10^4	4.7×10^{-1}
	6.20 (10)			4.75×10^{-1}
	8.93 (300)	1.24	2.30×10^4	0.99×10^0
	8.93 (10)			0.99×10^0
LiF:V	6.24 (300)	.347	42.0	6.4×10^{-4}
	6.36 (10)			4.7×10^{-4}
	8.17 (300)	.384	303.0	4.1×10^{-3}
	8.37 (10)			5.7×10^{-3}
LiF:Mn	8.10 (300)	.434	87.0	1.3×10^{-3}
	8.21 (10)			1.95×10^{-3}
	8.59 (300)	.484	160.0	2.7×10^{-3}
	8.73 (10)			3.55×10^{-3}
LiF:Fe	5.33 (300)	...	600	...
	5.33 (10)			
	7.44 (300)	.37	410	5.2×10^{-3}
	7.44 (10)			
LiF:Co	8.00 (300)	.40	120	1.7×10^{-3}
	8.11 (10)			2.05×10^{-3}
	9.18 (300)	.68	800	1.9×10^{-2}
	9.3 (10)			2.2×10^{-2}
LiF:Ni	9.3 (300)	.74	1.85×10^4	4.8×10^{-1}
	9.3 (10)			6.9×10^{-1}
NaF:Ti	5.9 (300)	1.24	805	3.5×10^{-2}
	5.9 (10)			
NaF:V	5.02 (300)	.57	86.0	1.7×10^{-3}
	5.15 (10)			
NaF:Mn	6.82 (300)
	6.94 (10)			
NaF:Co	7.01 (300)	.47	81.0	1.3×10^{-3}
	7.13 (10)			1.3×10^{-3}
NaF:Ni	7.94 (300)	...	~ 100	1.8×10^{-3}
	8.06 (10)			

Table 2.14. Peak positions, half-widths, and oscillator strengths of various color centers in LiF:Ti. [S. C. Jain and G. D. Sootha, Phys. Stat. Sol. 22, 505 (1967).]

Center	Peak Position		Half-width (eV)	Condition under which formed	Oscillator Strength
	(nm)	(eV)			
F	250	4.96	0.72	X-irradiated	0.32
E	207	5.99	0.72	Unirradiated	0.23
G	270	4.6	0.25	X-irradiated	0.07
H	240	5.16	0.20	X-irradiated	--

Sec. II-C LiF

McClure,^{2.18} Jain and Sootha,^{2.17} and Sootha^{2.19} all assigned the 640 nm band to the T_{2g} to E_g transition. The frequency is low because the energy spacing between the T_{2g} and E_g levels results entirely from the crystal field (the spacing being zero for an isolated Ti^{3+} ion).

The crystals of Jain and Sootha were light blue and contained 6×10^{-3} mole percent titanium. Upon cooling to 4.2 K, there was a slight increase in intensity but no energy shift.^{2.18} No electron-paramagnetic-resonance absorption due to Ti^{3+} or Ti^{2+} was found. The relatively high oscillator strength is due to the relaxation of the parity selection rule by the distorted environment. Since two charge compensators are required for trivalent ions in lithium fluoride, the local environment probably lacks a center of symmetry.

The strong absorption band at 207 nm (5.99 eV) in Fig. 2.14 is seen again in the second panel of Fig. 2.15, which also shows a strong absorption band centered at 139 nm (8.93 eV), and in curve 1 of Fig. 2.16. Three possible interpretations of this so-called E band at 207 nm have been proposed. The band could be an intra-ion transition related to the $4s, {}^2S_{1/2}$ to $4p, {}^2P_{3/2}$ transition which occurs at 5.95 eV (208 nm) in gaseous Ti^{3+} or to $3d, {}^2D_{5/2}$ to $4p, {}^3P_{3/2}$, which occurs at 9.30 eV (133 nm) in gaseous Ti^{2+} . The latter interpretation requires a large shift, from 9.30 eV to 5.99 eV, from gaseous state to incorporation into the crystal. The third possible assignment is the charge-transfer transition from the fluorine 2p (valence-band) to an unspecified level of the Ti ion. Chase and McClure^{2.18} suggested the charge-transfer process as the most likely, based on their observation that there was no pronounced blue shift when the temperature was lowered, as there was for V, Cr, Mn, Fe, and Co. The long-wavelength

Sec. II-C LiF

tail of the 207 nm absorption in Fig. 2.14 was attributed to the aggregates of Ti impurities and other defects of differing sizes.^{2.17}

An absorption band near 200 nm (6.2 eV) has been observed in dosimetry LiF doped with Mg and Ti at concentration levels of 80 - 160 and 5 - 15 ppm, respectively. In dosimetry LiF prepared using an Optran starting material, Rossiter and coworkers^{2.19a} observed a linear increase in the 200 nm band's absorption coefficient with Ti concentration, as shown in Fig. 2.16A. Subsequent work by Vora and coworkers^{2.19b} indicated that the 200 nm band is caused by titanium-hydroxyl complexes and that the data shown in Fig. 2.16A is characteristic of an LiF starting material containing sufficient background hydroxyl impurity to form complexes with all the available Ti ions. This is an example of the unexpected impurity effects that can occur in samples prepared under improperly controlled conditions; similar effects could be involved in other results discussed in various sections of this report.

Next consider the effect of X irradiation of Ti-doped LiF, as illustrated in Fig. 2.16 and tabulated in Table 2.14. After seven hours of room-temperature irradiation from a molybdenum target at 35 kV and 100 mA, curve 1 was converted to curve 4, which contains three bands: H at 240 nm (5.17 eV); F at 250 nm (4.96 eV); and G at 270 nm (4.59 eV). Jain and Sootha^{2.17} assign the G band to the capture of an electron by the E center (originally at 207 nm) since E centers are present in unirradiated crystals and the G centers can be thermally or optically bleached, which regenerates the E band. The extra electrons that are freed from the G center on bleaching are captured by anion vacancies to form F centers. Curves 2 and 3 of Fig. 2.16 show the results of the same X-ray dosage on LiF crystals containing

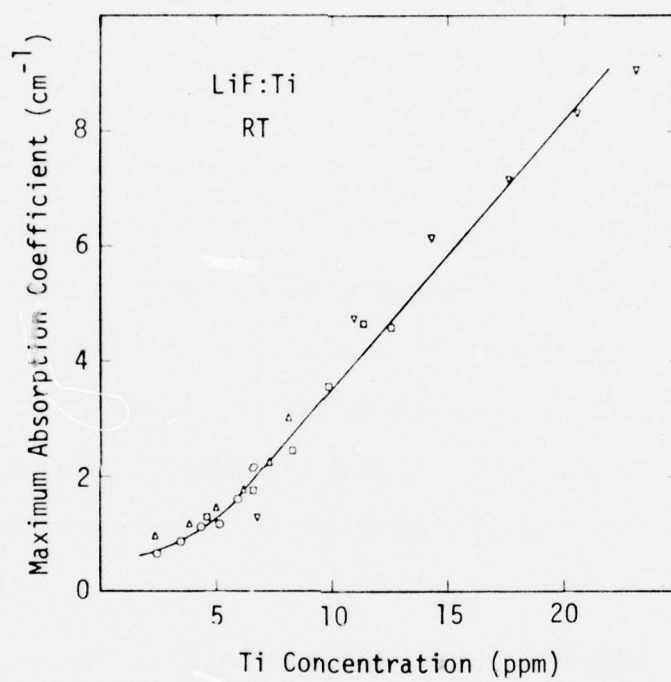


Fig. 2.16A. Titanium-concentration dependence of the 200 nm absorption band in LiF. [M. J. Rossiter, C. B. Rees-Evans, S. C. Ellis, and J. M. Griffiths, *J. Phys. D: Appl. Phys.* 4, 1245 (1971).]

Sec. II-C LiF

1 and 10 ppm, respectively, of background divalent cation impurities. The F-center absorption band is apparent in both cases.

Jain and Sootha^{2.17} attempted to distinguish between Ti^{2+} and Ti^{3+} plus a positive-ion vacancy by electron-spin-resonance experiments. Their negative results were attributed to a strong, complicated, temperature-independent background resulting from highly aggregated titanium.

b. V^{2+} in LiF. The spectrum^{2.18} of V^{2+} ($3d^3$)-doped LiF in the ultraviolet region is shown in Fig. 2.15. In the infrared and visible regions there were bands at 1.53 eV (810 nm), 2.29 eV (541 nm), and 3.53 eV (351 nm), all with half-widths of 0.12 eV and oscillator strengths less than 10^{-5} (no spectrum given).^{2.18} The crystals were light pink in color.

The bands centered at 199 nm (6.24 eV) (oscillator strength of 6×10^{-4}) and at 152 nm (8.18 eV) (oscillator strength of 4×10^{-3}) in Fig. 2.15 were not dependent on the crystal growth method, and both bands shift to higher photon energies with decreasing temperature. By contrast, the band centered at 179 nm (6.94 eV) was much more intense in some crystals (grown with only VF_3 as the impurity), and showed no shift with decreasing temperature. It was suggested that this 179 nm band possibly could be due to V^{3+} .

c. Cr in LiF. Chase and McClure^{2.18} report that they were unable to successfully dope LiF with chromium.

d. Mn^{2+} in LiF. The absorption spectrum^{2.18-2.19c} of $\text{LiF:Mn}^{2+}(3d^5)$ is shown in Figs. 2.15, 2.17, and 2.18. The absorption peaks of Fig. 2.17 were assigned to transitions between 3d levels. Corresponding to the d^5 configuration, the ground state of Mn^{2+} is ${}^6\text{A}_{1g}({}^6\text{S})$. The absorption bands

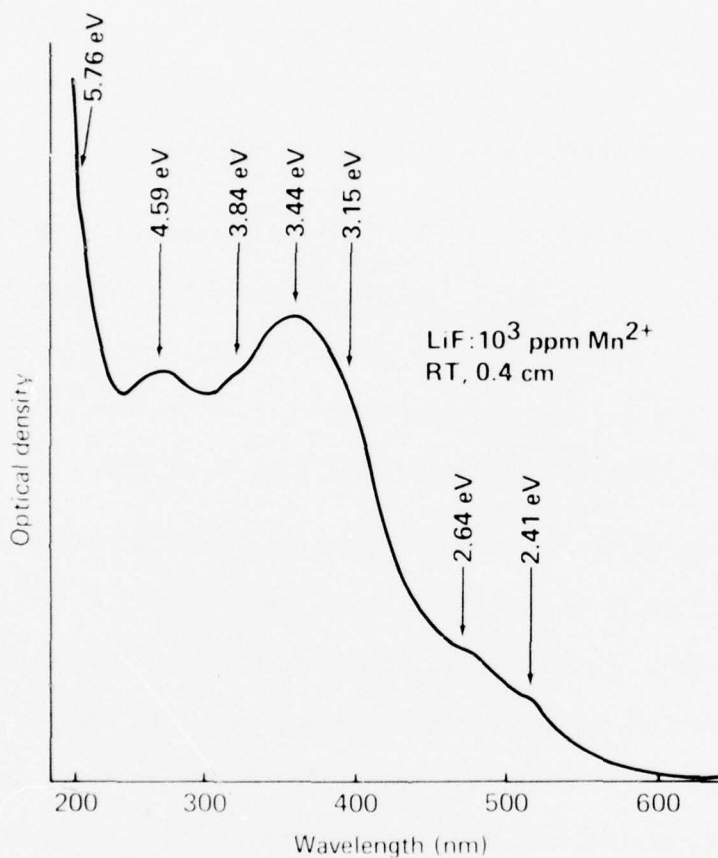


Fig. 2.17. Optical absorption of LiF:10³ ppm Mn²⁺.
[R. K. Bagai, R. K. Jain, and A. V. R. Warriar,
J. Phys. C 7, 1219 (1973).]

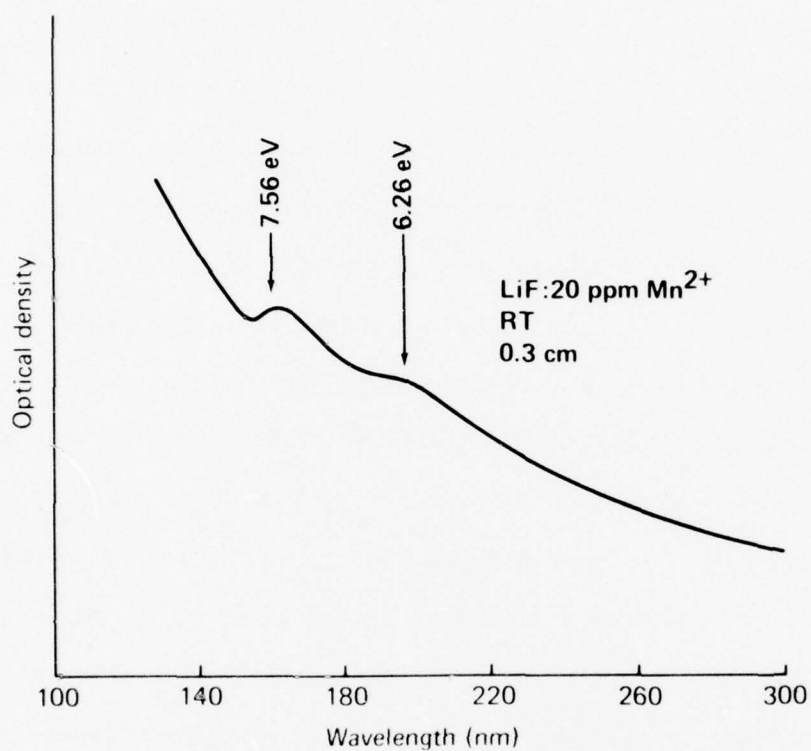


Fig. 2.18. Optical absorption of LiF:20 ppm Mn²⁺, in the wavelength region shorter than that of the previous figure. [R. K. Bagai, R. K. Jain, and A. V. R. Warriar, J. Phys. C 7, 1219 (1973).]

Sec. II-C LiF

due to the crystal field correspond to the transition from the ground state to the split levels arising from the terms 4G , 4D , 4P , and 4F . Since these transitions are forbidden by parity as well as spin selection rules, they are expected to be extremely weak. Crystals containing high concentrations (~ 1000 ppm) of Mn^{2+} were required in order to observe the absorption due to these transitions. The two bands observed in the visible region at 515 nm (2.41 eV) and 470 nm (2.64 eV) are assigned to the transition from ground state to the level $^4T_{1g}(G)$ and $^4T_{2g}(G)$, respectively. The broad band appearing in the ultraviolet region centered around 360 nm (3.44 eV) actually contains three bands with peak positions at 3.15, 3.44, and 3.84 eV. These bands are assigned to the transitions to $^4A_{1g}(G)$ or $^4E_g(G)$, $^4T_{2g}(D)$, and $^4E_g(D)$, respectively. The weak band at 270 nm (4.59 eV) is ascribed to $^6A_{1g} \rightarrow ^4T_{1g}(P)$, and the weak shoulder at 215 nm (5.76 eV) on the rising portion of a strong band is assigned to the transition to $^4T_{2g}(F)$. No bands were observed between these two, where one would expect the bands corresponding to $^6A_{1g} \rightarrow ^4A_{2g}(F)$ and $^6A_{1g} \rightarrow ^4T_{1g}(F)$. Perhaps these bands are masked by the other bands occurring in the same region.

e. Fe^{2+} in LiF. No visible and infrared absorption in samples containing up to 5×10^{-3} mole percent of iron could be detected.^{2.18} The vacuum ultraviolet spectrum (not shown in the reference) showed a broad band beginning near 233 nm (5.33 eV) and a stronger band at 167 nm (7.44 eV), both on a rising background (presumably due to scattering). The 167 nm band showed a blue shift with decreasing temperature, but the 233 nm band did not shift. The assignments of these two bands were uncertain, but the position of the 167 nm band seemed to fit the expected value for the 3d to 4s transition in Fe^{2+} .

Sec. II-C LiF

f. Co²⁺ in LiF. The ultraviolet spectrum ^{2.16} of Co²⁺(3d⁷) in LiF is shown in Fig. 2.15. The crystals were light pink in color. The band at 155 nm (8.00 eV), which has oscillator strength 1.8×10^{-3} , shifts to 153 nm (8.11 eV) as the temperature is lowered to 4.2 K. The apparent intensity increase may be the result of increased scattering. The band at 135 nm (9.17 eV) has an oscillator strength of 2.0×10^{-2} and shifts to the blue by 0.124 eV.

g. Ni²⁺ in LiF. The impurity spectrum ^{2.18, 2.20} of Ni²⁺(3d⁸) in lithium fluoride is shown in Figs. 2.15 and 2.19. The peak positions in Fig. 2.19 agree well with the values of Chase and McClure listed in Table 2.15, which also includes oscillator strengths and upper-state assignments. In Fig. 2.15, the scattered light became comparable to the transmitted light so that the spectrum at shorter wavelengths is not known. The oscillator strength of the room-temperature band at 133 nm (9.30 eV) is 0.51. This band does not shift as the temperature is lowered to 10 K. The apparent increase in intensity at the low temperature, which was not reproducible, was believed to be due to fogging of the sample at low temperature. At photon energies below 7.44 eV ($\lambda > 167$ nm) there was no absorption detected even when the path length was increased by one centimeter.

7. Trapped electron and hole centers in LiF.

a. F center in LiF. The F-center absorption spectra of LiF and several other alkali halides were shown in Fig. 2.5. A typical absorption spectrum of X-irradiated LiF at 78 K is shown ^{2.21} in Fig. 2.20, where the most prominent band, 5.0 eV (250 nm) is the F band. (A better spectrum ^{2.22} of the F band is given in Fig. 2.23 below.) The F center, which is an

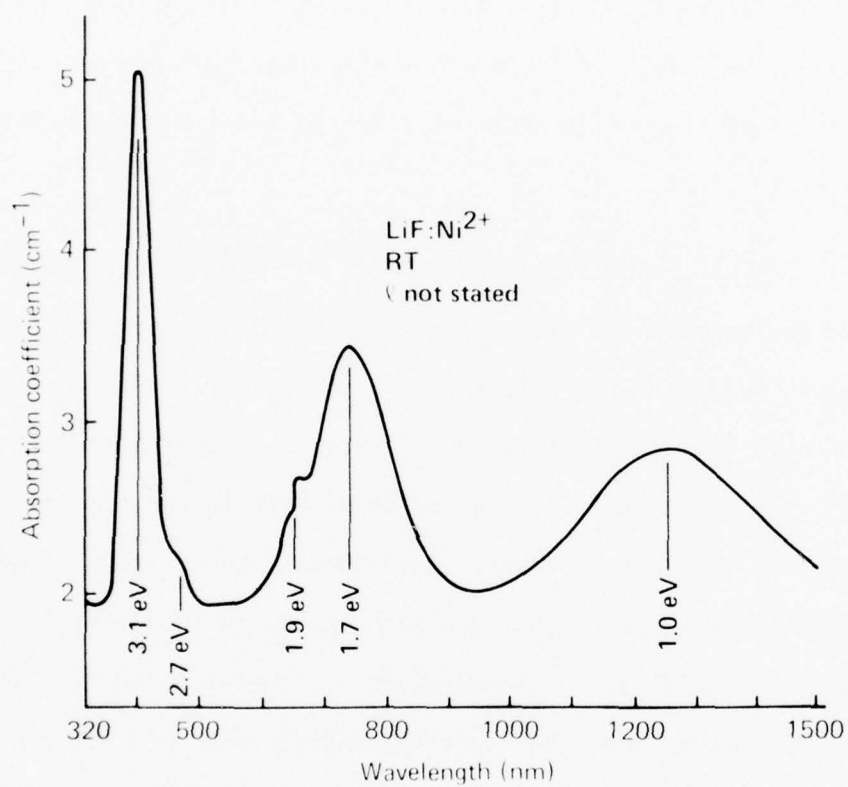


Fig. 2.19. Optical absorption spectra of LiF:Ni²⁺.
[P. Berge, M. Dubois, G. Blanc, and M. Adam-Benveniste,
J. de Physique 26, 339 (1965).]

Sec. II-C LiF

Table 2.15. Absorption bands in nickel-doped LiF.
[D. B. Chase and D. S. McClure, Jour. Chem. Phys.
64, 74 (1976).]

Peak position (eV)	1.01	1.67	1.88	2.75	3.06
Oscillator strength	0.87	2.5	-	-	4.7×10^{-5}
Upper state	3T_2	3T_1	1E	1T_2	3T_1

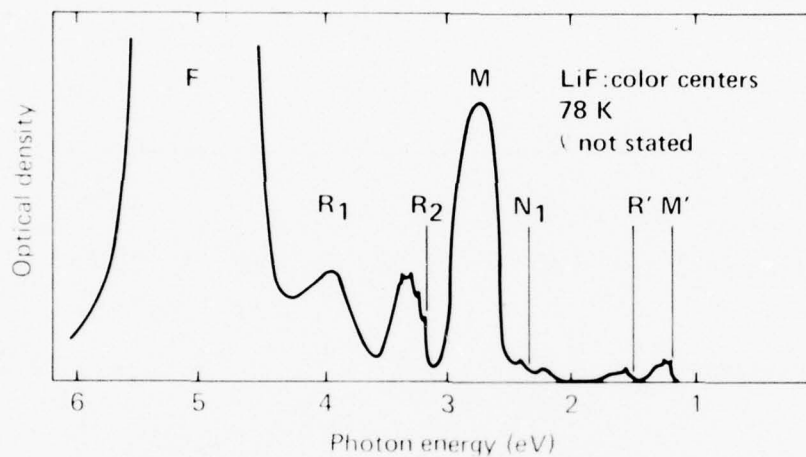


Fig. 2.20. Typical absorption spectra of X-irradiated LiF at 78 K. [D. B. Fitchen in Physics of Solids at High Pressure, C. T. Tomizuka and R. M. Emrick, eds., Academic Press, New York (1965), p. 383.]

Sec. II-C LiF

electron bound at a negative-ion vacancy, is stable at room temperature. Thermal annealing occurs at 100 C.

The antimorph to the F center is a hole trapped at a positive-ion vacancy. No such centers have been identified experimentally. It appears that holes prefer to be trapped in such other centers as V_K centers, rather than in the anti-F centers.

b. F-related centers. A typical spectrum in Fig. 2.20 of an irradiated sample shows M-, N-, and R-type absorption bands. See the definitions in Table 1.1. Such bands are seen typically in irradiated samples, but the details of the spectra depend on such factors as the type of irradiation, dose and irradiation temperature, thermal treatment, impurity content, and the time lapse before measurement. For heavily irradiated samples, colloid bands can appear, as discussed in Sec. 8 below.

c. V_K center, or self-trapped hole, in LiF. The absorption spectrum^{2.23} of the V_K center (see Table 1.1) in LiF, with a strong band centered at 348 nm (3.56 eV), is shown in Fig. 2.21. The absorption band of V_K centers aligned along the [011] direction is shown in Fig. 2.22. Since the V_K center is a hole trapped by a pair of neighboring negative ions, the V_K centers are aligned along [110] directions. The centers aligned along a specific [110] direction, such as $[0\bar{1}1]$ in Fig. 2.21, can be bleached in light polarized along that direction. The V_K center is stable at low temperatures ($T < 120$ K), and the optical absorption is only slightly affected by the crystalline environment.

d. V_3 center, or F_3^- molecular ion, in LiF. Figure 2.23a shows^{2.22} the V_3 -center absorption centered at 113 nm (11.0 eV), which was produced

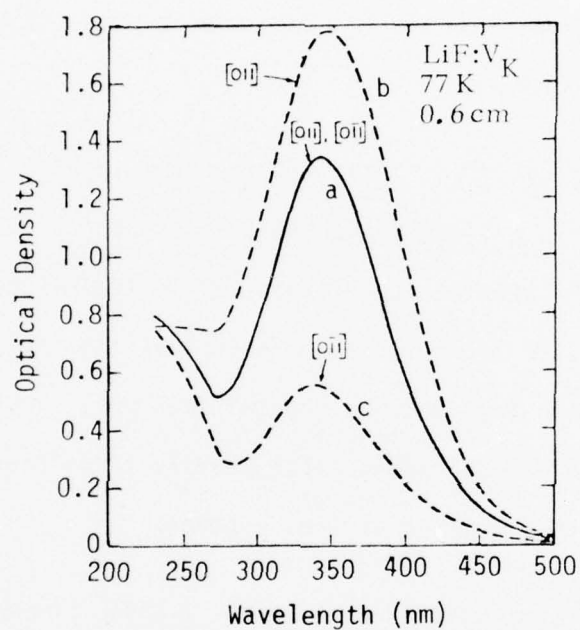


Fig. 2.21. Absorption spectra of spatially oriented V_K centers in LiF: (a) 30-minute X irradiation at 77 K, measured with either $[011]$ or $[0\bar{1}1]$ light; (b) $[011]$ light, and (c) $[0\bar{1}1]$ light, both after bleaching at 77 K for one hour in $[0\bar{1}1]$ light. [C. J. Delbecq, W. Hayes, and P. H. Yuster, Phys. Rev. 2, 1043 (1961).]

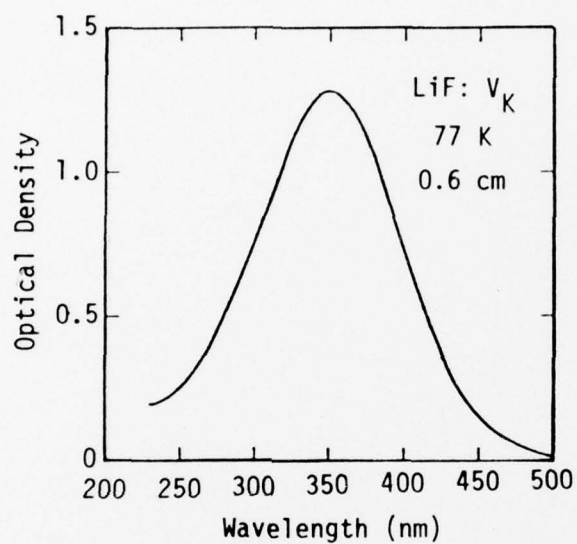


Fig. 2.22. Anisotropic absorption of V_K center in LiF, obtained by subtracting curve (c) from curve (b) in the previous figure. [C. J. Delbecq, W. Hayes, and P. H. Yuster, Phys. Rev. 121, 1043 (1961).]

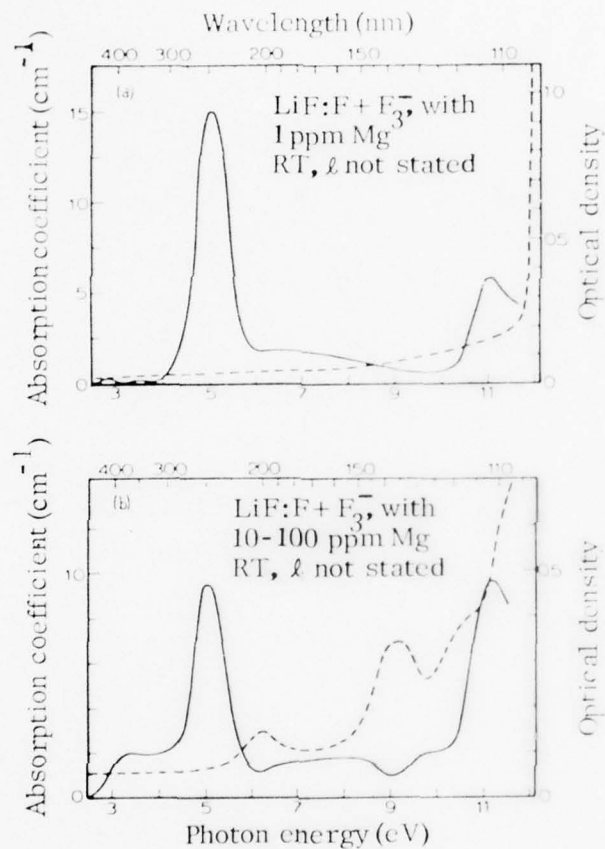


Fig. 2.23. Optical absorption of X-irradiated, magnesium-doped LiF: (dashed) before irradiation; (solid) after X irradiation, with dashed curve subtracted to give the solid curve. [M. R. Mayhugh and R. W. Christy, Phys. Rev. 2, 3330 (1970).]

Sec. II-C LiF

by X-irradiation of pure LiF at room temperature, in addition to the F band at 248 nm already discussed. Figure 2.23b, for X-irradiated, Mg-doped LiF, shows these same two bands plus bands centered at 380 nm (3.26 eV) and 310 nm (4.00 eV) and some structure between 5 and 11 eV. The F and F_3^- bands of OH^- -free LiF are shown^{2.15} in Fig. 2.24.

In the pure sample (1 ppm Mn) of Fig. 2.19a, the V_3 band is less than one-half as intense as the F band; while the two bands have nearly equal intensity in the manganese-doped sample (10 - 110 ppm Mn). The relative intensities of the F and F_3^- bands in Fig. 2.24 are obscured by the background absorption.

The V_3 center or F_3^- molecular ion is a linear molecule along a [100] direction consisting of three fluorine ions with one of the ions at a Li site plus two trapped holes.^{2.22, 2.24, 2.25} The center is stable at room temperature, but decays thermally at 100 C or above.

The positions of peaks of the V_3 bands of the alkali halides as a function of the negative-ion radius are shown in Fig. 2.6b.^{2.22} The positions are relatively independent of the positive-ion radius, as seen on the figure.

e. Color centers in magnesium-doped LiF. The absorption spectra^{2.26} of X-irradiated LiF:Mg for various quenching and bleaching conditions are shown in Figs. 2.25 and 2.26. The bands at 4.0 eV (310 nm) and 5.6 eV (220 nm), which are associated with the magnesium, are greatly enhanced by quenching the crystal prior to X irradiation. For the quenched sample of Fig. 2.25, bleaching with combined F and 4.0 eV light at room temperature leads to the disappearance of the 4.0 eV band, to a slower growth of the

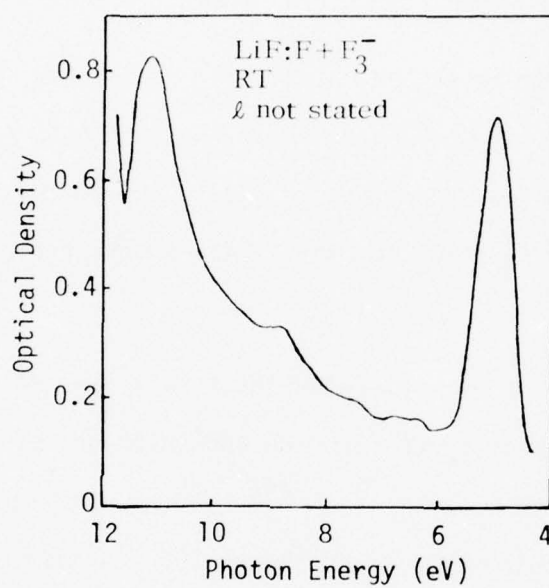


Fig. 2.24. Absorption spectrum of a γ -irradiated, OH^- -free LiF. The 11.2 eV band appears with the well known 5 eV F band in LiF. [T. Kamikawa, Bull. of Yamagata Univ., Nat. Sci. 8 (4) 519 (1975).]

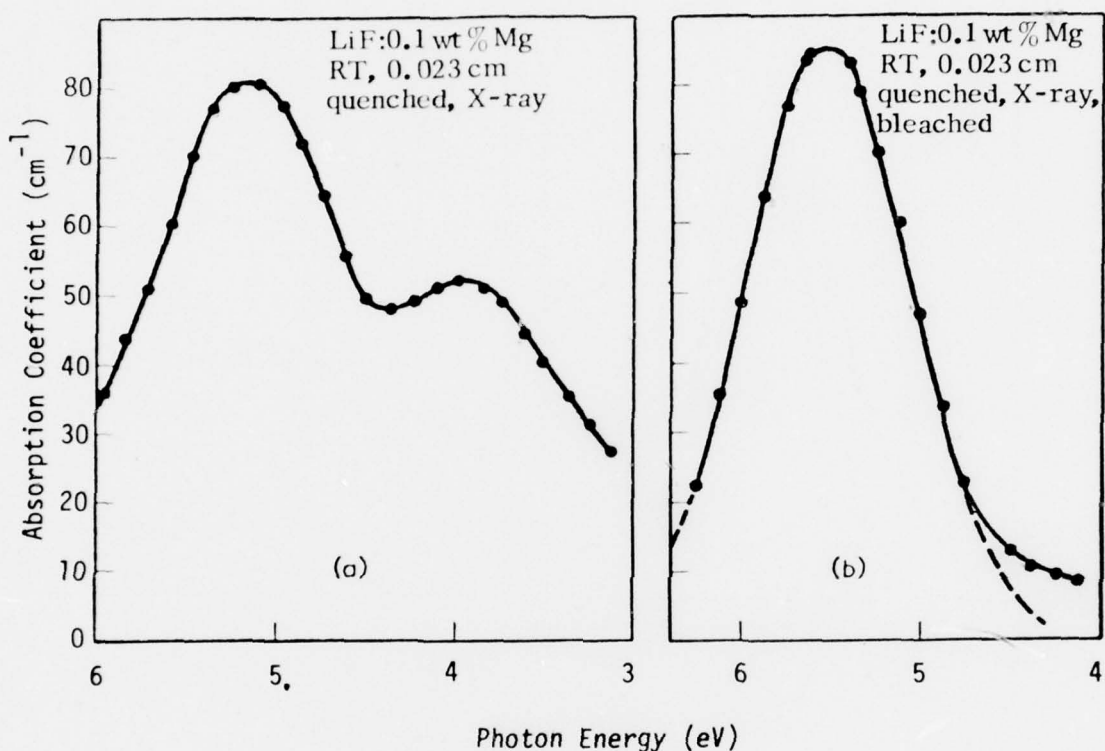


Fig. 2.25. Optical absorption of LiF:Mg quenched from 600 C and X-irradiated at room temperature: (a) before bleaching; (b) after bleaching with F and 4.0 eV light at room temperature for 105 hours. Dashed curve in (b) is a Gaussian with absorption maximum at 5.25 eV and 1.0 eV width. [J. Mort, Solid State Commun. 3, 263 (1965).]

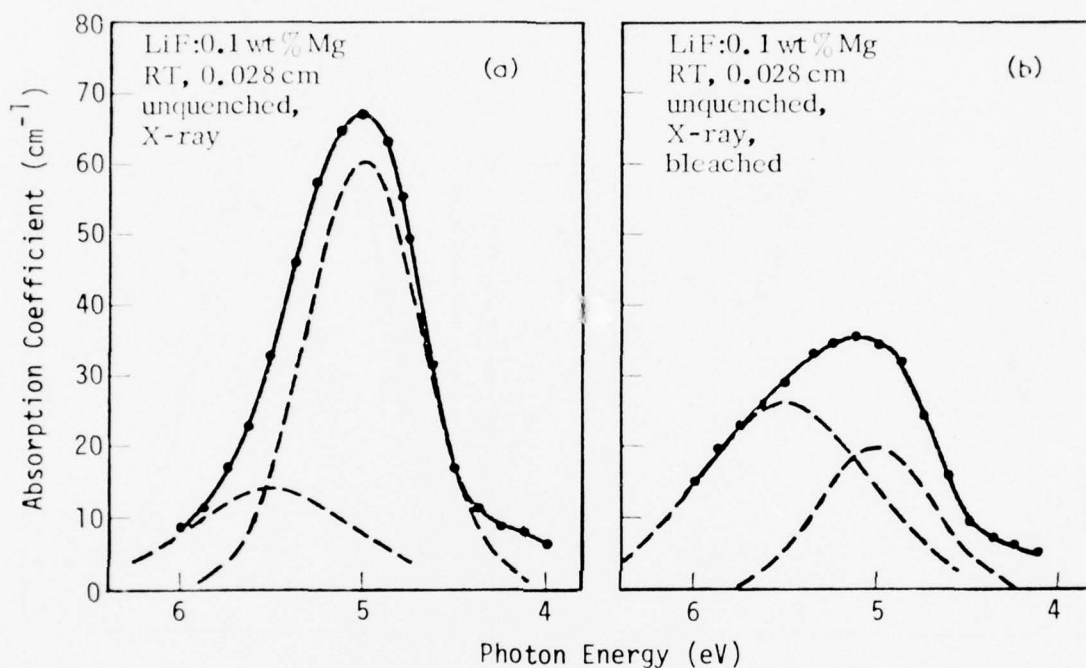


Fig. 2.26. Optical absorption of unquenched LiF:Mg, X-irradiated at room temperature: (a) before bleaching; (b) after bleaching with F and 4.0 eV light at room temperature for 105 hours. In both (a) and (b) the experimental curve is decomposed into two Gaussians. The full width at half maximum of the 5.5 eV band is 1.0 eV; and that of the F band at 5.0 eV is 0.74 eV. [J. Mort, Solid State Commun. 3, 263 (1965).]

Sec. II-C LiF

5.6 eV band, and essentially complete disappearance of the F band. By contrast, for the unquenched sample of Fig. 2.26, X irradiation does not generate the 4.0 eV band, and the same bleaching procedure gives a considerably smaller growth of the 5.6 eV band and does not eliminate the F band.

These results can be understood as follows: Divalent metal impurities in alkali halides tend to aggregate into clusters after either standing for long periods at room temperature or thermal annealing followed by slow cooling.^{2.27} On the other hand, elevating the temperature and quenching tends to disperse the divalent impurities throughout the lattice, some being isolated and some being compensated by cation vacancies. Furthermore, the Mg^{2+} -cation vacancy can be dissociated at high temperature, often quenched to give an increased number of isolated vacancies and Mn^{2+} ions at room temperature. The results of Figs. 2.25 and 2.26 are then consistent with the assignment, the author seems to imply, of the 4.0 eV band to the isolated Mg^{2+} and the 5.5 eV band to the Mg^{2+} -vacancy center (and the 5.0 eV F center from electrons trapped at the vacancy, of course). The isolated Mg^{2+} and Mg^{2+} -vacancy centers are more numerous in the quenched sample of Fig. 2.25.

8. Colloid bands in LiF. Figures 2.27 - 2.31 show the absorption spectra^{2.28-2.29} of positive-ion-irradiated and neutron-irradiated lithium fluoride: Li^+ (Fig. 2.27), Na^+ (Fig. 2.28), K^+ (Figs. 2.29 and 2.30), and neutron (Fig. 2.31). Implanting positive ions creates bands associated with the implanted ions in addition to those associated with damage of the lattice. For the self-positive-ion irradiation of $1.2 \times 10^{15} \text{ Li}^+$ per square centimeter (energy 2 MeV and range 5 μm), the spectrum in Fig. 2.27 shows bands centered at 290 nm (4.28 eV), 418 nm (2.97 eV), 445 nm (2.79 eV), and 500 nm (2.48 eV)

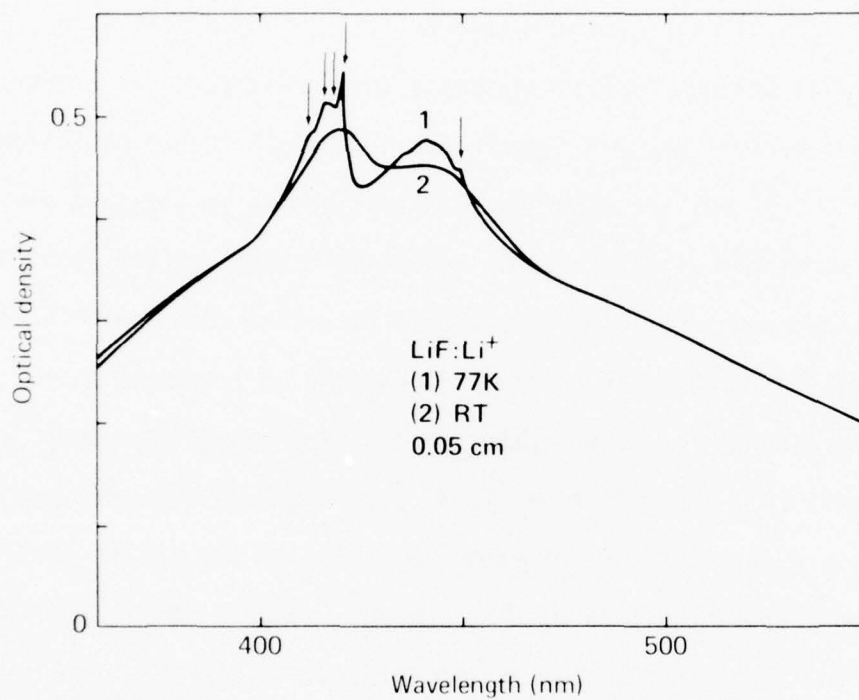


Fig. 2.27. Optical absorption spectra of LiF irradiated at room temperature with $1.2 \times 10^{15} \text{ Li}^+/\text{cm}^2$ and annealed at 200 C for four hours. [J. Davenas, A. Perez, P. Thevenard, and C. H. S. Dupuy, Phys. Stat. Sol. (a) 19, 679 (1973).]

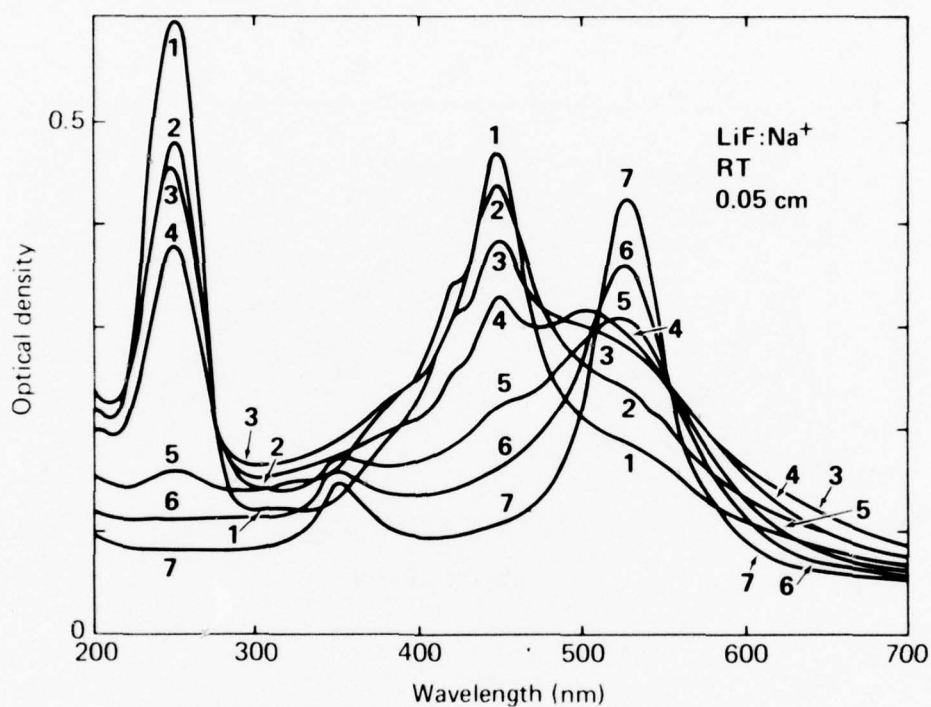


Fig. 2.28. Absorption spectrum evolution of a LiF sample: (1) irradiated at room temperature with 10^{16} Na^+ ions/ cm^2 ; (2) subsequently annealed using 15-minute periods at 140 C for a total time of 75 minutes and at 160 C for 105 minutes; (3) at 180 and 200 C; (4) at 220 and 240 C; (5) at 260 and 300 C; (6) at 340 C; and (7) at 380 and 420 C. Annealing times for (3) to (7) 105 minutes. [J. Davenas, A. Perez, P. Thevenard, and C. H. S. Dupuy, Phys. Stat. Sol. (a) 19, 679 (1973).]

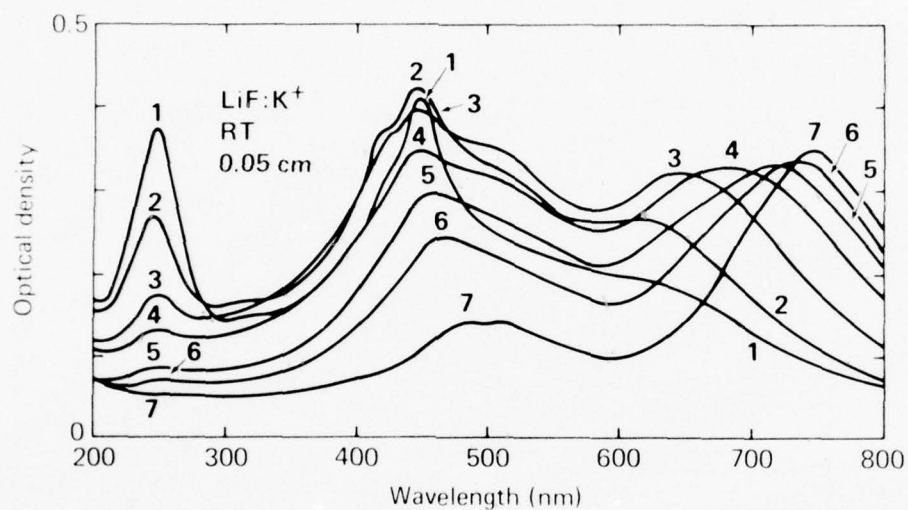


Fig. 2.29. Absorption spectrum evolution of a LiF sample: (1) irradiated at room temperature with $7 \times 10^{15} \text{ K}^+ \text{ ions/cm}^2$; (2) subsequently annealed using 15-minute periods at 140 C for a total time of 75 minutes and at 160 C for 105 minutes; (3) at 180 and 200 C; (4) at 220 and 240 C; (5) at 260 and 300 C; (6) at 340 C; and (7) at 380 and 420 C. Annealing times for (3) to (7) 105 minutes. [J. Davenas, A. Perez, P. Thevenard, and C. H. S. Dupuy, Phys. Stat. Sol. (a) **19**, 679 (1973).]

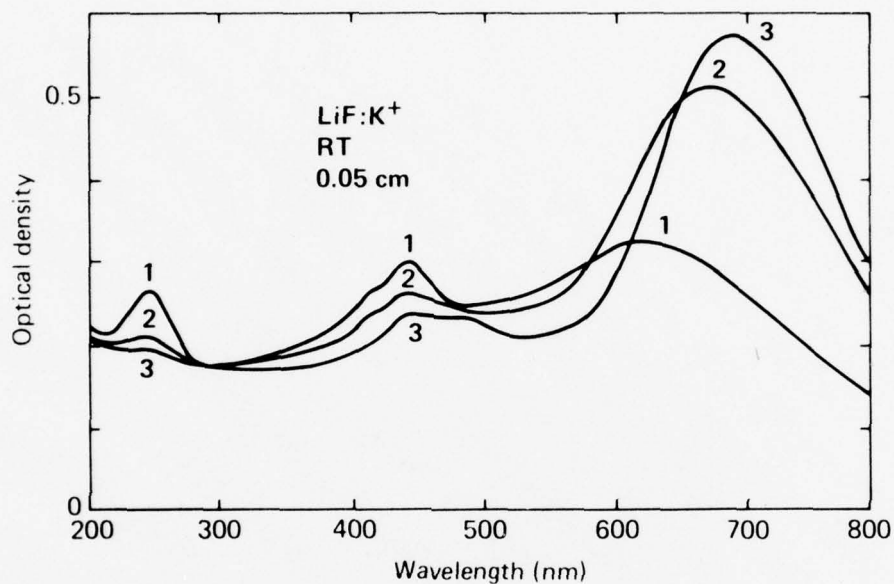


Fig. 2.30. Absorption spectrum evolution of a LiF sample: (1) irradiated at room temperature with $5.6 \times 10^{15} \text{ K}^+ \text{ ions/cm}^2$ and subsequently annealed for 30 minutes at 100 C; (2) at 150 C; (3) at 180, 200, and 230 C. The annealing duration was 30 minutes. [J. Davenas, A. Perez, P. Thevenard, and C. H. S. Dupuy, Phys. Stat. Sol. (a) 19, 679 (1973).]

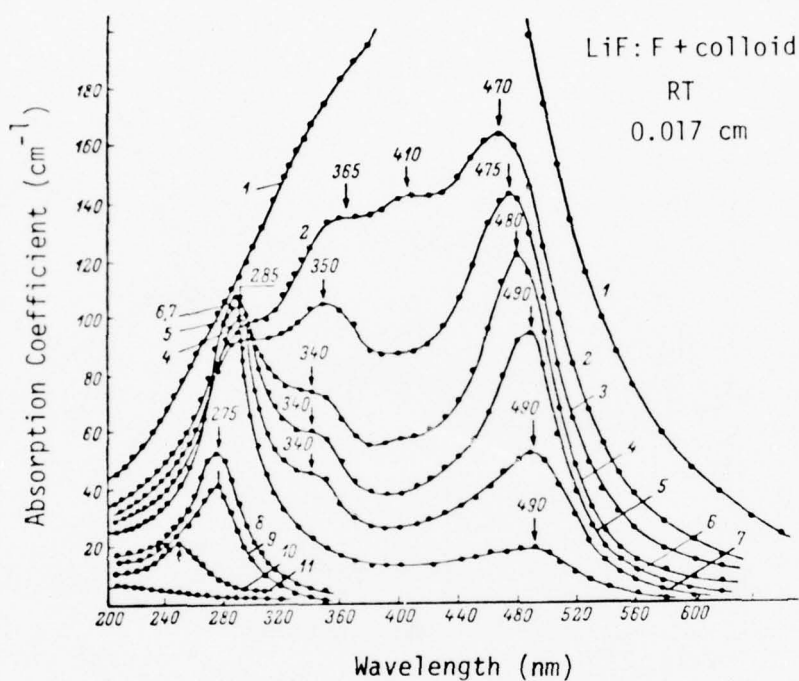


Fig. 2.31. Absorption spectra of LiF crystal irradiated with 10^{17} neutron/cm² and annealed at 350 C for the following times (in min.): (1) 60; (2) 120; (3) 180; (4) 240; (5) 300; (6) 360; (7) 420; (8) 1080; (9) 1590; (10) secondary annealing at 500 C for 60 min.; (11) holding at room temperature for 310 days. [N. G. Polotov and L. F. Vorozheikina, Soviet Phys.-Solid State 12, 277 (1971).]

Sec. II-C LiF

that had been observed previously in samples irradiated with neutrons, electrons, or ions, and assigned previously to colloidal centers. The main lithium-colloid band C in LiF is the 445 nm band.

Figure 2.28 for Na^+ -irradiated LiF shows the reduction of the F band at 250 nm and the lithium self-colloid C band at 445 nm (as these damage centers are annealed out) and the growth of the sodium-colloid band $C_A(\text{Na}^+)$ at 520 nm (as the sodium ions cluster to form the colloidal particles) for subsequent annealing at higher and higher temperatures. The corresponding results for K^+ -irradiated LiF, with the $C_A(\text{K}^+)$ potassium colloid band at 680 nm (1.8 eV), are shown in Fig. 2.29. The positions of the C bands in LiF, NaCl, and KC and the positions of the $C_A(\text{Na}^+)$ and $C_A(\text{K}^+)$ bands in LiF are summarized in Table 2.16.

The qualitative results are explained by the Mie theory^{2,30} of absorption by small particles, which gives

$$\lambda = \lambda_p (1 + 2n_H^2)^{1/2}$$

for the position of the colloid absorption peak, where λ_p is the bulk plasma wavelength of the metal and n_H is the index of refraction of the host (LiF in the present case).

Neutron irradiation at low dose levels, say $10^{14} - 10^{15}$ neutrons/cm², produces^{2,29} F, R, and M bands. See the definitions in Table 1.1. Annealing at high temperature dissociates these centers, and no new bands appear. By contrast, heavily irradiated samples show: colloidal bands, denoted W_2 and centered near 490 nm (2.5 eV) in Ref. 2.29; quasimetallic bands, W_2 near 365 nm (3.40 eV) and 410 nm (3.02 eV), assigned to colloids of metals

Table 2.16. Colloidal bands of Li, Na, and K (nm) in LiF
 [J. Davenas, A. Perez, P. Thevenard, and C. H. S. Dupuy,
 Phys. Stat. Sol. (a) 19, 679 (1973).], NaCl and KCl
 [A. Perez, P. Thevenard, and C. S. Dupuy, C. R. Acad. Sci.
 (France) 271 B, 519 (1970).]

Implanted Ions	Crystals		
	LiF	NaCl	KCl
Li ⁺	C: 445		
Na ⁺	C _A (Na ⁺): 520	C: 570	
K ⁺	C _A (K ⁺): 680		C: 760

Sec. II-C LiF

for which the lattice spacing and type of lattice do not correspond to those of the equilibrium metal^{2.31}; and atomic-center bands, W_1 near 285 nm. Figure 2.31 shows the development of the W_2 colloidal band, starting at 470 nm, and the atomic-center band, starting at 285 nm, for a series of annealings of a heavily irradiated (10^{17} neutrons/cm²) LiF sample.

D. Sodium Fluoride

Sodium fluoride has the highest melting point (1000 C) of all alkali halides. Because of this and its high reactivity, the background impurity contents of commercially available NaF single crystals are relatively high for most research purposes.

Sano^{2.32} has extensively studied the optical properties of Harshaw NaF and has reported that the exciton absorption tail is extrinsic in these crystals. Voszka, et al.,^{2.33} have developed purification procedures to obtain NaF crystals containing less than 1 ppm of impurities. The exciton absorption tails in these crystals at 100, 190 and 298 K are shown in Fig. 2.32; these tails are believed to be intrinsic.^{2.34} In Fig. 2.33 they are compared with the theoretical Urbach tails (continuous lines) and with the exciton absorption tails in the Harshaw NaF (dashed lines) reported by Sano.^{2.32}

The values of the absorption edge obtained by extrapolating the steep segments of the curves to $\beta = 5 \text{ cm}^{-1}$ are 128 nm (9.7 eV), 125 nm (9.9 eV), and 122 nm (10.2 eV) for 298, 190 and 100 K, respectively. The longer absorption tail extending from ~ 125 to 160 nm is characteristic of the alkali halides and is probably a result of extrinsic absorption.

The first exciton absorption in alkali halides involves charge transfer from one of the halide ions to the spatially extended conduction band. At low temperatures and with high resolution instruments, a doublet structure is often seen in this absorption because of the spin-orbit splitting of the halide ions. This feature is illustrated in Fig. 2.34, where the spectra of NaF crystals at room temperature and 78 K are compared in the

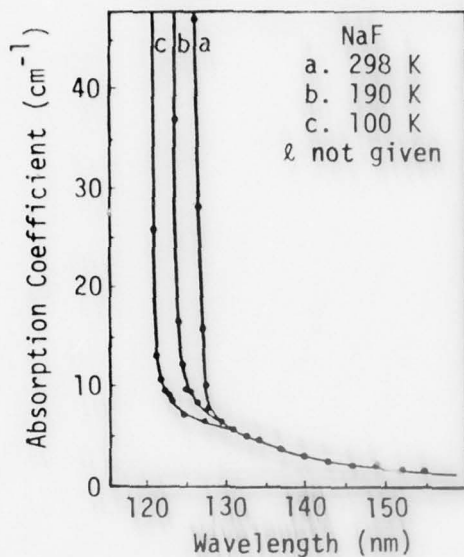


Fig. 2.32. Absorption spectra of NaF single crystals in the VUV region. [I. Földvári, R. Voszka, and R. Raksányi, Phys. Stat. Sol. (a) 26, K83 (1974).]

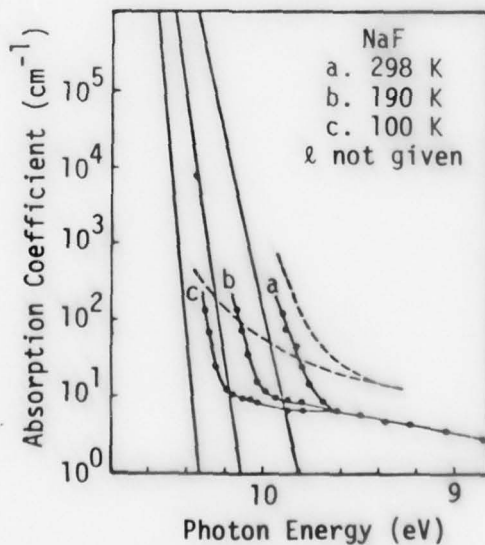


Fig. 2.33. Experimental and theoretical Urbach tails of NaF single crystals. Theoretical: continuous line, experimental: line with circles, previous experimental results of Sano: dashed line. [I. Földvári, R. Voszka, and R. Raksányi, Phys. Stat. Sol. (a) 26, K83 (1974).]

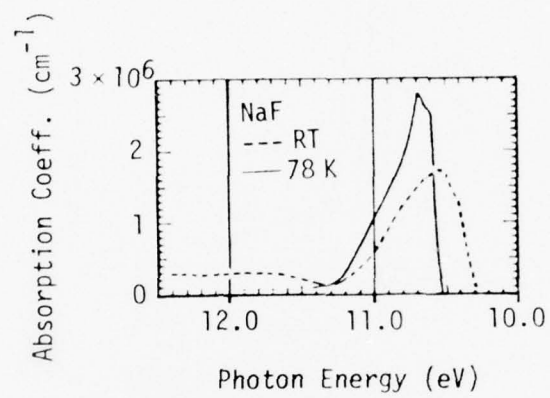


Fig. 2.34. Analyzed spectra of absorption constant in cm⁻¹.
[R. Sano, J. Phys. Soc. Japan 27, 695 (1969).]

Sec. II-D NaF

region of the first exciton absorption. These spectra were derived by Sano from reflectivity measurements made on Harshaw NaF crystals.^{2.32}

Sano^{2.32} has also derived the optical constants of NaF, both at room temperature and 78 K, in the spectral range 9.0 - 12.5 eV (137.8 - 99.2 nm). The refractive index of NaF between 6.67 and 0.05 eV (186 nm and 24 μ m) is tabulated in the American Institute of Physics Handbook.^{2.35} With increase in energy over this spectral range, the index value increases from 0.24 to 1.3930.

1. Negative-ion impurities in NaF. Several negative-ion impurities in alkali halides give rise to absorptions in the UV and VUV due to electronic transitions. In many cases these absorptions have been found to be similar to the first exciton absorptions in alkali halides in that they involve charge transfer from one of the impurity ions to the spatially extended conduction band. Kapphan and Lüty^{2.36} approximated the energy ($\hbar\omega$) required in such a charge-transfer process as:

$$\hbar\omega = E_A - E_I + \alpha_M \frac{e^2}{r_0} \quad , \quad (2.1)$$

where E_A is the electron affinity of the impurity, or the host halogen in the case of first exciton absorption, E_I the ionization energy of the alkali atom, α_M the Madelung constant, e the electronic charge, and r_0 the nearest-neighbor distance of the host lattice. The term E_I in (2.1) would be appropriate for the transfer of an electron from a negative impurity (or host) ion to a neighboring alkali ion. It is now believed the orbital of the added electron to the alkali ion would be so large that the overlap with many neighbors would be great. It is therefore more appropriate to consider

the transfer of an electron from a negative ion to a conduction band. In this case, replacing E_I by one-half the width of the valence band gives results that fit experiments as well as do the results from (2.1).

a. OH^- , O_2^- and H^- ions and F and M centers in NaF. The peak positions of the OH^- -, H^- - and F-center absorptions in alkali halides have been found to follow empirical (Ivey) relations. The Ivey plots of these three centers are shown in Fig. 2.35^{2,37}; in this figure, U refers to substitutional H^- ions.

Kapchan and Lütty^{2,36} found that relation (2.1) can be used successfully to predict the peak position of the ultraviolet absorption band of hydroxyl ions in an alkali halide if the electron affinity of the hydroxyl ion is assigned a value of 2.6 eV. In the case of NaF, $E_I \approx 5.14$ eV, $r_0 \approx 0.231$ nm, and $\alpha_M \approx 1.75$. When these values are substituted into relation (2.1), a value of 8.37 eV (148 nm) is predicted for the peak position of the hydroxyl absorption, as compared to the value of 8.1 eV (153 nm) obtained from the Ivey plot (Fig. 2.35). Freytag^{2,37} reports the peak position and half-width of the OH^- band in NaF at 190 K as 8.3 eV (149.4 nm) and 1.1 eV (1.127 μm), respectively (Fig. 2.36).

Since hydroxyl (OH^-) is a molecular impurity, it is susceptible to decomposition when a hydroxyl-doped crystal is X-irradiated or bleached with light in the wavelength region of OH^- absorption. Many of these decomposition products are optically active; thus, new absorption bands are observed on the low- and high-energy sides of the original hydroxyl absorption, as demonstrated below.

Optical spectra of an X-irradiated hydroxyl-doped NaF crystal are shown in Figs. 2.37a and 2.37b.^{2,37} Two bands are seen in Fig. 2.37a, the

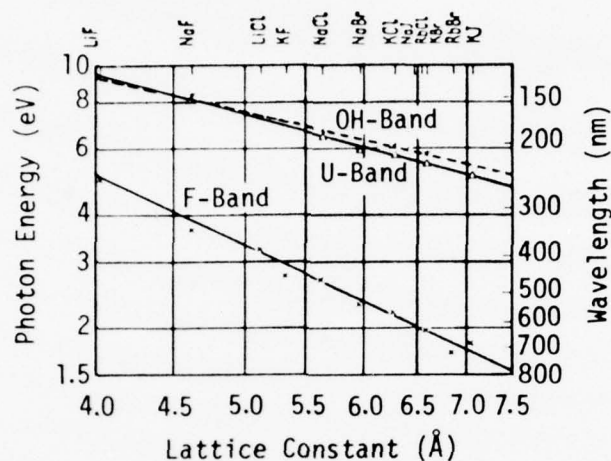


Fig. 2.35. Lattice-constant dependence of absorption maximum of OH⁻, U- and F-bands in various alkali halides. [E. Freytag, Z. Physik 177, 206 (1964).]

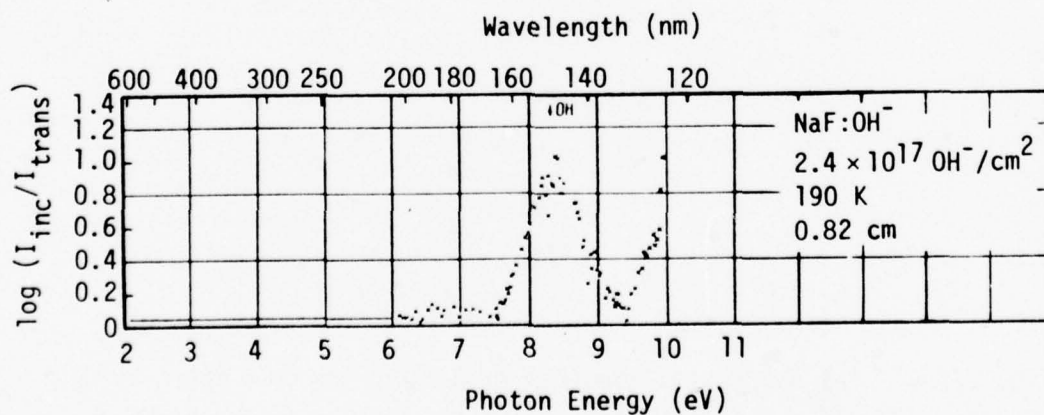


Fig. 2.36. Absorption spectrum of an unirradiated NaF crystal doped with OH⁻, measured at 190 K. [E. Freytag, Z. Physik 177, 206 (1964).]

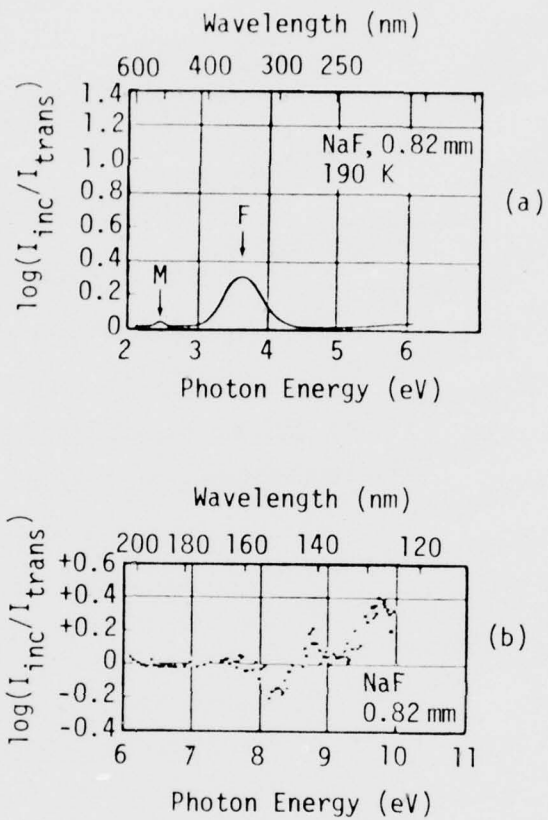


Fig. 2.37. (a) Absorption spectrum of NaF:OH⁻ crystal after being irradiated for 2.5 hours at 190 K. (b) The VUV spectrum of absorption difference, after and before the X irradiation. [E. Freytag, Z. Physik 177, 206 (1964).]

Sec. II-D NaF

F band at 3.65 eV (340 nm) and the M band at 2.46 eV (504 nm). The difference spectrum in Fig. 2.37b indicates that the X irradiation introduces two additional bands in the VUV region, the β band at 9.8 eV (126.5 nm) and another band at 8.8 eV (140.9 nm). X irradiation is also seen to reduce the intensity of the OH^- -absorption band at 8.3 eV (149.4 nm).

Optical absorption spectra of a UV-irradiated hydroxyl-doped NaF crystal are shown in Figs. 2.38a and 2.38b.^{2.37} It is seen that the changes produced in the optical spectra by UV and X irradiations are similar.

The F, M and β bands are also observed in irradiated hydroxyl-free NaF crystals, but at reduced intensity level. Freytag^{2.37} assigned the 8.8 eV (140.9 nm) band to neutral oxygen molecules (O_2^0). (Electron-spin-resonance results suggest O_2^- rather than O_2^0 , as discussed below.) The formation of these centers in irradiated crystals causes an apparent shift of the OH^- absorption to higher energy.

Meistrich made additional studies of irradiation-induced defects in the $\text{NaF}:\text{OH}^-$ system. Harshaw NaF crystals were used as the starting material for the growth of hydroxyl-doped crystals. The room-temperature optical absorption spectra of unirradiated and X-irradiated crystals are shown in Fig. 2.39. In the unirradiated crystal, the OH^- band peaks at 8.2 eV with a half-width of 0.87 eV, which is slightly smaller than the half-width of 1.1 eV reported by Freytag.^{2.37} Upon irradiation, the OH^- band shifts to lower energy due to the formation of a new band near 7.9 eV (157 nm), as shown in the difference spectrum of the same crystal in Fig. 2.40. Two additional bands, one near 8.9 eV (139.3 nm) and the β band at 9.8 eV (126.5 nm), are also seen in Fig. 2.40. The thermal stability of these

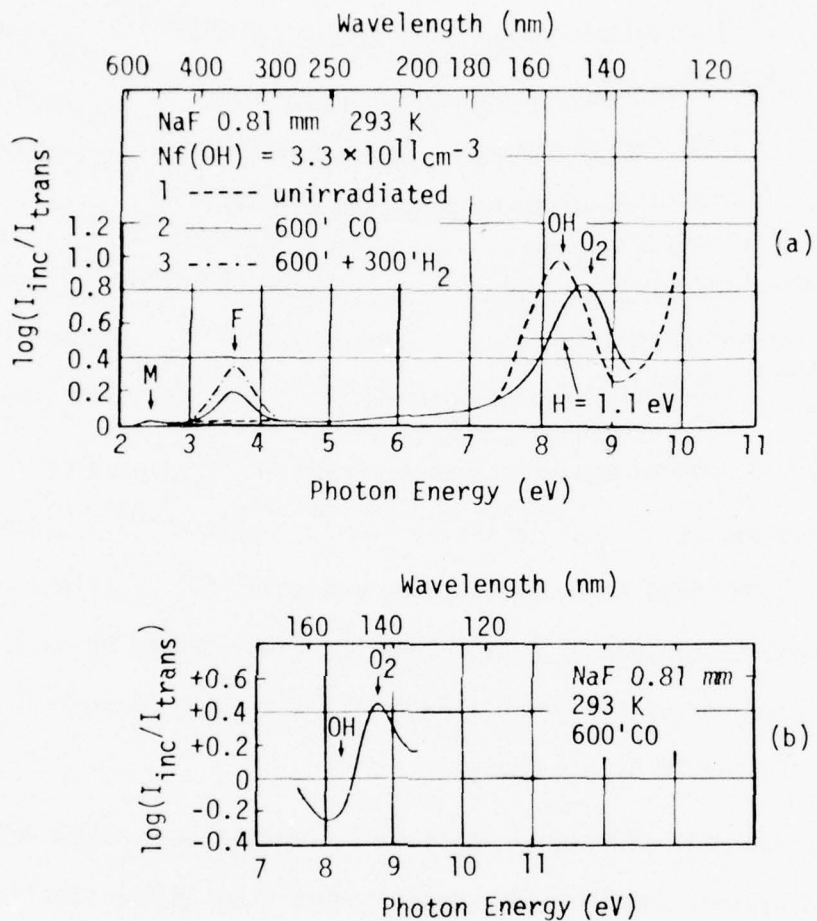


Fig. 2.38. (a) Absorption spectra of an OH^- -doped NaF before and after the irradiation in the OH^- band. (Curve 1 ----- unirradiated, curve 2 — irradiated for ten hours with CO emission, curve 3 -.-.- additional five-hour irradiation with hydrogen lamp.) (b) Change in vacuum ultraviolet absorption spectrum after irradiation in the OH^- band. [F. Freytag, Z. Physik, 177, 206 (1964).]

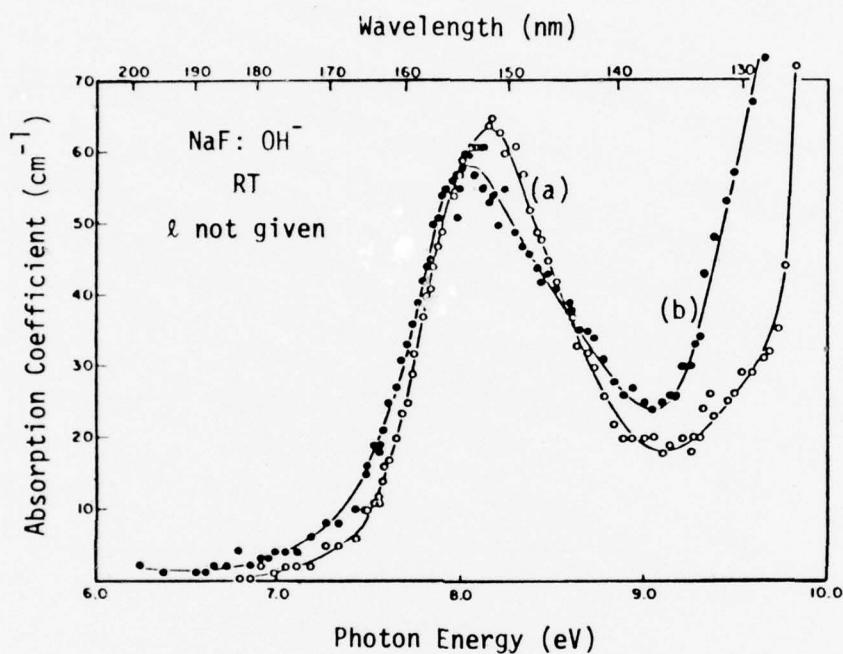


Fig. 2.39. Optical absorption of NaF:OH⁻ in vacuum UV region at room temperature. (a) Untreated (open circles); (b) X-irradiated at room temperature for two and one-half hours (solid circles). [M. L. Meistrich, J. Phys. Chem. Solids 29, 1119 (1968).]

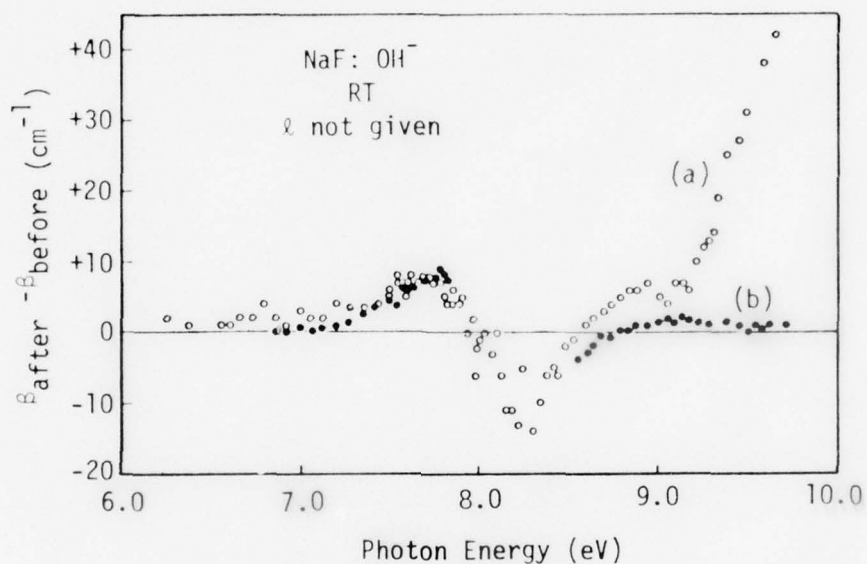


Fig. 2.40. Difference spectra (increase in absorption coefficient) of NaF:OH⁻ at room temperature. (a) Changes produced by two and one-half hours X irradiation; (b) changes produced by ten hours X irradiation plus heating to 350 C for one-half hour. [M. L. Meistrich, J. Phys. Chem. Solids 29, 1119 (1968).]

Sec. II-D NaF

two bands is less than that of the 7.9 eV (157 nm) band, as shown by curve b (filled circles) in Fig. 2.40.

On the basis of the Ivey relation (Fig. 2.35), Meistrich assigns the 7.9 eV (157 nm) band to U centers.^{2.38} His electron-spin-resonance data and the charge-transfer model of O_2^- ions in alkali halides indicate that the absorption band seen near 8.8 eV (141 nm) by him and by Freytag is due to O_2^- ions, not to neutral oxygen molecules as suggested earlier.^{2.37}

b. Cl^- and Br^- ions in NaF. The presence of a halogen impurity ion in an alkali halide gives rise to absorptions near the fundamental absorption edge of the host. These are referred to as localized exciton absorptions because of their similarity to the first exciton absorption of the host.

Földvári and Voszka^{2.39,2.40} have studied in detail the absorptions of Br^- and Cl^- ions in NaF, and they have also correlated their results with previously reported data on localized exciton absorptions in other alkali halides.

Optical absorption spectra of a Br^- -doped NaF crystal at room temperature and at 110 K are shown in Figs. 2.41a and 2.41b, respectively.^{2.39} Using a least-squares method, the observed absorption (continuous line) was resolved into four Gaussian components labeled a to d. The dotted line represents the sum of the four components. Bands a and d are due respectively to the Cl^- and OH^- ions introduced accidentally into the crystal. Bands b and c have been assigned to isolated Br^- ions because their integrated absorption increases linearly with an increase in Br^- concentration from 0 to 6 ppm (Fig. 2.42). At higher Br^- concentrations, the absorption

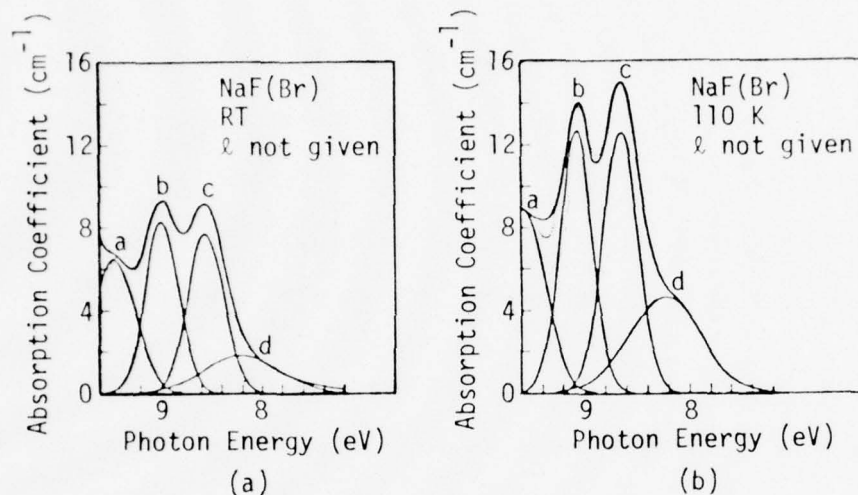


Fig. 2.41. The absorption spectra of NaF(Br) single crystals at (a) RT and (b) 110 K. The indicated absorption bands: (a) Cl^- , (b) and (c) Br^- , (d) OH^- . [I. Földvári and R. Voszka, Phys. Stat. Sol. (a) 31, 765 (1975).]

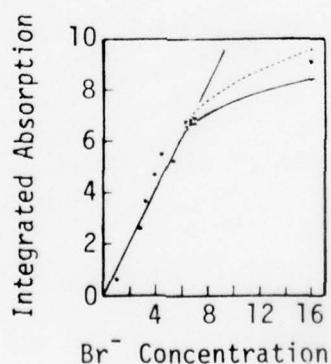


Fig. 2.42. Concentration dependence of the integrated absorption by Br^- before (continuous line) and after (dashed line) thermal treatment. [I. Földvári and R. Voszka, Phys. Stat. Sol. (a) 31, 765 (1975).]

Sec. II-D NaF

increases at a slower rate due to the formation of Br^- aggregates. When crystals containing high concentrations of Br^- ions are quenched after heating at 600 C for one hour, an increase in Br^- absorption is observed, as shown by the dotted line in Fig. 2.42. The thermal treatment apparently breaks up some of the Br^- aggregates and converts them into isolated Br^- ions. The spectral data for the Br^- bands b and c, including peak position, half-width, molar absorption coefficient, and oscillator strength are summarized at room temperature and 110 K in Table 2.17.

As noted earlier, a doublet structure is expected in the first exciton absorption of the alkali halides because the ground state of a halogen ion is a doublet. Accordingly, a doublet structure is also expected in the localized exciton absorptions, and the bands b and c observed in the $\text{NaF}:\text{Br}^-$ system are believed to be due to this effect.^{2.39}

In Table 2.18 the doublet separation in pure NaBr is compared with that of localized Br^- exciton in some alkali halides. By comparison, in the cases of KCl and NaCl at liquid nitrogen temperature, the higher energy component of the impurity doublet overlaps with the absorption edge of the host, and only one band due to the Br^- impurity is observed. In Table 2.18, ΔE is the energy separation between the lowest energy peaks of the impurity and host excitons; the significance of this value will be discussed shortly.

Optical-absorption spectra of NaF crystals containing varying concentrations of Cl^- ions are shown in Fig. 2.43.^{2.40} The absorption band seen near 131 nm (9.46 eV) is assigned to Cl^- ions because its absorption coefficient increases linearly with an increase in Cl^- concentration to 110 ppm (Fig. 2.44). The absorption spectra of a Cl^- -doped NaF crystal at room

Table 2.17. Parameters of the Br^- bands in $\text{NaF}(\text{Br})$ single crystals.
 [I. Földvári and R. Voszka, Phys. Stat. Sol. (a) 31, 765 (1975).]

	RT			110 K		
	b	c	b + c	b	c	b + c
Position (eV)	8.98	8.55		9.08	8.66	
(nm)	138.0	145.0		136.5	143.1	
Half-width (eV)	0.39	0.41		0.37	0.39	
Molar abs. coeff. ($\text{cm}^{-1} \text{ mol}^{-1}$)	1.35×10^6	1.26×10^6		2.07×10^6	2.05×10^6	
Oscillator strength	0.10	0.10	0.20	0.14	0.15	0.29

Table 2.18. Summary of Br⁻-band results of several investigators.
[I. Földvári and R. Voszka, Phys. Stat. Sol. (a) 31, 765 (1975).]

	ΔE (host-impurity band) (eV)	doublet separation (eV)
NaBr, 55 K	-	0.67
NaCl/NaBr mixed system, RT	-	0.60
NaCl(Br), LNT	0.25	-
KCl(Br), LNT	0.30	-
NaF(Br), RT	1.91	0.43
NaF(Br), 110 K	1.97	0.42

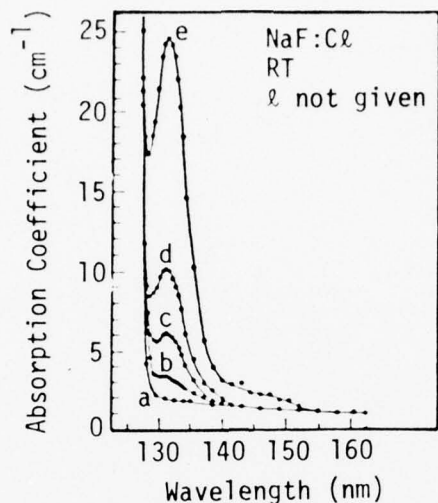


Fig. 2.43. Far UV absorption spectra of NaF(Cl) single crystals with different amounts of Cl ions; (a) starting material ($<10^{-6}$); (b) 3.1×10^{-6} ; (c) 8×10^{-6} ; (d) 13.3×10^{-6} ; (e) 28×10^{-6} . [I. Földvári and R. Voszka, Phys. Stat. Sol. (a) 28, 249 (1975).]

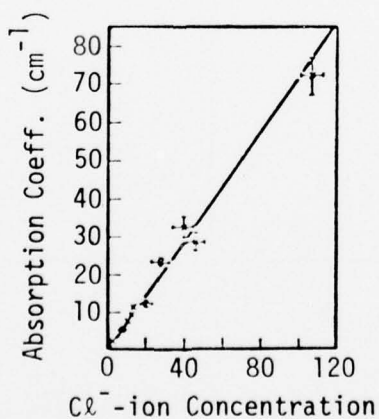


Fig. 2.44. Dependence of the absorption coefficient of the Cl band in NaF single crystals on the built-in Cl⁻-ion concentration (in ppm). [I. Földvári and R. Voszka, Phys. Stat. Sol. (a) 28, 249 (1975).]

temperature and at 110 K are shown in Fig. 2.45. The spectral data and the energy separation (ΔE) values of the Cl^- absorption band at various temperatures between 110 and 350 K are listed in Table 2.19.

According to the simple charge-transfer model of the exciton, relation (2.1), the energy separation ΔE between the halogen impurity-band maximum and the first exciton peak of the host should be equal to the difference $\Delta\alpha$ in the electron affinities of the respective halogens, in the first approximation. Table 2.20 summarizes the observed characteristics of localized excitons in various alkali halides. In the table, σ is the half-width of the impurity absorption and Δr is the differences in the ionic radii of the impurity and host halogens.

It is seen in Table 2.20 that the energy-separation values predicted by the simple charge-transfer model are in good agreement with the experimentally observed values in alkali-halide—halogen (impurity) systems with small Δr values. In other words, $\Delta\alpha \approx \Delta E$. In $\text{NaF}(\text{Cl})$ and $\text{KCl}(\text{I})$ systems, large Δr values result in the modification of the Madelung energy and give rise to strong halogen-halogen overlap. These factors can account for the differences observed between the ΔE and $\Delta\alpha$ values in the two systems.^{2.40}

2. Transition-metal ions in NaF. Absorption bands arising from the presence of transition-metal ions in fluoride host crystals may be observed over a wide spectral range, from near infrared to vacuum ultraviolet. Absorptions due to intra-d-shell transitions of the impurity ions are expected in the visible and near infrared, but they may not be observed because of their low oscillator strengths.

McClure, et al.,^{2.41,2.42} and Loh^{2.43} have analyzed the observed high-energy (5 to 10 eV or 248 to 129 nm) absorptions of the transition-metal

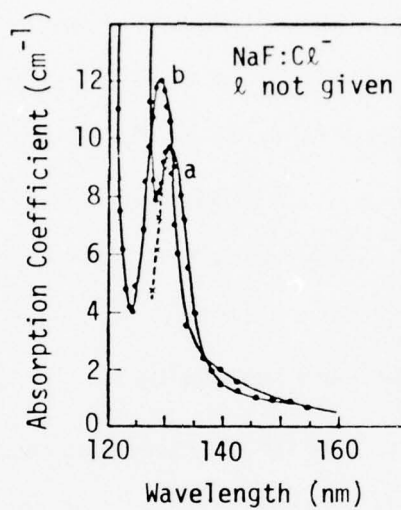


Fig. 2.45. Absorption spectra of the Cl band in NaF single crystals at different temperatures: (a) 298 K; (b) 110 K. [I. Földvári and R. Voszka, Phys. Stat. Sol. (a) 28, 249 (1975).]

Sec. II-D NaF

Table 2.19. Summary of the spectral data and the energy separation values of Cl^- band in NaF at various temperatures. [I. Földvári and R. Voszka, Phys. Stat. Sol. (a) 28, 249 (1975).]

		110 K	190 K	298 K	350 K
Position	(eV)	9.75	9.53	9.46	9.42
	(nm)	129.4	130.0	131.0	131.5
Half-width	(eV)	0.467	0.475	0.503	0.52
Molar abs. coeff. ($\text{cm}^{-1} \text{ mol}^{-1}$)		9.0×10^5	8.7×10^5	7.7×10^5	7.2×10^5
Oscillator strength		0.073	0.071	0.068	0.066
$\Delta E(\Gamma_{\text{NaF}} - \text{Cl}^-)$	(eV)	1.01	0.99	0.98	0.97

Table 2.20. Summary of the characteristics of the observed localized exciton absorptions in various alkali halides. [I. Földvári and R. Voszka, Phys. Stat. Sol. (a) 28, 249 (1975).]

	ΔE (eV)	σ (eV)	$\Delta\alpha$ (eV)	Δr (nm)
KCl(Br) LNT	0.3	0.19	0.25	0.014
KCl(I) LNT	1.06	0.2	0.55	0.035
NaCl(Br) LNT	0.25	—	0.25	0.014
KBr(I) LNT	0.4	0.2	0.30	0.021
NaBr(I) LNT	0.35	0.25	0.30	0.021
NaF(Cl) 110 K	1.01	0.467	0.4	0.045

Sec. II-D NaF

ions in the following fluoride host crystals: LiF, NaF, CaF_2 , MgF_2 and KMgF_3 .

McClure, et al.,^{2.41, 2.42} indicate that most of the absorption bands in the region of 222 - 147 nm (5.58 - 8.43 eV) may be assigned to the $3d \rightarrow 4s$ transitions of the impurity ions, on the basis of the following characteristics: (i) Their spectral positions are close to those of $3d \rightarrow 4s$ free-ion transitions appropriately corrected for crystal-field effects. (ii) They have moderate oscillator strengths, of the order of $10^{-3} - 10^{-4}$ at room temperature, which decrease on cooling. (iii) They shift to higher energy on cooling.

Loh^{2.43} attributes the higher energy bands, with transition energies ≥ 7.4 eV, to the $3d \rightarrow 4p$ spin-allowed transitions of the impurities, based on the following characteristics: (i) They have high oscillator strength, approximately an order of magnitude higher than the $3d \rightarrow 4s$ transitions, which increase on cooling. (ii) Their spectral positions correlate well with the corresponding free-ion data.

Optical absorption spectra in the region 335 - 125 nm (3.70 - 9.92 eV) of NaF crystals doped with various transition-metal ions are shown in Fig. 2.46.^{2.41} The spectral data, including peak position, half-width, extinction coefficient, and oscillator strength of various impurity-absorption bands, are summarized in Table 2.21.

Chase and McClure^{2.41} made the following interesting observations about transition-metal ions in NaF:

a. Titanium. In crystals doped with titanium ions, blue precipitates were observed. Thus, it is possible that only a fraction of the titanium

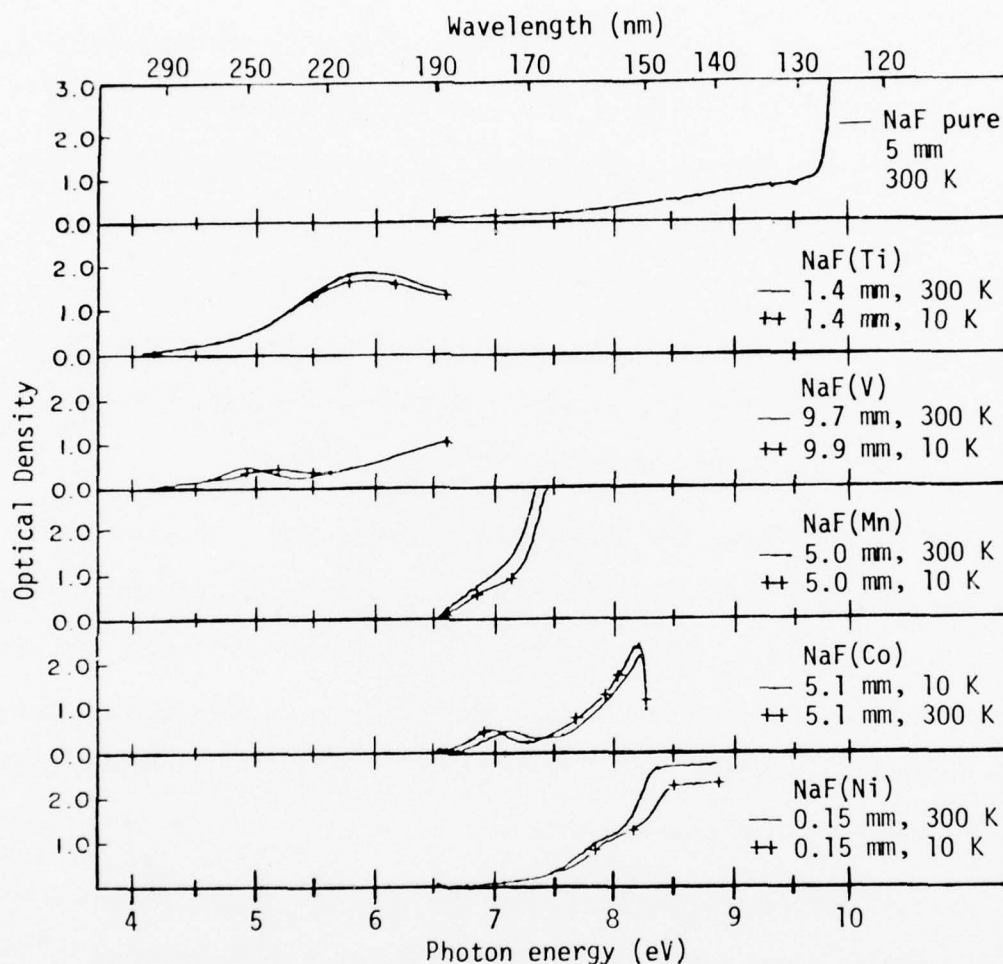


Fig. 2.46. Absorption spectra for NaF and for divalent transition-metal ions in NaF. Spectra at about 10 and 300 K are shown. Sample thickness is given in the legend. Concentrations are: Ti, unknown amount of dissolved Ti; V, 8×10^{-3} ; Mn, 1.8×10^{-2} ; Co, 2×10^{-2} ; Ni, 2.4×10^{-2} . [D. B. Chase and D. S. McClure, J. Chem. Phys. 64, 74 (1976).]

Sec. II-D NaF

Table 2.21. Ultraviolet bands observed in transition-metal ions in NaF. The energy of the peak of the band is given for temperatures 300 K and about 10 K. The width at half-height in cm^{-1} is given for the higher temperature. Also given are decadic molar extinction coefficients, ϵ , and the f number ($f = 4.31 \times 10^{-9} \int \epsilon d\bar{\nu}$, $\bar{\nu}$ in cm^{-1} , ϵ in $\text{l-moles}^{-1} - \text{cm}^{-1}$). f is approximated as $\epsilon_{\text{max}} \times \text{width at half-height}$. [D. B. Chase and D. S. McClure, J. Chem. Phys. 64, 74 (1976).]

Sample	Energy (cm^{-1})	Width (cm^{-1})	Extinction coefficient ($\text{M}^{-1} \text{cm}^{-1}$)	f
NaF:Ti	5.9 (300) 5.9 (10)	1.24	805	3.5×10^{-2}
NaF:V	5.02 (300) 5.15 (10)	.57	86.0	1.7×10^{-3}
NaF:Mn	6.87 (300) 6.94 (10)
NaF:Co	7.01 (300) 7.13 (10)	.47	81.0	1.3×10^{-3} 1.3×10^{-3}
NaF:Ni	7.94 (300) 8.06 (10)	...	~ 100	1.8×10^{-3}

Sec. II-D NaF

ions present in the crystal may be contributing to the absorption band seen at 210 nm (5.9 eV) in Fig. 2.46, and that the actual oscillator strength of the band may be higher than that indicated in Table 2.21. On cooling from room temperature to 6 K, a ten percent increase in the intensity of the 5.9 eV band was observed with no apparent shift in the peak position. It is believed that Ti^{3+} ions are present in the crystal and that the observed ultraviolet absorptions are due to fluorine-to-titanium transitions.

b. Vanadium. Paramagnetic resonance spectra of vanadium-doped NaF crystals indicated the presence of V^{2+} ions, but no optical absorption bands corresponding to the crystal-field transitions were observed in samples containing 8.0×10^{-3} mol percent V.

c. Manganese. NaF crystals containing 1.8×10^{-2} mol percent Mn were colorless and cloudy, but no evidence of aggregate formation was obtained from electron-spin-resonance studies. The vacuum-ultraviolet absorption spectrum of the crystal (Fig. 2.46) indicated the presence of a weak band at 182 nm (6.8 eV) and, on its high-energy side, a strong band with an estimated extinction coefficient of $90 \text{ mole}^{-1} \text{ cm}^{-1}$ at the band maximum. Since the weak band could not be resolved from the strong band, its oscillator-strength value does not appear in Table 2.21.

d. Cobalt. Sodium-fluoride crystals doped with 2.0×10^{-2} mol percent Co were pink in color. Electron-spin-resonance studies on heat-treated samples gave no indication of aggregate formation. In addition to the two VUV-absorption bands (Fig. 2.46), another band was observed in the visible at 515.5 nm (2.41 eV) with an oscillator strength of 5×10^{-5} . It was assigned to the ${}^4\text{T}_{1g} ({}^4\text{F}) \rightarrow {}^4\text{T}_{1g} ({}^4\text{P})$ transition of the Co^{2+} impurity.

Sec. II-D NaF

In another study of the optical properties of Co^{2+} -doped NaF, more absorption bands were observed in the visible and near-infrared regions, as shown in Fig. 2.47.^{2.44} The possible assignments for various transitions, their peak positions and oscillator strengths, are listed in Table 2.22.

e. Nickel. In NaF crystals containing 2.42 mol percent Ni, no crystal-field transitions were observed. The VUV spectrum of this crystal (Fig. 2.46) indicated the presence of two bands: a weak band at 156 nm (7.93 eV) with an oscillator strength of 1.8×10^{-3} , and another more intense band beyond 143 nm (8.68 eV). This latter band did not show a blue shift on cooling and was believed to be associated with the fluorine-to-metal charge-transfer processes.

The presence of iron impurity ions in NaF also gives rise to a strong absorption in the VUV. The absorption is structureless and appears in the form of a gently rising baseline, as shown in Fig. 2.48.^{2.33}

3. VUV spectra of some commercial-purity and high-purity NaF. It is seen from the above that most transition-metal and anionic impurities in NaF give rise to absorptions in the VUV. Therefore, a good indication of the relative purity of NaF crystals can be obtained from their VUV spectra. Vacuum-ultraviolet spectra of several commercial-purity and high-purity NaF crystals are shown in Fig. 2.49. In this figure, (a) and (b) refer respectively to the crystals grown from an analytical reagent grade NaF before and after chemical purification, (c) to a sample grown from Merck suprapure NaF, and (d) to a Harshaw NaF single crystal.

The band seen at 131 nm in spectrum (a) of Fig. 2.49 is due to Cl^- ions, and much of the residual absorption on the low-energy side of it is

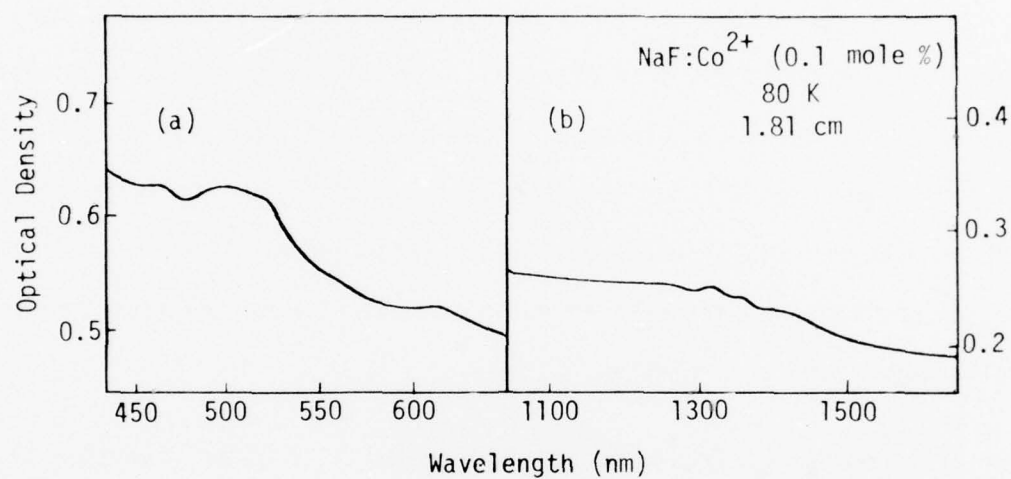


Fig. 2.47. Absorption spectrum of Co^{2+} -doped NaF. (a) Spectrum in the visible region. (b) Spectrum showing $4T_{2g}$ band in the infrared region. [J. P. Srivastava, J. Chem. Phys. 48, 5283 (1968).]

Sec. II-D NaF

Table 2.22. The experimental data at 80 K and the analysis of the absorption spectrum of Co^{2+} in NaF. [J. P. Srivastava, J. Chem. Phys. 48, 5283 (1968).]

Observed		f value $\times 10^6$	Calculated (eV)	Symmetry and free ion state
(nm)	(eV)			
1,412	0.88	1.08	0.935	$\left. \begin{array}{l} \Gamma_6 \\ \Gamma_8 \\ \Gamma_8 \\ \Gamma_7 \end{array} \right\} {}^4T_{2g}, {}^4F$
1,337	0.93		0.940	
1,312	0.94		0.952	
1,280	0.97		0.976	
966	1.28	0.21	1.29	$\Gamma_8 \quad {}^2E_g, {}^2G$
610	2.03		2.05	$\Gamma_8 \quad {}^4A_{2g}, {}^4F$
515	2.41	3.48	2.42	$\left. \begin{array}{l} \Gamma_7 \\ \Gamma_8 \\ \Gamma_8 \\ \Gamma_6 \end{array} \right\} {}^4T_{1g}, {}^4P$
			2.42	
			2.42	
500	2.48		2.48	
465	2.67		2.67	$\left. \begin{array}{l} \Gamma_8 \\ \Gamma_6 \end{array} \right\} {}^2T_{1g}, {}^2H$
			2.68	

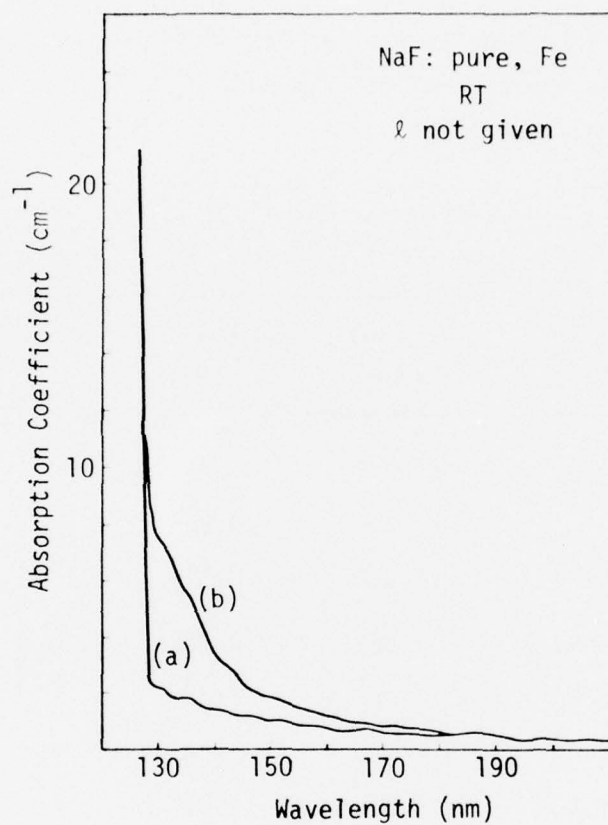


Fig. 2.48. Absorption spectra of NaF single crystals with Fe ion impurity. (a) Zone refined; (b) 10 $\mu\text{M}/\text{M}$ Fe added to the melt. [R. Voszka, K. Raksányi, and I. Földvári, *Kristall und Technik* 8, 1347 (1973).]

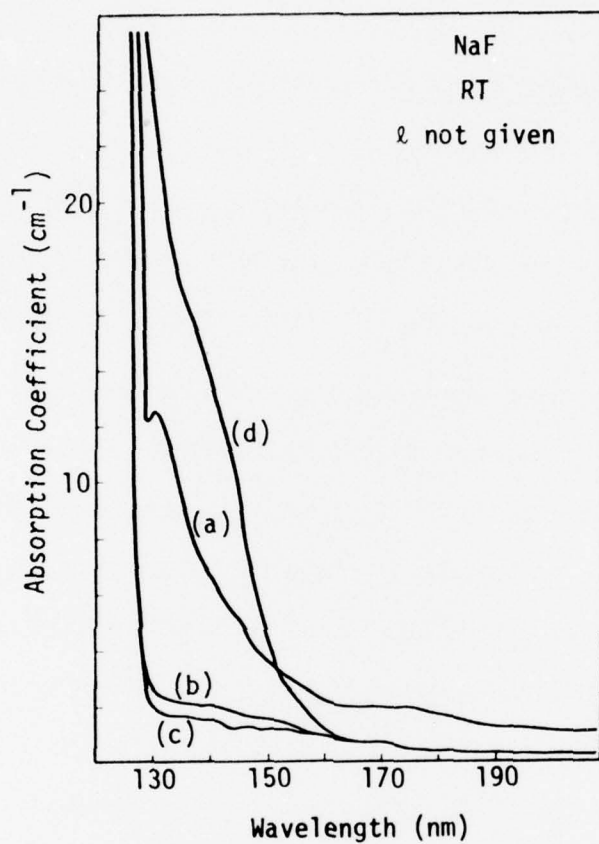


Fig. 2.49. Absorption spectra of NaF single crystals. (a) Grown from a.g. REANAL material; (b) after chemical purification; (c) grown from Merck suprapure material; and (d) Harshaw single crystal measured by SANO. [R. Voszka, K. Raksányi, and I. Földvári, *Kristall und Technik* 8, 1347 (1973).]

Sec. II-D NaF

believed to be due to the presence of transition-metal impurities (especially Fe) in the crystal.

4. Additive and electrolytic coloration of NaF. The color centers produced by additive or electrolytic coloration of NaF are strongly influenced by the background-impurity content, particularly hydroxyl, of the sample.^{2.45} Well defined F and M bands can be produced by additive or electrolytic coloration only if the NaF sample is of high purity.

The optical absorption spectrum of an additively colored crystal of commercial-purity NaF is shown in Fig. 2.50, curve A. In this crystal, precipitated particles up to 30 nm in diameter were observed after additive coloration, and the Mie scattering at these particles gave rise to the absorption seen in the region from 505 to 570 nm (2.46 to 2.18 eV). When the additively colored sample is annealed at 960 C for one hour in argon and cooled rapidly to room temperature, its spectrum changes as shown in curve B of Fig. 2.50. Curve C in Fig. 2.50 shows the well defined F and M bands produced by electrolytic coloration of high-purity NaF grown at the Naval Research Laboratory.

The maximum F-center concentration of $4 \times 10^{17} \text{ cm}^{-3}$ has been achieved by additive coloration of NaF.^{2.45} This value is approximately an order of magnitude less than that which can be achieved by radiative coloration.

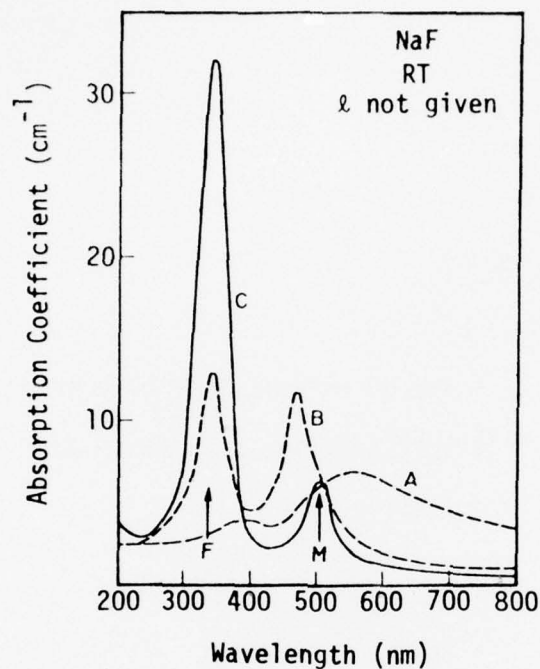


Fig. 2.50. Absorption spectra of several additively colored NaF crystals. The absorption band peaking at 340 nm is due to F centers; that at 505 nm is due to M centers; and those at 470 and 570 nm are due to small and large colloidal particles, respectively. A: Commercially available NaF, cooled in coloring bomb in 5 min. B: Same crystal, after removal from bomb, heated in argon to 960 C and quenched to room temperature. C: NRL-grown crystal, treated as B above. [W. C. Collins, I. Schneider, P. H. Klein, and L. R. Johnson, *Appl. Phys. Lett.* 24, 403 (1974).]

E. Potassium Chloride

The absorption peaks of impurities in KCl are summarized in Fig. 2.51.

1. Intrinsic exciton. The first exciton peak^{2.46} of KCl is at 7.7 eV (161 nm) at room temperature, Fig. 2.3.

2. U, U₁, U₂, α, OH⁻ and O⁻ bands in KCl. The spectral positions and half-widths of U, OH⁻, U₁, U₂, α and O⁻ bands in KCl, KBr and NaCl are listed in Table 2.23.^{2.47} The corresponding absorption spectra of the hydride- and hydroxide-doped crystals of these alkali halides are shown in Fig. 2.52 and Fig. 2.53, respectively.^{2.47}

3. H and H⁻ in KCl. The spectra of KCl:KH crystals are shown in Fig. 2.52. Fig. 2.52a shows the absorption band of substitutional H⁻ ions (U centers) at 300 K and at 20 K; the peak position of this band is seen to shift from 5.78 to 5.88 eV (215 to 211 nm) upon cooling. The two absorption bands shown in Fig. 2.52b were measured at 20 K subsequent to UV irradiation at the same temperature. The solid curve represents the spectrum after an exposure of 25 minutes with hydrogen lamp and the dashed curve for an additional 15-minute irradiation with a mercury lamp HB0200 and Schott filter UG1. The solid curve demonstrates the conversion of U centers at 5.88 eV (211 nm) to the following four centers: (a) U₁ centers (hydrogen ions at interstitial sites) with absorption in the range 4.0 - 4.6 eV (310 - 270 nm); (b) α centers (anion vacancies), which absorb near 6.96 eV (178 nm); (c) U₂ centers (hydrogen atoms at interstitial sites) with absorption near 5.27 eV (235 nm); and (d) F centers, which absorb near 2.3 eV (540 nm) in KCl.

These observations can be summarized by the following photochemical reactions:

EXPLANATORY NOTES FOR FIG. 2.51

Column 1: Lists properties of pure, doped, and irradiated materials. For doped or irradiated materials the properties appear in the following order:

1. impurity or dopant (O_2^- or LiO_2)
2. radiation (electrons, neutrons, etc.)
3. color centers or color bands (V_K , F, or α , β , etc.)
4. additional information (sample color, photochromic, etc.)

Column 2: Sample temperature.

Column 3: Peak positions ($|$), widths (H), and oscillator strengths (numbers) of impurity spectra. Ellipses indicate absorption structure above the absorption edge. Some lines are labeled by their color center or impurity.

Column 4: References: T2.1 stands for Table 2.1, F2.23 stands for Fig. 2.23, and II-C ¶ 6f indicates a paragraph in the text.

KCl	Temp.	Photon Energy (eV)							Ref.
		2	4	6	8	10	12	14	
Exciton peaks	RT								F2.3
Br ⁻	77K								F2.76
I ⁻	RT								F2.77 T2.27
α band	78K								T2.25
O ₂ ⁻	78K								T2.24
H ⁻ + OH ⁻	20K								F2.52 F2.54 T2.23
F	78K								F2.61
OH ⁻ UV irradiation	RT								F2.53

Fig. 2.51. Summary of the peak positions (|), widths (—), and oscillator strengths (numbers) of the impurity spectra for KCl. (See preceding page for key.)

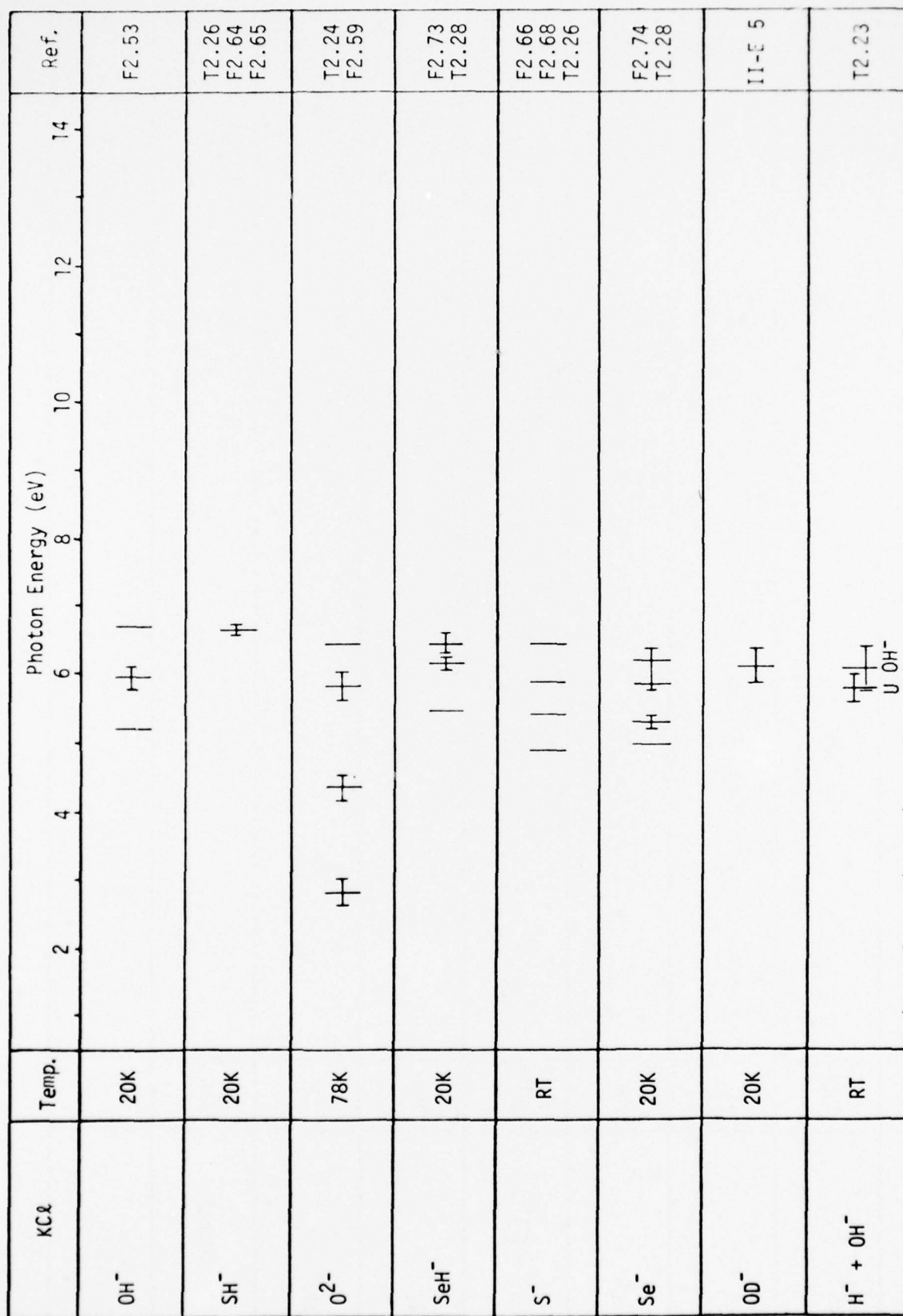


Fig. 2.51 (Continued)

KCl	Temp.	Photon Energy (eV)				Ref.
S ²⁻	78K		4	5	14	F2.71
S ²⁻	78K		3	4		T2.26 F2.69
K ₂ Se	20K		4	4		F2.75 T2.28
O ²⁻ + □	78K		3			T2.24
V _i	78K		3			F2.72
Se ²⁻	20K		3	3		F2.75 T2.28
F aggregates	78K		3			F2.70

Fig. 2.51 (Continued)

Table 2.23. Spectral positions and bandwidths [eV] of absorption bands in hydride- and hydroxide-doped NaCl, KCl and KBr crystals. [F. Kerkhoff, W. Martienssen, and W. Sander, Z. Physik 173, 184 (1963).]

Bands		KCl	KBr	NaCl
U Band				
Position	20 K	5.88	5.52	6.57
	300 K	5.78	5.44	6.50
Width	20 K	0.26	0.28	0.46
	300 K	0.57	0.58	0.81
OH ⁻ Band				
Position	20 K	6.05	5.71	6.75
	300 K	6.05	5.71	6.78
Width	20 K	0.62	0.55	~0.83
	300 K	0.75	~0.65	~0.92
U ₁ Band				
Shoulders	20 K	4.0 - 4.6	3.8 - 4.6	5.0 - 5.6
U ₂ Band				
	20 K	5.27	4.55	5.64
α Band				
	20 K	6.96	6.12	7.17
O ⁻ Band				
	20 K	6.77	6.37	7.27

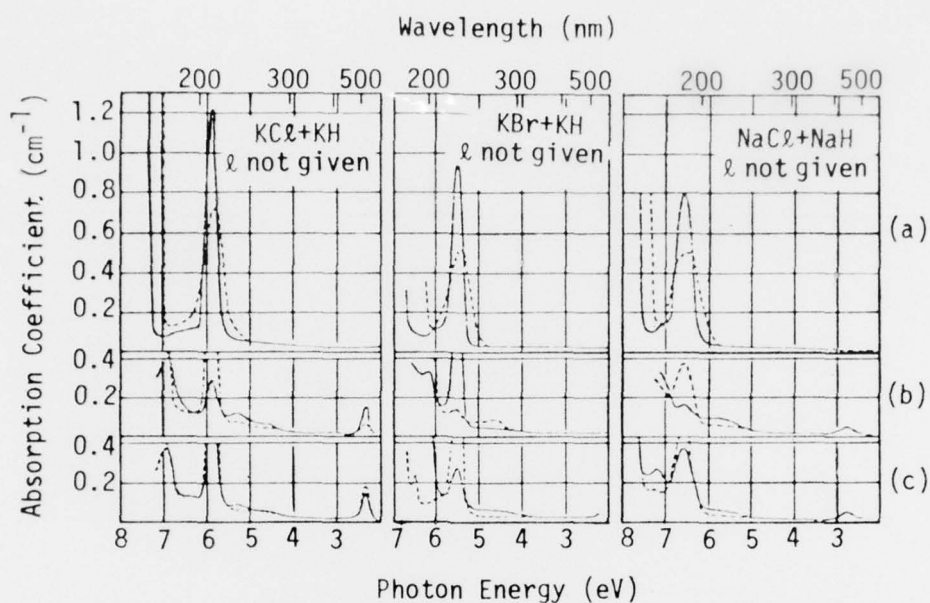


Fig. 2.52. Optical absorption of hydride-doped KCl, KBr, and NaCl, showing the effects of UV irradiation and thermal annealing. (a) starting condition, ---- measured at 300 K, — measured at 20 K. (b) UV irradiation at 20 K, measured at 20 K. KCl and NaCl: — after 25 min irradiation with hydrogen lamp, ---- additional 15 min irradiation with mercury lamp HBO200 with Schott filter UG1. KBr: — 3 min, ---- total of 25 min irradiation with the hydrogen lamp. (c) Change in spectra due to thermal annealing measured at 20 K. KCl: — additional irradiation with hydrogen lamp and annealing at 120 K, ---- annealed at 150 K. KBr: ---- annealed at 115 K, ---- annealed at 250 K. NaCl: — after irradiation with hydrogen lamp and annealed at 90 K, ---- annealed at 200 K. [F. Kerkhoff, W. Martienssen, and W. Sander, Z. Physik 173, 184 (1963).]

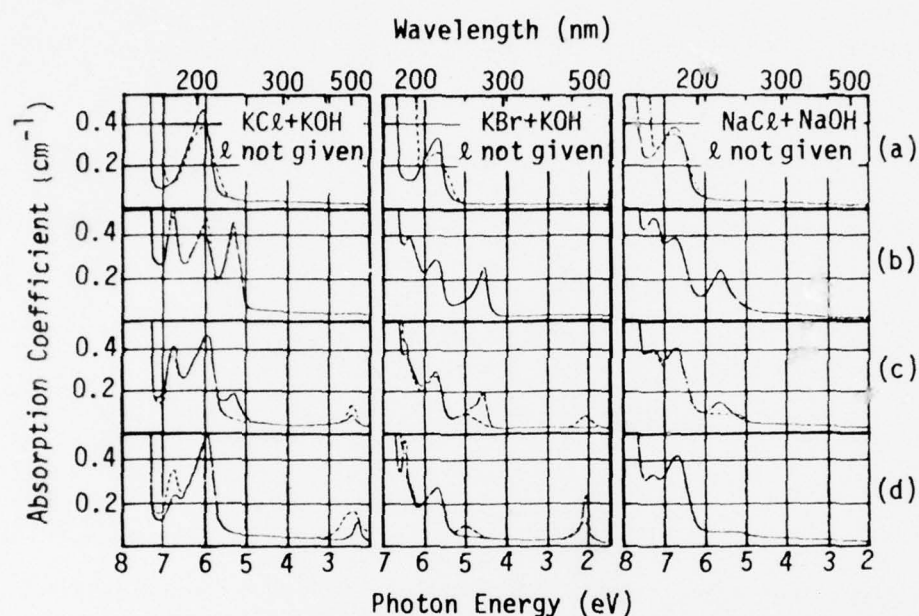
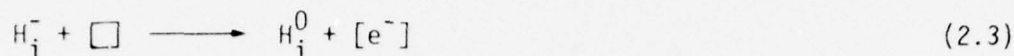
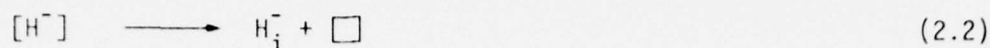
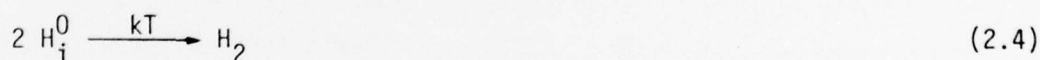


Fig. 2.53. Optical absorption of hydroxide-doped KCl , KBr , and NaCl , showing the effect of UV irradiation and thermal annealing. (a) Starting condition: ---- measured at 300 K, — measured at 20 K. (b) UV irradiation: KCl and KBr : — 15 min irradiation with hydrogen lamp, ---- additional 8 min irradiation with mercury lamp HB0200. NaCl : — 40 min irradiation with hydrogen lamp. (c) Thermal annealing measured at 20 K. KCl : — annealed at 120 K, ---- annealed at 160 K. KBr : — annealed at 110 K, ---- annealed at 130 K. NaCl : — annealed at 90 K, ---- annealed at 130 K. (d) Additional annealing measured at 20 K: ---- annealed at 200 K and — annealed at 300 K. [F. Kerkhoff, W. Martienssen, and W. Sander, *Z. Physik* **173**, 184 (1963).]



Here square brackets indicate that the species enclosed occupies normal lattice sites, \square designates an anion vacancy, and the subscript "i" refers to an interstitial site. The dashed curve in Fig. 2.52b demonstrates the recovery of the U band at the expense of U_1 , U_2 , F, and α bands, by irradiation with light on the long wavelength side of the U band. This is the reverse of the photochemical reactions (2.2) and (2.3).

The spectra in Fig. 2.52c, measured at 20 K, show the recovery of the U band by annealing at two different temperatures. The spectrum with the solid curve was taken after an additional hydrogen-lamp irradiation and three-minute annealing at 120 K, while the spectrum with the dashed curve was taken after further annealing at 160 K for three minutes. The spectra demonstrate the instability of H_i^- and H_i^0 against thermal annealing at 120 - 160 K. Presumably H_i^- converts to $[H^-]$ by the reverse of reaction (2.2) or to H_i^0 according to reaction (2.3). The $H_i^0 \longrightarrow [H^-]$ conversion during thermal annealing can be achieved through the following reactions:



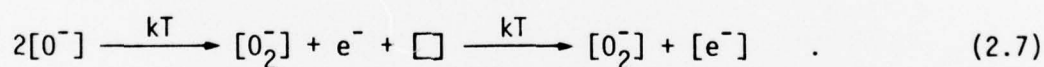
4. OH in KCl. The spectra of KCl:KOH crystals are shown in Fig. 2.53. Fig. 2.53a illustrates the shape of 6.05 eV (205 nm) OH^- band in KCl at 300 and 20 K. In Fig. 2.53b the solid curve represents the spectrum after UV

irradiation with a hydrogen lamp and the dashed curve corresponds to an additional eight-minute exposure to a mercury lamp HB0200. The solid curve shows the conversion of OH^- centers to U_2 centers and O^- centers, which respectively absorb near 5.27 eV (235 nm) and 6.77 eV (183 nm) according to the reaction:



Here, $h\nu (\text{OH}^-)$ indicates irradiation with a photon whose energy lies within the OH^- absorption band. The dashed curve in Fig. 2.53b indicates some recovery of the OH^- band. Apparently the radiation from the mercury lamp whose energy lies within the U_2 band drives the reaction (2.6) in the reverse direction.

Figures 2.53c and 2.53d demonstrate the conversion of U_2 and O^- bands to the U band at 5.88 eV (211 nm) and the F band at ~ 2.5 eV (~ 500 nm) by thermal annealing according to (2.4), (2.5), and the reaction:



Here equation (2.7) generates the F center on the far right-hand side, while in the case of $\text{NaCl}:\text{NaOH}$ equation (2.7) reaches only the middle step, $[\text{O}_2^-] + e^- + \square$, where $e^- + \square$ combine with $\frac{1}{2}\text{H}_2$ according to (2.5) to form U centers instead of F centers. In other words, the formation of F centers in $\text{NaCl}:\text{NaOH}$ during thermal annealing is suppressed by the competitive formation of U centers. In $\text{KCl}:\text{KOH}$ both U and F centers are formed in comparable numbers. On the other hand, the formation of the F band by thermal annealing in $\text{KBr}:\text{KOH}$ is more efficient than that of the U band, e.g., the

solid curve in Fig. 2.53d. Thus, it appears that U center formation is more efficient than F center formation in crystals with small lattice constants. The interstitial H_2 molecules, which are formed according to (2.4) possibly find it energetically more favorable to form U centers in crystals with smaller lattice constants because of the release of elastic strain at the interstitial position. Furthermore, the H_2 molecules out-diffuse more slowly in crystals with smaller lattice constants and hence are more readily available to participate in the combination reaction given in equation (2.5).

The O_2^- band predicted by equation (2.7) seems to be missing or very weak at 5 eV (250 nm) in KCl:KOH as shown in Figs. 2.53c and 2.53d. The spectra in Figs. 2.53c and 2.53d were taken at 20 K after a three-minute annealing. In (c) the annealing temperatures for the solid and dashed curves are 120 K and 160 K, respectively, while in (d) the temperatures for the dashed and solid curves are 200 K and 300 K, respectively. Figs. 2.53c and 2.53d demonstrate that the conversion of U_2 and O_2^- bands to U and F bands increases with the annealing temperature.

The U_2 band in alkali chlorides containing SH^- may be produced by UV irradiation through the reaction:

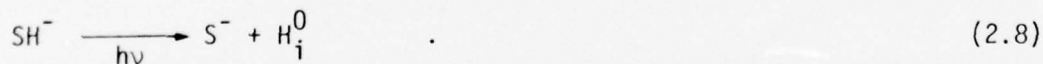


Figure 2.54^{2.48} illustrates the U_2 band in NaCl, KCl and RbCl at 20 K.

5. OD^- and OH^- in KCl. Fischer^{2.49} has measured the OD^- and OH^- bands in KCl crystals from 20 K to 600 K. At 20 K the OD^- band is at 6.10 eV (203 nm) with a half-width of 0.55 eV, while the OH^- band is at 6.05 eV (205 nm) with a half-width of 0.64 eV. Figures 2.55 and 2.56 show the

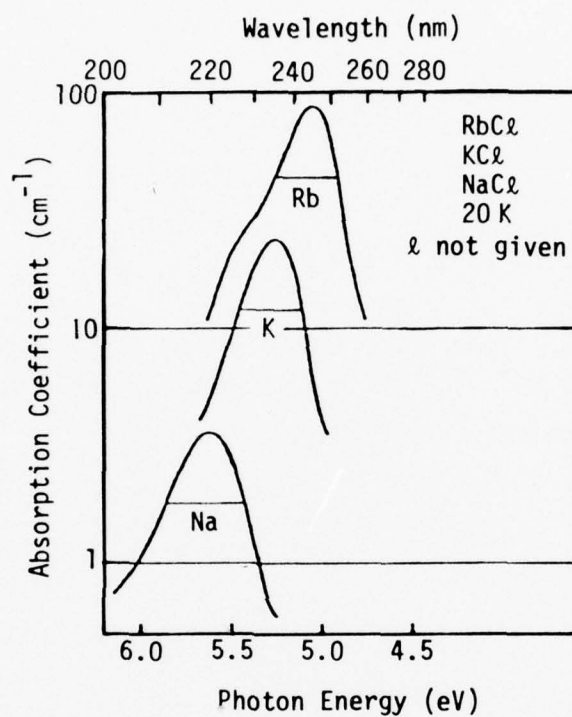


Fig. 2.54. U_2 -band absorption in NaCl , KCl , and RbCl . The curves have been shifted vertically with respect to each other. [F. Fischer, *Z. Physik* **204**, 351 (1967).]

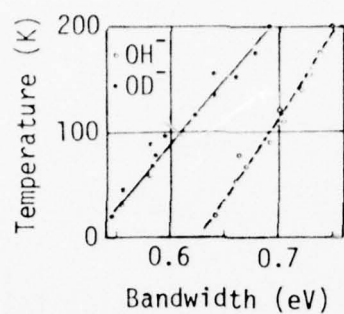


Fig. 2.55. Temperature dependence of the bandwidth at half maximum of OH^- and OD^- bands in KCl. [F. Fischer, Solid State Commun. 2, 51 (1964).]

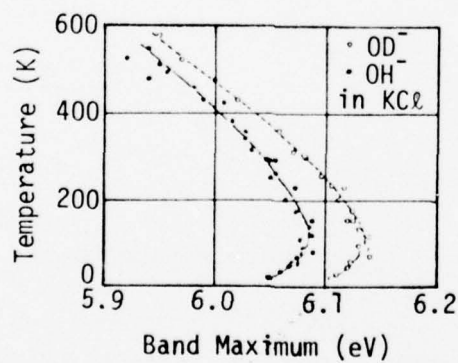


Fig. 2.56. Temperature dependence of the maximum of OH^- and OD^- bands in KCl. [F. Fischer, Solid State Commun. 2, 51 (1964).]

temperature dependence of the bandwidths and spectral positions of the OH^- and OD^- absorptions in KCl. There is an abnormality in the temperature shift of the band maxima, i.e., a blue shift instead of a red shift with increasing temperature, at temperatures below 100 K as shown in Fig. 2.56. This blue shift at low temperatures may be interpreted as the simultaneous excitation of the molecular vibrations of OH^- or OD^- along with the electronic transition.^{2.49}

6. O_2^- , O^- and O^{2-} in KCl. The O_2^- absorption in KCl at 5 eV (250 nm) is shown in Fig. 2.57 at 300 K.^{2.50} Fischer, Gründig, and Hilsch^{2.51} have systematically studied the O_2^- , O^{2-} , and O^- absorption bands in KCl, with high concentrations of O_2^- obtained in the starting crystals of $\text{KCl}:\text{K}_2\text{O}$ by strictly excluding spurious amounts of water, which would react to form OH^- . O^{2-} centers and anion vacancies were formed by reduction with F centers, i.e., by introducing an excess of potassium at 600 C followed by quenching to 20 C. The crystal becomes yellow through the reactions:



Both O_2^- and O^{2-} centers have several bands in the ultraviolet region. Fischer and coworkers interpreted the O^{2-} bands as electron transfer from the O^{2-} ion to the various excited states of the surrounding potassium ions. The highest-energy band at 7.1 eV (175 nm) at 78 K is the α band, which is expected to accompany the O^{2-} bands as indicated by the right-hand side of equation (2.9).

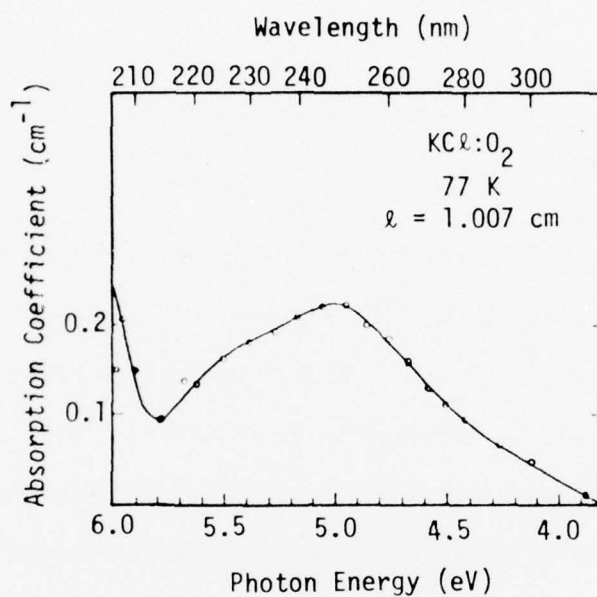


Fig. 2.57. Absorption spectrum of KCl grown in oxygen.
[J. Rolfe, F. R. Lipsett, and W. J. King, Phys. Rev.
123, 447 (1961).]

The O_2^- band is produced by irradiating the O^{2-} band with a high-pressure mercury lamp at 20 C through the photochemical reaction:



with the formation of F centers as by-products.

The O_2^- absorption of KCl:K₂O is shown in Fig. 2.58 by the solid and dashed curves at 78 K and 20 C, respectively. The absorption bands are at 7 eV (180 nm), 6.41 eV (193 nm), and 5.09 eV (244 nm) at liquid nitrogen temperature and are summarized in Table 2.24 along with other relevant centers in KCl.^{2.51}

The O^{2-} absorptions^{2.51} at a concentration of $7.5 \times 10^{17} \text{ cm}^{-3}$ in KCl are shown by the solid and dashed curves at 78 K and 20 C, respectively, in Fig. 2.59. There are four bands at 78 K at: $\sim 6.4 \text{ eV}$ ($\sim 195 \text{ nm}$), 5.77 eV (215 nm), 4.34 eV (286 nm), and 2.82 eV (440 nm). The parameters of O^{2-} bands are also summarized in Table 2.24.

7. Correlation of O^{2-} bands with the F and L bands in KCl. Fischer and coworkers^{2.51} drew an analogy between the four O^{2-} bands and the F and L bands of F centers in KCl. They applied the Klick-Kabler^{2.52} F-center charge-transfer model to O^{2-} centers. The F and L bands are interpreted as the transfer of an F-center electron to the surrounding K^+ ions. After transfer, the electron behaves as that on a neutral potassium atom; thus its electronic levels may be approximated by those of a free potassium atom. The F-center electron can be excited either to the ground state or to the excited states of the potassium atom. The F band at $\sim 2.3 \text{ eV}$ ($\sim 540 \text{ nm}$) corresponds to the transition to the ground state of the potassium atom,

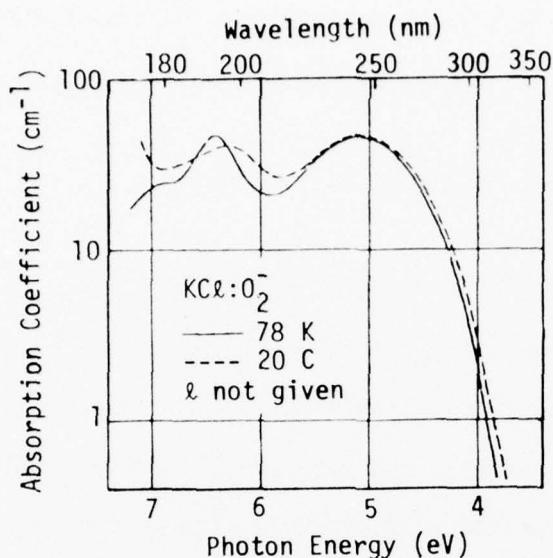


Fig. 2.58. Absorption spectra of KCl containing $3.1 \times 10^{18} \text{ cm}^{-3}$ O_2^- centers. [F. Fischer, H. Gründig, and R. Hilsch, Z. Physik 189, 79 (1966).]

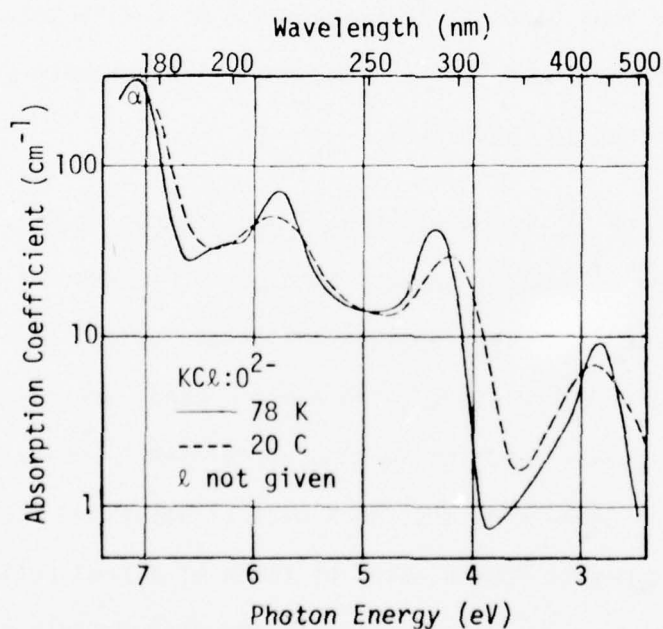


Fig. 2.59. Absorption spectra of KCl containing $7.5 \times 10^{17} \text{ cm}^{-3}$ O_2^- centers. [F. Fischer, H. Gründig, and R. Hilsch, Z. Physik 189, 79 (1966).]

Table 2.24. Spectral positions and bandwidth [eV] of oxygen bands in KCl at 78 K.
[F. Fischer, H. Gründig, and R. Hilsch, Z. Physik 189, 79 (1966).]

Centers	O_2^-		O^{2-}			α	O^-	Complex O^{2-} \square	OH^-
	Position [eV] [nm]								
Position [eV] [nm]	5.09 243	6.41 193	7.0 177	2.82 439	4.34 285	5.77 215	~6.4 194	6.7 185	6.08 204
	1.2	0.56		0.38	0.39	0.50			0.67
Width [eV]									

while the L bands at higher energies are interpreted as the electronic transfer to the excited states of the potassium atom. The spectral positions of the various L bands are approximately equal to those of the F band at ~ 2.3 eV (~ 540 nm) added to the various energy levels of the free potassium atom as illustrated by the circles in Fig. 2.60. The abscissa in Fig. 2.60 represents the photon energies of the F and L bands or that of the O^{2-} bands in KCl, while the ordinate is the energy level of the free potassium atom. Figure 2.60 also shows the correlation between the spectral positions of various O^{2-} bands in KCl and the energy levels of the potassium atom indicated by the crosses, suggesting that the O^{2-} bands are also due to the charge transfer from the O^{2-} ion to the surrounding cation sublattice.

Figure 2.60 indicates that the O^{2-} bands occur at energies higher than those of the corresponding F and L bands. The second electron on O^{2-} is more tightly bound to the O^{2-} than the F electron is to the F center. This might be expected since the excess charge on the O^{2-} in the monovalent lattice of alkali halides tends to polarize the lattice in the immediate neighborhood, causing self-stabilization. A free O^{2-} ion is not stable because it lacks the positive polarization cloud.^{2.51} The high-energy O^{2-} band, which should correspond to the L_4 band of the F-center series, may occur in the intrinsic region of KCl, as suggested by the extended dashed line on the O^{2-} -center series in Fig. 2.60.

Although there is a close correlation of spectral positions of the F-center and the O^{2-} -center series, as indicated in Fig. 2.60, the oscillator strengths of their corresponding transitions are quite different. For example, the high-energy O^{2-} bands are stronger than the low-energy O^{2-} band at 2.82 eV (440 nm), while the L absorption is only ~ 4 percent as

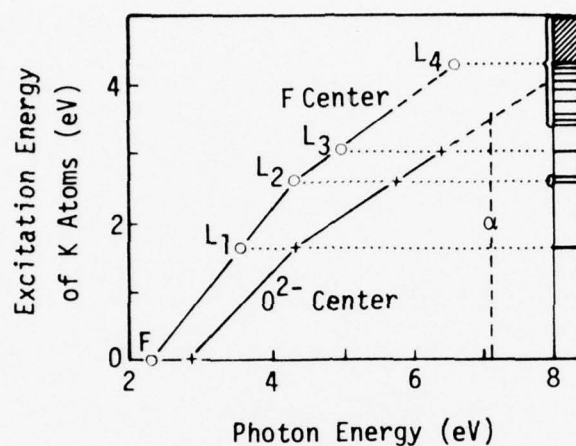


Fig. 2.60. Composition of various O^{2-} bands and the color-center bands in KCl. Both the O^{2-} bands and color-center bands in KCl are simply correlated with the various excited states of potassium atom. The ordinate represents the energy levels of the potassium atom. The abscissa represents position of F, L_1 , L_2 , L_3 , L_4 color-center bands with circles and the O^{2-} bands with crosses. [F. Fischer, H. Gründig, and R. Hilsch, Z. Physik. 189, 79 (1966).]

strong as the F band. This difference is presumably due to the symmetry of the ground states, since the F electron has essentially s-character while the O^{2-} electron has essentially p-character.^{2.51}

In order to construct the spectral correlation between the F and L bands and the energy levels of the free potassium atom as shown in Fig. 2.60, Fischer and coworkers^{2.51} needed to measure the formerly obscure L_4 band in KCl directly. The spectrum of the high-energy L bands of the zone-refined KCl:F-center at 78 K is shown in Fig. 2.61.

8. Photochemical production of O^- centers from O^{2-} centers. Blue KCl crystals containing O^- can be produced by the photochemical reaction in equation (2.10) by irradiating the O^{2-} centers in yellow KCl crystals with a mercury lamp.^{2.51} Figure 2.62 shows the corresponding changes in the respective spectra measured at 78 K. The O^{2-} spectrum shown in curve b was produced by reducing the O_2^- centers of curve a with F centers. The O^- spectrum is shown as the dashed curve c, which is obtained by UV irradiation of the O^{2-} centers at 20 C. Curve c shows the O^- band at 6.7 eV (185 nm) which agrees with the band found by Kerkhoff^{2.53} after UV irradiation of KCl:OH⁻ crystals. Curve c also shows the production of the F band at 2.3 eV (540 nm) superimposed on an absorption background from F aggregates which are the photochemical by-products of equation (2.10). A comparison of curves b and c in Fig. 2.62 indicates that the O^{2-} absorption bands at 4.34 eV (286 nm) and 5.77 eV (215 nm), and the α band at 7.1 eV (175 nm), are reduced by the same factor of ~ 40 percent of their original strength. This supports the model that: (i) the bands at 4.34 eV (286 nm) and 5.77 eV (215 nm) belong to the same center, O^{2-} , and (ii) the α center and the O^{2-} center are co-reactants in equation (2.10).

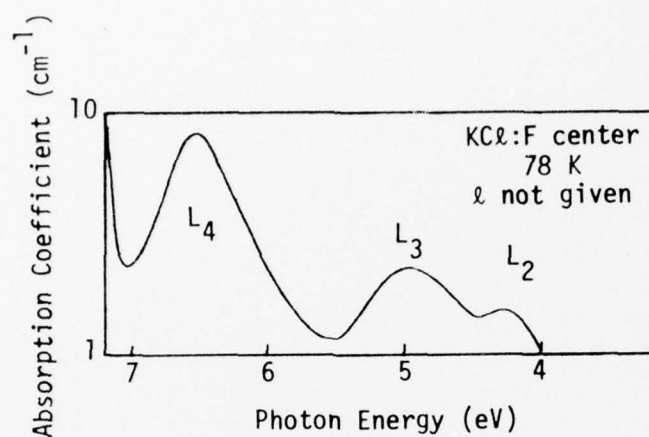


Fig. 2.61. Absorption spectrum of zone-refined KCl, showing color-center bands L_2 , L_3 , and L_4 . The absorption constant is plotted on a logarithmic scale. [F. Fischer, H. Gründig, and R. Hilsch, Z. Physik 189, 79 (1966).]

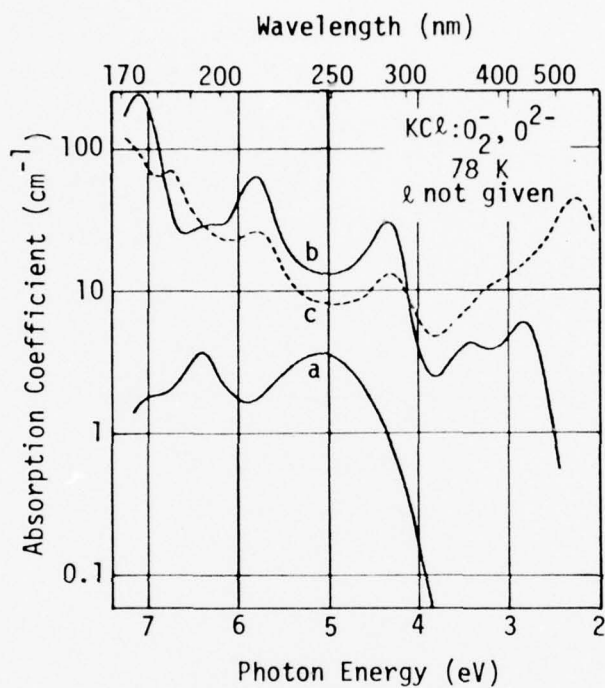


Fig. 2.62. Absorption spectra of KCl containing O_2^- and O^{2-} centers. (a) O_2^- centers at concentration $2.6 \times 10^{17} \text{ cm}^{-3}$. (b) After reduction with F centers. (c) After irradiation with ultraviolet light at 20 C. [F. Fischer, H. Gründig, and R. Hilsch, Z. Physik 189, 79 (1966).]

Curve b in Fig. 2.62 may be recovered from curve c by heating the photochemically transformed crystal briefly at 500 C, then quenching to 20 C. This photochemical reaction (curve b \rightarrow c) and the thermal annealing process (curve c \rightarrow b) can be repeated. However, prolonged annealing in air will introduce moisture, which diffuses into the crystal, combines with the O^- to form OH^- , and destroys the photochromic sensitivity by terminating the $O^{2-} \leftrightarrow O^-$ conversion process. Crystals containing O^{2-} are photochromically active only in the restricted temperature range from 220 K to 80 C. Below 220 K the quantum yield diminishes because the excited O^{2-} centers need thermal collisions to carry away their excited second electrons. At temperatures above 80 C, the crystal loses its $O^{2-} \leftrightarrow O^-$ conversion efficiency due to the formation of O^{2-} -anion vacancy complexes and the precipitation of K_2O , especially at high doping levels.

9. Annealing KCl crystals containing O^{2-} . The solubility of K_2O in KCl is high only at temperatures above 400 C. At lower temperatures, in order to retain high K_2O concentrations dissolved in KCl, quenching from temperatures above 400 C is required. However, prolonged storage of these KCl: K_2O crystals at room temperature causes precipitation of K_2O and loss of the crystal's yellow color. The photochromic capability of such "deteriorated" crystals may be restored by annealing above 400 C.

Precipitation of K_2O in KCl manifests itself by striking changes in the absorption spectra. For example, curve a in Fig. 2.63 is the spectrum of a quenched KCl crystal containing O^{2-} centers, and curve b is the spectrum after annealing at 300 C. The spectrum in curve b resembles the exciton structure in the spectra of pure K_2O thin films found by Rauch.^{2.54} The 4.21 eV (295 nm) peak indicates that the K_2O has already crystallized;

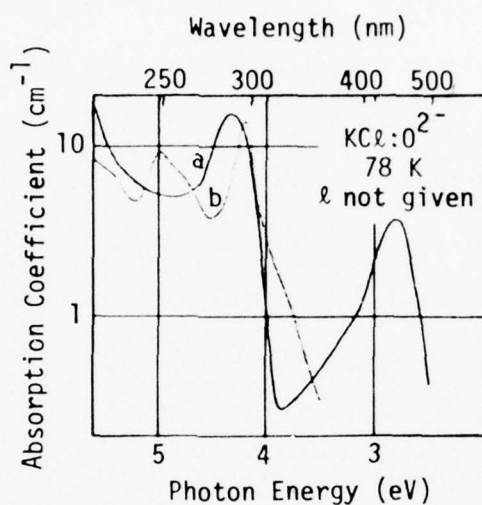
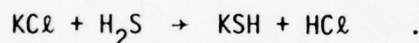


Fig. 2.63. Absorption spectra of KCl containing O^{2-} centers. (a) After being quenched from 600 C to 20 C. (b) After thermal annealing at 300 C. [F. Fischer, H. Gründig, and R. Hilsch, Z. Physik 189, 79 (1966).]

thus, the long-wavelength tail is presumably due to the effects of lattice distortion and crystallite size. Similar long-wavelength tails on exciton bands have been observed in highly distorted KI films.^{2.55} During the early stages of the K_2O precipitation, migration of O^{2-} centers and anion vacancies (driven by their mutual electrostatic attraction) and the formation of O^{2-} -anion vacancy complexes are expected. Presumably the 3.5 eV (350 nm) band in Fig. 2.62 is due to this complex. Its parameters are included in Table 2.24.

10. SH^- , S^- and S^{2-} in KCl. Fischer and Gründig^{2.56} have systematically studied the SH^- -related centers in KCl crystals grown under a nitrogen atmosphere containing H_2S . The H_2S reacts with the molten KCl to form KSH according to the reaction:



The SH^- absorption in KCl at 6.68 eV (186 nm) is shown in Figs. 2.64 and 2.65.

11. Photochemical conversion of SH^- to S^- . The SH^- band at 6.68 eV (186 nm) can be photochemically decomposed by UV irradiation from an aluminum arc with emission lines at 186, 193 and 199 nm (6.67, 6.42 and 6.23 eV). The reaction products are a U_2 band at 5.28 eV (235 nm) and a new band at 6.42 eV (193 nm). This new band can be assigned to S^- centers^{2.56} since it is similar to the O^- band obtained from the photochemical decomposition of OH^- centers according to (2.8).^{2.53} Figure 2.66 shows the photochemical decomposition of SH^- bands. The dashed curve represents the starting KCl with an SH^- band at 6.68 eV (186 nm), while the solid curve shows the

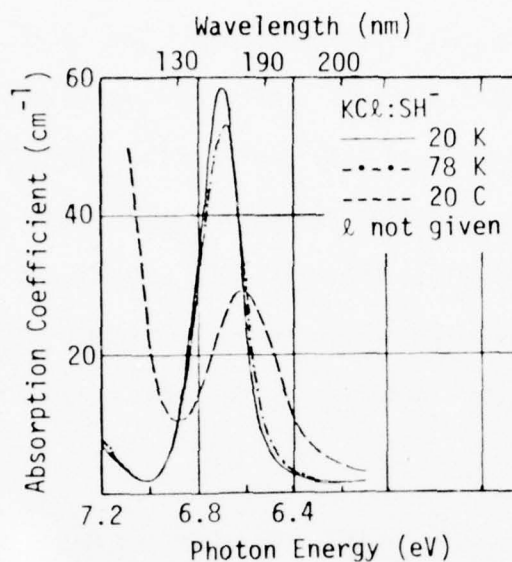


Fig. 2.64. Ultraviolet absorption of KCl:SH^- grown under 3 torr of H_2S partial pressure. [F. Fischer and H. Gründig, Z. Physik 184, 299 (1965).]

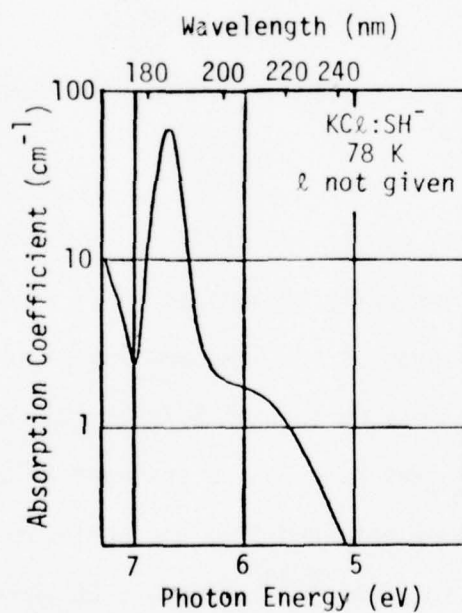


Fig. 2.65. Ultraviolet absorption of KCl:SH^- . [F. Fischer and H. Gründig, Z. Physik 184, 299 (1965).]

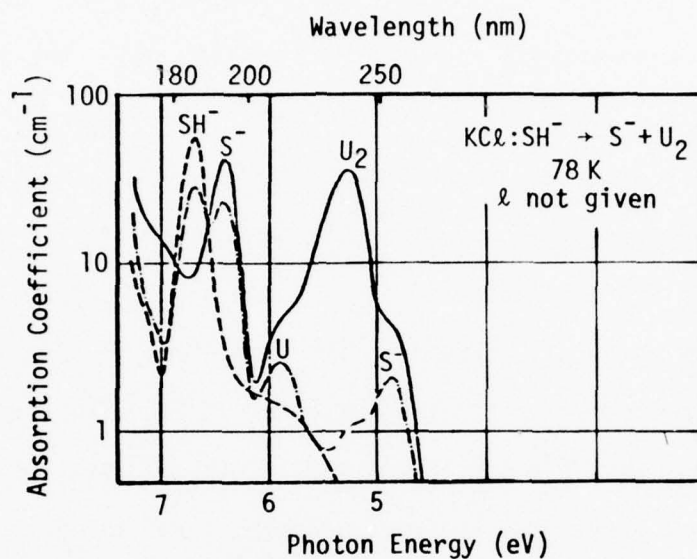


Fig. 2.66. Photochemical decomposition of SH^- : ----- original SH^- absorption; ——— SH^- centers decomposed to S^- and U_2 centers after irradiation with an aluminum arc lamp; -·-·-·- brief warming to 150 K mobilizes some U_2 centers to reform SH^- . [F. Fischer and H. Gründig, Z. Physik 184, 299 (1965).]

production of the U_2 band at 5.28 eV (235 nm) and the S^- band at 6.42 eV (193 nm) after UV irradiation at 78 K. The solid curve also shows a weak U band at 5.88 eV (211 nm) and an additional new band at 4.87 eV (255 nm) which always accompanies the S^- band at 6.42 eV (193 nm). The dot-dashed curve is the spectrum after the UV-irradiated crystal has been briefly warmed to 150 K, showing the disappearance of the U_2 band and the concomitant blue thermoluminescence. Since the U_2 centers are mobile above 110 K, some of the U_2 centers may recombine with S^- centers to reform SH^- . The remaining U_2 centers obviously recombine with themselves to form H_2 molecules. By repeating the procedure of UV irradiation at 78 K and subsequent annealing at 150 K, it is possible to convert most of the SH^- centers to S^- . For example, 75 percent conversion has been achieved after three cycles. The three curves in Fig. 2.66 cross at 6.57 eV (189 nm), which is called an isosbestic point. Other curves corresponding to the intermediate states of UV irradiation or annealing also form such points, but are not shown in Fig. 2.66 for clarity.

By UV irradiation between 120 K and 150 K, a complete SH^- to S^- conversion may be achieved with no interference from U and U_2 centers. Figure 2.67 shows the absorption spectrum of a $KCl:SH^-$ crystal after irradiation at 150 K by an aluminum arc. Accompanying the large S^- band at 6.42 eV (193 nm), is a band at 4.87 eV (255 nm) that presumably belongs to the S^- center. Figure 2.68 presents the 78 K spectrum of Fig. 2.67 replotted to show the weak absorption structure between 4.87 eV (255 nm) and 6.42 eV (193 nm).

The SH^- ions are only partially decomposed by UV irradiation at 300 K. On warming to 430 K, the SH^- band regains its original strength because the

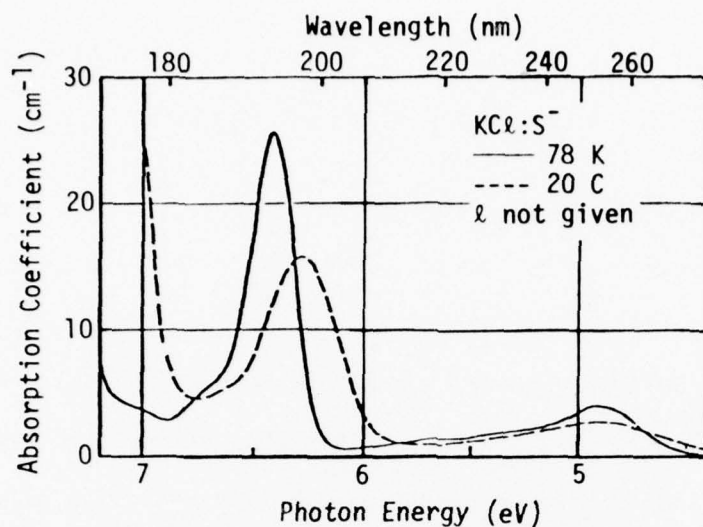


Fig. 2.67. Absorption of S^- centers in KCl at 78 K and 20 C. [F. Fischer and H. Gründig, Z. Physik 184, 299 (1965).]

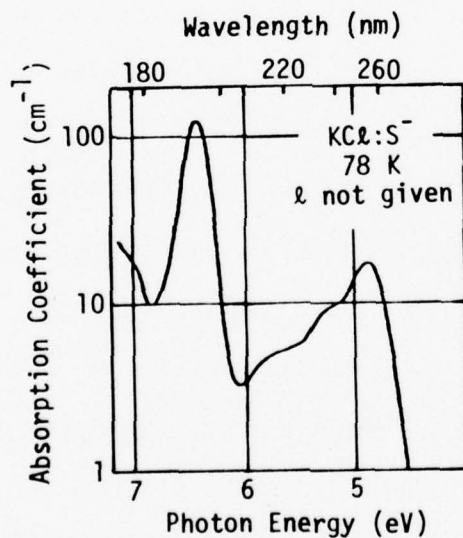
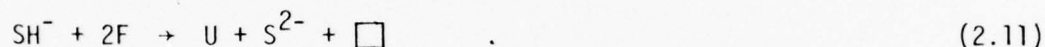


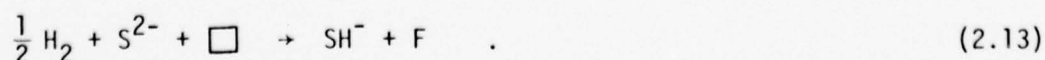
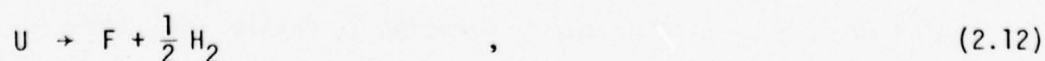
Fig. 2.68. Absorption spectrum of $KCl:S^-$ showing the weak absorption band between the strong S^- bands at 4.87 eV and 6.42 eV. [F. Fischer and H. Gründig, Z. Physik 184, 299 (1965).]

interstitial hydrogen atoms diffuse to the S^- ions and recombine to form SH^- . At 20 C the S^- will be converted to SH^- in 40 hours.

12. Reduction of SH^- with F centers to produce S^{2-} . KCl crystals containing SH^- turn yellow after reduction with F centers, which are formed by the introduction of excess potassium at 600 C. The absorption spectrum of KCl: SH^- crystals which have been reduced by F centers is shown in Fig. 2.69. A reproducible spectrum can be obtained only if the sample is quenched from 700 C just before cooling to 78 K. The reaction is similar to that of equation (2.9) for O_2^- :



The reaction products have a strong U band at 5.88 eV (211 nm), an α band at 7.1 eV (175 nm) due to anion vacancies, and an intense new band at 3.15 eV (394 nm). This new band accounts for the yellow color of the reduced crystals and is assigned to the S^{2-} ions. A neighboring band at 3.85 eV (322 nm), which becomes stronger in slowly quenched crystals, may be due to the absorption of S^{2-} -anion vacancy complexes, which are analogous to the O_2^- -anion vacancy complexes at 3.5 eV (350 nm) shown in Fig. 2.62. Toward the higher-energy region in Fig. 2.69 there are three maxima at ~ 4.7 eV (~ 265 nm), 5.0 eV (250 nm), and 5.3 eV (235 nm). The first maximum at 4.7 eV (265 nm) is probably attributable to the S^{2-} center. Finally, the weak SH^- peak at 6.7 eV (185 nm) is produced by the reverse reaction to (2.11). At 700 C the U center dissociates easily according to the reactions:



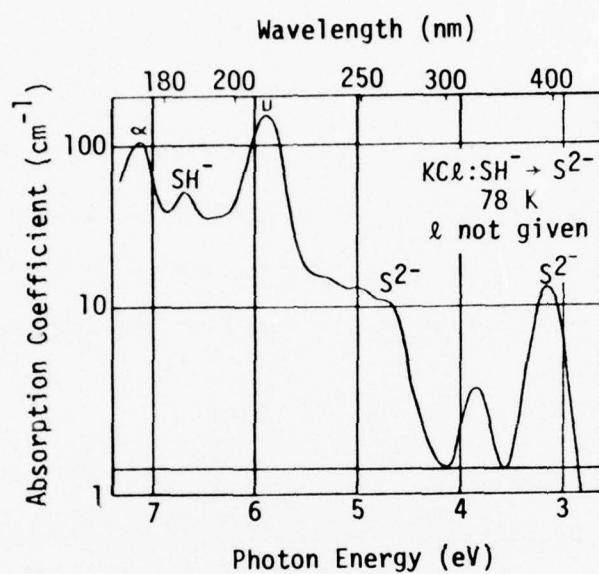


Fig. 2.69. Absorption spectrum of a SH^- -doped KCl crystal after reduction with F centers. [F. Fischer and H. Gründig, Z. Physik 184, 299 (1965).]

A single SH^- band is recovered if the reduced crystals are held at 700 C for a longer period in order to facilitate the out-diffusion of the F centers. This process is accelerated by an applied electric field.

The crystals, which have been reduced with F centers and quenched to room temperature, will produce an orange fluorescence upon UV excitation that grows stronger at lower temperatures. The fluorescence does not have spectral fine structure, unlike the fluorescence bands reported by Schulman and Kirk on powdered samples.^{2.57} The fluorescence observed here is presumably from the S^{2-} centers whose presence may be inferred from equation (2.11).

13. Photochemical bleaching of S^{2-} in KCl. According to equation (2.11), the SH^- in KCl crystals will turn to S^{2-} centers and anion vacancies after the reduction with excess potassium. The crystal now is photochromically sensitive. This process is similar to that for the O^{2-} centers in equation (2.10) where the crystal turned blue upon UV excitation. A high-pressure mercury lamp (Osram HB020) may be used for the excitation of S^{2-} . In order to avoid the excitation into the U band, a 1 cm thick KI plate can be used as a cutoff filter for photons with energies above ~ 5.4 eV (230 nm). No photochemical conversion of S^{2-} occurs at low temperatures; conversion begins near room temperature.

Figure 2.70 shows the change in spectra corresponding to $S^{2-} \rightarrow S^-$ conversion. The dashed curve shows the S^{2-} bands of a crystal which has been quenched after reduction by F centers. Aside from S^{2-} centers and anion vacancies, the crystal has U, F, and SH^- centers. The latter two centers were produced by thermal decomposition of U centers and recombination with S^{2-} centers following equations (2.12) and (2.13). The solid curve is the

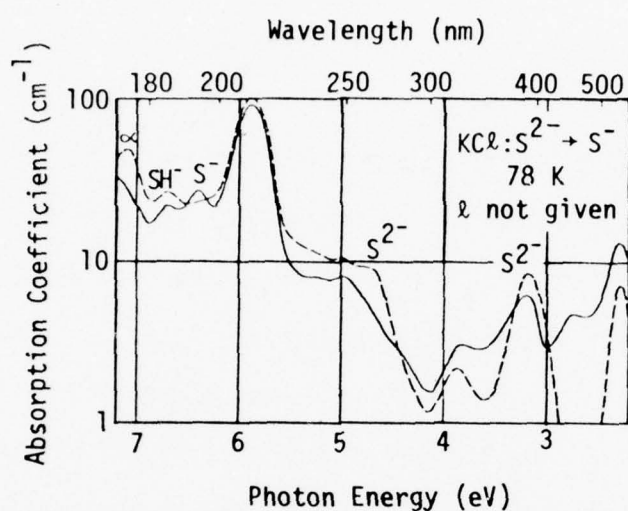


Fig. 2.70. Optical-absorption spectra showing the effect of photochemical conversion of S^{2-} to S^- . The dashed curve represents the spectrum of $KCl:SH^-$ after being reduced by F centers to produce the S^{2-} . The solid curve shows the conversion of the S^{2-} band at 3.15 eV and the α band at 7.1 eV to the S^- band at 6.42 eV. [F. Fischer and H. Gründig, *Z. Physik*, 184, 299 (1965).]

spectrum at 78 K after UV excitation at 20 C. It shows the reduction of both the S^{2-} band at 3.15 eV (394 nm) and the α band at 7.1 eV (175 nm) with the concomitant rise of the S^- band at 6.42 eV (193 nm). The F band grows and broadens from the formation of F-center aggregates, which are probably the origin of the band at 2.75 eV (451 nm). The plateau in the dashed curve near 5 eV (250 nm) does not decrease uniformly to the solid curve. Among the three overlapping structures in the plateau, only the lowest band at 4.7 eV (265 nm) decreases appreciably and has been assigned to the S^{2-} center. The photochemical bleaching of the S^{2-} centers can be achieved only by excitation in the plateau region around 5 eV (250 nm). A selective excitation in the S^{2-} band at 3.15 eV (394 nm) will not induce the photochemical reaction even at 70 C. Table 2.25 summarizes the spectral positions and bandwidths of the sulfur-related centers in KCl.

14. Annealing of S^{2-} centers in KCl. All the previous spectra of crystals containing S^{2-} have been measured immediately after quenching from 700 C. These crystals are yellow in appearance and produce an orange fluorescence upon UV excitation. If the quenched crystals were annealed between 100 C and 400 C, they will lose their yellow color and ability to fluoresce, as demonstrated in Fig. 2.71. The dashed curve is the spectrum at 78 K of a crystal quenched from 700 C to 20 C. The solid curve shows the exciton spectrum of precipitated K_2S after a fifteen-minute annealing at 400 C. If the crystal is reheated and quenched, the original spectrum will appear again with the recovery of the S^{2-} centers and anion vacancies as the K_2S dissolves again into the lattice. The crystals will attain intermediate states, i.e., a mixture of the two spectra in Fig. 2.71, if stepwise annealing of the crystals is carried out at increasingly higher temperatures.

Table 2.25. Spectral positions and bandwidths of SH^- -related centers in KCl at 78 K. [F. Fischer and H. Gründig, Z. Physik 184, 299 (1965).]

Center	SH^-	S^-	S^{2-}	α	U	U_2
Position [eV]	6.68	6.42	3.15	7.1	5.88	5.28
Width [eV]	0.21	0.23	0.31	—	0.35	0.39

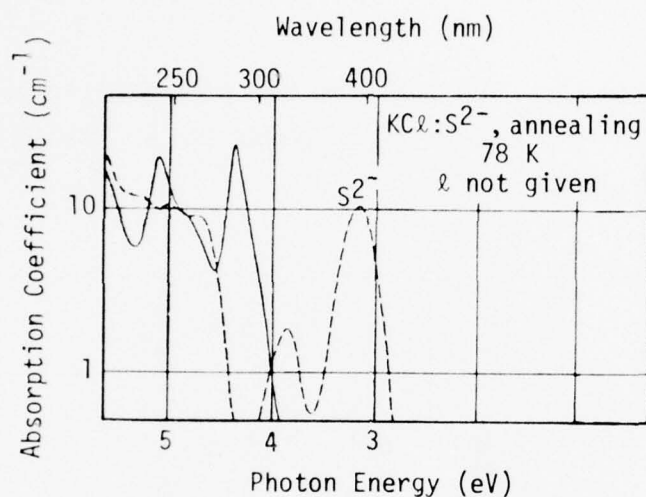


Fig. 2.71. Spectra showing the effect of annealing on S^{2-} centers in KCl crystals. The dashed curve represents the spectrum, measured at 78 K, of the crystal quenched from 700 C to 20 C. The solid curve shows the precipitation of K_2S with exciton peak at 4.4 eV after 15 min annealing at 400 C. [F. Fischer and H. Gründig, Z. Physik 184, 299 (1965).]

15. Comparison of SH^- and OH^- centers. The photochemical reactions of SH^- and OH^- centers are similar to each other. UV irradiation at 78 K will convert these two centers, via equations (2.8) and (2.6), respectively, to the U_2 band and a new band, which is the O^- band^{2.53} in the case of OH^- and the S^- band in the case of SH^- .

Sander^{2.58} has observed the electron-spin resonance of O^- centers. The electron-spin resonance of the homologous S^- , H_2S^- , and Se^- ions in KCl and KBr doped with KSH and KSeH, respectively, has been observed by Hausmann^{2.59} at 20 K. The signal appears only if the UV-irradiated crystals have been annealed at 110 K for a few seconds. The effect of annealing at 110 K is to mobilize the UV-released U_2 centers which in turn react with the sulfur complex $(\text{S}^-)_2$ formed at low temperatures, thus making the S^- or Se^- ions available for electron-spin resonance. The reactions are $(\text{S}^-)_2 + \text{H}^0 \rightarrow \text{S}^- + \text{SH}^-$ and $\text{SH}^- + \text{H}^0 \rightarrow \text{H}_2\text{S}^-$.^{2.59}

A distinction between SH^- centers and OH^- centers is that the former can be photochemically converted to the single S^- band free from the interference of SH^- and U_2 bands as shown in Figs. 2.67 and 2.68, while it is not possible to produce a single O^- band photochemically at, say 130 K, since the O^- centers are already mobile^{2.53} at 130 K. In addition, the S^- centers recombine very slowly with the molecular hydrogen to reform SH^- , which is not the case with the recombination of O^- with H_2 to form OH^- . The OH^- centers are not reduced by F centers to form O^{2-} , but the SH^- centers will be converted to S^{2-} centers since the binding of the hydrogen atom to the oxygen is stronger than the hydrogen atom to the sulfur.

16. Photochemical conversion of SH^- to S^- in KCl. Rolfe^{2.60} has investigated the photochemical conversion of SH^- to S^- in KCl and KBr.

Sec. II-E KCl

Figure 2.72 shows the absorption spectra of a KCl:KSH crystal at 78 K. The solid curve shows the initial state of the crystal with the SH^- band at 6.67 eV (186 nm). After 85 minutes of irradiation with an AH-4 mercury lamp at 78 K, the spectrum changes to the dashed curve which shows the decomposition products of SH^- , i.e., the "S" band at 6.39 eV (194 nm) and the U_2 band at 5.3 eV (235 nm). The dotted curve shows the partial recovery of the SH^- band with the concomitant generation of U and F bands after a 24-hour annealing at 300 K. Table 2.26 summarizes the data of Rolfe and includes the iodide band^{2.61} which is very similar to the hydrosulfide band.

17. SeH^- in KCl. The absorption spectra^{2.62} of SeH^- in KCl at 20 K, 78 K, and 20 C, are shown in Fig. 2.73. The doublet at 6.4 eV (195 nm) and 6.13 eV (202 nm) shifts toward lower energy and broadens as the temperature is increased above 20 K. The doublet splitting of 0.27 eV is attributed to the spin-orbit splitting of the outer electrons on the SeH^- radical. This double-band spectrum, and the SH^- spectrum of Fig. 2.65, are superimposed on a broad, weak background which increases with increasing temperature.

18. Photochemical conversion of SeH^- to Se^- . As with KCl:KSH crystals, the SeH^- centers can be converted to Se^- and U_2 centers by UV irradiation from an aluminum arc lamp at 20 K,



Figure 2.74 shows the spectra at 20 K before and after the photochemical conversion of the SeH^- to Se^- in KCl. The solid curve shows the original spectrum of the SeH^- ions. The dashed curve exhibits the well known U_2 band at 5.27 eV (235 nm) which confirms the decomposition of SeH^- into Se^-

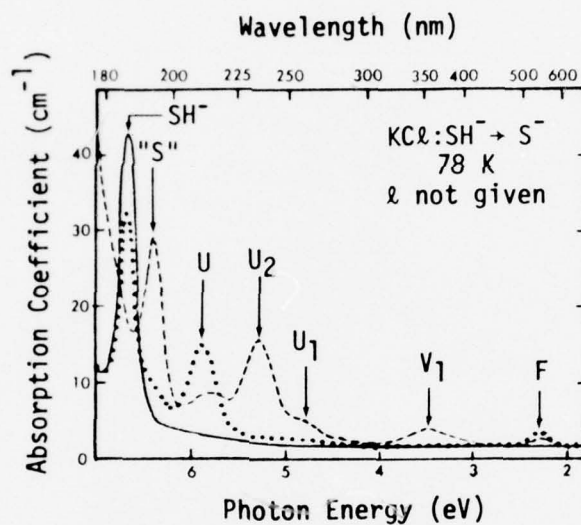


Fig. 2.72. Absorption spectra of KCl:KSH. Solid line, before irradiation; dashed line, after 85 min irradiation with AH-4 lamp at 78 K; dotted line, after warming to 300 K for 24 hr. [J. Rolfe, Appl. Phys. Lett. 6, 66 (1965).]

Sec. II-E KCl

Table 2.26. Absorption bands of SH^- , I^- , and S^- in KCl and KBr crystals. [J. Rolfe, Appl. Phys. Lett. 6, 66 (1965).]

		KCl		KBr	
		nm	eV	nm	eV
SH^- Band					
Peak position	300 K	188.4	6.58	a	a
	78 K	185.8	6.67	193.6	6.40
Half-width	300 K		0.33		a
	78 K		0.20		0.21
I^- Band					
Peak position	300 K	188.7	6.57	a	a
	78 K	184.7	6.71	193.8	6.40
Half-width	300 K		0.39		a
	78 K		0.27		0.20
S^- Band					
Peak position	300 K	198.2	6.26	205.5	6.03
	78 K	194.0	6.39	203.2	6.10
Half-width	300 K		~0.4		
	78 K		0.21		~0.3

^aObscured by fundamental absorption edge.

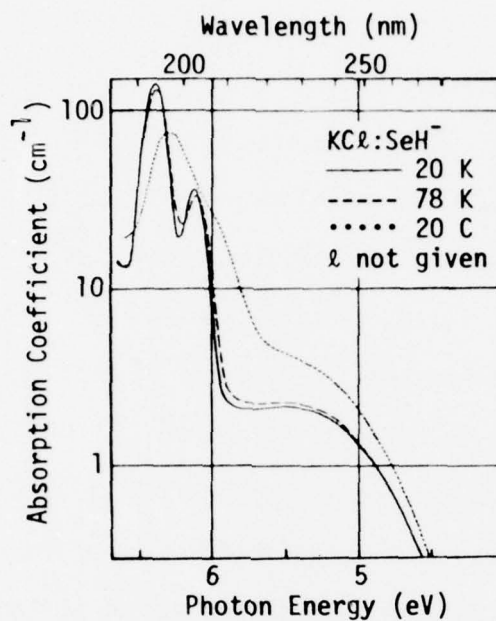


Fig. 2.73. Absorption spectra of SeH^- in a KCl crystal. [F. Fischer, *Z. Physik* 187, 262 (1965).]

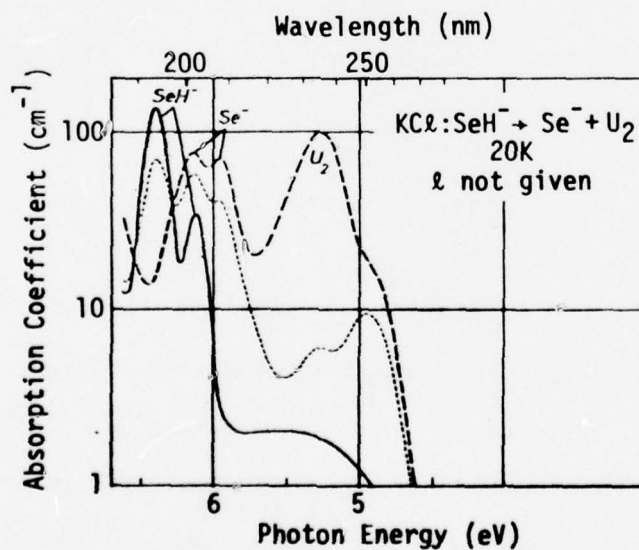
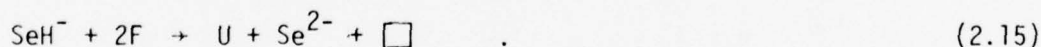


Fig. 2.74. Photochemical decomposition of SeH^- in KCl : — original spectrum; ---- spectrum after irradiation at 20 K with an aluminum arc; spectrum after a brief warming to 150 K. [F. Fischer, *Z. Physik* 187, 262 (1965).]

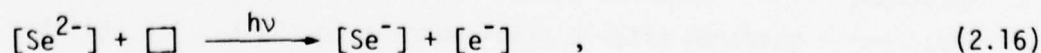
and interstitial hydrogen after illumination by an aluminum arc lamp. This curve has a new pair of bands at 6.15 eV (202 nm) and 5.96 eV (208 nm) which may be attributed to the Se^- bands by their similarity to the photochemically produced O^- and S^- bands from the OH^- and SH^- ions, respectively.^{2.47, 2.56} The dotted curve in Fig. 2.74 represents the irradiated crystal after a brief annealing at 150 K. The U_2 centers have partly recombined with Se^- centers to reform some of the SeH^- , and partly recombined with themselves to form hydrogen molecules at interstitial sites. In the spectral region of the U_2 band, there appear absorption bands at 4.95 eV (250 nm) and 5.28 eV (235 nm) which may be assigned to Se^- centers by analogy with the S^- centers in Fig. 2.68. It is not possible to produce a single Se^- band by photochemical conversion of SeH^- between 120 and 150 K without interference from U or U_2 centers, as in the case of SH^- .

19. Reduction of SeH^- by F centers, and thermal annealing. SeH^- can be reduced with an excess of potassium, which creates F centers, according to the reaction:



After quenching from 700 C to 20 C, the yellow, reduced crystal^{2.62} is characterized by a Se^{2-} double band at 3.14 eV (395 nm) and 3.41 eV (364 nm), and the U band at 5.87 eV (211 nm) as shown by the dashed line in Fig. 2.75.

In this state, the crystal will fluoresce a yellow-orange color upon UV excitation. In addition, the Se^{2-} ions may be converted to Se^- ions and F centers by the reaction:



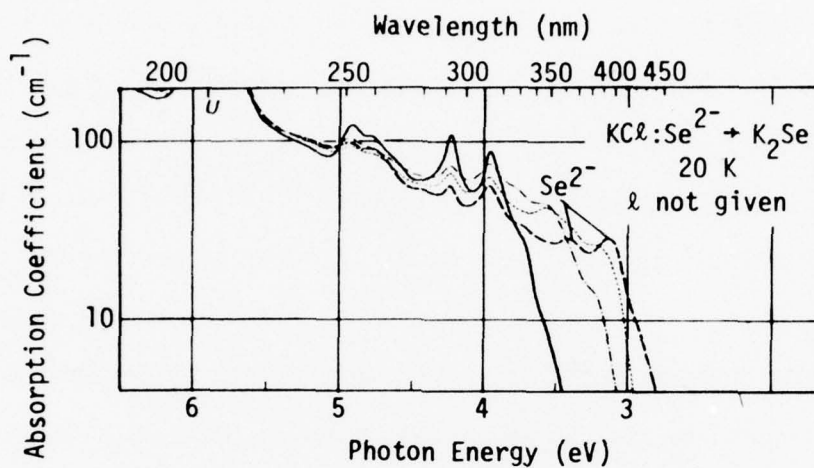


Fig. 2.75. The formation of the precipitated K_2Se double band after annealing of quenched $KCl:Se^{2-}$: ----- reduced with F centers and quenched from 700 C to 20 C. The remaining curves demonstrate thermal annealing which causes the growth of the precipitated K_2Se double band at 3.96 eV and 4.23 eV at the expense of the Se^{2-} double band and the U band. Spectrum of 10-min annealing at: ----- 90 C, 140 C, ——— 340 C. [F. Fischer, Z. Physik 187, 262 (1965).]

or the Se^{2-} ions may recombine with anion vacancies to precipitate as K_2Se at temperatures above 20 C. The dotted, dot-dashed, and solid curves in Fig. 2.75 are the spectra of $\text{KCl}:\text{Se}^{2-}$ after ten-minute annealings at 90 C, 140 C, and 340 C, respectively. These curves demonstrate the growth under thermal annealing of the K_2Se double band at 4.23 eV (293 nm) and 3.96 eV (313 nm) at the expense of the Se^{2-} double band and the U band. Note that the dashed curve in Fig. 2.75 shows the presence of the precipitated K_2Se double band at 3.96 and 4.23 eV (313 and 293 nm) even before thermal annealing. This indicates that the quenching speed is not fast enough to prevent the precipitation of K_2Se , which apparently has low solubility in KCl crystals and has already reached the solubility limit at high temperatures. By brief annealing at 600 C and subsequent quenching, the crystal will return to its original condition, i.e., the dashed curve, from the conditions corresponding to the other curves in Fig. 2.75. The reactions and spectra of SeH^- under reduction by F centers, UV excitation, and thermal annealing are quite analogous to those for OH^- and SH^- .

20. Spin-orbit splitting of the selenium bands. Table 2.27 summarizes the important bands and isosbestic points of selenium-related centers in KCl and KBr crystals along with the energy separations ΔE between the bands in the selenium double-band series. For SeH^- , Se^{2-} , and precipitated K_2Se , ΔE is 0.27 eV independent of the host crystal. For Se^- , ΔE is ~ 0.18 eV which differs from the other centers because it has one less electron in the outer shell. Here the SeH^- ion has been treated like Se^{2-} by considering the hydrogen in the SeH^- as a proton, H^+ .

Saum and Hensley^{2.63} have obtained values of the spin-orbit splitting ΔE of singly charged negative chalcogen ions, i.e., O^- , S^- , Se^- , and Te^-

Table 2.27. Absorption bands of SeH^- -related centers in KCl and KBr crystals at 20 K. [F. Fischer, Z. Physik 187, 262 (1965).]

	KCl			KBr		
	[nm]	[eV]	ΔE [eV]	[nm]	[eV]	ΔE [eV]
SeH^-	193.6	6.40	0.27	202.3	6.13	0.26
	202.4	6.13		211.4	5.87	
Se^-	201.6	6.15	0.19	212.6	5.83	0.17
	208.6	5.96		219	5.66	
Se^{2-}	364	3.41	0.27	374	3.32	0.27
	395	3.14		406.5	3.05	
K_2Se	293	4.23	0.27	293	4.23	0.27
	313	3.96		313	3.96	
U_2	235.4	5.27		272	4.56	
U	211.4	5.87		225	5.52	
New Center	—	—		249	4.98	
Isosbestic Points	188.5	6.58		195.5	6.34	
	197.2	6.29		206.8	6.00	

(all presumably being unstable), by extrapolating the values of ΔE from their isoelectronic series, e.g., the series Rb^{2+} , K^+ , Br^0 , ..., for Se^- . They obtained $\Delta E = 0.29$ eV for Se^- which agrees well with the value of 0.27 eV for Se^{2-} (or SeH^- and K_2Se in Table 2.27) whose valence shell has one less electron upon UV absorption and hence is equivalent to Se^- . The above extrapolation procedure for obtaining ΔE for Se^{2-} centers in crystals is presumably valid, since ΔE is experimentally known to be insensitive to the crystalline environment and the temperature.

For Se^0 , the spectroscopic table^{2.64} gives $4^3\text{P}_1 - 4^3\text{P}_2 = 0.25$ eV and $4^3\text{P}_0 - 4^3\text{P}_2 = 0.31$ eV, which disagree with the experimental value of 0.19 eV for Se^- in Table 2.27. This discrepancy may be related to the absence of paramagnetic resonance signals associated with Se^- bands; possibly Se^- ions form $(\text{Se}^-)_2$ molecules in the crystal.

21. Br^- and I^- in KCl. The Br^- absorption band^{2.65} at 7.47 eV (166 nm) in KCl at 78 K is shown in Fig. 2.76. The I^- absorption band at 6.58 eV (188 nm) in KCl at 300 K is shown in Fig. 2.77 for various iodine concentrations.^{2.61}

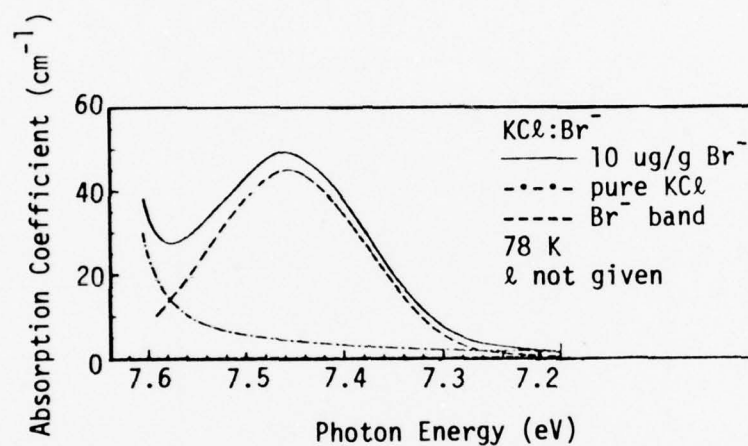


Fig. 2.76. The absorption spectrum of Br^- in KCl. [D. Hinks and S. Susman, Phys. Stat. Sol. (b) 52, K 53 (1972).]

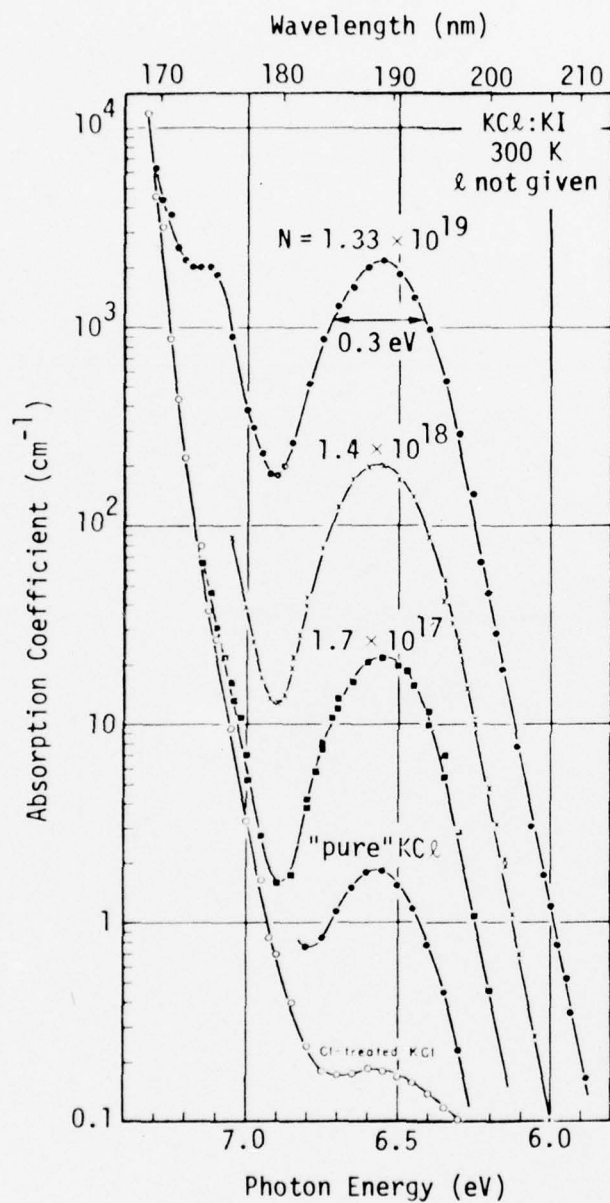


Fig. 2.77. Absorption bands of I^- in KCl for various iodine concentrations N (I^- ions per cm^{-3}). [H. Mahr, Phys. Rev. 125, 1510 (1962).]

REFERENCES*

- 2.1 T. Tomiki and T. Miyata, Jour. Phys. Soc. Japan 27, 658 (1969).
- 2.2 A. Milgram and M. P. Givens, Phys. Rev. 125, 1506 (1962).
- 2.3 J. E. Eby, K. J. Teegarden, and D. B. Dutton, Phys. Rev. 116, 1099 (1959).
- 2.4 K. J. Teegarden and G. Baldini, Phys. Rev. 155, 896 (1967).
- 2.5 C. Kittel, Introduction to Solid State Physics, Fourth Edition, John Wiley and Sons, New York, 1971.
- 2.6 R. S. Knox and K. J. Teegarden, in Physics of Color Centers, W. B. Fowler, ed., Academic Press, New York, 1968, p. 1-51.
- 2.7 American Institute of Physics Handbook, Third Edition, McGraw-Hill, New York, 1972, p. 9-151.
- 2.8 F. Lüty, in Physics of Color Centers, W. B. Fowler, ed., Academic Press, New York, 1968.
- 2.9 I. V. Smushkov, L. M. Soifer, and M. I. Shakhnovich, Fiz. Vak. Ultraviolet Izluch. 59 (1974) (Russ.).
- 2.10 R. J. Davis, J. Opt. Soc. Am. 56, 837 (1966).
- 2.11 D. A. Patterson and W. H. Vaughan, J. Opt. Soc. Am. 53, 851 (1963).
- 2.12 J. H. Beaumont, J. Bordas, A. J. Bourdilon, and M. R. Hayns, J. Phys. C: Solid State Phys. 7, L 349 (1974).
- 2.13 J. H. Schulman and W. D. Compton, Color Centers in Solids, Pergamon Press, New York, 1962.
- 2.14 J. A. Pople and D. L. Beveridge, Approximate Molecular Orbital Theory, McGraw-Hill, New York, 1970.
- 2.15 T. Kamikawa, Bull. of Yamagata University, Nat. Sci. 8 (4), 519 (1975).

*References for Sec. I are on pages 58 and 59.

Sec. II - References

- 2.16 I. V. Smushkov and M. I. Shakhnovich, *Monokrist. Tekh.* No. 5, 62 (1971) (Russ.).
- 2.17 S. C. Jain and G. D. Sootha, *Phys. Stat. Sol.* 22, 505 (1967).
- 2.18 D. B. Chase and D. S. McClure, *Jour. Chem. Phys.* 64, 74 (1976).
- 2.19 G. D. Sootha, *Phys. Stat. Sol.* (a) 1, 363 (1970).
- 2.19a M. J. Rossiter, D. B. Rees-Evans, S. C. Ellis, and J. M. Griffiths, *J. Phys. D: Appl. Phys.* 4, 1245 (1971).
- 2.19b H. Vora, J. H. Jones, and T. G. Stoebe, *J. Appl. Phys.* 46, 71 (1975).
- 2.19c R. K. Bagai, R. K. Jain, and A. V. R. Warriar, *J. Phys. C: Solid State Phys.* 7, 1219 (1973).
- 2.20 P. Berge, M. Dubois, G. Blanc, and M. Adam-Benveniste, *J. de Physique* 26, 339 (1965).
- 2.21 D. B. Fitchen, in *Physics of Solids at High Pressures*, C. T. Tomizuka and R. M. Emrick, eds., Academic Press, New York, 1965, p. 383.
- 2.22 M. R. Mayhugh and R. W. Christy, *Phys. Rev. B* 2, 3330 (1970).
- 2.23 C. J. Delbecq, W. Hayes, and P. H. Yuster, *Phys. Rev.* 121, 1043 (1961).
- 2.24 E. M. Winter, D. R. Wolfe, and R. W. Christy, *Phys. Rev.* 186, 949 (1969).
- 2.25 M. R. Mayhugh, *J. Appl. Phys.* 41, 4776 (1970).
- 2.26 J. Mort, *Solid State Commun.* 3, 263 (1965).
- 2.27 G. D. Watkins, *Phys. Rev.* 113, 79 (1959).
- 2.28 J. Davenas, A. Perez, P. Thevenard, and C. H. S. Dupuy, *Phys. Stat. Sol.* (a) 19, 679 (1973).
- 2.29 N. G. Politov and L. F. Vorozheikina, *Soviet Phys.-Solid State* 12, 277 (1971).
- 2.30 G. Mie, *Ann. Phys.* 25, 377 (1908); W. T. Doyle, *Phys. Rev.* 111, 1067 (1958); *Proc. Phys. Soc.* 75, 649 (1960).

Sec. II - References

- 2.31 A. E. Glauber and N. A. Tsal', Fiz. Tverd. Tela. 10, 935 (1968)
[Sov. Phys.-Solid State, 10, 739 (1968)].
- 2.31a A. Perez, P. Thevenard, and C. S. Dupuy, C. R. Acad. Sci. (France)
271 B, 519 (1970).
- 2.32 R. Sano, J. Phys. Soc. Japan 27, 695 (1969).
- 2.33 R. Voszka, K. Raksányi, and I. Földvári, Kristall und Technik 8,
1347 (1973).
- 2.34 I. Földvári, R. Voszka, and K. Raksányi, Phys. Stat. Sol. (a) 26,
K83 (1974).
- 2.35 American Institute of Physics Handbook, Third Edition, McGraw-Hill,
New York, 1972, p. 6-45.
- 2.36 S. Kapphan and F. Lüty, J. Phys. Chem. Solids 34, 969 (1973).
- 2.37 E. Freytag, Z. Physik 177, 206 (1964).
- 2.38 M. L. Meistrich, J. Phys. Chem. Solids 29, 1119 (1968).
- 2.39 I. Földvári and R. Voszka, Phys. Stat. Sol. (a) 31, 765 (1975).
- 2.40 I. Földvári and R. Voszka, Phys. Stat. Sol. (a) 28, 249 (1975).
- 2.41 D. B. Chase and D. S. McClure, J. Chem. Phys. 64, 74 (1976).
- 2.42 J. F. Sabatini, A. E. Salwin, and D. S. McClure, Phys. Rev. B 11,
3832 (1975).
- 2.43 E. Loh, to be published.
- 2.44 J. P. Srivastava, J. Chem. Phys. 48, 5283 (1968).
- 2.45 W. C. Collins, I. Schneider, P. H. Klein, and L. R. Johnson, Appl.
Phys. Lett. 24, 403 (1974).
- 2.46 J. E. Eby, K. J. Teegarden, and D. B. Dutton, Phys. Rev. 116, 1099
(1959).
- 2.47 F. Kerkhoff, W. Martienssen, and W. Sander, Z. Physik 173, 184 (1963).
- 2.48 F. Fischer, Z. Physik 204, 351 (1967).

Sec. II - References

- 2.49 F. Fischer, *Solid State Commun.* 2, 51 (1964).
- 2.50 J. Rolfe, F. R. Lipsett, and W. J. King, *Phys. Rev.* 123, 447 (1961).
- 2.51 F. Fischer, H. Gründig, and R. Hilsch, *Z. Physik* 189, 79 (1966).
- 2.52 C. C. Klick and M. N. Kabler, *Phys. Rev.* 131, 1075 (1963).
- 2.53 F. Kerkhoff, *Z. Physik* 158, 595 (1960).
- 2.54 W. Rauch, *Z. Physik* 116, 652 (1940).
- 2.55 F. Fischer, *Z. Physik* 139, 328 (1954).
- 2.56 F. Fischer and H. Gründig, *Z. Physik* 184, 299 (1965); *Phys. Lett.* 13, 113 (1964).
- 2.57 I. H. Schulman and R. D. Kirk, *Solid State Commun.* 2, 105 (1964).
- 2.58 W. Sander, *Z. Physik* 169, 353 (1962).
- 2.59 A. Hausman, *Z. Physik* 192, 313 (1966).
- 2.60 J. Rolfe, *Appl. Phys. Lett.* 6, 66 (1965).
- 2.61 H. Mahr, *Phys. Rev.* 125, 1510 (1962).
- 2.62 F. Fischer, *Z. Physik* 187, 262 (1965).
- 2.63 G. A. Saum and E. B. Hensley, *Phys. Rev.* 113, 1019 (1959).
- 2.64 Landoit-Börnstein: 6th Edition, Volume 1, Part 1. Berlin-Göttingen-Heidelberg: Springer (1950).
- 2.65 D. Hinks and S. Susman, *Phys. Stat. Sol. (b)* 52, K53 (1972).

CONTENTS OF PRESENT AND PREVIOUS REPORTS

First Technical Report, March 1972

1. Introduction
 2. Calculation of Multiphonon Absorption Coefficients
 3. Calculation of Extrinsic Absorption Coefficient
 4. Effects of Pressure on Operation of Windows
 5. Recommendations for an Experimental Program
 6. Experimental Data from the Literature
 7. Nonlinear Processes
- App. A - Elementary Introduction to the Theory of Infrared Absorption Spectra

Second Technical Report, June 1972

1. Introduction
 2. Calculation of Multiphonon Absorption Coefficient
 3. Green's Function Analysis and Sjolander-Type Approximations
 4. Rigid-Ion, Next-Near-Neighbor Model for the Scattering Hamiltonian
 5. Pressure-Induced Optical Distortion in Laser Windows
 6. Plans for Continued Research
- App. A - Tabulation of Pressure-Induced Optical-Distortion Results
- App. B - Eigenvectors for the Rigid-Ion, Next-Near-Neighbor Model

Final Technical Report, December 1972

- A. Introduction
- B. Theory of Multiphonon Infrared Absorption
- C. Theory of Infrared Absorption and Material Failure in Crystals
Containing Inclusions
- D. Collection of Experimental Results for $B(\omega)$
- E. References to Previous Multiphonon Calculations

First Technical Report, June 1973

- A. Introduction
- B. Theory of Infrared Absorption and Material Failure in Crystals
Containing Inclusions
- C. Theory of Multiphonon Absorption in Insulating Crystals
- D. Temperature Dependence of Multiphonon Infrared Absorption
- E. Theory of Infrared Absorption by Crystals in the High Frequency
Wing of Their Fundamental Lattice Absorption
- F. Temperature Dependence of the Absorption Coefficient of Alkali
Halides in the Multiphonon Regime
- G. Temperature and Frequency Dependence of Infrared Absorption as a
Diagnostic Tool
- H. Short-Pulse Operation of Infrared Windows without Thermal Defocusing

Second Technical Report, December 1973

- A. Introduction
- B. Extrinsic Absorption
- C. Extrinsic Absorption in 10.6 μm Laser Window Materials Due to Molecular-Ion Impurities
- D. Very High-Intensity Effects
- E. Explanation of Laser-Damage Cone-Shaped Surface Pits
- F. Nonlinear Infrared Absorption from Parametric Instabilities of Phonons
- G. High-Power 2-6 μm Window-Material Figures of Merit with Edge Cooling and Surface Absorption Included
- H. High-Power 10.6 μm Window-Material Figures of Merit with Edge Cooling and Surface Absorption Included
- I. Explicit Exponential Frequency Dependence of Multiphonon Infrared Absorption
- J. Quasiselection Rule for Infrared Absorption by NaCl-Structure Crystals
- K. The Absorption Coefficient of Alkali Halides in the Multiphonon Regime: Effects
- L. Vertex Corrections for Multiphonon Absorption
- M. Negligible Intrinsic-Absorption Processes
- N. Summary of Publications and Results
- App. - Simple Pendulum Instability

Third Technical Report, June 1974

- A. Introduction and Summary
- B. Intensity Limits of High-Intensity Vacuum Ultraviolet Materials
- C. Multiphoton Absorption
- D. Calculated Reflectance of Aluminum in the Vacuum Ultraviolet
- E. Total-Internal-Reflection Devices
- F. The Scattering and Absorption of Electromagnetic Radiation by a Semi-Infinite Crystal in the Presence of Surface Roughness
- G. Infrared Absorption by the Higher-Order-Dipole-Moment Mechanism
- H. Stimulated Raman and Brillouin Scattering: Parametric Instability Explanation of Anomalies
- I. Extrinsic Absorption in 10.6 μm Laser Window Materials
- J. Erratum, High-Power 2- to 6- μm Window-Material Figures of Merit with Edge Cooling and Surface Absorption Included
- K. List of Recent Publications

Fourth Technical Report, December 1974

- A. Introduction and Summary
- B. Stimulated Raman Scattering: Enhanced Stokes Gain and Effects of Anti-Stokes and Parametric Phonon Processes
- C. Enhanced Stimulated Raman Scattering and General Three-Boson Parametric Instabilities
- D. Theory of Laser-Materials Damage by Enhanced Stimulated Raman Scattering

Fourth Technical Report, December 1974 (Cont.)

- E. Surface Roughness and the Optical Properties of a Semi-Infinite Material; The Effect of a Dielectric Overlayer
- E. App. — Construction of the Green's Functions for the Electromagnetic Wave Equation
- F. Theory of Laser Heating of Solids: I. Metals
- G. Current Status of High-Intensity Vacuum Ultraviolet Materials
- H. Impurity Absorption in Halide Window Materials
- I. List of Recent Publications

Fifth Technical Report, June 1975

- A. Introduction and Summary
- B. Current Status of Electron-Avalanche-Breakdown Theory
- C. Preliminary Theory of Electron-Avalanche Breakdown in Dielectric by Laser and dc Fields
- D. VUV Window Failure by Multiphoton Absorption and Electron Defocusing, Avalanche, and Absorption
- E. Optical Distortion from the Nonlinear Refractive Index
- F. Studies of Optical Properties of Alkali Halide Crystals
- G. A Possible Mechanism for Extrinsic Absorption in Insulators below the Fundamental Absorption Edge
- H. Multiphonon Absorption of Alkali Halides and Quasiselection Rules
- I. Enhanced Stimulated Raman Scattering and General Three-Boson Parametric Instabilities
- J. List of Publications

Sixth Technical Report, December 1975—Special Report on Optical Coatings

- I. Summary of Results
- II. Near-Term Recommendation
- III. Background Information
- IV. Possible Sources of Additional Absorption in Coatings
- V. Suggested Measurements
- VI. Other Problems
- VII. Laser Heating of Coatings
- VIII. Laser Damage of Coatings
- IX. Laser Damage of Detached Coatings
- X. Guidelines for Selecting New Materials
- XI. Candidate 10.6 μm Coating Materials
- XII. Candidate 2-6 μm Coating Materials
- XIII. Excerpts and Results from Literature, with Comments

Seventh Technical Report, June 1976

- A. Introduction and Summary
- B. Polymer Coatings for Protection of Optical Components
- C. Electronic Properties of the LiF Valence Band; Surface States and the Local Density of States Near the Surface
- C. App. — Explicit Form of the Hamiltonian for the N Layer LiF Slab

Seventh Technical Report, June 1976 (Cont.)

- D. Localized Electronic States in Alkali Halides Associated with a Substitutional Anion Impurity
- E. Classical Transport Equation for Electron-Avalanche Breakdown
- F. Evaluation of Two-Center Integrals of Slater Atomic Orbitals
- G. Quasiselection Rules for Multiphonon Absorption in Alkali Halides
- H. Irradiance Limits for Vacuum-Ultraviolet Material Failure
- I. Materials for High-Power Window and Mirror Coatings and Multilayer-Dielectric Reflectors

Eighth Technical Report, December 1976

- A. Summary and Introduction
- B. Optical Distortion and Failure in High-Power Reflectors
 - B. App. - Heat Flow in Many-Layered Structures
- C. Thermal Stresses and Expansion in Multilayer Dielectric Reflectors
 - C. App. - Useful Thermal-Stress Results
- D. Failure Thresholds of Near-Ultraviolet Transparent Materials
- E. Laser-Induced Electron Avalanches in Insulating Solids
 - E. App. A - Deviation of the Classical Transport Equation
 - E. App. B - Contribution of Electronically Inelastic Collisions to the Transport Equation
- F. Overview of Materials for High-Power Visible and Ultraviolet Lasers

Ninth Technical Report, June 1977
Special Report on Impurity Absorption, Vol. I

- I. Introduction
- II. Alkali Halides
 - A. Intrinsic Properties of Alkali Halides
 - B. Comparisons of Alkali-Halide Impurity Spectra
 - C. Lithium Fluoride
 - D. Sodium Fluoride
 - E. Potassium Chloride

LIST OF PUBLICATIONS

All publications of this program and the previous programs are included in the following list:

1. M. Sparks, Immediate Needs of the High-Power Infrared Window Program and Methods of Reducing Thermally Induced Optical Distortion, Rand Corporation Report WN-7243-PR, June 1971.
2. M. Sparks, Stress and Temperature Analysis for Surface Cooling or Heating of Laser Window Materials, Parke Mathematical Laboratories TM-1, July 1971.
3. M. Sparks, Temperature and Stress Analysis for Bulk- and Surface-Heated Slabs, Parke Mathematical Laboratories TM-2, August 1971.
4. M. Sparks, Optical Distortion by Heated Windows in High-Power Laser Systems, Rand Corporation Report R-545-PR, September 1971.
5. M. Sparks, Calculated Temperature Distributions in Slabs Heated in a Thin Surface Layer, Parke Mathematical Laboratories TM-3, September 1971.
6. M. Sparks, "Optical Distortion by Heated Windows in High-Power Laser Systems," J. Appl. Phys. 42, 5029 (1971).
7. M. Sparks, "Introduction to the High-Power Infrared Window Material Problem," AFCRL Conference on High-Power IR Laser Window Materials, December 1971.
8. M. Sparks, "Engineering Approaches to High-Power Infrared Window Problems," AFCRL Conference on High-Power IR Laser Window Materials, December 1971.
9. M. Sparks and T. Azzarelli, Theoretical Studies of High-Power Infrared Window Materials, Xonics Quarterly Technical Progress Report No. 1, Contract DAHC15-72-C-0129, March 1972.
10. M. Sparks, "Recent Developments in High-Power Infrared Window Research," NBS Spec. Publ. 372, 4th ASTM Symposium on Laser Induced Damage in Optical Materials, Boulder, Colo., June 14-15, 1972.
11. M. Sparks and T. Azzarelli, Theoretical Studies of High-Power Infrared Window Materials, Xonics Quarterly Technical Progress Report No. 2, Contract DAHC15-72-C-0129, June 1972.

12. M. Sparks and L. J. Sham, "Theory of Multiphonon Infrared Absorption," AFCRL Conference on High-Power IR Laser Window Materials, Hyannis, Mass., Oct. 30 - Nov. 1, 1972.
13. M. Sparks and M. Cottis, "Pressure-Induced Optical Distortion in Infrared Windows," AFCRL Conference on High-Power Infrared Laser Window Materials, Hyannis, Mass., Oct. 30 - Nov. 1, 1972.
14. M. Sparks, Theoretical Studies of High-Power Infrared Window Materials, Xonics Final Report, Contract DAHC15-72-C-0129, December 1972.
15. M. Sparks and L. J. Sham, "Exponential Frequency Dependence of Multiphonon Summation Infrared Absorption," Solid State Commun. **11**, 1451 (1972).
16. C. J. Duthler and M. Sparks, "Theory of Material Failure in Crystals Containing Infrared Absorbing Inclusions," NBS Spec. Publ. 387, 5th ASTM-ONR-NBS Symposium on Laser Induced Damage in Optical Materials, Boulder, Colo., May 15-16, 1973.
17. M. Sparks, Theoretical Studies of High-Power Infrared Window Materials, Xonics First Technical Report, Contract DAHC15-73-C-0127, June 30, 1973.
18. M. Sparks, Physical Principles, Materials Guidelines, and Materials List for High-Power 10.6 μ Windows, Rand Corporation Report R-863-PR, September 1973.
19. M. Sparks, C. J. Duthler, H. C. Chow, L. J. Sham, A. A. Maradudin, and D. L. Mills, "Theoretical Studies of High-Power Infrared Window Materials," AFCRL Conference on High-Power Infrared Laser Window Materials, Hyannis, Mass., Nov. 12-14, 1973.
20. M. Sparks and H. C. Chow, "High-Power 10.6 μ m Window Material Figures of Merit with Edge Cooling and Surface Absorption Included," AFCRL Conference on High-Power Infrared Laser Window Materials, Hyannis, Mass., Nov. 12-14, 1973.
21. M. Sparks and C. J. Duthler, Theoretical Studies of High-Power Infrared Window Materials, Xonics Second Technical Report, Contract DAHC15-73-C-0127, Dec. 6, 1973.
22. M. Sparks, "Short-Pulse Operation of Infrared Windows without Thermal Defocusing," Appl. Opt. **12**, 2033 (1973).
23. M. Sparks, "Temperature and Frequency Dependence of Infrared Absorption as a Diagnostic Tool," Appl. Phys. Lett. **23**, 368 (1973).
24. M. Sparks and M. Cottis, "Pressure-Induced Optical Distortion in Laser Windows," J. Appl. Phys. **44**, 787 (1973).
25. M. Sparks and C. J. Duthler, "Theory of Infrared Absorption and Material Failure in Crystals Containing Inclusions," J. Appl. Phys. **44**, 3038 (1973).

26. M. Sparks, "Stress and Temperature Analysis for Surface Cooling or Heating of Laser Window Materials," J. Appl. Phys. 44, 4137 (1973).
27. D. L. Mills and A. A. Maradudin, "Theory of Infrared Absorption by Crystals in the High Frequency Wing of Their Fundamental Lattice Absorption," Phys. Rev. B 8, 1617 (1973).
28. M. Sparks and L. J. Sham, "Theory of Multiphonon Absorption in Insulating Crystals," Phys. Rev. B 8, 3037 (1973).
29. M. Sparks and L. J. Sham, "Temperature Dependence of Multiphonon Infrared Absorption," Phys. Rev. Lett. 31, 714 (1973).
30. A. A. Maradudin and D. L. Mills, "Temperature Dependence of the Absorption Coefficient of Alkali Halides in the Multiphonon Regime," Phys. Rev. Lett. 31, 718 (1973).
31. C. J. Duthler and M. Sparks, "Extrinsic Absorption in Laser Window Materials," NBS Spec. Publ. 414, 6th ASTM-ONR-NBS Symposium on Laser Induced Damage in Optical Materials, Boulder, Colo., May 22-23, 1974.
32. M. Sparks and C. J. Duthler, Theoretical Studies of High-Power Ultraviolet and Infrared Materials, Xonics Third Technical Report, Contract DAHC15-73-C-0127, June 30, 1974.
33. M. Sparks and C. J. Duthler, "Current Status of High-Intensity Vacuum Ultraviolet Materials," 4th ARPA Conference on Infrared Laser Window Materials, Tucson, Ariz., Nov. 18-20, 1974.
34. C. J. Duthler, "Impurity Absorption in Halide Window Materials," 4th ARPA Conference on Infrared Laser Window Materials, Tucson, Ariz., Nov. 18-20, 1974.
35. M. Sparks and C. J. Duthler, Theoretical Studies of High-Power Ultraviolet and Infrared Materials, Xonics Fourth Technical Report, Contract DAHC15-73-C-0127, Dec. 6, 1974.
36. C. J. Duthler, "Explanation of Laser-Damage Cone-Shaped Surface Pits," Appl. Phys. Lett. 24, 5 (1974).
37. M. Sparks and H. C. Chow, "High-Power 2-6 μ m Window-Material Figures of Merit with Edge Cooling and Surface Absorption Included," J. Appl. Phys. 45, 1510 (1974).
38. C. J. Duthler, "Extrinsic Absorption in 10.6 μ m Laser Window Materials Due to Molecular-Ion Impurities," J. Appl. Phys. 45, 2668 (1974).
39. L. J. Sham and M. Sparks, "Explicit Exponential Frequency Dependence of Multiphonon Infrared Absorption," Phys. Rev. B 9, 827 (1974).
40. C. J. Duthler and M. Sparks, "Quasiselection Rule for Infrared Absorption by NaCl-Structure Crystals," Phys. Rev. B 9, 830 (1974).

41. M. Sparks and H. C. Chow, "Parametric Instabilities of Phonons: Nonlinear Infrared Absorption," Phys. Rev. B 10, 1699 (1974).
42. D. L. Mills and A. A. Maradudin, "The Absorption Coefficient of Alkali Halides in the Multiphonon Regime: Effects of Nonlinear Dipole Moments," Phys. Rev. B 10, 1713 (1974).
43. M. Sparks, "Infrared Absorption by the Higher-Order-Dipole-Moment Mechanism," Phys. Rev. B 10, 2581 (1974).
44. M. Sparks, "Stimulated Raman and Brillouin Scattering: Parametric Instability Explanation of Anomalies," Phys. Rev. Lett. 32, 450 (1974).
45. M. Sparks and C. J. Duthler, Theoretical Studies of High-Power Ultra-violet and Infrared Materials, Xonics Fifth Technical Report, Contract DAHC15-73-C-0127, June 30, 1975.
46. M. Sparks, "Current Status of Electron-Avalanche-Breakdown Theories," NBS Spec. Publ. 435, 7th ERDA-ASTM-ONR-NBS Symposium on Laser Induced Damage in Optical Materials, Boulder, Colo., July 29-31, 1975.
47. C. J. Duthler and M. Sparks, "Irradiance Limits for Vacuum Ultra-violet Material Failure," NBS Spec. Publ. 435, 7th ERDA-ASTM-ONR-NBS Symposium on Laser Induced Damage in Optical Materials, Boulder, Colo., July 29-31, 1975.
48. C. J. Duthler, J. Harrington, F. Patten, and M. Hass, "Multiphonon Absorption of Alkali Halides and Quasiselection Rules," 5th DARPA Conference on Infrared Laser Window Materials, Las Vegas, Nevada, Dec. 1-4, 1975.
49. M. Sparks, Theoretical Studies of Materials for High-Power Infrared Coatings, Xonics Sixth Technical Report, Contract DAHC15-73-C-0127, Dec. 31, 1975.
50. H. C. Chow and M. Sparks, "Calculated Reflectance of Aluminum in the Vacuum Ultraviolet," J. Appl. Phys. 46, 1307 (1975).
51. M. Sparks, "Theory of Laser-Materials Damage by Enhanced Stimulated Raman Scattering," J. Appl. Phys. 46, 2134 (1975).
52. M. Sparks, "Stimulated Raman Scattering: Enhanced Stokes Gain and Effects of Anti-Stokes and Parametric Phonon Processes," Phys. Rev. A 11, 595 (1975).
53. A. A. Maradudin and D. L. Mills, "The Scattering and Absorption of Electromagnetic Radiation by a Semi-Infinite Crystal in the Presence of Surface Roughness," Phys. Rev. B 11, 1392 (1975).
54. D. L. Mills and A. A. Maradudin, "Surface Roughness and Optical Properties of a Semi-Infinite Material: The Effect of a Dielectric Overlayer," Phys. Rev. B 12, 2943 (1975).

55. M. Sparks and J. H. Wilson, "Enhanced Stimulated Raman Scattering and General Three-Boson Parametric Instabilities," *Phys. Rev. B* 12, 4493, (1975).
56. M. Sparks and C. J. Duthler, Theoretical Studies of High-Power Ultra-violet and Infrared Materials, Xonics Seventh Technical Report, Contract DAHC15-73-C-0127, June 30, 1976.
57. M. Sparks, "Overview of Materials for High-Power Visible and Ultra-violet Lasers," DARPA Infrared Laser Window Materials Meeting, Boulder, Colo., July 12, 1976.
58. M. Sparks, "Materials for High-Power Window and Mirror Coatings and Multilayer-Dielectric Reflectors," NBS Spec. Publ. 462, 8th NBS-ASTM-ONR-ERDA-DARPA Symposium on Laser Induced Damage in Optical Materials, Boulder, Colo., July 13-15, 1976.
59. C. J. Duthler, "Quasiselection Rules for Multiphonon Infrared Absorption in Alkali Halides," American Physical Society Meeting, Atlanta, Ga., Mar. 29-Apr. 1, 1976. Abstract published: *Bull. Am. Phys. Soc.* 21, 419 (1976).
60. C. J. Duthler, "Simplified Method for Calculating Multiphonon Infrared Absorption in Alkali-Halide Window Materials," Topical Meeting on Optical Phenomena in Infrared Materials, Annapolis, Md., Dec. 1-3, 1976.
61. M. Sparks and C. J. Duthler, Theoretical Studies of High-Power Ultra-violet and Infrared Materials, Xonics Eighth Technical Report, Contract DAHC15-73-C-0127, Dec. 31, 1976.
62. M. Sparks, "Theory of Laser Heating of Solids: Metals," *J. Appl. Phys.* 47, 837, 1976.
63. C. J. Duthler, "Quasiselection Rules for Multiphonon Absorption in Alkali Halides," *Phys. Rev. B* 14, 4606 (1976).
64. J. A. Harrington, C. J. Duthler, F. W. Patten, and M. Hass, "Multiphonon Absorption of Alkali Halides and Quasiselection Rules," *Solid State Commun.* 18, 1043 (1976).
65. P. Sen, "A Reply to Electronic Excitations in LiF: 10-70 eV," submitted to *Physical Review*.
66. M. Flannery and M. Sparks, "Protective Polymer Coatings," to be submitted to *Applied Optics*.
67. M. Sparks, "A Simple Method for Calculating the Optical Properties of Multilayer-Dielectric Reflectors," submitted to *J. Opt. Soc. Am.*
68. M. Sparks and P. N. Sen, "Possible Reduction of Laser-Fusion Target Illumination by Enhanced Stimulated Raman Plasmon Scattering," submitted to *Phys. Rev. Lett.*

69. M. Sparks, "Optical Distortion and Failure in High-Power Reflectors," in preparation.
70. M. Sparks, "Thermal Stresses and Expansion in Multilayer Dielectric Reflectors," in preparation.
71. H. Vora, M. Flannery, and M. Sparks, Tabulation of Impurity Absorption Spectra - Ultraviolet and Visible, Xonics Ninth Technical Report, Contract DAHC15-73-C-0127, June 30, 1977.
72. M. Sparks and E. Loh, Jr., "Theoretical Thresholds for Damage to High-Power Metallic Reflectors," in preparation.
73. M. Flannery, M. Sparks, and E. Loh, Jr., "Theory of Highly Reflecting Dielectric Mirrors," in preparation.
74. M. Sparks and E. Loh, Jr., "Theory of Badly Degraded Optics," in preparation.
75. P. Sen and M. Sparks, "Theory of the Time Dependence of Enhanced Raman Scattering," in preparation.
76. P. Sen and M. Sparks, "Ferromagnetic Instability Results from the Mode-Amplitude Equations; Relation to Enhanced Raman Scattering," in preparation.
77. P. Sen and M. Sparks, "Comments on the Resolution of Discrepancies in Enhanced Raman Scattering," in preparation.